The immobilisation of TiO_2 in various heterogeneous hosts for the photocatalytic oxidation of cyanide.

By

Gerard James Morgan

A Thesis presented to the University of Dublin for the degree of Doctor in Philosophy.

Department of Chemistry,
University of Dublin,
Trinity College.

August 2000.

Ammended Declaration

I give permission for the library of the university of Dublin to lend or copy this thesis upon request.

Gerard Morg .

Gerard Morgan.

Acknowledgements

Is this really the end, many of you will continue to ask, including myself, well I can put your minds at ease, because I promised myself that I wouldn't put pen to paper for this, the most important and probably the most interesting section of this thesis, until I was fully sure. After serving what has felt like a life sentence at D.I.T, my release date has finally come.

Firstly I would like to thank my supervisor, Dr. Declan Mc Cormack (DIT) for his continual encouragement and support. I would also like to thank Dr Donall MacDonaill (TCD), for his assistance and support.

I owe much appreciation to all the technical staff at D.I.T Kevin St. for their valuable expertise, assistance and generosity during my post graduate years. Financial assistance in the form of a scholarship grant awarded by D.I.T is also greatly appreciated and acknowledged.

Throughout my years as a postgraduate student at D.I.T, I have had the opportunity of working with a number of brilliant individuals: Aaron Ryder, Devin Donnelly, Stephen Bradley, John O'Gorman, Dave Butler and Enda Howard. Good Luck Lads!

Going further back to my undergraduate years at D.I.T, top of the list is Toffo (Derek Farrell) who always told me 'you'll do one of those Ph.D.'s one day'. 'Well Toff yet again looks like you were right'. I would also like to mention Derek's family particularly Mick (RIP) and Bernie who always gave me a warm welcome on my many weekend excursions to Mullingar.

I am also indebted to my own family, particularly my parents who stood by me and encouraged me all the way through, thanks Mam, and Dad for the hugs and prayers throughout. You have both been a great support and I can assure you both that I won't return to college, not for a few years anyway. I would also like to thank John and Antoinette for the use of their computer.

Finally there is just one other person I would like to mention, without whom this thesis would not be possible. Caroline, thanks, not necessarily for coming along at the right time, but for the very special person you are, you gave continual support and had an incredible amount of patience with me as I struggled to finish. Your persistence and continual encouragement throughout the last number of years has been wonderful……

Yes, it's really done!

Summary

The main focus of this study lies in the preparation and characterisation of TiO_2. The formation of a nanoparticulate semiconductor may offer interesting photophysical properties and have applications as a photocatalyst. Thus the immobilisation and characterisation of nano particulate TiO_2 in both Nafion ionomer membranes, Langmuir-Blodgett (LB) films and surfactant stabilised sols have been attempted.

Initial LB studies have focussed on examining the pressure-area isotherm behaviour associated with a number of different carboxylic acids, namely stearic acid (octadecanoic acid, $CH_3(CH_2)_{16}COOH$), palmitic acid (hexadecanoic acid, $CH_3(CH_2)_{14}COOH$) and oleic acid (octadec-9-enoic acid, $CH_3(CH_2)_7CH{=}CH(CH_2)_7COOH$) at the air-water interface. Studies have been extended to the investigation of identical monolayers, on aqueous subphase solutions containing divalent metal cations such as Cd^{2+} and Zn^{2+} in the concentration range 10^{-5}-10^{-3} mol dm^{-3}. Increasing the concentration of either Cd^{2+} or Zn^{2+} under monolayers of stearic and palmitic acid resulted in a corresponding decrease in both the number of observed phase transitions and molecular area (25Å^2-21Å^2) changing the entire isotherm shape. Oleic acid exhibits a comparatively unchanged isotherm shape throughout a similar concentration range. Cd^{2+} ions beneath monolayers of stearic, palmitic or oleic acid show a greater decrease in monolayer molecular area compared to Zn^{2+}. Monolayer stability appears highest using Cd^{2+} ions, particularly at 10^{-5} mol dm^{-3}. A number of cadmium stearate (Cd-St) multilayer LB films were successfully deposited on quartz slides. A similar methodology has been developed for the examination of isotherm behaviour and subsequent film transfer, for LB films of stearic acid containing trivalent metal cations at similar concentrations to those described above. Trivalent monolayers show greater condensing characteristics compared to their divalent counterparts. Transfer of Ti-St films appears most uniform at a surface pressure of 15mN/m from an aqueous subphase containing 10^{-5} mol dm^{-3} Ti^{3+} ions. Multilayer films (250 layers) of Ti-St were prepared using this technique and were subsequently oxidised to TiO_2.

Nano particulate TiO_2 films were formed and electron diffraction studies revealed the anatase form. Uv-vis measurements indicate an absorption onset of 337 nm. This corresponds to an average particle size of 21.5Å and blue shift in the absorption spectra of 0.48 eV from the bulk band gap (3.2 eV). The corresponding TEM data suggests a maximum particle diameter of 70Å indicating quite a large particle size distribution. Atomic force microscopy measurements show a significantly smooth TiO_2 ceramic film.

An alternative method to that described above was used for forming well-defined TiO_2 particles with a narrow particle size distribution. Cetyltrimethylammonium bromide, (CTAB, $CH_3(CH_2)_{15}N(CH_3)_3Br$) and dioctadecyldimethylammonium bromide (DODAB, $(CH_3\ (CH_2)_{16}CH_2]_2N(CH_3)_2Br$ stabilised TiO_2 particles exhibit absorption bands at 329 nm (3.77 eV) and 336 nm (3.69 eV). DODAB stabilised TiO_2 appears more stable from an LB viewpoint, compared to CTAB stabilised TiO_2.

Nafion ionomer membranes were also investigated as heterogeneous hosts for the incorporation of TiO_2 particles within or at the membrane surface. Nano particulate TiO_2 was precipitated in Nafion 117 membranes using the ion exchange (Ti^{3+}) technique, followed by exposure to KOH. TiO_2 particles exhibit absorption onsets between 314 and 320 nm, corresponding to a particle size distribution and band gap energy range of 17.9-18.7 Å and 3.88-3.95 eV respectively, while TEM analysis shows larger particle aggregates up to 100Å.

Reaction rate constants for cyanide photo-oxidation using unsupported TiO_2 (Degussa P-25, 75% anatase, 25% rutile, particle size of 0.015-0.040 μm and Kronos APF 100 mg, 100% anatase, particle size: 0.075-0.2 μm) were recorded and compared with rate constants obtained for a similar reaction, however using Nafion and LB supported TiO_2. Degussa P-25 exhibits the highest rate constant of 2.1×10^{-2} min^{-1} followed by Nafion bound TiO_2 (2.0×10^{-2} min^{-1}) containing 16.9 mg TiO_2. Kronos APF shows intermediate catalytic activity having a rate constant of 1.1×10^{-2} min^{-1}. Finally TiO_2 films formed using the LB technique showed promising photocatalytic activity with rate constants of 2.3×10^{-3} and 3.9×10^{-3} min^{-1} using only 1.5μg and 6.3 μg of TiO_2 respectively.

Table of contents

Chapter 5: Discussion

Chapter 1

General introduction to the thesis

Chapter 1: General introduction

1.1.1 Photocatalysis An overview

The environment and everything connected with it has been a major concern of the public because most of our ecological systems such as air, water and soil are being continuously polluted by domestic, industrial and military pollutants[1].

It is essential that further pollution be prevented and that controls be introduced and enforced to curtail avoidable pollution and to minimise the risk of accidental pollution. The challenge is to seek the safest and most economical means by which this can be achieved. Many processes have been proposed over the years and are currently employed to destroy a wide variety of both organic and inorganic pollutants[2]. Such processes include chlorination, ozonation, solidification, and more recently the adsorption of contaminants onto activated carbon and photocatalytic oxidation. (The above processes are reviewed in chapter 2.1.1 and 2.1.2.

The photocatalytic process has been discussed in the scientific literature as an alternative method to those described above for the cleaning of polluted water since the 1970's.[3] Compilations of substances susceptible to photocatalytic oxidation are now available[1]. Several review articles have recently been published discussing the underlying processes, illustrating numerous laboratory and field studies[4].

Photocatalytic oxidation of contaminants in solution can occur on reactive or non-reactive solid supports.

---

[1] U.S. Aithal, T.M. Aminabhavi, S.S. Shukla. J. Hazardous Materials. 1993, 33, 369-400.
[2] R.W. Matthews, Pure & Appl. Chem. 1992, 64,1285-1290.
[3] R. Dillert, D. Bahnemann, E.P.A. Newsletter. 1994, 52 33-53.
[4] M.R. Hoffmann, S.T. Martin, W. Choi, D.W. Bahnemann, Chem. Rev., 1995, 95, 69-96.

I. Non-reactive surfaces such as silica and alumina provide a three-dimensional arrangement; these surfaces are capable of controlling photochemical efficiencies by assisting the transfer of electrons between two absorbed species. This phenomenon is absent in otherwise homogeneous solutions.

II. Reactive metal oxide surfaces such as TiO_2 particles can participate in photochemical reactions by adsorbing incident uv-vis energy. This energy in the form of electron/hole pairs (e^-/h^+) can then be transferred to an adsorbed species on the surface of the particle and hence participate in photocatalytic oxidation of contaminants. In contrast with I above, reactive metal oxide surfaces provide both the solid support and source of electron/hole pairs during photocatalysis.

In this study attention has been focused on photochemical processes occurring on a reactive inorganic metal oxide surface for two reasons:

I. These surfaces are capable of efficient heterogeneous photocatalytic oxidation involving a wide range of contaminants.

II. Reactive metal oxide surfaces can photocatalyse both chromophoric and non-chromophoric species present in solution.

1.1.2 Nanoparticulate semiconductors.

Investigations of semiconductor particles for solar energy conversion and photochemical processes[5] are now well established. Research into colloidal TiO_2 semiconductor particles began in the late 1970's[6]. These investigations have resulted in TiO_2 particles exhibiting band gap properties of the bulk solid[7,8,9,10,11,12].

---

[5] M. Grätzel, 'Heterogeneous photochemical electron transfer'. 1989, CRC Press Inc. New York.
[6] M. Visca, E. Matijevic. J. Colloid and Interface Science. 1979, 68(2), 308.
[7] M.A. Fox, Top. Curr. Chem. 1987, 142, 71.
[8] R.W. Matthews. Solar Energy. 1987, 38, 405.
[9] D.F. Ollis, Environ. Sci. Technol. 1985, 19, 480.
[10] S.I. Nishimoto, B. Ohtani, H. Shirai, S. Adzuma, T. Kagiya, Polym. Commun. 1985, 26, 292.
[11] D.Duonghong, J. Ramsden, M. Grätzel, J. Am. Chem. Soc. 1982, 104, 2977.
[12] J. Moser, M. Grätzel, J. Am. Chem. Soc. 1983, 105, 6547.

However, in the years following, Anpo et al.[13] reported the preparation of nano-particle TiO_2 which exhibited size quantised effects, such as increasing band gap energies with decreasing particle size and a corresponding blue-shift in the uv-vis spectrum upon charge injection. This size dependency is a requirement for successful photo-oxidation and is important when examining photocatalytic efficiencies. A second characteristic feature of nano-particle semiconductors, which distinguishes them from their bulk counterparts, is their large surface to volume ratio and subsequent high level of contaminant adsorption at the surface. Large particle surface areas may also control the chemical nature of the surface and creates the possibility of enhancing the separation efficiency of e^-/h^+ pairs at the semiconductor surface.

In this study, semiconductor photocatalysis (with a particular focus on TiO_2) has been investigated. The choice of TiO_2 as a suitable photocatalyst derives from the fact that TiO_2 has already been applied to a variety of environmental pollutants[13]. The use of TiO_2 as a photocatalyst offers certain advantages over preceding conventional oxidation processes:

I. This method of oxidation is comparable in terms of efficiency when compared to other conventional methods.

II. The consumption of large amounts of expensive oxidising chemicals is not required, the oxidant is usually oxygen and the catalyst is comparatively cheap, non-hazardous, widely available and reusable.

III. This particular semiconductor absorbs wavelengths of light ≤ 380 nm that can be transmitted by glass, so that the reaction may be driven by the natural component of sunlight if necessary.

IV. The process is easily controlled.

---

[13] M. Anpo, T. Shima, S. Kodama, Y. Kubokawa, J. Phys. Chem. 1987, 91, 4305.

However there are a number of limitations associated with such systems:

I. The use of unsupported suspensions of semiconductor particles during photocatalysis requires separation and recycling of the catalyst following oxidation.

II. Aggregation of semiconductor particles over time can lead to a decrease of photocatalytic efficiency. This decrease is a direct result of lower band edge driving forces arising out of lower energy, higher wavelength uv-vis light absorption. Ultimately this will lead to a reduction in the number of charged species at the particle surface, which are responsible for photocatalytic oxidation. An increase in particle aggregation corresponds to a decrease in the particle surface area; this will result in a reduction of available defect sites present at the surface of the particle. It is the defect sites that are responsible for trapping the e^- /h^+ pairs long enough so that photocatalytic oxidation of contaminants can occur.

However alternative methods for synthesising colloidal semiconductor particles have been attempted in order to limit the above problems. These methods involve the use of solid matrices. Nano-particle semiconductors have been precipitated in a variety of media[14] including zeolites, glass beads, clays and LB films. Immobilisation of semiconductor particles in heterogeneous hosts can control the size and shape of the semiconductors. The morphology and size of the microscopic voids contained in the host template where precipitation occurs are the controlling factors influencing the semiconductor size.

In this study, two methods for synthesising nano-particle semiconductor aggregates were chosen. Both methods involve the use of solid matrices.

1.1.3 Langmuir-Blodgett (LB) Films

The Langmuir-Blodgett technique is a method for the deposition of ultra-thin organic films. It features precision control of molecular thickness and orientation. LB films are formed by transferring floating organic monolayers onto solid substrates using an instrument known as an LB trough. This technique was predominately developed by Irvining Langmuir[15] and his associate Katherine Blodgett between 1917-1935[16] (For a detailed historical review of Langmuir-Blodgett activity see section 2.3.1 and 2.3.2. By varying a number of experimental conditions such as subphase concentration, pH and surface pressure it may be possible to produce LB films containing nano-particle semiconductors.

1.1.4 Nafion

The second heterogeneous medium investigated for the precipitation of TiO_2 nano-particles was Nafion®, an ion exchange membrane produced by Dupont de Nemours & Co. The choice of Nafion as a suitable host can be attributed to the following properties:

I. Nafion is a remarkably robust and inert ion exchange membrane, which can be used under extreme conditions of pH and in the presence of strong oxidising and reducing reagents. This is an important criterion for photocatalytic behaviour.

II. The microstructure of Nafion can facilitate the production of TiO_2 particles (as outlined in section 2.4.1).

III. Nafion transmits uv-vis light (200 nm-800 nm) and is thus a suitable medium for examining the optical properties of semiconductors.

---

[14] A. Hagfeldt, Chem. Rev. 1995, 95, 49-68 and refs. therein.
[15] I. Langmuir, J. Am. Chem. Soc. 1917, 39, 1848-1906.

1.1.5 Cyanide: A model contaminant

Cyanide was chosen as the model contaminant for photocatalytic studies in this research particularly because of its toxic nature and also because of the fact that the mechanism associated with cyanide photo-oxidation is well documented[17,18,19,20].

The photo oxidation of cyanide catalysed by TiO_2 was one of the earliest systems studied by Frank and Bard[21]. The use of cyanide as a model contaminant may allow for the development, characterisation and optimisation of different semiconductor preparation techniques. This development may be achieved, firstly by investigating the photophysical properties of the semiconductor particles in the micron to nano size regime. Secondly, the semiconductor particles can be finely tuned in terms of their size, so that optimum photocatalytic activity is achieved.

1.1.6 Scope of this thesis.

In summary, this thesis is concerned with the preparation, analysis and characterisation of TiO_2 nano-particles. This is an area of materials chemistry, which is important in such diverse fields as photography, information storage, photocatalysis and solar energy conversion[5].

Kinetic data is presented and compared for cyanide photocatalytic oxidation using both unsupported commercially available micron sized TiO_2 particles and TiO_2 nano-particles immobilised in two heterogeneous hosts, namely LB films and Nafion.

---

[16] K.B. Blodgett, J. Am. Chem. Soc. 1935, 57, 1007-22.
[17] BV. Mihaylov, J.L. Hendrix. J. Photochem. Photobiol. 1993, 72, 173-177.
[18] H. Hidaka, T. Nakamura, A. Ishizaka, M. Tsuchiya, J. Zhao. J. Photochem. Photobiol. A: Chem., 1992, 66, 267-274.
[19] C.H. Pollema, J.L. Hendrix. J. Photochem. Photobiol. A: Chem. 1992, 66, 235-244.
[20] M.S. Ahmed, Y.A. Attia. J. Non-Crystalline Solids 1995, 186, 402-407.
[21] S.N. Frank, A.J. Bard. J. Phys. Chem. 1977, 81, 1484.

Chapter 1: General Introduction

Chapter 2 introduces the area of heterogeneous photocatalysis and highlights the importance and advantages, of particularly semiconductor photocatalysis as a technique for cyanide oxidation over other conventional methods. A comparison is made between nano-particle semiconductors and their bulk counterparts. The two different heterogeneous host materials, LB films and Nafion, which were used to incorporate TiO_2 particles, are described.

Chapter 3 is concerned with the experimental methodology used for the preparation of TiO_2 particles in different heterogeneous hosts. Two methods for the detection of cyanide remaining in aqueous solution after photolysis are discussed. The photochemical set-up along with the exact experimental conditions is described for cyanide photocatalytic degradation. Several characterisation techniques are described which include Atomic Force microscopy, UV-Vis spectroscopy, Scanning Electron and Transmission Electron microscopy, Energy Dispersive X-ray Analysis (EDAX), Electron Diffraction and Powder X-ray diffraction

Chapter 4 is by far the most comprehensive chapter of the thesis, results are presented under three main sections; namely Langmuir-Blodgettry, optical properties of immobilised TiO_2, photochemical experiments and characterisation techniques incorporating sub-sections on: AFM, SEM, EDAX, TEM, ED and XRD.

Chapter 5: Incorporates the discussion of results and highlights novel results recorded throughout this study.

Chapter 6: General Conclusion and describes future work in this area of materials chemistry.

Chapter 2

Introduction to the thesis

Chapter 2, Section I: Heterogeneous photocatalysis

2.1.1 Introduction.

Pollution caused by chemical materials in waste water effluent from industrial plants such as electroplating and mining has become a very serious global problem. The U.S. Environmental Protection Agency (EPA) has identified hundreds of compounds as 'priority pollutants[1]. Cyanide falls into this category and has been the model contaminant chosen for degradation studies in this research. It is a highly toxic compound which is fatal to some aquatic species and humans at concentration levels as low as 0.02 ppm and 180-200 ppm respectively[2].

The use of cyanides in industries is ever increasing. The main source of cyanide is industrial waste streams containing free and complexed cyanides from coking plants, pyrolysis and incineration plants and from metal finishing industries during electroplating and heat treating operations[3, 4, 5]. Extraction of gold from ores requires free cyanide for recovery, producing at the same time large volumes of toxic cyanide wastes[6].

2.1.2 Conventional methods for the treatment of cyanide waste.

The cleanup processes associated with these chemical wastes have met with new and stricter regulations for their safe disposal[7]. Many conventional waste disposal techniques are available for the treatment of cyanide, including: alkaline chlorination[8], uv/hydrogen peroxide and uv/hydrogen peroxide/O_3 processes[9] and solidification[10].

---

[1] U.S. Environmental Protection Agency. Fed. Regist. 1979, 44, 233.
[2] H.Cy. Pollema, J.L Hendrix, J. Photochem, Photobiol. A, Chem., 1992, 66,235-244.
[3] M.S. Ahmed, Y.A. Attia, J. Non-Crystalline Solids 1995, 186, 402-407.
[4] S.Q. Hassan, M.P.Kupfele, D.W. Grosse, J. Air Waste Manage. Assoc 1991, 41, 710.
[5] D.W. Grosse, J. Air Pollution Control Assoc, 1986, 603.
[6] B V. Mihaylov, J.L. Hendrix, J. Photochem, Photobiol A chem: 1993, 72, 173-177.
[7] D. Bhakta, S.S. Shukla, M.S. Chandrasekharaiah, J.L. Margrave. Environ. Sci. Technol. 1992, 26, 625-75626.
[8] F.E. Bernardin, J. WPCF. 1973, 45, 221.
[9] R. Venkatadri, R.W. Peters, Hazardous Waste & Hazardous Materials. 1993, 10, 107.
[10] C.D Hills, C.J Sollars, R. Perry, Cement and Concrete Research. 1994, 24, 707-714.

However there are a number of drawbacks associated with such techniques. The alkaline chlorination process (the most widely used unit process for controlling cyanide levels) is only capable of oxidising the free cyanide as CN^-, leaving behind the complex cyanides (e.g. iron, cobalt and nickel cyanides) in a sludge to be disposed of by landfill[3]. Similar action is required with solidification[10]. Secondly a highly toxic cyanogen chloride gas (CNCl) gas is formed during the alkaline chlorination treatment process:

$$NaCN + Cl_2 \rightarrow CNCl\uparrow + NaCl \qquad [2.1.1]$$

Alternative oxidation reagents including $KMnO_4$ and O_3 are not as efficient. Oxidation of cyanide to cyanate using H_2O_2 is reported to be limited to waste water streams containing low levels of cyanide[9]

The use of activated carbon has been investigated more recently, both as an adsorbent and as a catalyst for the removal and oxidation of cyanide. Adams[11] has recently reported the enhanced removal of cyanide from aqueous cyanide solutions with 50% removal over an 8 hour period at pH 10. Increased rates of cyanide removal were observed at pH 7 and lower, however these increased rates are clearly related to the production of large volumes of HCN gas which impose a high risk factor on humans and their ecological system. Bernadin[8] has observed an increase of cyanide removal from activated carbon solutions containing copper ions. However, the carbon becomes deactivated by organic adsorbtion over time so that this process of cyanide removal is limited to waste waters containing a low organic concentration. Clearly a degradation process is required which is capable of reducing both free and complex cyanides to an acceptable level, (0.02 ppm) while limiting the amount of toxic intermediates or end products.

[11] M.D. Adams. Minerals Engineering. 1994, 7, (9), 1165-1177.

Chapter 2, Section I: Heterogeneous photocatalysis

In the search for a better method for the detoxification of hazardous waste materials, semiconductor photocatalysis exists as one possibility. The advantages of this technique are complete degradation of a wide range of organic and inorganic pollutants including chlorinated aliphatics[12] or aromatics[13], phosphorous organics[14], pesticides[15], metallic organics[16], polymers[17] and surfactants[18]. These systems require relatively short periods of time, complete mineralisation into e.g. CO_2 and HCl can be achieved, and these processes require inexpensive reusable catalysts with high turnover.

2.1.3 Semiconductor photocatalysis

Research in the area of photocatalysis using semiconductor particles has been reported since the early 1970's. Fujishima and Honda first discovered that water could be split into its constituents upon illuminating a TiO_2 single crystal[19]. These findings prompted further work in this area and researchers began to learn that novel redox reactions of organic and inorganic compounds could be induced by irradiation of a variety of semiconductor particles with uv-vis light. Interest in this area is attributed to the possible applications associated with these particles, particularly in the area of solar energy conversion. However in the last decade, research in this area has focussed on using these particle dispersions as catalysts for environmental protection[20,21,22,23], and the examination of electron transfer reactions[24] for redox processes.

---

[12] D.F. Ollis, C.Y. Hsiao, L. Budiman, C.L. Lee, J. Catal. 1984, 88, 418.
[13] R. Borello, C. Minero, E. Pramauro, E. Pelizzetti, N. Serpone, H. Hidaka, Environ. Toxicol. Chem. 1989, 8, 997.
[14] C.K. Grätzel, M. Jirousek, M. Grätzel, J. Mol. Catal. 1990, 60, 375.
[15] E. Pelizzetti, V. Maurino, C. Minero, O. Zerbinati, E. Borgarello, Chemosphere 1989, 18, 1436.
[16] D. Lawless, A. Res, R. Harris, N. Serpone, C. Minero, E. Pelizzetti, H. Hidaka, Chim. Ind. (Milan). 1989, 67, 623.
[17] H. Hidaka, J. Zhao, S. Suenaga, N. Serpone, E. Pelizzetti, J. Jpn. Oil Chem. Soc. 1990, 39, 963.
[18] H. Hidaka, J. Zhao, E. Pelizzetti, N. Serpone, J. Phys. Chem. 1992, 96, 2226.
[19] A. Fujishima, K. Honda, Nature 1972, 37, 238.
[20] D.F. Ollis, Environ. Sci. Technol. 1985, 19, 480.
[21] R.W. Matthews, J. Phys. Chem. 1987, 91, 3328.
[22] M. Schiavello, Ed. Photocatalysis and Environment; Kluwer Academic: Dordrecht. 1988.
[23] D. Bahnemann, D. Bockelmann, R. Goslich, Sol. Energy Mater. 1991, 24, 564.
[24] C.A. Koval, M.N. Howard, Chem. Rev. 1992, 92, 411.

In this process, semiconductors (including TiO_2, CdS, PbS, ZnO and WO_3) can act as sensitisers for light induced redox processes due to their electronic band structure, which is characterised by a filled valence band and an empty conduction band [25]. When a photon with energy hυ matches or exceeds the band gap energy (Eg) of the semiconductor, electrons are promoted from the valence band (V.B.) into the conduction band (C.B.), leaving positive holes ($h_{v.b}^+$) behind in the valence band as illustrated in Fig. 2.1.

The fate of the excited state conduction band electrons and valence band holes depends on the chemical nature of the surface. The presence of surface traps, suitable doping agents or adsorbed donor or acceptor species may promote separation for a time sufficiently long for a photochemical reaction to occur. In their absence the e^-/h^+ pair may recombine and dissipate their energy as heat. The time scale associated with charge carrier recombination for an intrinsic semiconductor is normally in the picosecond regime[26] and hence reduces the probability of photocatalysis, since photo-excited electron/hole pairs recombine readily. Decreasing the particle size of a semiconductor results in an increase in its surface area. This can distinguish small semiconductor particles from their bulk counterparts and is an important consideration when examining semiconductor photocatalytic efficiency.

[25] M.R. Hoffmann, S.T. Martin, Wonyong Choi, and D.W. Bahnemann, Chem. Rev. 1995, 95, 69-96.
[26] A. Mills, R.H. Davies, D.Worsley, Chem Soc. Rev.1993, 417-425.

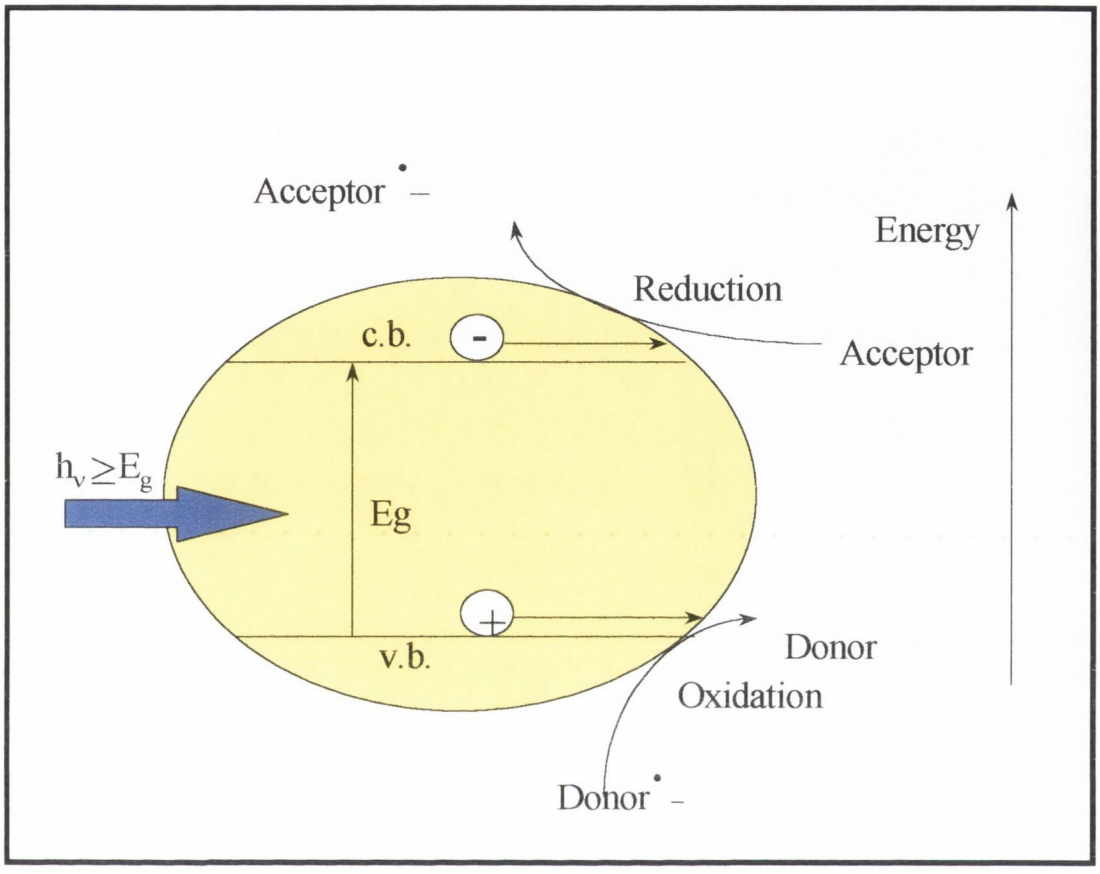

Figure 2.1: Energetic principles of semiconductor photocatalysis

The primary criterion for efficient semiconductor photocatalysis of acceptor or donor molecules in aqueous solution is that the redox potential of the $H_2O/^{\bullet}OH$ ($OH^- = OH^{\bullet} + e^-$; $E^\circ = -2.8$ V) couple lies within the band gap domain of the particular semiconductor material. It is also important that the particles are stable over prolonged periods of time. Figure 2.2 shows the band edge energies and corresponding redox potentials for a number of different semiconductors at pH 0 vs standard hydrogen electrode (NHE).

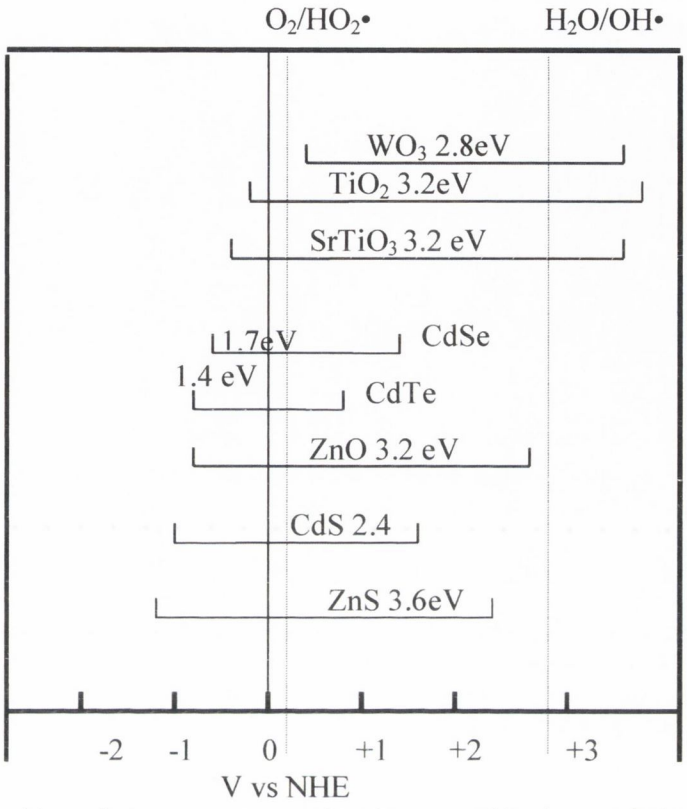

Figure 2.2: Band positions of common n-type semiconductors used in photocatalysis and the redox potentials of the H_2O/OH• and O_2/HO_2• redox couples at pH 0[27].

CdS has been the most widely studied semiconductor for photochemical transformations owing to its chemical simplicity and insensitivity to impurities[28]. CdS is an n-type wide band gap semiconductor with a threshold energy of 2.4eV (516nm) and is capable of absorbing light across a considerable portion of the visible spectrum for use in photochemical reactions. However the metal sulphide semiconductors are unsuitable, based on stability requirements, in that they readily undergo photoanodic corrosion (Eg = 2.4 eV), with respect to water oxidation $H_2O/^{\bullet}OH$ ($OH^- = OH^{\bullet} + e^-$; $E° = -2.8$ V, CdS +

[27] A. Mills, R.H. Davies, D.Worsley, Chem Soc. Rev.1993, 417-425.
[28] C.Y. Hyeong, Y.M. Tricot, J.H. Fendler, J.Phys. Chem. 1987, 91, 581-586.

$2h^+ \rightarrow Cd^{2+} + S\downarrow$). ZnO appears to be suitable from a energy aspect (Eg = 3.2 eV), however ZnO is unstable with respect to hydroxyl adsorption [29] to yield Zn $(OH)_2$ on the ZnO particle surface thus leading to catalyst inactivation over time. TiO_2 has emerged as the most preferred photocatalyst based on both it energy requirements and stability against photocorrosion.

2.1.4 TiO_2 as an efficient photocatalyst.

TiO_2 is usually encountered as one of three different crystallographic modifications: anatase, rutile and brookite. Anatase and rutile TiO_2 have many applications, which include the production of high quality paper coatings, pigments in aqueous and solvent-based paints, cosmetics, soaps, textile printing inks and toothpaste. The anatase and rutile forms of TiO_2 are of particular interest for photocatalysis. Anatase TiO_2 is stable up to 800°C, above this temperature a transition from anatase to rutile TiO_2 occurs. The low stability of brookite TiO_2 makes it difficult to isolate and use this particular modification as an efficient photocatalyst.

Both anatase and rutile crystallise in a tetragonal lattice, however the two modifications are significantly different owing to their surface structure. Each Ti ion is co-ordinated octahedrally to six oxygen atoms. Figures 2.3 and 2.4 show the structures of both anatase and rutile TiO_2. The ability of both anatase and rutile TiO_2 to act as photocatalysts is attributed to both the amount of hydroxyl groups present at their surface and also to the position of their band gap energies relative to their redox potentials. The degree of surface hydroxylation is dependent on the temperature during TiO_2 formation.

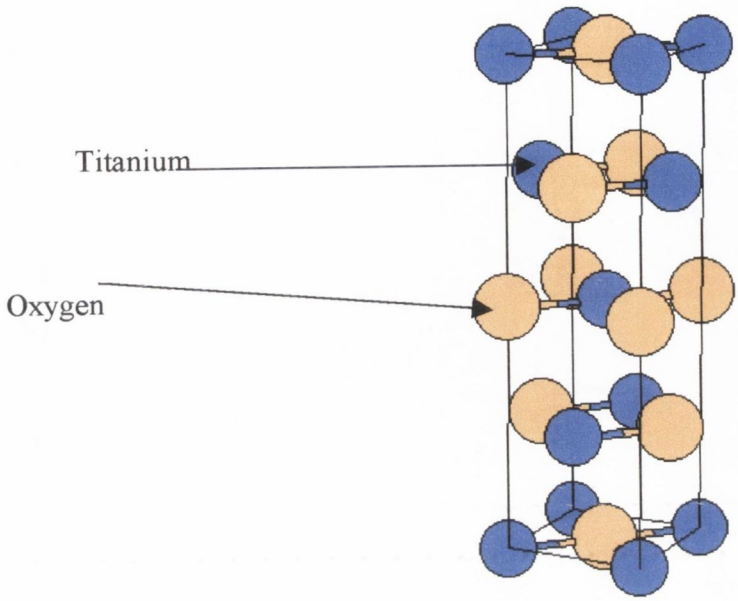

Figure 2.3: Crystal structure of anatase TiO_2

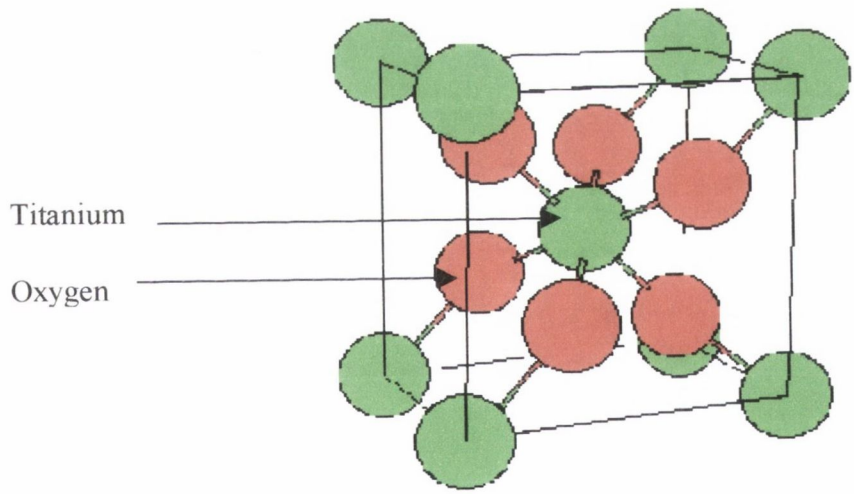

Figure 2.4: The crystal structure of rutile TiO_2

[29] D.W. Bahnemann, C. Kormann, M.R. Hoffmann, J. Phys. Chem. 1987, 91, 3789-3798.

Chapter 2, Section I: Heterogeneous photocatalysis

Charge separation within semiconductors induces the formation of various chemical species, which are useful for oxidation reactions. In TiO_2, these chemical species occur as follows:

(a) $TiO_2 + h\nu \rightarrow TiO_2 (e^-_{c.b.} + h^+_{v.b.})$

(b) $\{Ti^{IV}_{surface}\} + e^-_{c.b.} \rightarrow \{Ti^{III}_{surface}\}$

(c) $A_{ads.} + e^-_{c.b.} \rightarrow A^{\bullet-}_{ads.}$

(d) $O_{2\,ads.} + e^-_{c.b} \rightarrow O_2^{\bullet-}$

(e) $\{Ti^{IV}\text{-}O^{2-}\text{-}Ti^{IV}\} + h^+_{v.b} \rightarrow \{Ti^{IV}\text{-}O^{\bullet-}\text{-}Ti^{IV}\}$

(f) $D_{ads.} + h^+_{v.b.} \rightarrow D^{\bullet+}_{ads.}$

(g) $\{Ti^{IV}_{surface}\text{—}OH\} + h^+_{v.b.} \rightarrow \{Ti^{IV}_{surface}\text{—}{}^{\bullet}OH\}^+$

(h) $\{Ti^{IV}_{surface}\text{—}OH_2\}^+ + h^+_{v.b.} \rightarrow \{Ti^{IV}_{surface}\text{—}{}^{\bullet}OH\}^+ + H^+$

(i) $\{Ti^{IV}_{surface}\text{—}{}^{\bullet}OH\}^+ + D \rightarrow \{Ti^{IV}_{surface}\} + D^{\bullet+}\text{-}OH$

Conduction band electrons are trapped at the Ti^{IV} surface (b) or by extrinsic traps (e.g. adsorbed electron acceptors) or (c) via interfacial electron transfer. Adsorbed oxygen normally serves as the acceptor of electrons, forming the superoxide radical anion species (d). The valence band hole $h^+_{v.b.}$ can be trapped at intrinsic oxygen sites (e) or by adsorbed electron donors $D_{ads.}$(f). In the case of a highly hydrated and hydroxylated TiO_2 surface, the valence band holes may become trapped at surface bound OH and $^+OH_2$ sites to yield hydroxyl radicals (g) and (h). Hydroxyl radicals may add to a contaminant molecule, which may be adsorbed at the TiO_2 surface or may diffuse in solution according to equation (i).

2.1 5 Photocatalytic oxidation of cyanide.

Frank and Bard[30] have previously tested various semiconductor materials including ZnO, CdS and TiO_2 for cyanide photo-oxidation and found that while all three semiconductors were active, TiO_2 had the best overall stability towards photocorrosion. No photocatalytic activity was observed for Fe_2O_3 and WO_3 since the conduction band edge positions of these semiconductors are outside the relevant redox potential for cyanide oxidation which is equal to – 0.97V vs NHE[31].

Frank and Bard have previously reported the photo-oxidation of cyanide in the presence of TiO_2 in both anatase and rutile forms. The amount of cyanide reacted was determined by potentiometric titration with silver nitrate solution. The results were independent of the amount of TiO_2 but were highly dependent on the light intensity. Control experiments run in the absence of TiO_2 photocatalyst or light showed no or very little oxidation of CN^-. The efficiency of CN^- oxidation decreased by 90% in the absence of O_2. TiO_2 in the anatase form appears to be the more photo-active and the most practical form among the two semiconductors for widespread environmental applications.

The kinetics associated with the photocatalytic oxidation of cyanide at various concentrations was determined and a confirmed mechanism based on their results is as follows[32]:

$$TiO_2 + 2h\upsilon \rightarrow (TiO_2^*) + 2h^+ + 2e^- \qquad [2.1.2]$$

$$0.5\ O_2 + 2e^- + 2H_2O \rightarrow 2OH^- \qquad [2.1.3]$$

$$2OH^- + 2h^+ \rightarrow H_2O_2 + 2OH^\bullet \qquad [2.1.4]$$

$$2OH^\bullet + CN^- \rightarrow CNO^- + H_2O \qquad [2.1.5]$$

[30] S.N. Frank, A.J. Bard, J. Phys. Chem. 1977, 81, 1484.
[31] T.L. Rose, C. Nanjundiah, J. Phys. Chem, 1985, 89, 3766.
[32] S.N. Frank, A.J. Bard. J. Phys. Chem. 1977, 81, 1484.

Further oxidation of cyanate (OCN^-) was anticipated but they found no evidence for this process.

More recent investigations by Mihaylov et al[6] into the photochemically induced reactions of cyanide in the presence of TiO_2 have clearly shown that cyanide is initially oxidised to cyanate (both compounds were detected by ion chromatography).

Following this work, other investigators such as Yoneyama et al.[33] have measured the rate of cyanide photo-oxidation as a function of platinisation of catalyst. It was found that platinisation enhanced the rate of oxygen reduction but at the same time, reduced the rate of cyanide oxidation by increasing the rate of photo-oxidation of water. The cyanide ion concentration was determined using the ion selective electrode method.

In an effort to enhance the rate of cyanide photo-oxidation, Rose and Nanjundiah[31] have investigated the rate of cyanide photo-oxidation as a function of solution pH, TiO_2 particle size and platinisation of photocatalyst. A first order dependence on cyanide concentration was observed and the rate of cyanide oxidation was found to decrease with decreasing pH. The rate of cyanide oxidation was also observed to increase with both decreasing particle size and platinisation. Increased rates of cyanide oxidation have also been reported for cyanide solutions containing Cu^{2+} ions.
Several researchers have focussed on the detection of reaction intermediates and end products for cyanide photo-oxidation. Peral et al.[34] were able to demonstrate that CN^- can be photochemically converted to CO_3^{2-}. These authors proposed that OCN^-, which is formed according to Frank and Bard[32], is further oxidised by the following process:

$$OCN^- + 2H_2O + 3h^+ \rightarrow CO_3^{2-} + 0.5\ N_2\uparrow + 4H^+ \qquad [2.1.6]$$

[33] K. Kogo, H. Yoneyama, H. Tamura. J. Phys Chem. 1980, 84, 1705-1710.
[34] J. Peral, J. Munóz, X. Domènech. J Photochem. Photobiol. A Chem., 1990, 55, 251.

Pollema and Hendrix[2] have examined cyanide photo-oxidation and have verified that CN^- is first oxidised to cyanate. Ion chromatographic analysis has shown that cyanate is subsequently oxidised to nitrate (NO_3^-) via nitrite (NO_2^-) at pH values below 10.

Hidaka and co-workers[23] have investigated CN^- photocatalysis in aqueous solutions of pH 12. Evidence of O_2 consumption and OCN^- formation was presented, using gas chromographic analysis. The amount of CN^- oxidation was measured spectrophotometrically by complexation of the free unreacted CN^- with sodium 4-pyridine carboxylate and 1-phenyl-3-methyl pyrazolone at 637nm.

In the present work, the kinetics of cyanide photo-oxidation over TiO_2 was investigated. The study included the determination of the amount of cyanide photo-oxidation under different experimental conditions such as pH, particle size, particle environment and amount of catalyst.

Chapter 2, Section II: Photophysical properties of Semiconductors

2.2.1 Overview

The colloid chemical approach for the formation of stable nano-particles was developed many decades ago. However very little was known about these small particles (often called sub-colloidal particles since they were not detectable with the ultra microscope). Lucas first discovered nano-particle semiconductors and observed a change in solution colour for a decrease in CdS particle size[35]. However it was Berry, in 1967 who fully characterised CdS particles[36]. The arrival of high-resolution electron microscopy has resulted in an increase of interest in this area.

The first systematic approach relating the photophysical properties of CdS particles to their size came in the early 1980's when Papavassiliou[37] examined the Raman excitation and luminescence profiles for CdS of different particle sizes and observed higher frequency shifts for a decrease in CdS particle size. Following these observations, research in the area of small nano-sized semiconductor particles has intensified. An excellent review of this literature is that by Henglein.[38] and more recently by Wang et al.[39]

A theoretical approach investigating the transition between nano-particle and bulk semiconductors was first shown by Brus[40], who related the size dependence properties of CdS particles to their onset of absorption in terms of the confinement of electrons (e^-) and holes (h^+) present in the conduction and valence bands respectively.
The direct relationship between band gap absorption and particle size has resulted in an increase in research involving the preparation of nano-particle semiconductors with specific band gap energies, for applications including non-linear optics, photocatalysis,

---

[35] M. Lucas. Bull. Soc. Chim. 1896, 15, 40.
[36] C.R. Berry. Phys. Rev. 1967, 161, 848.
[37] G.C. Papavassiliou. J. Solid State Chem. 1981, 40, 330-335.
[38] A. Henglein. Chem. Rev. 1989, 89, 1861-1873.
[39] Y.Wang, Adv. Photochem., 1997, 19, 179, (and references within).
[40] R. Rossetti, S. Nakahara, L.E. Brus. J. Chem. Phys. 1983, 79, 1086.

microelectronics, and chemical sensors sensitisation [41,42,43]. Semiconductor particles such as CdS[44], PbS[45], TiO_2[46] and ZnO[47] have been widely investigated for photocatalysis.

Another interesting characteristic feature of nano-size semiconductor particles is their large surface to volume ratio compared to their bulk counterparts. This characteristic can influence certain properties associated with the semiconductor, including higher contaminant adsorption capability and increased defect surface traps. These characteristic features are particularly useful when examining redox reactions. The trapping of e^-/h^+ pairs can also affect the physicochemical properties, such as absorption and emission of the semiconductor. e^-/h^+ pair trapping can result in a decrease of charge carrier energy and defect (red) emission may occur.

Various methodologies have been investigated for preparing semiconductors with limited surface defects. For example sodium polyphosphate $(NaPO_3)_6$ and polyvinyl alcohol (PVA)[48,49,50] have been investigated as stabilisers for precipitating semiconductor particles with limited surface defects.

2.2.2 Size quantisation in semiconductor particles.

Bulk semiconductors possess an electron structure involving a continuum of valence band states separated from a conduction band continuum by a band gap E_g, typically of

---

[41] A. Hagfeidt, M. Grätzel, Chem. Rev., 1995, 95, 49.
[42] A. Henglein, Top. Curr. Chem., 1988, 16, 314.
[43] A. Kornowski, M. Giersig, R. Vogel, A. Chemseddine, H. Weller, Adv. Mater., 1993, 5, 634.
[44] L.E. Brus. J. Phys. Chem. 1986, 90, 2555-2560.
[45] A. Henglein, H. Weller. J. Phys. Chem. 1988, 92, 4706.
[46] C. Kormann, D.W. Bahnemann. M.R. Hoffmann. J. Phys. Chem. 1988, 92, 5196-5201.
[47] D.W. Bahnemann, C. Kormann, M.R. Hoffmann. J. Phys. Chem. 1987, 91, 3789-3798.
[48] A. Eychmuller, A. Hasselbarth, L. Katsikas, H. Weller, J. Lumines. 1991 49, 745-749.
[49] A. Hasselbarth, A. Eychmuller H. Weller, Chem. Phys. Letts, 1993, 203, 271.
[50] T. Vossmeyer, L. Katsikas, M. Giersig, L.C. Popovic, K. Deisner, A. Chemseddine, A. Eychmuller, H. Weller, J. Phys Chem. 1994, 98, 7665-7673.

the order 1.5-3.2 eV for most semiconductors. The band gap is the minimum energy necessary for promoting an electron from the valence band to the conduction band.

Energies greater than the band gap will accomplish this transition. The optical absorbance associated with such transitions gives rise to onsets in the uv-vis spectrum at distinct wavelengths depending on the particular semiconductor under investigation. The onset of absorption can thus provide a means of estimating the band gap experimentally.

Semiconductor particles with diameters >100 Å absorb close to Eg (depending on the specific material), however as the particle size decreases, the electronic structure begins to change from that of a continuum model to a discrete molecular model, this is the quantum size effect. Semiconductors that exhibit size dependent optical and electronic properties are termed quantum particles.

In simple terms, quantum effects are due to the fact that nanosize semiconductors have discrete energy levels. Two theoretical approaches have been used to explain the optical and electronic properties of various semiconductor particles. A molecular orbital (MO) model can be used to explain the quantum effects of these particles during their growth from molecular to bulk sizes. Increasing the particle size, corresponds to an increase in the number of energy levels contributing to the bond, the energy gap between the lowest unoccupied molecular orbital (LUMO) and highest occupied molecular orbital (HOMO) decreases, as a result. These changes result in a corresponding red shift in the accompanying optical transition. In contrast, decreasing the available MO's leads to an increase in the band gap and an apparent blue shift in the optical transition. Figure 2.5 shows particle growth of a semiconductor from an atomic level to a bulk material.

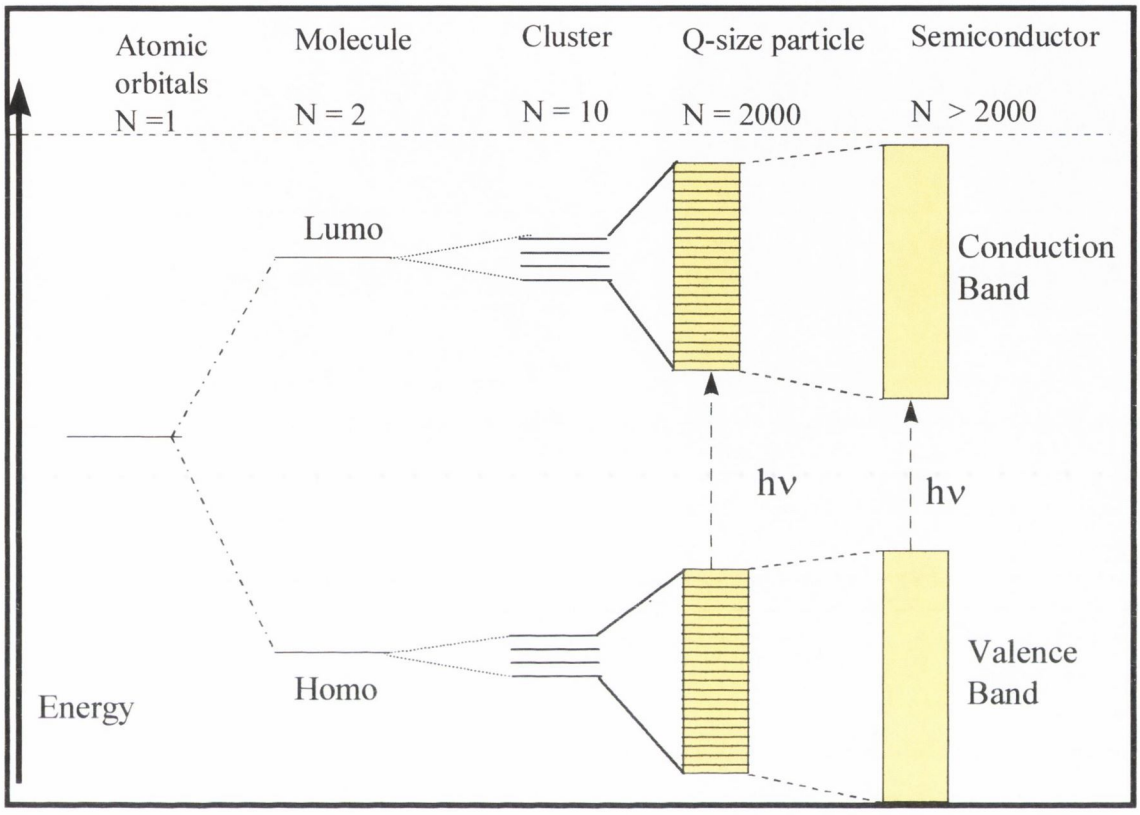

Figure 2.5: Schematic MO particle growth for a semiconductor material from an atomic to bulk level.

The second approach used to describe quantisation in semiconductor particles involves using a quantum mechanical model, based on an electron-hole pair in a box. Brus[51] used such a quantum mechanical approach rather than a MO approach and yielded the following formula for the calculation of the band gap energy in quantum-size materials.

$$\Delta E_g \cong \frac{\hbar^2 \pi^2}{2R^2} \cdot \frac{1}{\mu} - \frac{1.8e^2}{R\varepsilon} \qquad [2.2.1]$$

[51] L.E. Brus, J. Chem. Phys. 1984, 80, 4403

Where ΔEg corresponds to the Band gap shift as the particle radius R is increased or decreased. μ is the reduced mass of the exciton or effective mass of e^-/h^+ pair, e is the charge of the electron and ε the dielectric constant. According to [2.2.1] the band gap will always increase for small R values.

Under band gap excitation, photo-generated electron-hole pairs are formed within either bulk or nano-size semiconductor materials and are weakly bound to each other by coulomb interaction (the third term in the Brus equation above). The formation of a bound electron-hole pair known as a Wannier exciton is usually only observed for bulk semiconductors at cryogenic temperatures, since at room temperature, thermal energy is sufficient to break up the exciton and form free charged carriers at the surface of the particle. Exciton absorbance can however be observed at room temperature for nano-particle semiconductors. This may be attributed to charge carrier confinement arising from the formation of discrete energy levels. Figure 2.6 shows the effect of size quantisation of semiconductor particles and formation of an exciton in the bulk material. The absorption of the exciton will occur at a higher wavelength, since the band edge of this species is lower than the corresponding band edge of free charge carriers.

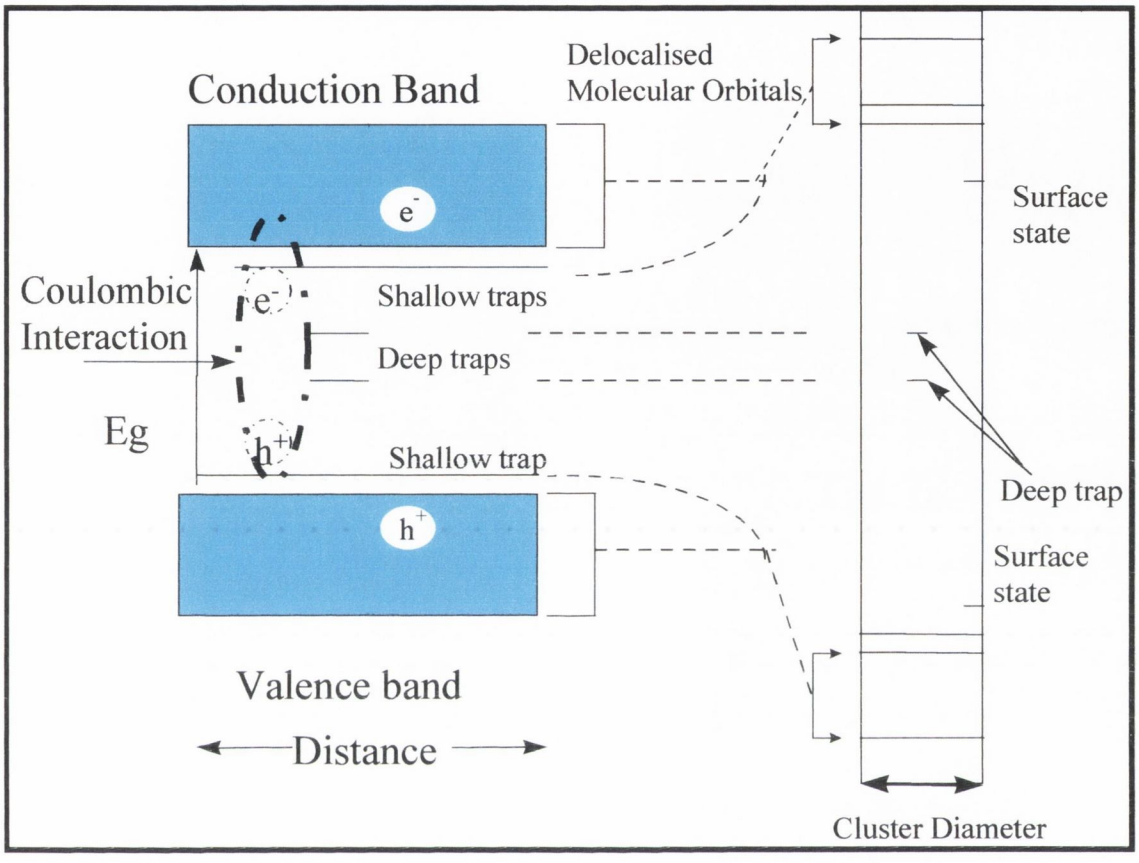

Figure 2.6: Electronic structure of bulk semiconductor and nano-size semiconductor clusters.

Size quantisation of semiconductor particles occurs when the Bohr radius (distance between e^- and h^+) of excitation in the particle becomes equal to or larger than the size of the particle. The Bohr radius of the exciton is related to the respective effective mass by equation:

$$a_B = [h/2\pi]^2\varepsilon/(e)^2[1/m_{e^-} + 1/m_{h+}] \qquad [2.2.2]$$

Where: a_B = radius of the exciton, m_{e^-}= effective mass of electron, m_{h+} = effective mass of a hole (h^+) and ε = dielectric constant.

The Bohr radius of the exciton (a_B) depends on the particular semiconductor, for example CdS has an effective electron mass ($*m_e^-$) of $0.2m_e^-$ and dielectric constant of $\varepsilon = 8.9$, this implies a Bohr radius (a_B) of 24Å, while for TiO_2 $*m^-_e = 30\ m^-_e$, $\varepsilon = 170$ and the $a_B = 3$Å. Thus quantum size effects are expected for CdS and TiO_2 particles with a particle size < 25 Å and 3Å respectively[52]. Quantum size effects are evident by a change in the optical absorption onset, blue shifted from the bulk material. However the absorbance of an exciton containing a coulombic interaction should occur at higher wavelengths (lower E_g) in comparison to free charge carriers and this absorption should be superimposed on the absorption band of the cluster.

A broad particle size distribution will result in absorption over a range of wavelengths which may have a masking effect on the exciton absorption. Surface defects responsible for hole trapping at the semiconductor surface can reduce the intensity of excitonic absorption which is related to the overlap of hole with electron charge carriers as illustrated in figure 2.6. This reduction in excitonic absorption is attributed to a decrease in coulombic attraction between the e^-/h^+ pair.

2.2.3 Immobilisation of nano-particle semiconductors.

The formation of many nano-particle semiconductor materials (<100 nm.) has been previously reported. It is nearly 20 years since Grätzel published the first accounts on light driven redox reactions involving nanocrystalline systems[53]. Since then there has been considerable interest in this field due to advances in techniques associated with materials characterisation. Particularly well-studied nano-particles[54] include: TiO_2, ZnO, WO_3, V_2O_5, Ag_2O, ZnS, CdS, PbS, Cu_2S, MoS_2 and CdSe. Most nano-particle research has been performed with particles suspended in solution.

---

[52] M. Gratzel. 'Heterogeneous photochemical electron transfer', 1989, CRC Press, Inc. New York.
[53] M. Grätzel, Acc. Chem. Res. 1981, 14, 376.
[54] A. Hagfeldt, M. Gratzel,. Chem. Rev. (1995), 95, 49-68 and refs. Therein.

Alternative methods for synthesising colloidal titania semiconductor aggregates involve the use of solid matrices[55]. The main focus of this research lies in the preparation, characterisation and containment of a well-defined semiconductor. Two independent methods for the immobilisation of TiO_2 nano-particles are investigated in this study, both methods comprise the use of solid matrices and involve precipitation of TiO_2 in LB films and Nafion membranes. Both of these methods were selected based on the fact that each technique is capable of restricting the size of the environment for TiO_2 precipitation, the materials used are inert, and the TiO_2 particles may be easily characterised while so immobilised.

Using the LB method it is possible to control the orientation and spatial arrangement of the LB matrix. This enables the restriction of the size of the space in which the particle is formed and precipitated. In the case of Nafion membranes the degree of membrane hydration and the chosen chemical reactant concentration for particle precipitation, are the factors which can affect particle size.

[55] A. Henglein, Chem. Rev. 1989, 89, 1861-1873.

Chapter 2, Section III: Langmuir-Blodgett films

2.3 1 An historical review.

According to Sugi[56] the earliest technical application of organic monolayer films on solid surfaces is believed to be the Japanese printing art called 'Sumi-Nagashi'. The dye, comprising a suspension of sub-micron carbon particles and protein molecules, is first spread on a water surface. The application of gelatin, grease or soap solution to the monolayer film, changes the film into a network of dark and colourless domains. These distinctive patterns can then be transferred by lowering a sheet of paper onto the water surface.

Benjamin Franklin made the first scientific study of floating organic films in the 18th century. His famous communication[57] to the Royal Society of Chemistry in 1774 reporting how a teaspoonful of oil had a calming effect over half an acre of a pond on Clapham Common, has been described as the first recorded scientific experiment in surface chemistry. Following the work of Franklin, it was Lord Rayleigh who was given the distinction of first suspecting that the maximum extension of oil on water represented a layer one molecule thick[58]. For a direct measurement of molecular size Rayleigh was indebted to Agnes Pockels who devised many of the standard methods used in surface chemistry[59]. Her pioneering work, investigating monolayer activity, was carried out in her kitchen sink. This simple apparatus has now become the model for what is now termed a Langmuir-Blodgett trough. In 1899 Rayleigh reported the precise thickness of a monomolecular layer of castor oil on water to be 1 nm[60]. This significant observation went unrecognised until monolayer theory was more fully developed by Irving Langmuir in the 1920's[61]. Langmuir made a distinctive contribution regarding monolayer activity

---

[56] M. Sugi, J.Molecular Electronics. 1985, 1, 3-17.
[57] B. Franklin, Phil. Trans. R. Soc. 1774, 64, 445.
[58] Lord. Rayleigh, Proc. Soc. 1890, 47, 364.
[59] A. Pockels, Nature. 1891, 43, 437.
[60] Lord. Rayleigh, Phil. Mag. 1899, 48, 321.
[61] I. Langmuir, J. Am. Chem. Soc. 1917, 39, 1848.

on water surfaces and together with his associate Katherine Blodgett in 1935[62], they developed a method of transferring monolayers to solid surfaces, more commonly known as substrates. Most of the experiments were investigated using a well-defined series of fatty acid salts. A detailed account of the results of these investigations can be found in a monograph by G.L. Gaines[63], whose book[64] provides a comprehensive treatment of the subject up to 1966.

Investigations involving the transfer of floating organic monolayers to solid substrates became dormant in the 1940's with the outbreak of the Second World War. The renaissance of LB investigations came in the 1960's when Kuhn and his co-workers[65] demonstrated how one could utilise monolayers to construct precise supermolecular structures. Kuhn et al. successfully carried out optical and energy transfer experiments using LB films composed of fatty acid salts and long chained substituted dye molecules. Their earlier electrical measurements on LB films[66] stimulated similar investigations by other research groups. During the 1970's studies began to be reported for LB films, suggesting possible applications of organic films in the field of electronics[67]. Roberts et al[68] in 1978 reported a field-effect transistor (FET) with an LB layer using InP, on which no satisfactory insulating layer had previously been formed.

Several review articles have been published which give a historical introduction of LB films, their preparation, and the various methods of characterisation involved. Particular emphasis is placed on their potential applications, especially in areas related to electronics[69,70,71,72,] e.g. as photo- or electron-beam resists, information storage systems,

---

[62] K.B. Blodgett, J. Am. Chem. Soc. 1935, 57, 1007-22.
[63] G.L. Gaines, Thin Solid Films. 1983, 99, 9.
[64] G.L. Gaines, 'Insoluble Monolayers at Liquid-Gas Interface' 1966, New York: Interscience.
[65] H. Kuhn, D. Möbius, H. Bücher, in 'Techniques Of Chemistry', Ed. A. Weissberger, B.W. Rossiter. Wiley, New York, 1973, 1, 577.
[66] V.K. Agarwal. Electrocomput. Sci. Technol. 1975, 2, 1, 75.
[67] P.S. Vincett, G.G. Roberts. Thin Solid Films, 1980, 68, 135.
[68] G.G. Roberts, K. P. Pande, W.A. Barlow. J. Solid-State Electron Devices. 1978, 2, 169.
[69] G.G. Roberts. Adv. Phys. 1985, 34, 475-512.
[70] L.M. Blinov. Sov. Phys. Usp. 1988, 31, 623-643.

barrier layers, chemisensors, frequency converters, optical switches, wave guides or infrared sensors.

2.3 2 Recent years.

Langmuir-Blodgett films have figured prominently in pure research since the 1930's and in applied research since the 1970's. However the technology of the early 1990's has not yet exploited them sufficiently and relies instead on other competitive techniques for device fabrication. The LB film process must compete against liquid-crystal, electro-active polymers and self assembled material processes[73]. There is now a greater potential for LB films, arising out of close co-operation between physicists, chemists, biologists and electronic engineers. The revival in this area is attributed to advances in LB trough technology[74,75], together with a progression in surface analysis techniques and the emergence of completely different molecular structures [76,77]. If LB film technology is to be a successful and commercially viable technique, it must address problems of film quality, non-uniformity, fragility and thermal stability.

2.3.3 The pressure area (π-A) isotherm.

A common objective in studies of floating organic monolayers is to monitor some physical parameter during compression. The conventional means of representing monolayer behaviour is the surface pressure-area (π-A) isotherm. Basic information, including film stability, molecular area and orientation can be deduced from the behaviour of a monolayer at the air-water interface during compression. A considerable

---

[71] B.Tieke. Adv. Mater. 1990, 5, 222-231.
[72] J.D. Swalen. Annu. Rev. Mater. Sci. 1991, 21, 373-408.
[73] N.A. Kotov, I Dékany, J.H. Fendler, J. Phys. Chem. 1995, 99, 13065-13069.
[74] G.G. Roberts, 'Electronic & Photonic Applications of Polymers'. Am. Chem. Soc. 1988, 4, 225-270.
[75] P. Martin, M. Szablewski, 'Tensiometers & Langmuir-Blodgett Troughs', Operating Manual 4th Ed. F. Grunfeld, Nima Technology Ltd. 1995.
[76] M. Vandevyver, A. Barraud, J. Molecular Electronics. 1988, 4, 207-221.
[77] R.H. Tredgold, 'Order in thin organic films'. Cambridge University Press. 1994.

number of such measurements were undertaken and reviewed by Gaines[78]. However more recent techniques including Brewster angle microscopy[79], neutron-scattering[80], Raman spectroscopy[81] and fluorescence microscopy [82]have been developed, and play an important role in the elucidation of the structure of amphiphilic molecules at the air-water interface.

We briefly consider the forces determining the π-A isotherm. The reduction of the surface tension is known as surface pressure (π). Surface pressure increases as the area available to the surfactant molecules is reduced. The direct measurement of surface pressure, as a function of area occupied per molecule can be accomplished provided that the number of molecules deposited on the surface is known. After initial deposition of a known concentration of the surfactant molecules at the air-water interface, and when no external pressure is applied to the monolayer, the film may behave like as a two-dimensional gas. In the limit of extremely low pressure, where the area per molecule, A, is large, we observe an analogue of the ideal gas law[83]:

$$\pi A = kT \qquad [2.3.1]$$

Where: π = the surface pressure of a particular surfactant, A = area per molecule, k = Boltzmann constant and T = thermodynamic temperature. The ideal behaviour suggested in eqn. 2.3.1 is rarely observed because the effective pressures in these 2-D monolayers are much higher than one would expect, and are attributed to intermolecular forces of attraction and repulsion, above and below the subphase respectively. An increase in the pressure because of a shift of a floating barrier causes Eq. [2.3.1] to be disobeyed. The

---

[78] G.L. Gaines,'Insoluble Monolayers at Liquid-Gas Interfaces, Interscience, New York, 1966.
[79] A. Angelova, D. Vollhardt, R.Ionov, J. Phys. Chem. 1996, 100, 10710-10720.
[80] D. Vakinin, K. Kjaer, J. Als-Neilsen, M. Lösche, J. Biophys. 1991, 59, 1325-32.
[81] T. Takeneka, H. Fukuzaki, J. Raman Spectrosc. 1979, 8, 51.
[82] M. Losche, H. Mohwald, Rev. Scient. Instrum. 1984, 55, 1968.
[83] L.M. Blinov. Sov. Phys. Usp. 1988, 31, 623-643.

two dimensional analogue of the Van der Waals equation can be used to described the transitions arising out of molecular interaction:

$$\left(\pi + \frac{a}{A^2}\right)(A - b) = kT \qquad [2.3.2]$$

Where coefficient *a* allows for the correction to the pressure because of the interaction of amphiphilic molecules with one another, i.e. dispersive attraction of the hydrocarbon chains and the Coulomb repulsion between the polar head groups. Coefficient *b* corresponds to the minimum area occupied by a molecule in a continuous monolayer.

Forces of attraction and repulsion associated with surfactant molecules are responsible for lowering the surface tension of the water and controlling the behaviour of the π-A curve. These forces are ionic in nature[84]. In the absence of suitable metal cations these forces are repulsive. When molecules are squeezed together, the nuclear and electronic repulsions associated with each molecule begin to dominate the attractive forces. The repulsions increase steeply with decreasing separation. The forces between the molecules are van der Waals interactions. They are proportional to $-1/r^6$ and are attractive at long range. At close inter-nuclear separation the repulsions dominate and are proportional to $1/r^{12}$. The sum of the repulsive and attractive interactions is given by Eq. [2.3.3] and is called the Lennard-Jones potential[85].

$$V = \frac{C_n}{R^n} - \frac{C_6}{R^6} \qquad [2.3.3]$$

[84] P. Martin, M. Szablewski, F.Grunfeld, 'Tensiometers & Langmuir-Blodgett Troughs', Operating Manual 4th Ed. Nima Technology Ltd. 1995.
[85] P.W. Atkins 'Physical chemistry' 3rd Ed. Oxford university press, 1988, p587.

2.3.4 Phase transitions of LB monolayers

The isotherm structure is usually interpreted in terms of the transitions between various distinct and physically different 2-D phases throughout monolayer compression. Dervichian[86] argued that there is a close connection between monolayer phases and the three-dimensional phases of the same substance. In addition to two-dimensional gaseous and liquid phases, one would expect to find solid phases in the monolayers with packing analogous to those observed in crystalline structures.

The study of fatty acids by Stenhagen[87] showed seven monolayer phases: gas (g), liquid-expanded (LE), and five more condensed phases that are observed at molecular areas less than 25Å^2 for single amphiphiles. These five phases are labelled: LS (low viscosity liquid phase), L_2 (liquid expanded phase), S (high pressure solid phase), L'_2 (liquid condensed phase), and CS (close packed solid phase). The presence or absence of each of these phase transitions is largely dependent on subphase conditions such as pH, ionic strength, metal ion concentration and temperature. There are several systems of nomenclature described by Gaines[88]. However the labels 'gas', 'liquid expanded' 'liquid condensed' and 'solid' are the first four phases encountered by Harkins[89] and are the most widely accepted.

Monolayer films at the air-water interface can give rise to three distinctly different shaped isotherms, with different numbers of phase transitions, (namely condensed, expanded and gas type) depending on the particular surfactant used. Condensed (solid) films are those in which the molecules are closely packed and orientated normal to the air-water interface. There is incomplete separation of the molecules at the interface and this is attributed to the strong cohesive properties associated with each hydrocarbon chain. The cohesive properties are strong enough to maintain the film in small domains as shown in figure 2.7. This cohesive nature is present in fatty acids such as stearic acid,

---

[86] D.G. Dervichian. J. Chem. Phys. 1939, 7, 931.

[87] E. Stenhagen, 'In determination of organic structures by physical methods' ed E.A. Braude, F.C. Nachod. New York:Academic Press, 1995.

[88] G.L. Gaines, 'Insoluble Monolayers at Liquid-Gas Interfaces. Interscience, New York, 1966.

palmitic acid and higher chain fatty acids. 2-D gas isotherm behaviour is absent throughout monolayer compression. At high trough areas the cohesive nature of such films allows them to organise in small domains with the remaining area consisting of empty space. However a rapid rise in surface pressure will occur as the molecules become tightly packed as shown in figure 2.7.

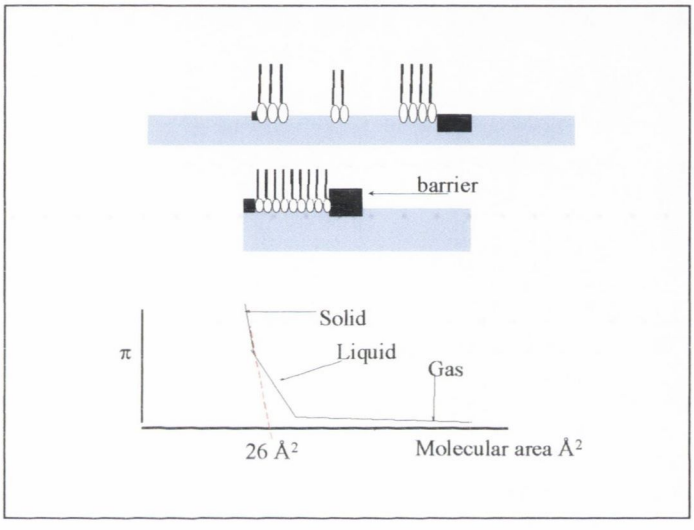

Figure 2.7: Monolayer compression and corresponding pressure-area (π-A) Isotherm for a condensed LB film.

The expanded film was the second type of monolayer film that was investigated in this study. Expanded monolayer films show similar packing characteristics to condensed films in that they consist of regions containing 2-D molecular domains separated by regions of 2-D vacuum. However expanded monolayer films start to pack at higher molecular areas. An example of such a film is oleic acid, a C_{18} fatty acid similar to stearic acid but containing a double bond. The double bond character of this material reduces the cohesive properties between adjacent molecules so that on compression, the film takes longer to become more ordered as shown in figure 2.8.

[89] W.D. Harkins, 'Physical Chemistry of Surface Films' Reinhold, New York. 1952, p106-117.

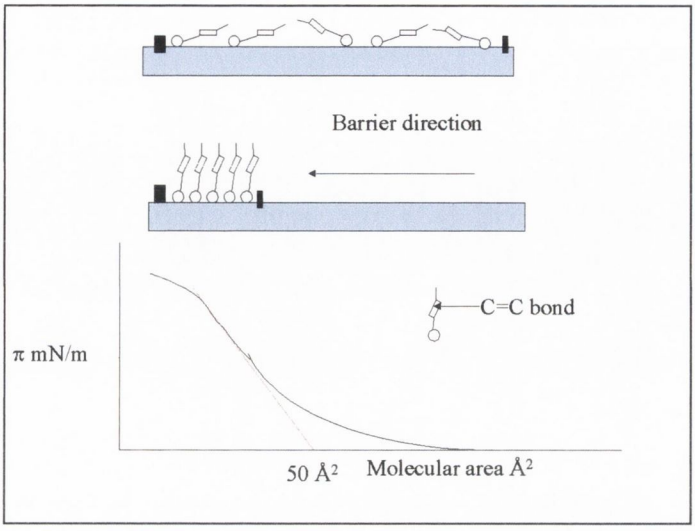

Figure 2.8: Pressure-area (π-A) Isotherm for expanded-type LB film

The third particular type of LB film studied was the gaseous film. In gas-type LB films the molecules of the monolayer are completely separated and can move around the interface independently of one another. Gaseous molecules have negligible size compared to intermolecular distance and obey the 2-D ideal gas equation. Cetyltrimethylammonium bromide, (CTAB, $(CH_3(CH_2)_{15}N(CH_3)_3Br)$) and dioctadecyldimethylammonium bromide (DODAB, $([CH_3\ (CH_2)_{16}CH_2]_2N(CH_3)_2Br)$), both cationic surfactants, are examples of compounds that exhibit a gas-type isotherms when spread at the air-water interface. The molecules of this monolayer continuously repel each other so that on applying an external pressure to the monolayer, the value of π is relatively large at all points on the π-A curve. The π-A curve resembles that of an expanded isotherm however with gas-type LB films the increase of surface pressure is observed at higher molecular areas as shown in figure 2.9.

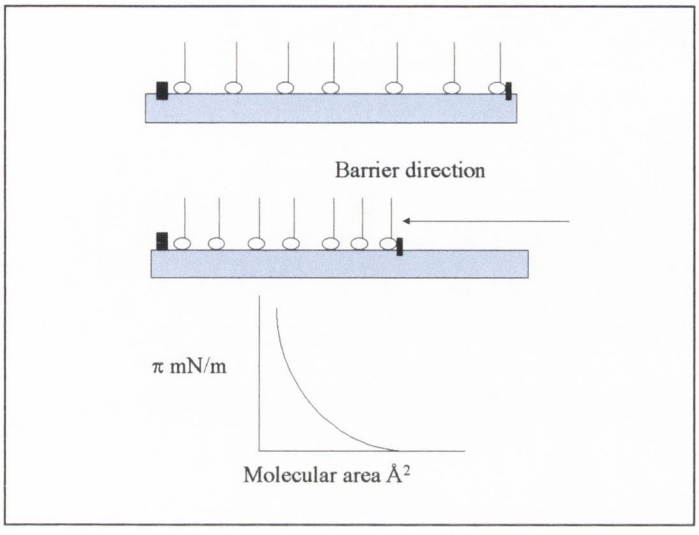

Figure 2.9: Pressure-area (π-A) Isotherm for gas-type LB film.

It is well established that the stability and structure of monolayer materials of simple fatty acids are greatly affected by the pH value of the subphase and the presence of multivalent cations. Different divalent cations have been shown to have very different effects on the properties of such monolayers and on the LB films subsequently formed, under otherwise identical conditions [90, 91, 92, 93, 94]. Fundamental studies of LB films have often been carried out using subphases containing divalent metal ions. Deposition of simple fatty acid materials from cadmium subphase solutions has remained the most common and standard procedure.

2.3.5 Effect of multivalent cations on the phase behaviour of monolayers.

The influence of different metal divalent cations for changing the number of isotherm phases is measured using surface potential energy. The surface potential energy is a measure of the film stability at the air-water interface. Significantly greater negative surface potentials associated with fatty acid monolayers on divalent subphases, enhances the condensed nature of the monolayer in comparison to a monovalent (Na^+) subphase.

---

[90] K. Kobayashi, K. Takaoka, S. Ochiai, Thin Solid Films. 1988, 159, 267.
[91] C. Vogel, J. Corset, M. Dupeyrat, J. Chim. Phys. 1979, 76, 903.
[92] H. Hasmonay, M Vincent, M. Dupeyrat, Thin Solid Films 1980, 68, 21.
[93] J.P. Rabe, J.D. Swalen, D.A. Outka, J. Stöhr, Thin Solid Films 1998, 159, 275.
[94] D.A. Outka, J. Stöhr, J.P. Rabe, J.D. Swalen, H.H. Rotermund, Phys. Rev. Lett. 1987, 59, 1321.

The surface potential arises from an uneven distribution of free or bound charges at the interface. There is a change in surface potential on going across the interface, which can be easily measured using a Kelvin probe. Increasing the cation concentration causes greater negative surface potentials. Yazdanian et al. [95] have studied the effects of various divalent cations on the surface potentials of some fatty acid monolayers spread at the air-water interface. They observed that both Pb^{2+} and Cd^{2+} show significantly greater negative surface potentials and increased monolayer film condensing capabilities, for simple fatty acids such as stearic and arachidic acid compared to divalent cations of Ba^{2+}, Ca^{2+} and Mg^{2+}. These differences appear to arise because of the ability of Pb^{2+} and Cd^{2+} to interact with the carboxylic groups through specific covalent binding, while the other ions interact essentially through non-specific electrostatic attraction. Similar results have also been reported by Gericke and Hühnerfuss[96], while studying the influence of cadmium, lead and calcium on the properties of stearic acid monolayers at the air water interface using Infrared reflection-absorption spectroscopy (IRRAS). The same authors have more recently extended their investigations by examining additional divalent cations such as Ba^{2+}, Cu^{2+}, Ni^{2+} and Zn^{2+} using the same technique[15]. They were able to assign co-ordination types to the respective alkanoic acid/cation system and observed a chelating bidentate complex for zinc stearate monolayers at pH 6.7, which adjusted to an ionic interaction as the pH was decreased to 5.0.

Deposition of fatty acid materials over trivalent subphase solutions on the other hand is considered difficult[97], owing to the instability of the monolayer on the subphase, arising from the large forces of interaction between the trivalent cation and monolayer material. Nevertheless, fabrication of many stearates has been reported in the literature using a variety of trivalent cations (e.g. Al^{3+} [98], Cr^{3+} [99], Fe^{3+} [100] and La^{3+} [101]).

---

[95] M. Yazdanian, Y. Hyuk, G. Zografi, Langmuir, 1992, 8, 630-636.
[96] J. Simon-Kutscher, A. Gericke, H. Hühnerfuss, Langmuir, 1996, 12, 1027-1034.
[97] D.J. Johnson, D.T. Amm, T. Laursen, S.K. Gupta, Thin Solid Films, 1993, 232, 245-251.
[98] T. Zheng, L. Liu, W. Wang, J. Zheng, Y. Shen, Z. Zhang, Thin Solid Films, 1991, 195, 301.
[99] M. Simovic, L. Dolbrilovic, J. Radioanal. Chem. 1978, 44, 345.
[100] M. Prakash, J.B. Peng, J.B. Ketterson, P. Dutta, Thin Solid Films, 1987, 146, L15.

This study complements earlier work by investigating the condensing effects of different fatty acids, using various subphase concentrations of Cd^{2+}, Zn^{2+} and Ti^{3+}, by examining the shape, position and collapse pressure for different monolayer materials.

2.3.6 LB film transfer

For LB monolayer transfer, it is important to consider deposition from the viewpoint of the substrate. Successful deposition of an LB film onto a substrate support depends greatly on chemical nature of the support. The process of transferring a floating insoluble monolayer to a solid surface by raising the substrate through the monolayer-covered liquid surface was first described by Langmuir described in 1920 [102]. He demonstrated the importance of the nature of the substrate involved, and showed that monolayer attachment was greatly influenced by the chemical nature of the substrate support. Sometimes the monolayer would float off the substrate after each subsequent deposition, in other cases the deposition film would adhere so strongly that only chemically destructive treatments, such as high temperature oxidation or etching of the underlying substrate would completely remove the film. A number of suitable LB substrates have been developed in recent years they include silicon (111), highly organised pyrolytic graphite (HOPG), as well as mica, glass and polished synthetic quartz[103]. All of the above substrates provide smooth homogenic chemical surfaces at molecular levels and they can be easily rendered hydrophobic or hydrophilic by chemical treatment. Figure 2.10 shows the LB film process and the different modes of film transfer. The most common mode of transfer is Y-type deposition and most simple amphiphiles deposit in this head to head, tail to tail fashion on both the upward and downward stroke of a substrate, leading to centrosymmetric structure as shown in figure 2.10 (b). Both X and Z-type deposition lead to non-centrosymmetric structures.

---

[101] R. Aveyard, B.P. Binks, N. Carr, A.W. Cross, Thin Solid Films, 1990, 188, 361.
[102] I. Langmuir. Trans. Faraday Soc. 1920, 15, 62.
[103] G. Leggett, 'Surface analysis-The principal techniques', Ed. J. Vickerrman, Wiley & Sons, 1997, 393.

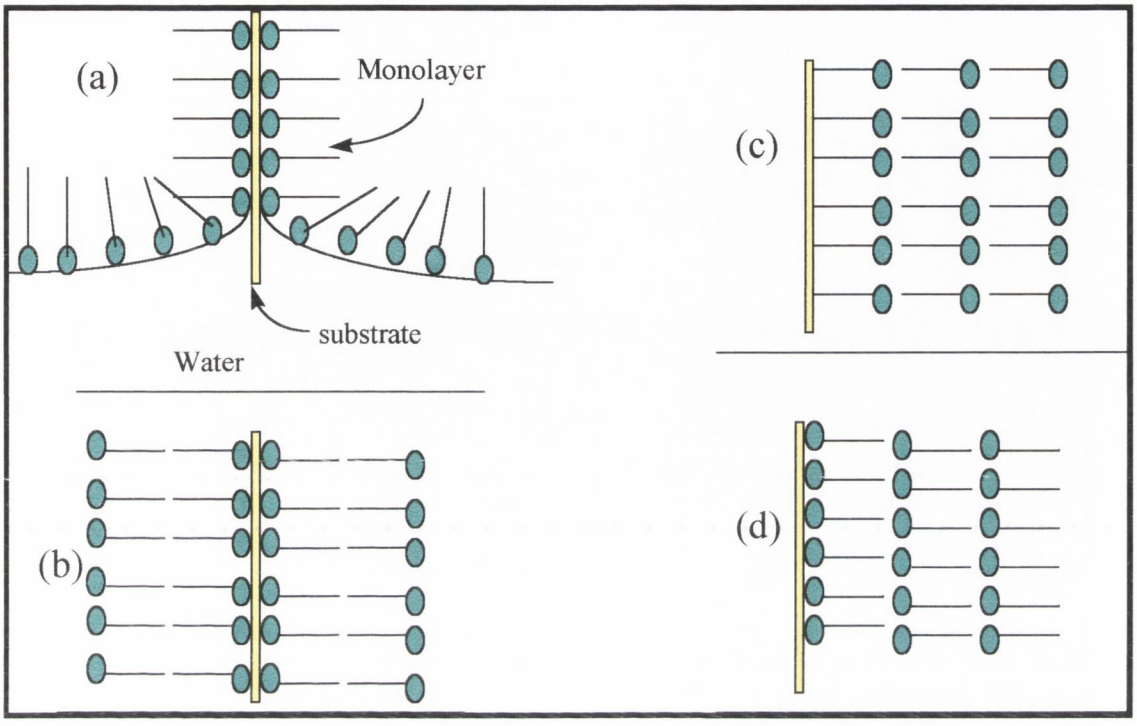

Figure 2.10: The LB deposition process (a) and the different modes of film transfer (b) Y-type, (c) X-type and (d) Z-type.

Both X and Z type arrangements are difficult to maintain and often appear to undergo some kind of rearrangement back to Y-type after deposition. At present there is no complete understanding of why some molecules dip in the X or Z manner, although such arrangements are desirable for electrochemical and non-linear optical properties, where non-centrosymmetric structures are required. Examples of compounds that undergo X or Z-type deposition include: azobenzene derivatives[104, 105], polymethylmethacrylate[106], and phenylene-vinylene[107] compounds.

[104] R.H. Tredgold, R.A. Allen, P. Hodge, Thin Solid Films. 1987, 155, 343-355.
[105] R. Jones, R.H. Tredgold, A. Hoofer, R.A. Allen, P. Hodge, Thin Solid Films. 1985, 134, 57-66.
[106] S.J. Mumby, J.D. Swalen, J.F. Rabolt, Macromolecules. 1986, 19, 1054-1059.
[107] M. Kakimoto, M. Suzuki, T. Konishi, Y. Imai, M. Iwamoto, T. Hino, Chem Lett. 1986, 823-826.

2.3.6 Semiconductors in LB films

The Langmuir-Blodgett (LB) method, as a molecular assembly technique, has been used for the preparation of ordered assemblies containing inorganic nano-particles since the late 1980's. However, the first observation of quantum size (Q-sized) effects in the optical absorption spectra was made by Weller[108] and Bard [109] who observed a decrease in the wavelength of absorption with a decrease in CdS particle size, for particles incorporated in LB films of arachidic acid (eicosanoic acid, $CH_3(CH_2)_{18}COOH$). Following these observations, there has been considerable interest in the controlled growth of CdS and many other semiconductor Q-sized particles, particularly for new technologies such as catalysis and non-linear optics. There are essentially three approaches used for the formation of Q-sized semiconductor particles.

The first approach has involved mainly the incorporation of CdS nano-particles between the head groups of a series of 'conventional' amphiphilic LB films similar to arachidic acid, by slow infusion of H_2S gas between multilayer films of the transferred cadmium salt. Similar amphiphilic head groups in LB films obtained by Y-or X-type deposition Figure 2.10, have provided suitable sites for nano-particle CdSe, CdTe, CdS_xSe_{1-x}, $CdSe_xTe_{1-x}$ and PbS semiconductors. These particles have been generated by exposure of the LB films to H_2S (or H_2Se, H_2Te). Du et al. [110] have investigated the formation of 54Å CdS nano-particles between the head groups of behenic acid (docosanoic acid, $CH_3(CH_2)_{20}COOH$) by transferring several monolayers of cadmium behenate and subsequently exposing the film to H_2S gas. A variety of long chain conventional amphiphilic molecules have been used for the formation of nano-particulate CdS using the above technique. Fendler et al.[111] have investigated the formation of CdS nano-particles between the head groups of amphiphilic amines and has demonstrated the formation of uniform controllable diameter particles, by slow infusion of H_2S gas

[108] H. Weller, H.M. Schmidt, U. Koch, Chem. Phys. Letts. 1986, 124, 557.
[109] E.S. Smotkin, C. Lee, A.J. Bard, A. Campion, M.A. Fox, T.E. Mallouk, S.E. Webber, J.M. White, Chem. Phys. Lett. 1988, 152(2-3), 265-8.
[110] Z. Du, Z. Zhang, W. Zhao, Z. Zhu, J. Zhang, Z. Jin, T. Li, Thin solid films. 1992, 210-211(1-2), 404-6.
[111] K.C. Yi, J.H. Fendler, Langmuir. 1990, 6, 1519-1521.

between these head groups. The pH dependency of the Cd^{2+} metal ion complexation with the amphiphile head group has been applied to control the size of the semiconductor particles. Confined sulphides of lead, zinc and copper as well as a mixture of cadmium and lead sulphides have been synthesised in LB matrices using stearic acid as the film forming agent. Pan et al. have examined the transfer properties using the LB technique at different surface pressures for both Cd^{2+} and Pb^{2+} stearate as precursors for CdS formation.[112]

The second approach reported by Fendler et al.[113] has investigated the morphological nature of non-annealed CdS particles incorporated in arachidic acid by slow infusion of H_2S gas between the monolayer-Cd^{2+} interface with subsequent transfer to a solid support. 30-50Å CdS particles were observed which exhibit band gap energies substantially higher than the corresponding bulk materials. A number of different semiconductor particles, including ZnS, PbS, CdSe and PbSe have also been chemically grown, in situ, under monolayers using this method[113].

A third procedure used for the formation of semiconductor particulate films involves spreading surfactant-stabilised nano-particles on aqueous solutions and transferring them to solid surfaces. The organisation of surfactant-coated nano-particles on aqueous solution surfaces depends on the hydrophobicity and surface charges of the particles. Stable Q-state CdS[114] particles have been formed by Fendler et al. using this technique. Alternatively, appropriately charged nano-particle sols of CdS stabilised with sodium hexametaphosphate (HMP) have been electrostatically attracted from solution to an oppositely charged monolayer surface such as dioctadecyldimethyl ammonium chloride (DODAC)[115] and dioctadecyldimethyl ammonium bromide (DODAB)[116] which are both

[112] Z. Pan, J. Liu. Langmuir, 1996, 12, 851-853.
[113] J.H. Fendler, F.C. Meldrum, Adv. Mater. 1995, 7, 607.
[114] H.J. Watzke, J.H. Fendler. J. Phys. Chem.. 1987, 91, 854-861.
[115] S. Xu, X.K. Zhao, J.H. Fendler, Adv. Mater. 1990, 2, 183.
[116] Y. Tian, C.Wu, J.H. Fendler, J. Phys. Chem. 1994, 98, 4913-4918.

cationic surfactants. Subsequent monolayer transfer of the stabilised sols between the DODAC and DODAB head groups has been achieved. Conventional LB films are not always sufficiently physically or chemically stable for practical device applications. The formation of CdS nano-particles has also been investigated in alternative amphiphilic media. Fendler and co-workers[117] have reported the in situ formation of CdS and ZnS generated using thiol functional groups under monolayers or between the head groups of LB films of octadecanol mercaptan. Zhu[118] and Furlong[119] have examined the possibility of using alternative LB film forming materials such as the straight chain diacetylenic acid including; pentacosa-10,12-diynoic acid and icosanoic acid for the incorporation of Q-sized CdS particles. Such materials provide a more thermally stable environment for the semiconductor.

In recent years there has been a tendency to return to the conventional LB film forming materials for the incorporation of semiconductor particles, for three main reasons:

I. The formation of CdS particles in simple amphiphilic media has allowed for the investigation and exploitation of a number of recent surface analysis techniques.

II. The use of conventional LB film materials for CdS incorporation has provided a simple matrix for investigating the photo-electrochemical and optical-electronic properties of the CdS particles. Grieser et al[120] have examined the photoelectrochemical properties of Q-state CdS in arachidic acid, with the particles showing good stability over several scanning cycles. Asai et al[121,122,123] have extensively studied the optical and electronic properties associated with CdS Q-state particles incorporated in arachidic acid. These particles exhibit both

---

[117] K.C. Yi, J.H. Fendler, Synthetic Metals 1995, 71, 2109-2110.
[118] R. Zhu, Y. Wei, C. Yuan, S. Xiao, Z. Lu, J.H. Schmitt. Solid State Commun. 1992, 84, 449-51.
[119] D.N. Furlong, R. Urquhart, F. Grieser, K. Tanaka, Y. Okahata, J. Chem Soc. Faraday Trans., 1993, 89, 2031-2035.
[120] H.S. Mansur, F. Grieser, R.S. Urquhart, D.N. Furlong, J.Chem. Soc. Faraday Trans. 1995, 91, 3399, 404.
[121] K. Asai, K. Ishigure, H Shibata, J. Lumin. 1995, 63, 215-22.
[122] K Asai, T. Yamaki, K. Ishigure, H. Shibata, Thin Solid Films. 1996, 285, 541-544.
[123] K Asai, T. Yamaki, K. Ishigure, H. Shibata, Thin Solid Films. 1996, 277, 169-174.

radiative and non-radiative fluorescence emission centred around 440 nm, 510 nm, 590 nm, 640 nm and 800 nm. Subsequent irradiation of the samples with high energy radiation results in an increase of radiative excitonic fluorescence and a corresponding decrease of non-radiative emission attributed to a decrease in surface traps.

III. The dissolution of semiconductor nano particles with subsequent re-precipitation forming larger particles, a phenomenon known as Ostwald ripening may be reduced to some extent, by incorporating semiconductor nano particles in simple systems such as LB films.

2.3.7. Nano-particle TiO_2 films

The recent past has seen increased interest in transparent porous nanocrystalline films[124] For example their use as photoanodes in regenerative photoelectrochemical cells[125] has attracted considerable attention along with other applications including electrochromic windows[126]. Evidence for the formation of a TiO_2 film has been reported by Hugot-le-Goff[127], where an oxide layer on Ti metal is believed to exhibit the TiO_2 (rutile) local ordering and thickness of about 6nm. TiO_2 films of thickness ca. 2-20 nm have also been reported using anodic oxidation of Ti metal[128]. However ultra-thin TiO_2 films formed using this technique appear to be photoelectrochemically inactive and are composed of mixed oxides TiO and Ti_2O_3. An apparent disadvantage of the above technique is that the growth of TiO_2 thin films is restricted to Ti metal surfaces. Recently, Grätzel et al. have shown that thin TiO_2 films can electrochemically be grown on various other electrically conducting supports by anodic oxidative hydrolysis of $TiCl_3$ solution[129]. Layers with thickness above ca. 200 nm, annealed at 450°C, show the structure and photoelectrochemical properties of bulk anatase TiO_2. However this technique is limited to conducting solid supports.

---

[124] A. Hagfeldt and M. Grätzel, Chem Rev. 1995, 49-68.
[125] B. O'Regan, M. Grätzel, Nature 1991, 353, 737.
[126] X. Marguerettaz, R. O'Neill, D. Fitzmaurice, J. Am. Chem. Soc. 1994, 116, 2629.
[127] A. Hugot-le-Goff, Thin Solid Films. 1986, 142, 193-197.
[128] J.F. McAleer, L.M. Peter, Faraday Discuss. Chem. Soc. 1980, 70, 67.
[129] L. Kavan, B. O'Regan, A. Kay, M. Grätzel, J. Electroanal. Chem. 1993, 346, 291.

Chapter 2, Section III: Langmuir-Blodgett films

A number of attempts to anchor TiO_2 on supports including glass beads[130], fibre glass[131,132,133] silica[134], electrodes[135], clays[136] and zeolites[137] have produced materials which fail to meet all the requirements necessary for efficient photocatalytic activity. Supported TiO_2 is reported to be less photo-active than the corresponding TiO_2 alone[138]. The major disadvantage associated with using immobilised photocatalysts is the loss of photocatalytic efficiency. This loss is attributed to photon wasting, from limited adsorption of surface contaminants. This does not occur with colloidal suspensions because the contaminant molecule to semiconductor distance is always very small. There are a small number of reports suggesting formation of stable TiO_2 layers using the LB technique. Recently Paranjape et al.[139] have reported an excellent quality thin TiO_2 film by thermal decomposition of n-octadecyl amine-titanyl oxalate, an LB film precursor. The corresponding TiO_2 films were characterised by X-ray diffraction (XRD) and photoelectron spectroscopy (P.E.S). The films were mostly amorphous in nature. There was no evidence for the formation of anatase TiO_2 even at low firing temperatures. The XRD data were not always reproducible and there was only some evidence for rutile TiO_2 at temperatures of 800°C. The film thickness was ca. 24± 1Å per dip[140] (consisting of one upward and one downward stroke). A transfer ratio of 50Å would be expected per dip for Y-type deposition if one considered the chain length of n-octadecyl amine to be 25Å. This rather unusual transfer ratio may arise from X- or Z-type deposition or by interdigitation of the hydrocarbon chains.

---

[130] Y. Xu, X. Chen, Chem. Ind. (London) 1990, 6, 497.
[131] Y. Xu, P.E. Menassa, C.H. Langford, Chemosphere 1988, 17, 1971.
[132] R.W. Matthews, Solar Energy 1987, 38, 405.
[133] K. Hofstandler, R. Bauer, S. Novalic, G. Heiser, Environ. Sci. Technol. 1994, 28, 670
[134] M. Anpo, H. Nakaya, S. Kodama, Y. Kubokama, K. Domen, T. Onishi, J. Phys. Chem. 1986, 90, 1633.
[135] K. Vinodgopal, S. Hotchandani, P.V. Kamat, J. Phys Chem. 1993, 97, 9040.
[136] H. Yoneyama, S. Haga, S. Yamanaka, J. Phys. Chem. 1989, 93, 4833.
[137] O. Legrini, E. Oliveros, A.M. Braun, Chem. Rev. 1993, 93, 671.
[138] R.W. Matthews, Pure and Appl. Chem. 1992, 64, 1285-1290.
[139] D.V. Paranjape, M.Sastry, P. Ganguly, Appl. Phys. Lett. 1993, 63, 18-20.
[140] P. Ganguly, D.V. Paranjape, M.Sastry, Langmuir 1993, 9, 577.

A second approach used for the formation of TiO_2 LB films was reported by Fendler et al.[141]. The formation of monoparticulate layers of surfactant stabilised TiO_2 sols with controllable interparticulate distances have been demonstrated. Similar procedures have been adopted for the preparation of a number of different surfactant stabilised nanoparticles including, cadmium sulphide, magnetite and silver[142]. These procedures all require sufficient particle hydrophobicity for successful monolayer spreading. Fendler has already reported and stressed the need for appropriate hydrophobicity, if the TiO_2 surfactant coating is too thick, this will cause aggregation and particle stacking, whereas if the nanoparticles are not hydrophobic enough they will sink into the subphase. This method involves the arrested hydrolysis of titanium tetraisopropoxide by water in a mixture of chloroform and propanol in the presence of a cationic surfactant: cetyltrimethyl ammonium bromide (CTAB, $CH_3(CH_2)_{15}N(CH_3)_3Br$). The presence of CTAB allows for stable TiO_2 dispersions and prevents aggregation over time. Fendler has examined the surface pressure area characteristics for the sols, before and after heat treatment. The uniformity of the TiO_2 sol on an aqueous subphase was examined using Brewster angle microscopy at different stages during compression. Subsequently Fendler has shown that these monoparticulate films could be transferred from an aqueous surface to a solid substrate using the LB technique[143]. More recently, Li and co-workers[144] have investigated the formation of stable TiO_2-stearate monolayers using a TiO_2 (anatase) hydrosol in the LB trough subphase. The hydrosol was formed by the arrested hydrolysis of $TiCl_4$ in HCl. The sol pH was adjusted to 5.0 after dialysis to remove excess H^+ and Cl^- ions. Prior to LB deposition the sol pH was adjusted to 3 using HCl and stearic acid in chloroform was spread at the air sol interface. Ti-St films were deposited onto a solid substrate. Transmission electron microscopy images shows a dense packing of TiO_2 particles throughout the whole substrate. Electron diffraction for a selected area of TiO_2-stearate indicated that the anatase crystal form was present.

---

[141] N.A. Kotov, F.C. Meldrum, J.H. Fendler, J. Phys. Chem. 1994, 98, 8827-8830.
[142] J.H. Fendler, F.C. Meldrum, Adv. Mater. 1995, 7, 607.
[143] J.H. Fendler, Current Opinion in Colloid & Interface Sci. 1996, 1, 202-207.

Chapter 2, Section III: Langmuir-Blodgett films

This project was attempted with a view to forming stable TiO_2 films with increased photocatalytic activity over prolonged periods of time. Furthermore such films would reduce the need for TiO_2 filtration after irradiation. To the best of our knowledge there has not been any other research performed relating the photocatalytic properties of TiO_2 formed using the LB technique for the decomposition of cyanide. Our investigation has focussed on examining whether the simplicity and elegance of the LB technique can be exploited in the fabrication of stable TiO_2 thin films possessing suitable photocatalytic properties. Initial experiments focussed on investigating the LB characteristics of a number of conventional LB films. The characteristic properties such as molecular area and collapse pressure associated with these films have been investigated using a number of divalent cations at different concentrations. Studies have been extended to trivalent metal ions.

[144] L. Li, Y. Chen, S. Kan, X. Zhang, X. Peng, M. Liu, T. Li, Thin Solid Films 1996, 285, 592-595.

Chapter 2, Section IV: Nafion Ionomer membranes

2.4.1 Nafion

Nafion was the second heterogeneous medium investigated for the preparation of TiO_2 nano-particles. Nafion is an ionic co-polymer with a polytetrafluoro ethylene backbone (PTFE, Teflon) as can be observed from Figure 2.11.

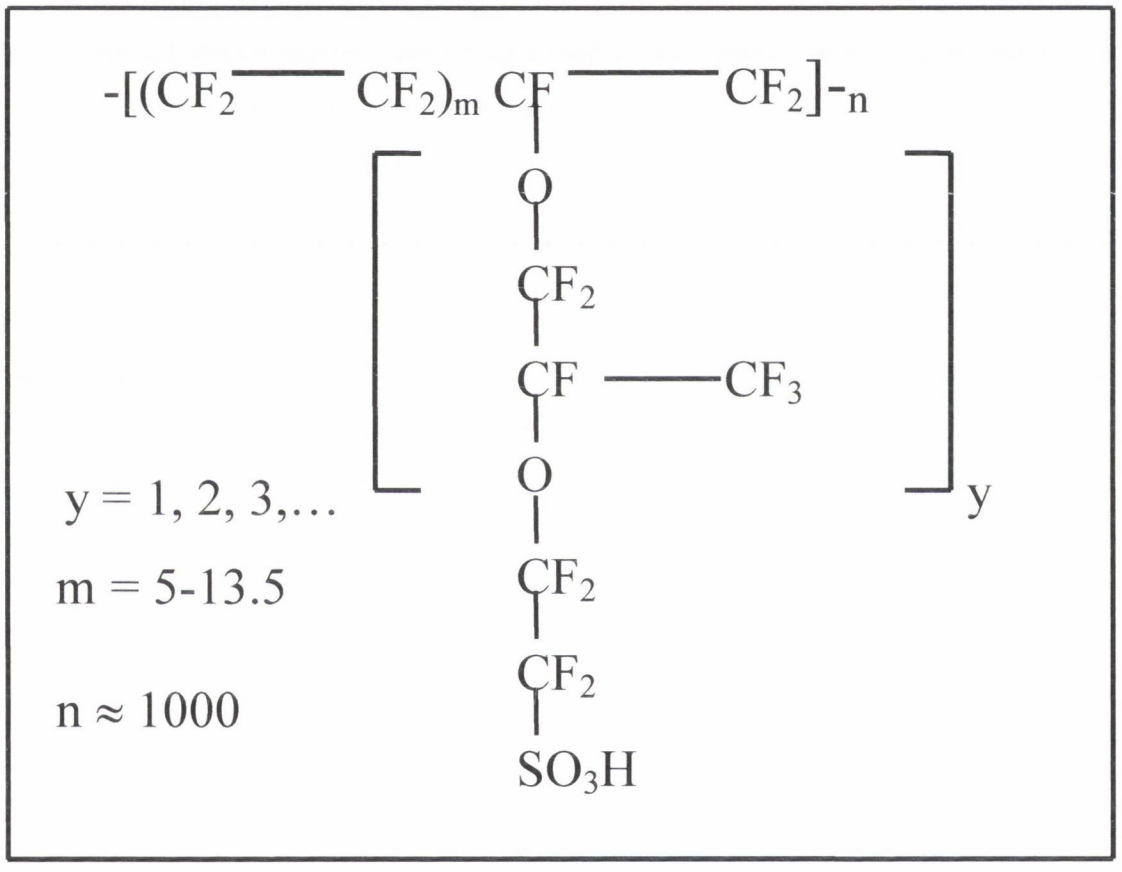

Figure 2.11: Repeating unit of Nafion®

The values of n and m can be varied to produce ion exchange membranes of different ion exchange capacities. Variation in the value of m from 5 to 13.5 yields equivalent weight (EW) from 900 - 1800. (Equivalent weight is defined as the weight required of the acid form to neutralise one equivalent of base). The EW of the membranes used (Nafion 117) was taken to be 1200 g/mol.

Chapter 2, Section IV: Nafion Ionomer membranes

The microstructure of Nafion has been investigated by a variety of techniques [145]. A commonly accepted model for the microenvironment of Nafion is the three-phase model first proposed by Rodmacq and co-workers[146] and later improved by Yeager and Steck [147]. This model consists of three regions:

I. A fluorocarbon hydrophobic backbone some of which might be in microcrystalline form.

II. An interfacial region: containing pendant side chains, sulphonic groups and a certain amount of absorbed water and counter ions.

III. Ionic clusters: containing sulphonated ion exchange sites counterions and sorbed water.

However the most widely accepted model for its microstructure is that proposed by Hsu and Gireke[148] in the early 1980's (Figure 2.12). Nafion ion exchange sites appear to form unique domains or clusters separated by narrow channels of 10 nm. The diameter of these clusters is controlled by the degree of hydration, Nafion ionomer membranes can absorb relatively large amounts of water and other solvents (ca. 10-50% of its weight) depending on its equivalent weight, counter-ion content and equilibrium temperature[149]. It has been previously reported that at high hydration levels, the maximum diameter of the ionic clusters is 40 nm[123]. The cluster arrangement in Nafion as shown in figure 2.12, adds to its stability. Nafion is resistant in alkaline and acidic media and can withstand attack from powerful oxidising agents. Nafion alone has thermally stability up to about 200°C.

---

[145] Z. Porat, J.R. Fryer, M. Huxham, I. Rubinstein, J. Phys Chem. 1995, 99, 4667-4671.
[146] B. Rodmacq, J.M. Coey, M. Escoules, E. Roche, R. Duplessix, A. Eisenberg, M. Pinery, In 'Water in Polymers'; R.A. Rowland. Ed.; ACS Symposium Series 257; Am Chem. Soc: Washington D.C. 1980 chaper 28.
[147] H.L. Yeager, A. Steck, J. Electrochem Soc. 1981, 128, 1880.
[148] T.D. Gierke. W.Y. Hsu, Macromole. 1982, 15, 101
[149] A. Eisenberg, H.L. Yeager, 'Perfluorinated Ionomer Membranes', ASC, Symp. Series. 1982, 180.

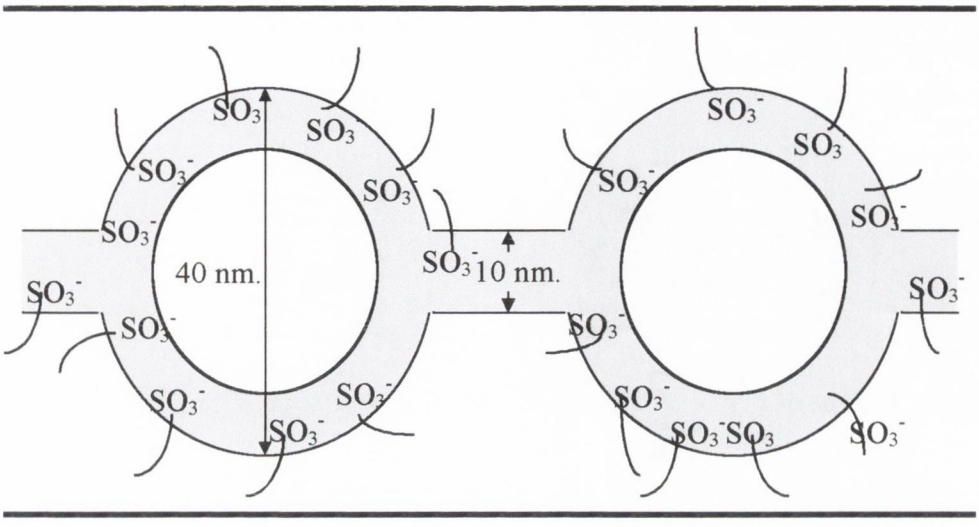

Figure 2.12: Cluster model for Nafion®

The restriction of cluster diameter containing sulphonic groups, allows for the microencagement of size quantised semiconductor particles within Nafion. Nafion in the acid form contains many SO_3^- sites to which the Ti^{3+} ions are attracted in solution. The Ti^{3+} ions readily diffuse into the coordination sphere, and 3 SO_3^- exchange sites can coordinate with one Ti^{3+} ion. Upon addition of a base, the Ti^{3+} ions are readily hydrolysed and oxidised through a series of mixed oxides to TiO_2. The precipitation of TiO_2 by hydrolysis with KOH gives hydrous oxides. In aqueous solutions high acidities are required to prevent hydrolysis for example:

$$[Ti(H_2O)_6]^{3+} + OH^- \rightarrow [Ti(H_2O)_5\,(OH)]^{2+} + H^+ \qquad K = 1.3 \times 10^{-4} \quad [2.4.1]$$

Extensive Ti^{3+} hydrolysis occurs above pH 4 initially forming binuclear species as shown in figure 2.13, attainment of equilibrium becomes increasingly difficult and soon colloidal gels are formed. Ultimately, hydrous TiO_2 is precipitated.

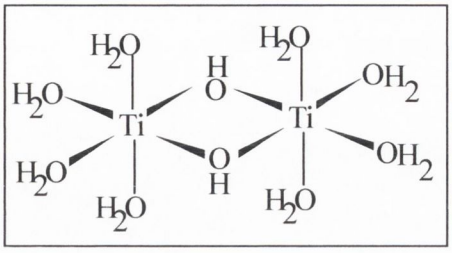

Figure 2.13: Proposed binuclear species formation during hydrolysis of Ti^{3+} to TiO_2

The size of the TiO_2 particles precipitated either within or at the membrane material is dependent on the concentration of hydroxide used. At low hydroxide concentrations the membrane is more selective to OH^- ions. This occurs as a result of the Donnan effect which is related to the difference in relative diffusion rates of cations and ions through a membrane. At high concentrations of KOH, typically >1 mol dm^{-3} there is a build up of negative charge at the membrane surface as anions try to penetrate the membrane. In doing so, Ti^{3+} ions within the cluster network will diffuse to the membrane surface in order to counterbalance the negative charge that is present. Decreasing the concentrations of KOH lowers the Donnan potential across the membrane surface so that most of the Ti^{3+} ions will remain within the ionomer clusters during hydrolysis. TiO_2 particles were immobilised in Nafion membranes, their size and photocatalytic efficiency was examined and a comparison was made between these particles and those produced using the LB technique, together with unsupported TiO_2.

Chapter 3

Experimental

3.1.1 Isotherm measurement

In this research, preliminary LB studies have focused on examining and comparing the shape, position and collapse pressure of π-A curves formed for monolayers of stearic acid (octadecanoic acid, $CH_3(CH_2)_{16}COOH$), palmitic acid (hexadecanoic acid, $CH_3(CH_2)_{14}COOH$) and oleic acid (octadec-9-enoic acid, $CH_3(CH_2)_7CH{=}CH(CH_2)_7COOH$) on different LB subphases, including: pure water, solutions of aqueous HCl, $CdCl_2$, $ZnSO_4$ and $TiCl_3$. Although similar studies have been previously reported using the above named fatty acids, however as part of our preliminary investigations, it was necessary to repeat these experiments.

Stearic acid was Analar grade (99% pure by capillary GC) (Sigma) and palmitic acid was purchased from B.D.H (99% pure), both acids were used without further purification. The straight-chained unsaturated, oleic acid was purchased from B.D.H (99% pure) and was further purified by distillation under vacuum (0.5 mbar at 153°C). The purity of all three fatty acids was established by T.L.C. using a solvent system containing petroleum ether (60:40), diethyl ether and acetic acid in the ratio 9:2:1. All three fatty acids showed no impurities and distinct separation on fluorescent T.L.C. plates after illumination with a UV lamp. The water used in all subphase solutions was Elgastat UHQ grade, which was previously distilled in an all glass still. The conductivity of the water was always less than $1\mu Scm^{-1}$ and the surface tension at 25°C was always greater than 71.5 mNm^{-1}. Extra pure chloroform (99% pure) (Riedel-de-Haen) was used to clean the LB trough and syringes. Chloroform used as the solvent to prepare monolayer spreading solutions (1mg fatty acid /1ml. chloroform) was further purified by first drying with $CaCl_2$ (Riedel-de-Haen, 95%) followed by refluxing over a molecular sieve type 4A. The $CdCl_2$ and $ZnSO_4$ were Analar grade reagents from Aldrich and used as supplied. $TiCl_3$ (15% solution in 10% HCl) was purchased from Riedel-de-Haen and was stored under N_2 until needed. The Langmuir-Blodgett trough was cleaned before and after use with chloroform using surfactant-free tissues. Occasional cleaning of the trough was also carried out using sodium hydroxide (0.1M) at 50°C for 30 min, followed by rinsing with clean water.

Monolayers of stearic acid, palmitic acid and oleic acid were prepared on a water subphase in a Nima model 611D conventional LB trough (figure 3.1). The pH of the subphase was 5.5 and the monolayers were formed by spreading between 30 and 60 µl of the particular surfactant in chloroform (1mg/ml.) at the air-water interface of the LB trough. It was necessary to keep the syringe tip as close as possible to the water surface without immersion in order to prevent monolayer sinking into the subphase. The chloroform was allowed evaporate from the surface for 2 minutes in all experiments after which the surfactant molecules in each case were compressed by reducing their available area. π-A curves were obtained for the three individual fatty acids and were recorded on the PC using the Nima trough software (version 4.70).

3.1.2 Deposition of LB films

All films were deposited onto quartz or glass slides of a size 75mm × 25mm × 1.0mm (Quartz International Ltd and Chance Propper Ltd). The slides were cleaned by sonication for 30 min. at 40°C in sodasil (Aldrich) followed by rinsing in deionised water (Elgastat UHQ grade) and immersion in 2-propanol for a further 30 min. Finally the slides were rendered hydrophobic by coating them with Analar ferric stearate $Fe(C_{17}H_{35}COO)_3$ (T.C.I. Japan). LB films of cadmium stearate and stearic acid were constructed using a vertical dipping procedure and film deposition was investigated at different target pressures (10, 15 and 20 mN/m) at a dipping rate of 5 mm/min. A delay time of 3 minutes between each dip was allowed for each monolayer film to dry. Monolayers were prepared by spreading between 30 and 60 µl of fatty acid (3.5×10^{-3} mol dm^{-3}, 1mg/ml.) solution in chloroform via a Hamilton micro-syringe taking care not to immerse the syringe tip beneath the surface during monolayer spreading. Cadmium stearate was deposited on the slides from an aqueous $CdCl_2$ subphase (10^{-5}M) at pH 5.0, beginning with a down stroke. Similar procedures to that described above were adopted for the immobilisation of Ti^{3+} ions between the headgroups of stearic acid LB films. However the subphase used in this instance was a 0.1mM $TiCl_3$ solution and had a resultant pH of 3.0, after dilution from a stock 1 mol dm^{-3} $TiCl_3$ containing 10% HCl. The LB trough was

encapsulated in an atmosphere bag, filled with N_2 gas. This yielded an oxygen free environment necessary to prevent the oxidation of Ti^{3+} to Ti^{4+} during deposition.

3.1.3 Precipitation of TiO_2 from LB films

Early attempts were made to precipitate TiO_2 from titanium stearate LB films. These films were previously deposited on quartz microscope slides as outlined on page 52. Titanium stearate films were immersed in 5 mol dm^{-3} KOH in order to hydrolyse the Ti^{3+} to TiO_2. However the film dissolved within seconds. A second attempt was made to hydrolyse Ti^{3+} to TiO_2 by immersing a film (100 layers) in tetra-butyl ammonium hydroxide. It was thought that this particular base may hydrolyse the Ti^{3+} to TiO_2 and simultaneously covert stearate to tetrabutylammonium stearate, making the film more insoluble in aqueous solution, however the film again dissolved. Finally a titanium stearate film was deposited on quartz at a target pressure of 15 mN/m and was then fired in an oven at 450°C for 30 min. The uv-vis absorbance spectrum of the film was recorded immediately after firing and at regular time intervals after immersion in buffer pH 7 and 10, in order to verify the stability of the film. This was achieved by placing the film deposited on quartz in the sample beam of the uv-vis spectrometer. A blank quartz slide was placed in the path of the reference beam and absoption due to the TiO_2 was measured by the calculated difference $quartz_{film}$-$quartz_{blank}$. The film formed using this method of oxidation showed increased stability with little or no change in the corresponding uv-vis spectrum over time.

3.1.4 Preparation of nano-particle TiO_2 sols

An alternative method for forming nanoparticulate semiconductor films was also used. This method involved the preparation of TiO_2 particles within surfactant stabilised sols. This method of TiO_2 preparation is fundamentally different with respect to the method described above in that the TiO_2 particles are formed before monolayer spreading at the air-water interface. This involved spreading surfactant-stabilised nano-particle sols of TiO_2 on aqueous solutions and transferring them to

solid surfaces. The organisation of surfactant-coated nano-particles on aqueous solution surfaces relies on the appropriate hydrophobicity and surface charges of the particles. Films formed from colloidal systems of this nature are notoriously sensitive to parameters such as barrier speed, spreading solvents and subphase ion concentration and scrupulous attention must be paid to their purity[1].

TiO_2 nanoparticles were successfully formed and stabilised using two commercially available cationic surfactants, namely cetyltrimethyl ammonium bromide (CTAB) and dioctadecyldimethyl ammonium bromide (DODAB). TiO_2 particles were formed by the arrested hydrolysis of titanium tetraisopropoxide (TTIP 4.5×10^{4}moles) by water (20μl) in a mixture of chloroform (Extra pure 99% pure Riedel-de-Haen, 60 ml.) and propanol (Aldrich, HPLC grade, 40ml.) Briefly, TTIP (Aldrich 99%, 0.5ml.) was dissolved in propanol (Aldrich, HPLC grade, 4.5ml.) and 1.25ml. ($4.5x10^{4}$moles) of the resulting solution was added to the chloroform/propanol/surfactant solution prepared above in the presence of a catalyst, tetramethylammonium hydroxide (Aldrich 98%, 0.2g) at a rate of 0.1ml./10 min. The presence of either surfactant: CTAB, Aldrich 99%, 0.153g (4.2×10^{-3} mol dm^{-3}) or DODAB Aldrich 99%, 0.265g (4.2×10^{-3} mol dm^{-3}) allows for the formation of stable TiO_2 dispersions and prevents aggregation of TiO_2 particles over time. The sols, were stable for 1 month when kept in the dark below 4°C. The absorbance of the TiO_2 sols was measured and their π-A behaviour examined.

3.1.5 Nima 611D Langmuir-Blodgett trough

The Nima 611D Langmuir-Blodgett trough shown in figure 3.1 allows for the analysis and manipulation of molecular organic layers, such as amphiphilic molecules and lipids. The instrument consists of a precision-machined PTFE trough and well (total area 600 cm^2) with a single PTFE barrier supported by an anodised aluminium backing plate. PTFE is essentially chemically inert and can be subjected to rigorous cleaning procedures, making this material most suitable as a lining material for the

trough . The dipper and pressure sensor are mounted at one end of the trough, so that the substrate; typically slides of glass or quartz, can be coated with LB films if required. The barrier and dipping mechanism operates with smooth dynamic control. The trough has channels in the aluminium backing plate through which thermostatted water may be circulated for temperature control.

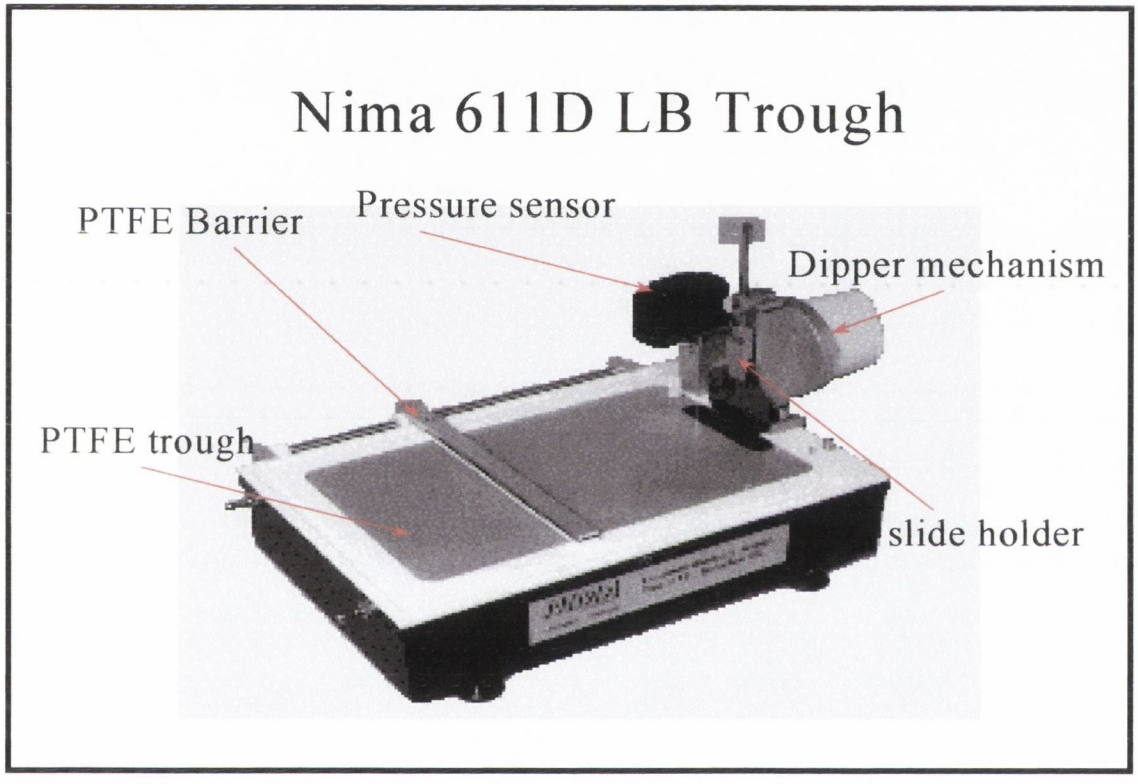

Figure 3.1: LB trough used for the investigation and deposition of monolayers.

3.1.6 Surface pressure measurements.

The basis of pressure measurement for the trough used in this study is the Wilhelmy plate method[2] (figure 3.2). The Wilhelmy plate exists as a strip of chromatography paper, which when suspended at the air-water interface, is pulled down into the bulk of the subphase by the surface tension of the water. If a contaminant is present on the water surface, the surface tension of the water will decrease. The force acting on the

[1] J.H. Fendler, Current Opinion in Colloid & Interface Sci. 1996, 1, 202-207.
[2] R.J. Hunter, 'Introduction to modern colloid science', 1st Ed. Oxford science publications, 1993, 184.

plate is measured by an electronic microbalance. The forces on the plate are gravity and surface tension acting downwards into the subphase and buoyancy due to displaced water acting upwards.

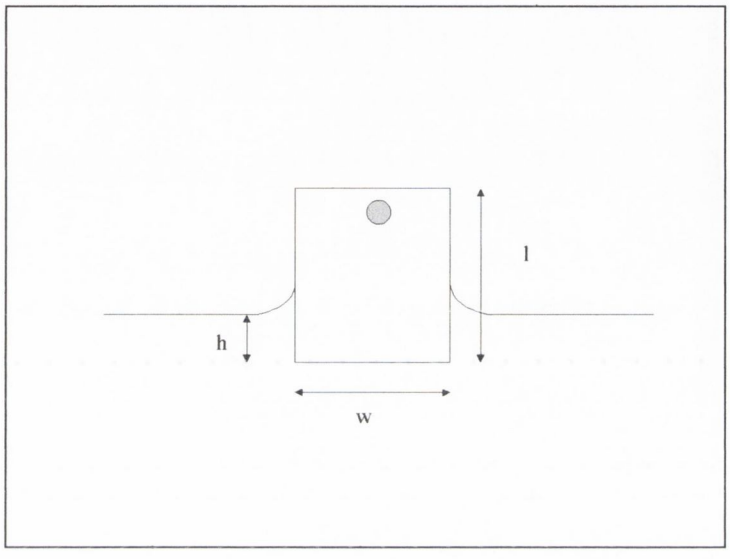

Figure 3.2: Wilhelmy plate used for pressure measurement in Nima's LB trough.

If the plate has dimensions $l \times w \times t$ (length x width x thickness) and a density ρ, and is immersed in water to a depth, h, then the net force acting downwards, F, can be described by the equation:

$$F = \rho glwt - \rho' ghwt + 2\gamma(t + w)\cos\theta \qquad [3.1.1]$$

(Force = weight-uptrust + surface tension)

Where: γ = surface tension of the liquid, θ = contact angle of the plate to the liquid (0° for a completely wetted paper plate), g = acceleration due to gravity (10 m/s^2) ρ' = density of the pure water subphase and ρ = density of the Wilhelmy plate. The difference in downward force ΔF, experienced by the Wilhelmy plate between immersion in pure water and immersion in surfactant-covered water is given by equation [3.1.2]

$$\Delta F = 2(\gamma' - \gamma)(t + w) \qquad [3.1.2]$$

γ' = Surface tension of pure (clean) water (72.8mN/m)[3] at 298K, γ = surface tension of surfactant covered water. The weight and upthrust are eliminated from the equation when the balance is zeroed before measurement. If the plate is considered to have negligible thickness (t) compared to its width, then equation [3.1.2] can be further simplified:

$$\Delta F = 2\Delta\gamma \qquad [3.1.3]$$

Where $\Delta\gamma$ is the difference between the surface tension of clean water and that of surfactant covered water. $\Delta\gamma$ is defined as the surface pressure, π:

$$\Delta\gamma = \gamma' - \gamma = \pi \qquad [3.1.4]$$

So that, $$\Delta F = 2\pi \qquad [3.1.5]$$

For a 10 mm wide paper plate with zero contact angle, the measured force (in mg) is twice the surface tension (in mN/m) if g is taken as 10 m/s^2.

3.2.1 Cleaning the Nafion membranes.

The third heterogeneous host used for incorporation of TiO_2 particles was Nafion 117 (section 2.4.1). This membrane (200 mm x 200 mm, Aldrich) when received, showed a brown colouration. Examination of the non-cleaned Nafion material by uv-vis absorption confirmed the presence of contaminants, i.e. a clean Nafion membrane shows zero absorption from 200-900nm. Strong oxidising agents such as HNO_3 or H_2O_2 were used to remove contaminants from the membrane. The cleaning procedure adopted in this study involved the use of the above oxidising agents; this procedure is described as follows:

The Nafion membranes were marked and cut into rectangular strips 4.5 cm × 1.0 cm approx. The membranes were placed in 6% H_2O_2 (150 cm^3) at 45°C for one hour. H_2O_2 oxidised the surface bound contaminants from the membrane. Excess H_2O_2 was removed from the membrane by immersion in deionised water. The Nafion membrane was then pre-treated by reflux in 300 ml. of lead free HNO_3 (65% conc.) for 1 hour. The reflux was repeated in fresh HNO_3 for a further hour. The membrane was washed in deionised water and dried with surfactant and dust free tissues (kimwipes). Clarity of the membrane was checked by uv-vis spectroscopy. All of the above solutions were prepared with triply deionised water (UHQ, HPLC grade) of a similar standard to the water used in LB studies.

3.2.2 Preparation of TiO_2 particles in the Nafion membranes

The formation of TiO_2 incorporated Nafion was attempted in two different solvent systems. Namely aqueous-$TiCl_3$ and MeOH-$TiCl_3$ solutions. The choice of two different solvent systems is attributed to the fact that Nafion cluster diameter is reported to be dependent on the degree of membrane swelling[3]. A fully hydrated Nafion membrane has a maximum cluster diameter of 40 nm as previously described in section 2.4.1. Therefore the degree of membrane swelling is dependent on the particular solvent used. By controlling the degree of hydration it may be possible to control the particle size within the membrane.

[3] A. Eisenberg, H.L. Yeager, 'Perfluorinated Ionomer Membranes', ASC, Symp. Series. 1982, 180.

Chapter 3, section II: Preparation of Nafion bound materials

Ti (III)-exchanged Nafion was prepared by immersing the clean and thoroughly washed Nafion membrane in a 0.1M aqueous solution of deoxygenated $TiCl_3$ (Riedel-de Haen 15% in @10% HCl). The solution was magnetically stirred and N_2 outgassed for 3 hrs. Outgassing the system creates a completely oxygen free environment and prevents oxidation of Ti^{3+} to TiO_2 prior to Ti^{3+} incorporation in Nafion. Ti^{3+} in aqueous solution exists as the hexaqua ion $[Ti(H_2O)_6]^{3+}$. This ion with its d^1 electronic configuration shows a d-d transition and appears violet in colour.

The second route investigated for the incorporation of Ti^{3+} ions in a Nafion membrane involved the use of deoxygenated MeOH as the solvent. Clean Nafion membranes were placed in a deoxygenated methanol solution, which was bubbled with N_2 gas overnight. The exchange of Ti^{3+} ions into 5 different Nafion membranes was accomplished again using a similar concentration of $TiCl_3$ as outlined above, however this solution was prepared in deoxygenated MeOH. The light purple Ti (III)-incorporated Nafion membranes exchanged in both solvents were then washed with deaerated H_2O. Formation of the corresponding metal oxide was investigated by exposing the highly reactive Ti^{3+} metal ions incorporated in Nafion to various concentrations of KOH (0.01, 0.1, 0.25, 0.5 and 5 mol dm^{-3}) solution overnight. After $\approx$ 10 – 15 minutes the membranes particularly those immersed in higher KOH concentrations changes from its initial pale violet colour to a very dark black colour, indicating possible formation of higher oxides, Ti_2O_3 (purple/violet) and Ti_3O_5 (blue/black)[4]. After about 1 hour the membranes become opaque and white indicating the TiO_2 formation. The incorporation of Ti^{3+} ions into the Nafion was observed using uv-vis spectroscopy. The crystallographic nature and size of the resulting metal oxide particles were examined using, X-Ray diffraction (XRD), energy dispersive X-Ray analysis (EDAX) and transmission electron microscopy (TEM).

---

[4] D. Mc Cormack, Ph.D. Thesis 1990, 96

3.3.1 Overview.

In this study photochemical experiments were carried out by examining the photocatalytic decomposition of cyanide using TiO_2. The reasons behind the choice of cyanide as a model contaminant and TiO_2 as a suitable catalyst was already outlined in section 1.1.5 and 2.1.4 respectively.

Two independent methods of cyanide analysis were employed for investigating the kinetic behaviour of cyanide photo-oxidation using TiO_2 as a photocatalyst: a colorimetric and a potentiometric method. Both methods were found to be capable of detecting low levels of cyanide in aqueous solutions (< 1ppm.) Two different commercial samples of TiO_2: Degussa P-25 and Kronos APF were investigated as active photocatalysts towards cyanide photo-oxidation.

3.3.2 Colorimetric method

The colorimetric method is based on the reaction of free cyanide with pyridine barbituric acid in aqueous solution. The pyridine barbituric acid was prepared as follows: barbituric acid (15g) (Aldrich 99%, Mol. Wt. 128.09g/mol.) was placed into a volumetric flask (250 ml.). The sides of the vessel were washed with deionised water, and pyridine (C_5H_5N) (75 ml.) (Riedel-de-Haen, 99%) was then added. Hydrochloric acid (15 ml.) (Riedel-de-Häen, min. assay 38% conc.) was slowly added to the barbituric acid and complex decomposition was prevented by maintaining the temperature below 25°C using an ice bath. Finally, the reaction mixture was diluted to the mark with deionised water.

Principal CN^- (free cyanide excluding complex cyanides) in aqueous solution is converted to cyanogen chloride (CNCl) by reaction with chloramine T (CAT) solution. ($CH_3C_6H_4SO_2N(Na)Cl$). 1g of CAT solid (B.D.H. 99% pure)(Mol. Wt. 281.69g/mol) was dissolved in deionised water (100 ml.) in a volumetric flask. The addition of CAT solution to free CN^- in solution forms cyanogen chloride (CNCl). Addition of pyridine barbituric acid to CNCl forms a red-blue complex. At high pH values the CNCl will be hydrolysed to cyanate (CNO^-), thus the pH of the

solution must be reduced to 6 with CH_3COOH (1 mol dm^{-3}) prior to addition of CAT solution. In the colorimetric method the cyanide concentration is monitored by measuring the absorbance of the cyanide complex with pyridine barbituric acid in aqueous solution at 582 nm [5].

A series of standards (1-10) containing CN^- between 0.1 and 1ppm were prepared by successive dilution of the stock cyanide solution (2.5g KCN and 2g KOH in 1000ml.) using NaOH (0.05M). Each standard (20 ml.) was buffered at pH 6 with the addition of 1M sodium di-hydrogen phosphate (4 ml.). Chloramine –T solution (2 ml.) was added to each of the buffered standards. The solution was mixed thoroughly and pyridine-barbituric acid (5 ml.) was added to each standard. The solutions (1-10) were diluted to the mark with deionised water in separate volumetric flasks (50 ml.). The absorbance of the standard cyanide-complex was measured at 582 nm. A proposed mechanism for cyanide complexation with pyridine barbituric acid is given in section (4.3.3).

3.3.3 Photocatalytic activity of TiO_2 in cyanide

The photocatalytic process associated with removing cyanide from aqueous solution was adopted in this particular study for examining the efficiency of both unsupported and supported TiO_2 particles. The efficiency of photocatalysis is dependent on the particle size, which in turn is related to both the contaminant adsorption capacity and ability for forming charge carriers.

Photochemical experiments were carried out in a quartz photoreactor (Figure 3.3). With photochemical experiments involving unsupported micron size TiO_2, 0.2g of TiO_2 was added to 200ml of 20 ppm cyanide. Experiments were performed in the presence of oxygen and at pH 10. The pH was adjusted as before using 1M CH_3COOH (5ml.). The oxygen aided in stirring the solutions and this maintained a homogeneous environment. The solution was briefly gassed with oxygen prior to

[5] Standard Methods of Analysis, Inorganic Non-metals 320-330.

illumination, in order to obtain a constant atmosphere during photo-oxidation. The solution was illuminated for approximately 120 minutes through a cylindrical quartz immersion well that transmitted wavelengths > 200 nm, using a medium pressure mercury lamp (400 W Applied PhotoPhysics Ltd. immersion well photochemical reactor) as shown in figure 3.3.

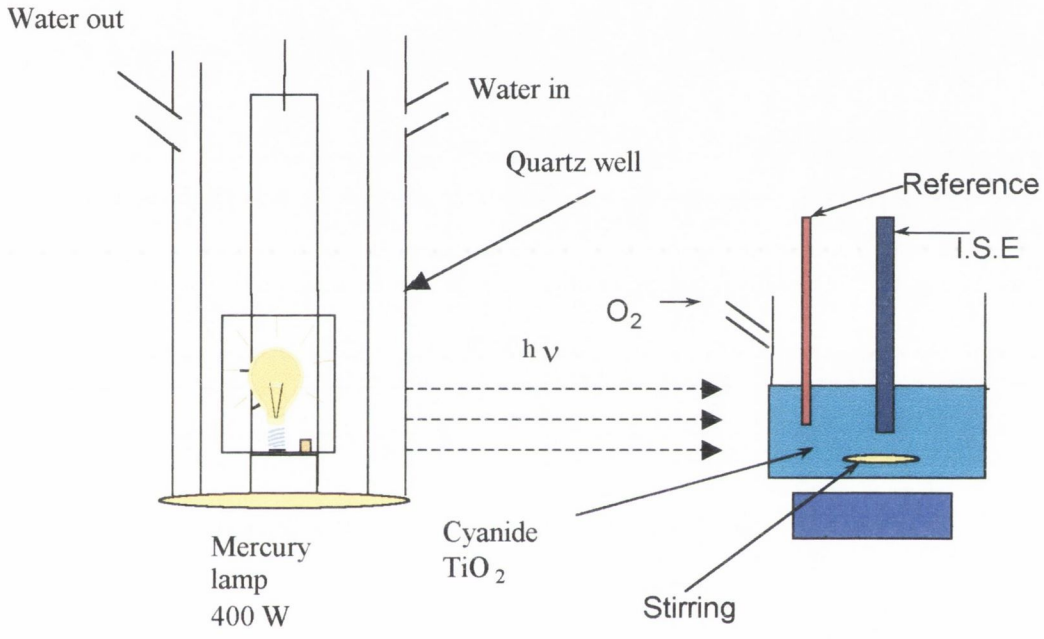

Figure 3.3: Photochemical reactor used for investigation of cyanide photocatalysis

Samples were withdrawn from the reactor every five minutes during the reaction. TiO_2 was removed from the samples prior to cyanide analysis using presterilised and nonpyrogenic filter units, (Sartorius, Ministart unit filters, 0.2μm pore size. Each sample solution (1ml.) was diluted with NaOH (0.05M, 1 in 20 dil.) to prevent HCN formation and complexed with pyridine-barbituric acid reagent in order to determine the amount of cyanide remaining in solution using the procedure described in section 3.3.2.

3.3.4 Potentiometric method: photocatalytic activity of TiO_2 in cyanide.

The concentration of cyanide remaining in solution during photocatalysis was also determined using a cyanide specific ion selective electrode (Orion model 94-06). The electrode potential was measured relative to a double junction reference electrode (Orion model 90-02). Both electrodes were connected to a microprocessor ion analyser (Orion research model 901). From this data a kinetic analysis was carried out in order to determine the order and rate of cyanide decomposition. The initial concentration of cyanide and amount of TiO_2 were 20ppm/200ml and 0.2g respectively. The slurry solutions were irradiated as described previously, (section 3.3.3). Oxygen was bubbled through the solution at pH 10. The stock cyanide solution 20ppm was prepared using triply deionised water so as to prevent interfering ions such as Cl^-, I^- and S^{2-} forming a layer of salt on the membrane surface of the electrode, and affecting the diffusion of CN^- into the membrane.

The maximum detectable concentration of cyanide using an I.S.E is 26ppm [6]. Above 26 ppm the membrane's lifetime is adversely effected. The I.S.E was frequently polished to restore the etched or coated membrane (Polishing strips, Orion Cat. No. 948201). The electrode was calibrated before use by measuring the change in voltage for a ten fold increase in cyanide concentration from 0.1 ppm to 1.0 ppm; this change in voltage was always 57mV +/- 3mV.

3.3.5 Photocatalytic activity of TiO_2 particles in Nafion and LB films

Kinetic data was recorded for cyanide photocatalytic oxidation using TiO_2 incorporated Nafion membranes and LB films. The initial concentration of CN^- was again 20 ppm. The change in concentration of cyanide was measured using the I.S.E method as described previously section (3.3.4). The photochemical reaction was carried out in the presence of oxygen at pH 10.

[6] Orion Research Inc. Lab. Products, 'group Instruction Manual for cyanide electrode'.

3.4.1 Introduction

The atomic force microscope (AFM), or scanning force microscope (SFM) was developed in 1982 by Binnig, et al[7]. This technique offers, in principle, the possibility of obtaining atomic resolution images with, in many cases a minimum of prior preparation of samples. A consequence of this has been the application of the AFM technique across a broad spectrum of scientific research, from analysis of biological systems, polymers and solid-state physics[8, 9, 10]. Several possible applications of AFM also exist in the field of materials chemistry. They include substrate roughness determination (wafers), determination of step formation during thin film deposition, pinhole and other defect detection during oxide growth, defect analysis in photolithography masks and determination of microscratches and other defects in optical components[11].

3.4.2 Basic principles of operation

The AFM is a stylus-type instrument in which a sharp probe (tip) moves over a sample surface in a raster scan. The probe is attached to one end of a cantilever, the forces of interaction between the tip and the sample which include Van der Waals, capillary, magnetic and electrostatic forces are all attractive in nature and are long range forces. Forces such as adhesion and frictional forces are repulsive and contribute short-range forces. The cantilever bends in response to these forces and light from a laser is reflected from a mirror at the back of the cantilever onto a photodiode. Figure 3.4 shows the principle components of the AFM. A variety of optical methods have been devised to detect the cantilever deflection.

[7] G. Binnig, C. Quate, Phys. Rev. Lett., 1986, 56, 930-933.
[8] B. Drake, C. Prater, A. Weishorn, S. Gould, T. Albrecht, Science, 1989, 243, 1586.
[9] N. Brown, H. You, R.J. Forster and J.G. Vos, J. Mater. Chem. 1991, 1, 517.
[10] G. Binnig, H. Rohrer, C. Gerber, E. Weibel, Surf. Sci. 1983, 131, L379.

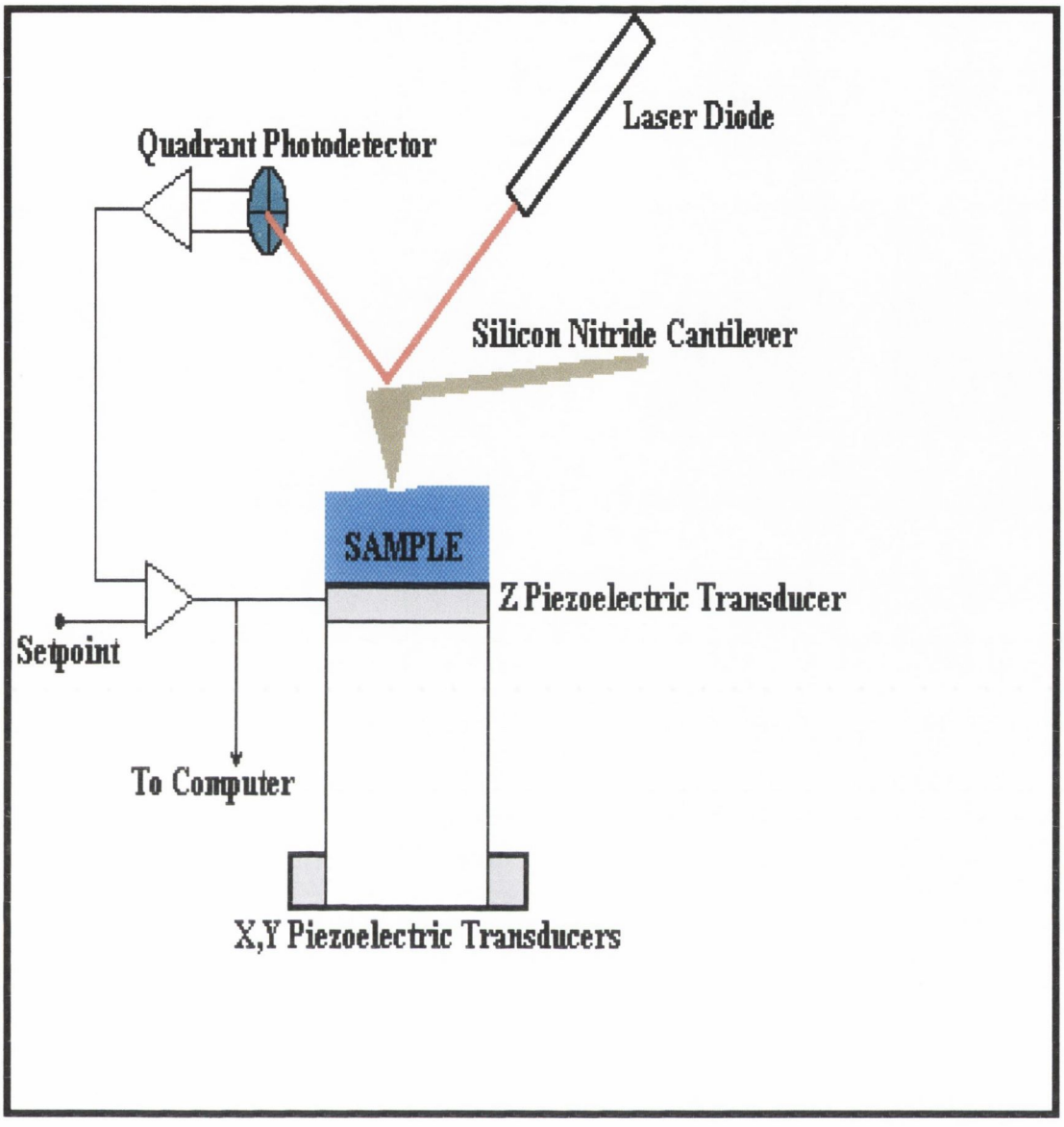

Figure 3.4: Schematic representation of a typical AFM instrument.

3.4.3 Modes of operation

The AFM measures the interaction forces between a tip and sample surface. The large area of the tip contributes the long-range forces while the small tip apex contributes the short-range forces. When operating the AFM with a sample tip separation of a few nanometers, known as non-contact mode, the long-range attractive forces dominate. These attractive forces diminish, with increasing tip sample separation at a much slower rate than the repulsive as shown in figure 3.5. In non-contact mode the image is relatively poor because the image data is a convolution of the macroscopic shape of the tip. However when the tip-sample distance is reduced to

less than 1nm, the repulsive forces dominate (contact mode). The repulsive forces are larger in magnitude than attractive forces and they are localised to a much smaller area at the tip head, thus higher image resolution is achieved only at they expense of tip or sample damage.

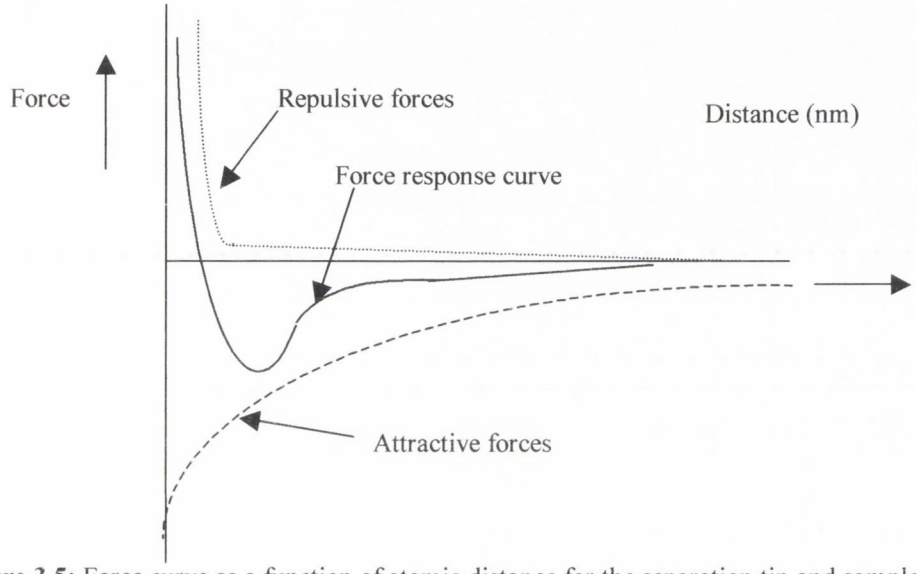

Figure 3.5: Force curve as a function of atomic distance for the separation tip and sample.

3.4.4 AFM measurements

AFM measurements were performed with a Burleigh Aris-3500 personal AFM in air at room temperature using a silicon nitride tip of length 10-15 μm and radius 100 Å on a cantilever with a spring constant of 0.045N/m and resonant frequency of 8-18 kHz. All imaging was carried out in the non-contact mode where an electronic feedback loop keeps the interaction force constant so that it is possible to follow changes in the surface features as fast as possible without the tip damaging the sample. The advantage of operation in the non-contact mode is that the larger distance of the tip from the sample reduces any possible sample damage. This mode was particularly useful for examining soft LB films of Ti-St and Cd-St. AFM topographic images were recorded for amorphous glass slides $1cm^2$, glass slides containing ferric stearate and LB films of titanium stearate (maximum 25 monolayers) prepared as outlined in section 3.1.2) and fired at 450°C for 2hrs. All

samples were placed on $1cm^2$ circular aluminium stubs prior to AFM imaging. Before imaging, the AFM was allowed to stabilise for at least 30 min after being switched on. All images were filtered using line and plane removal and the software high pass filtering option was also used in order to eliminate low frequency noise due to external interference and vibrations. The minimum and maximum allowable sample scan area which may be recorded was 3.5 × 3.5 μm and 70 × 70 μm respectively.

3.5.1 Introduction

Uv-vis spectroscopy is the measurement of the wavelength and intensity of absorption of near-ultraviolet and visible light by a sample. Ultraviolet and visible light is energetic enough to promote electrons from highest occupied molecular orbitals (HOMO) to lowest unoccupied molecular orbitals (LUMO). Uv-vis spectroscopy was particularly useful for determining the band gap and indirectly the size of TiO_2 particles within LB films, Nafion ionomer membranes and surfactant stabilised sols. The wavelength of absorption and indirectly, the band gap of TiO_2 was estimated from each of the absorption spectra as shown by the example below figure (3.5a).

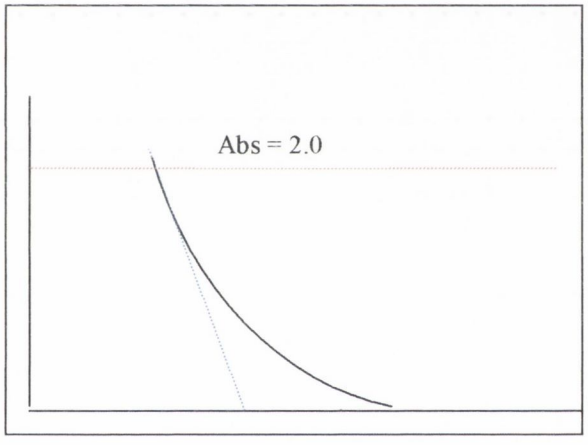

Figure 3.5(a) Absorption spectrum showing the tangent to the curve at Abs = 2.0.

3.5.2 Uv-vis measurements.

All absorption spectra were recorded on a double beam uv-vis spectrometer, model Shimadzu UV-2101PC in the spectral range 190 to 800 nm, using a medium scan speed, monochromator slit width of 0.2 nm, and sampling interval 0.5 nm. Uv-vis measurements were recorded using LB film samples deposited on quartz slides, for Nafion incorporated TiO_2 membranes, a second untreated Nafion membrane was used as a reference sample, during uv-vis measurements. Quartz cuvettes having a path length of 1cm were used for uv-vis measurements of surfactant stabilised TiO_2 sols.

3.6.1 Introduction

Scanning and transmission electron microscopy are considered as common investigative techniques particularly for materials characterisation. The illumination source is a tungsten filament, also known as the electron gun, which is heated to a high temperature (2700 K) causing electrons to be released from the tip of the filament. Lenses focus the electron beam and the lenses and the sample stage are mounted in a vertical, lead-lined cylindrical column that allows the interior to be maintained under vacuum. The samples are coated with gold to provide a conductive surface or path to carry the current that is produced from the high-energy impact of the beam with the sample. Sample gold sputtering prevents surface charging which otherwise could destroy the sample or cause beam deflection and result in considerably reduced elemental detection

Both techniques involve the narrow focussing of an accelerated high-energy electron beam (60-100 keV) towards a sample surface. These high-energy electrons are capable of interacting with the sample atoms and produce characteristic secondary particles and radiation that are important for providing size and structural information regarding a particular sample.

A high vacuum is needed (10^{-7} torr) so that the electrons do not collide with air molecules and get deflected before they reach the specimen. The elastically scattered electrons, (backscattered electrons) i.e., those that have changed their direction but not lost any energy on interaction with the specimen, interfere with the unscattered electrons to produce a phase contrast image. The secondary electrons, formed as a result of inelastic interactions of the incident beam with electrons in the sample, have low energy and are only capable of escaping from the surface and being detected at shallow depths (figure 3.6).

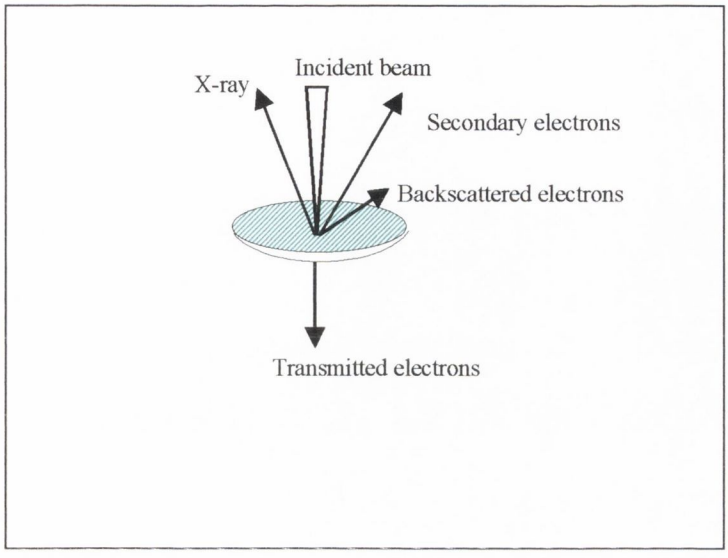

Figure 3.6: High energy incident and diffraction radiation using SEM or TEM

3.6.2 TEM measurements

TEM measurements provide information regarding, the size of particles that make up a particular material. Transmission electron microscopy was performed using a Hitachi H-700 electron microscope. All samples were examined on either Nickel or copper (100-mesh) grids, which had been previously coated with a hydrophobic material called formvar. This material acts as a support capable of holding the sample on the grid during measurement. The TEM technique was used for the size characterisation of TiO_2 semiconductor particles; these particles were formed and stabilised using two distinct and fundamentally different preparation procedures, the LB method (section 3.1.2), and a Nafion bound TiO_2 method (section 3.2.2).

3.6.3 Scanning Electron Microscopy

In the scanning electron microscope (SEM), a beam of accelerated electrons slightly lower in energy to that used in TEM studies scans the surface features of specimens. The surface topography of a specimen is generated by the backscattered or secondary electrons that are produced from a gold or gold-palladium-coated specimen. This is accomplished by focusing a narrow, intense beam of electrons to form a very small spot of illumination (between 2Å & 200Å diameter) on the specimen. This fine beam of electrons is then deflected across the specimen at fixed distances corresponding to

the diameter of the narrow intense beam. The probe spot is then returned to a new scan line on the specimen one spot diameter above or below the original starting point. This line of the sample is then scanned. The process is repeated until the selected area of the sample is fully scanned by the probe of electrons. The scan pattern is called a raster which provides the 3D nature of the SEM data. The energy of the backscattered and secondary electrons in each scan line are projected onto a cathode ray tube where the image contrast is formed.

3.6.4 Scanning electron microscopy measurements

Scanning electron micrographs were obtained for a number of commercially available powdered samples of TiO_2, namely Degussa P25, Kronos APF. Micrograph images were also recorded for Nafion samples containing TiO_2. All samples were coated with gold to render them conducting, using sputtering and applying a DC voltage of 30 mA across argon for approximately 3-4 minutes under vacuum. A raster scan pattern was used rather than a spot scan at different regions of each individual sample so as to prevent 'sample burn up'.

3.6.5 Energy dispersive X-Ray analysis (EDAX)

Energy dispersive X-Ray analysis (EDAX) was used in conjunction with SEM studies. EDAX imaging is a useful microprobe technique for the determination of different elemental deposits present in a material. This technique proved highly useful for the investigation of elemental deposits, in both Nafion and LB films. The technique involves bombarding a sample with a spot beam (<1μm) of sufficient energy (10-30 keV), and analysing the resulting energy X-ray dispersive wavelengths. The X-Ray emission is attributed to initial electronic excitation of inner core electrons to outer shells; this arises from inelastic scattering (secondary scattering) between the electrons present in the beam and the sample. The sample electrons lose their energy with final re-emission of lower energy (x-rays) in the form of photons as shown in figure 3.7. The emitted X-rays are characteristic of the elements under investigation and a fingerprint of different element relative intensities at specific energies is obtained. Semi quantitative analysis is possible by comparing

sample line intensities with a known amount of pure material. Energy dispersive X-ray detectors are capable of recording the emitted photons of energy.

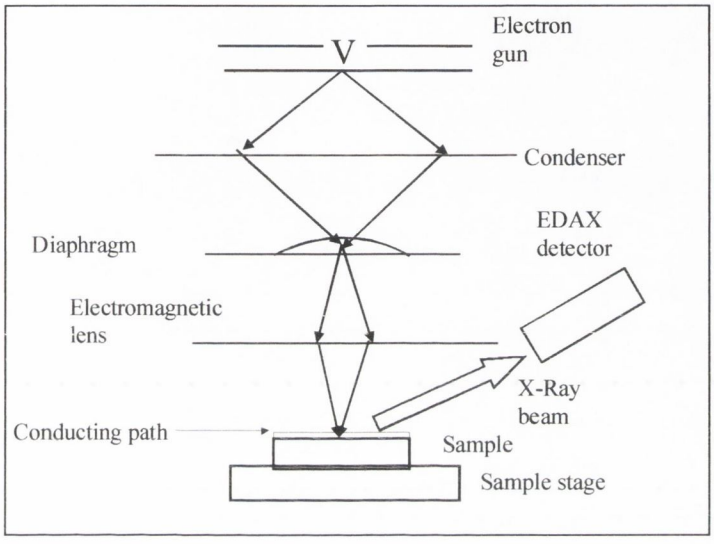

Figure 3.7: Schematic representation of the EDAX technique

EDAX measurents were performed on samples of Nafion and LB films, both containing TiO_2.

3.7 1 Electron diffraction

Electron diffraction (ED), in its simplest application, is used to identify crystalline substances based on the spacing of atomic planes within particles. The angle and intensity of electron diffraction for a given sample will depend on the spatial arrangement of the atoms in the crystal, and on the energy (wavelength) of the incident electron beam respectively. A diffraction pattern consists of a central spot and a number of other diffraction spots or rings. Diffraction spots will predominate over diffraction rings if the material under measurement is crystalline and of one particular orientation.

A sharper ring structure indicates a crystalline material as opposed to an amorphous material for a given sample. The distance of the spots or rings R (mm) from the centre spot is related to the lattice spacings using the following equation:

$$R.\, d = \lambda.\, L \qquad [3.7.1]$$

Where: λ = Wavelength of electron beam, d = lattice spacings for a particular sample and L = Camera length (mm). Figure 3.8 shows the basic experimental set up used for electron diffraction measurements

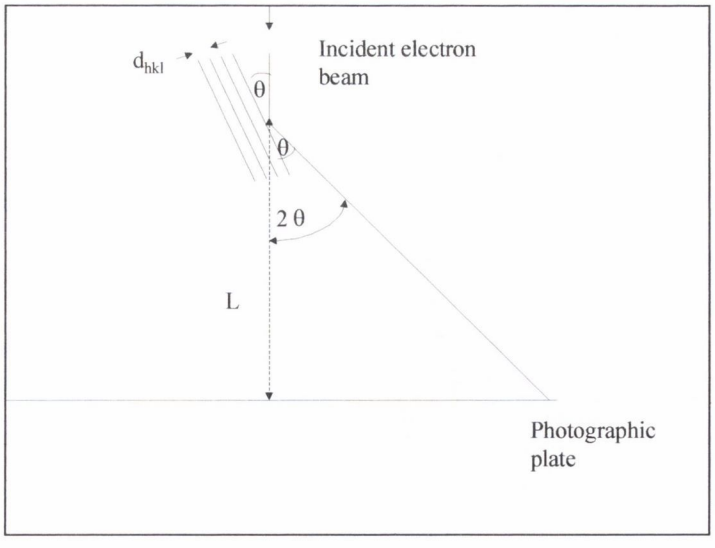

Figure 3.8: Basic schematic set up employed for powder electron diffraction measurements.

3.7.2 Electron diffraction measurements.

Knowing the camera length and wavelength of incident radiation λ, and by measuring the ring or spot distances R, it is possible to determine the lattice spacings d for the sample concerned. Electron diffraction was used to determine the lattice spacings for TiO_2 particles that were formed using the techniques outlined in section 3.1.3 and 3.2.2. The calculated experimental d-spacings associated with these particles were compared with the d-spacings for the three crystalline forms of TiO_2[11] (anatase, rutile and brookite). The accelerating voltage applied to the electron gun was 100 kV for all ED measurements, this provides a source of electrons of wavelength $\lambda_{el} = 0.0037$ nm.

3.7.3 X-ray Diffraction

When X-rays bombard a crystalline material, the electrons surrounding each atom bend, or diffract, the X-ray beam, which then forms an X-ray diffraction pattern. Crystalline samples will diffract X-rays at specific angles depending on the particular structure under investigation. Powder X-ray diffraction patterns were recorded for TiO_2 particles formed in LB films, and Nafion as described previously. The crystallographic nature of the particles were then compared to the three most common TiO_2 crystallographic patterns anatase, rutile and brookite.

X-ray diffraction patterns were also recorded for each of the commercially available TiO_2 samples (Degussa P25 and Kronos APF) that were used for cyanide photocatalytic studies.

X-Ray diffraction measurements were obtained for TiO_2 powdered samples by placing a small amount of the material on a glass slide followed by a few drops of acetone. The acetone increases adhesion between the powder and the glass slide and prevents loss of sample material during measurement. Thin film measurements were recorded for LB films of cadmium stearate, titanium stearate and fired titanium

[11] Joint Committee on Powder Diffraction Standards and the International Center for Diffraction Data.

stearate (TiO_2) at small angles typically between 2θ 1°-10°. Figure 3.9 shows the basic experimental set up for powder X-Ray diffraction.

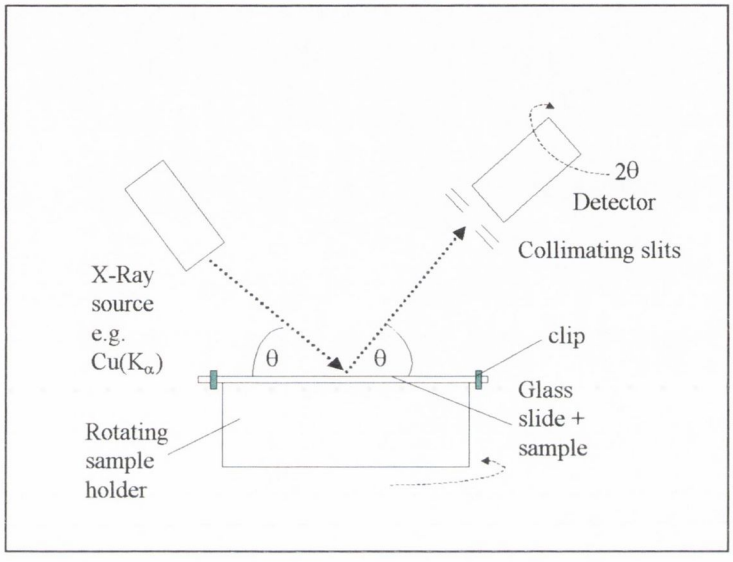

Figure 3.9: Basic schematic set up employed for powder X-Ray diffraction measurements

Chapter 4

Results

4.1.1 Phase behaviour in LB films.

In this study surface pressure-area isotherms were recorded for stearic, palmitic and oleic acid at the air-water interface of an LB trough as previously described (section 3.1.1). Representative examples are shown in figure 4.1. The LB characteristic properties associated with each of these amphiphilic molecules were examined. Information was easily obtained regarding monolayer stability, orientation and size by investigating the collapse pressure, shape and position of each monolayer formed.

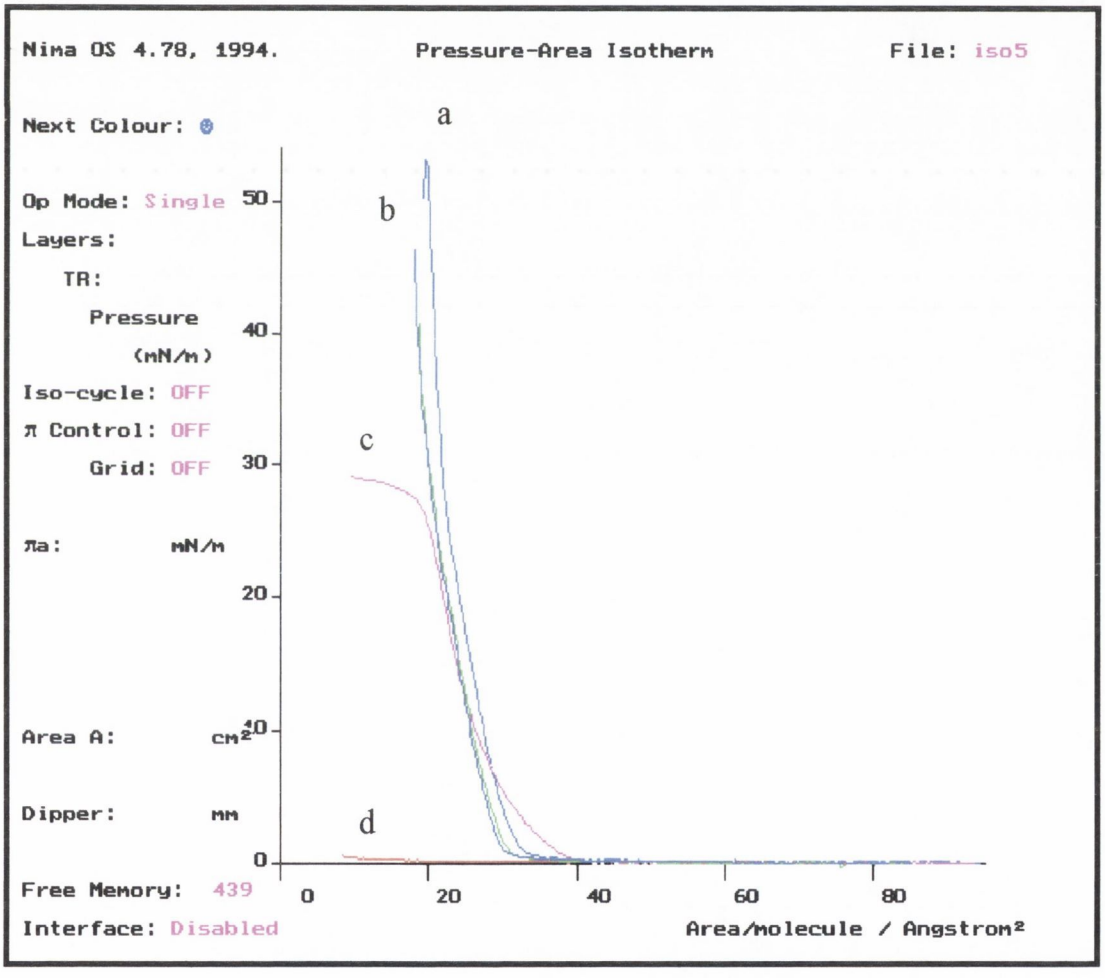

Figure 4.1: π-A isotherms for (a) stearic, (b) palmitic (2 compressions) and (c) oleic acid monolayers at the air-water Interface. (d) triply deionised surfactant free water .

The π-A isotherms for stearic acid (a) and palmitic acid (b) on a pure water subphase at pH 5.5 and 293 K are shown in figure 4.1. It is evident from both isotherms that

each monolayer material undergoes transition between at least two phases during compression. Each monolayer isotherm shows a change in direction at each phase transition. Phase changes were identified in each isotherm by extrapolating each curve to $\pi = 0$ at the point where there is a change in isotherm direction.

Both stearic and palmitic acid appear to show two successive (stepwise) phase transitions throughout compression. A liquid-condensed phase transition occurs at 1mN/m for each of the monolayers at 32Å^2 and 30Å^2 per molecule respectively. A liquid to condensed-solid phase transition is also observed at π = 20mN/m and molecular area 25Å^2 per molecule for stearic acid. A similar phase transition appears at 24 mN/m and a molecular area of 23Å^2 per molecule for palmitic acid. The apparent lower molecular area associated with palmitic acid at each phase transition compared to stearic acid may be attributed to the fact that palmitic acid is more soluble in the water subphase. The cross sectional molecular area for each monolayer material was estimated by extrapolating each individual isotherm to $\pi = 0$ at a surface pressure within the solid phase. The maximum collapse pressure recorded for stearic and palmitic acid was ca. 50mN/m.

Figure 4.1 (c) also shows a typical surface pressure-area isotherm for oleic acid at the air-water interface of an LB trough under similar conditions of temperature and pH. The π-A isotherm for oleic acid shows a smoothly increasing surface pressure with decreasing area until a collapse pressure of 30 mN/m is reached. There is little or no evidence for phase transitional behaviour during monolayer compression. This type of isotherm illustrates the influence of the double bond towards decreasing the packing capability of the monolayer at the air-water interface. The low packing ability of oleic acid is reflected in the stability of the monolayer, in that a relatively low collapse pressure of 30 mN/m is observed, in contrast to a relatively high collapse pressure of 50 mN/m required using stearic or palmitic acid.

4.1.2 Effect of divalent cation concentration on LB phase behaviour.

It has been already established[1] that successful transfer of film forming materials such as stearic, oleic and palmitic acid onto suitable substrates is normally carried out at a surface pressure within the liquid condensed-solid region of the isotherm, generally between 20-30 mN/m as shown in figure 4.2.

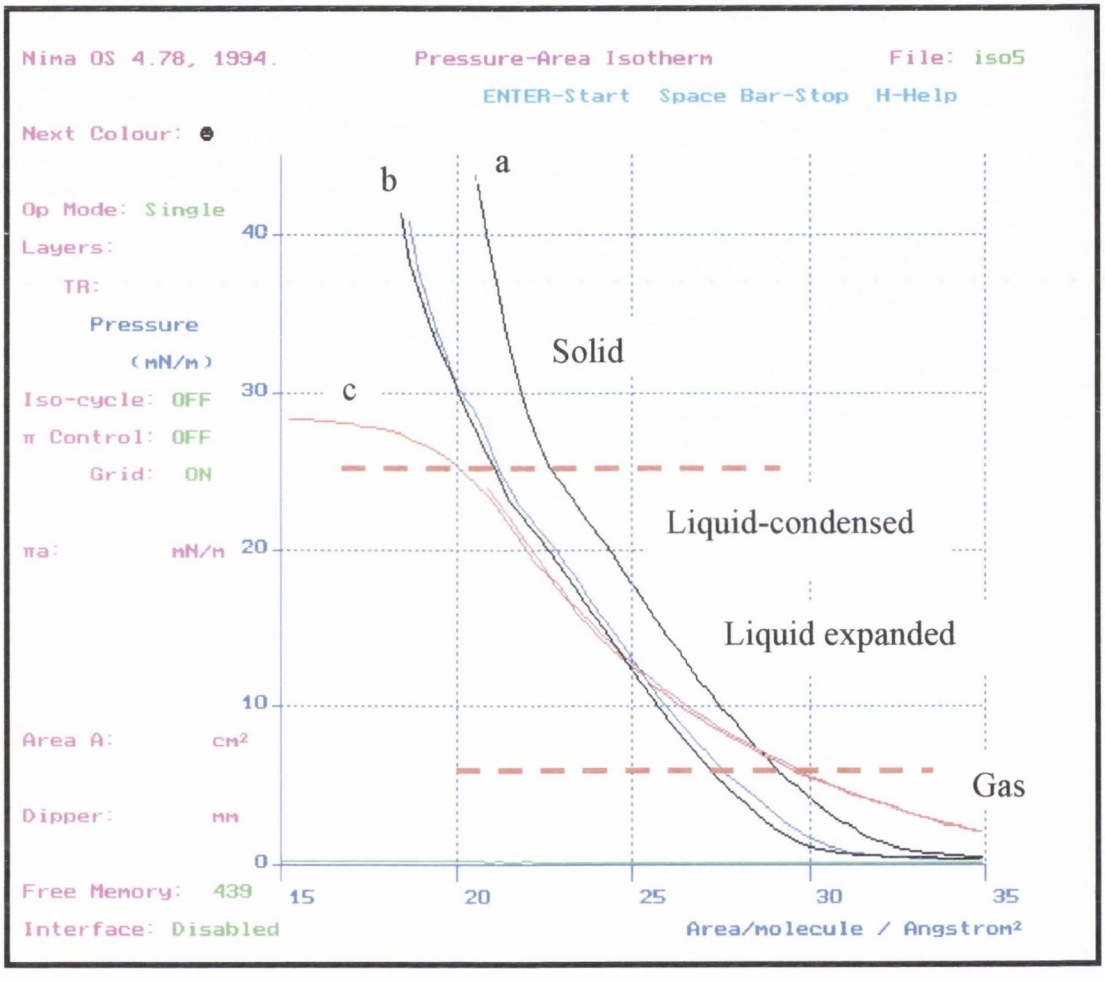

Figure 4.2: π-A curve for stearic (a), palmitic (b) and oleic acid (c) on water with each corresponding phase transition.

In order to achieve successful monolayer deposition it was necessary to highlight or extend the liquid condensed-solid regions of the isotherm. This process was achieved by introducing metal ions into the aqueous subphase. Divalent metal ions such as

[1] T. Richardson, Chemistry in Britain. 1989, 12, 1218.

Cd^{2+} and Zn^{2+} in the concentration range 10^{-5}M - 10^{-3}M were introduced into the water subphase of the LB trough. The effects of their introduction on the isotherm behaviour are reported for the three different carboxylic acids: stearic, palmitic and oleic acid at a predetermined pH of 5.5.

Figures 4.3 and 4.4 show the π-A isotherms of stearic acid spread on different subphase concentrations of 10^{-5}-10^{-3} mol dm^{-3} $CdCl_2$ and $ZnSO_4$ respectively.

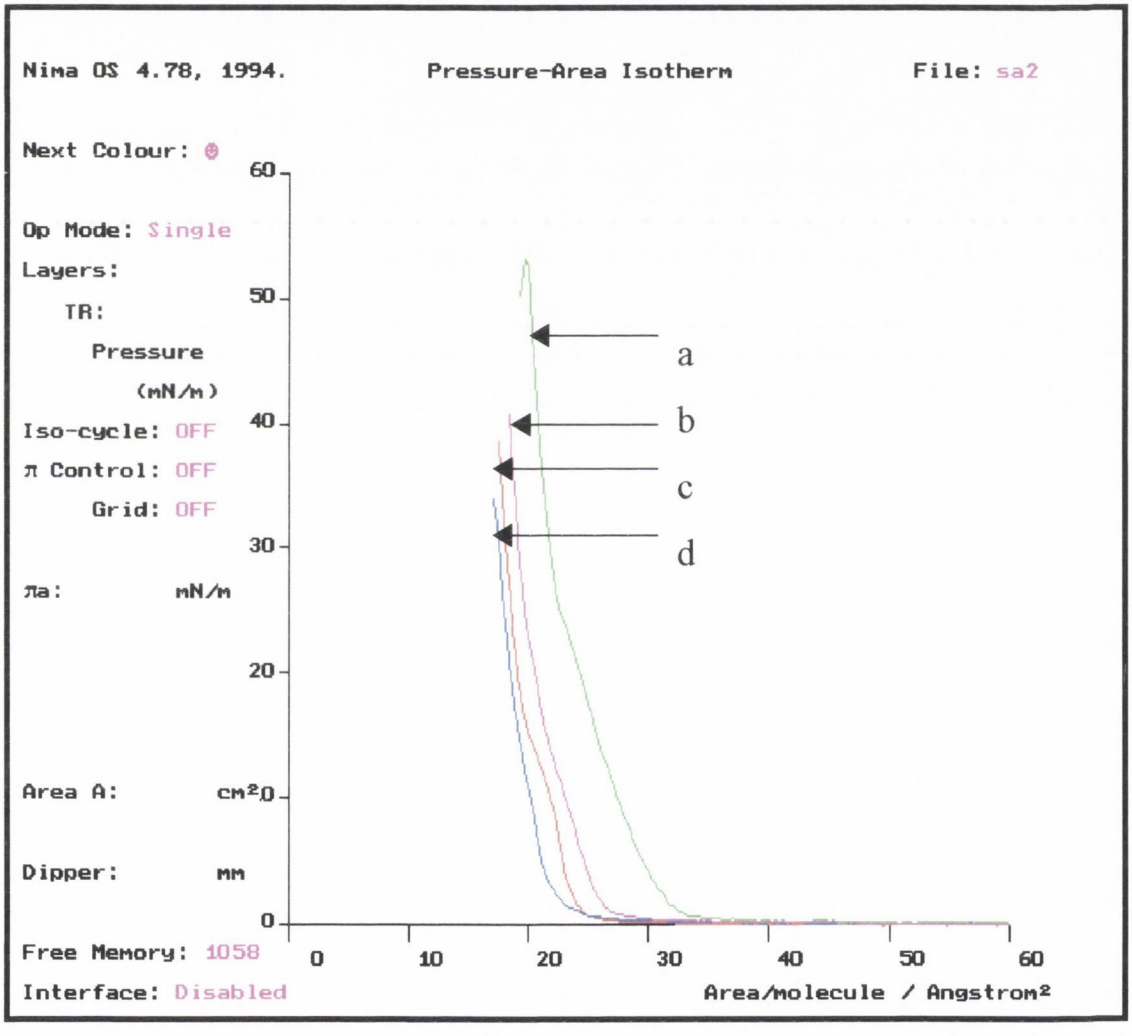

Figure 4.3: π-A isotherms for stearic acid on pure water (a) and on $CdCl_2$ 10^{-5} M (b), 10^{-4} M (c) and 10^{-3}M (d).

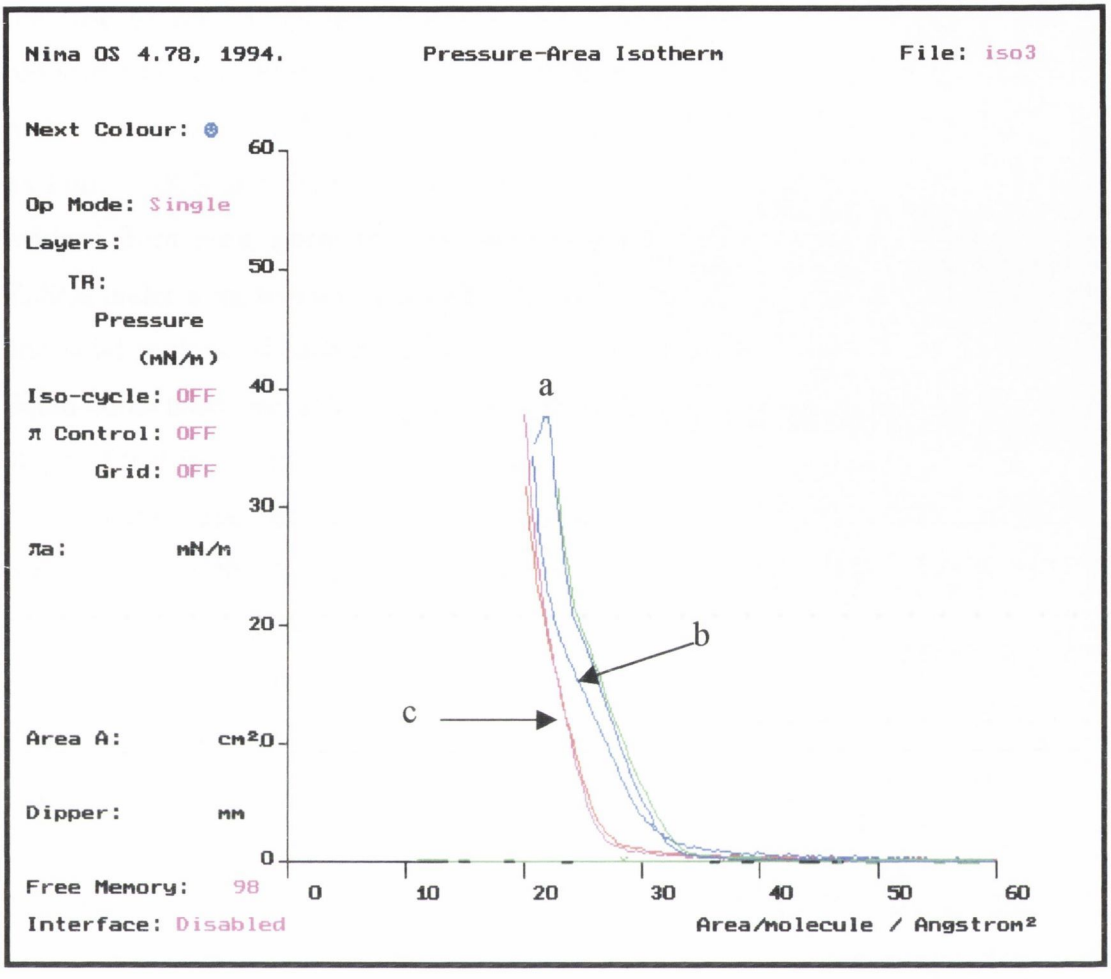

Figure 4.4: π-A isotherm for stearic acid (a) on pure water (2 compressions) (b) $ZnSO_4$ 10^{-5} M and (c) $ZnSO_4$ 10^{-3}M (2 compressions).

Comparing the stearic acid isotherms while increasing both $CdCl_2$ and $ZnSO_4$ metal ion concentrations confirms the well-known phenomenon that both cations exert a considerable increased condensing effect on stearic acid, yielding solid type monolayers at lower surface pressures. Metal ion incorporation in an aqueous subphase beneath a stearic acid monolayer appears to effect the gas and liquid-expanded region of the isotherm. Increasing the metal ion concentration causes a decrease in the molecular area. The number of observed phase transitions is reduced and the solid phase predominates at a metal ion concentration of 10^{-3} mol dm^{-3}. Collapse pressure remains constant at 40 mN/m in the case of Cd^{2+} and 30mN/m in

the case of Zn^{2+} subphase solutions. The area per molecule in the solid phase is reduced from an initial molecular area of 25 $Å^2$ for stearic acid on water, to a final molecular area of 21 $Å^2$ and 22 $Å^2$, for stearic acid on an aqueous subphase of 10^{-3} mol dm^{-3} $CdCl_2$ and $ZnSO_4$ respectively. By examination of figures 4.3 and 4.4, it is evident from each isotherm, that increasing the concentration of either $CdCl_2$ or $ZnSO_4$ under a monolayer of stearic acid, promotes the onset of the liquid condensed and solid regions of each monolayer at low surface pressures. The extension of the liquid-condensed and solid region of each isotherm is illustrated by a change in the slope of that isotherm as the concentrations of metal ions are increased. The change of isotherm slope for each monolayer was observed by extrapolating the surface pressure at π = 20 mN/m. These results are summarised in Table 4.1 p85.

Comparable isotherms were also obtained for metal ions under a monolayer of palmitic acid. This particular carboxylic acid shows complete disappearance of gas, liquid expanded and liquid condensed phases if a subphase concentration of $\geq 10^{-3}$ mol dm^{-3} is used, with inclusion of either Zn^{2+} or Cd^2 metal ions in the subphase. Figures 4.5 and 4.6 show this decrease in molecular area with increasing metal ion concentration.

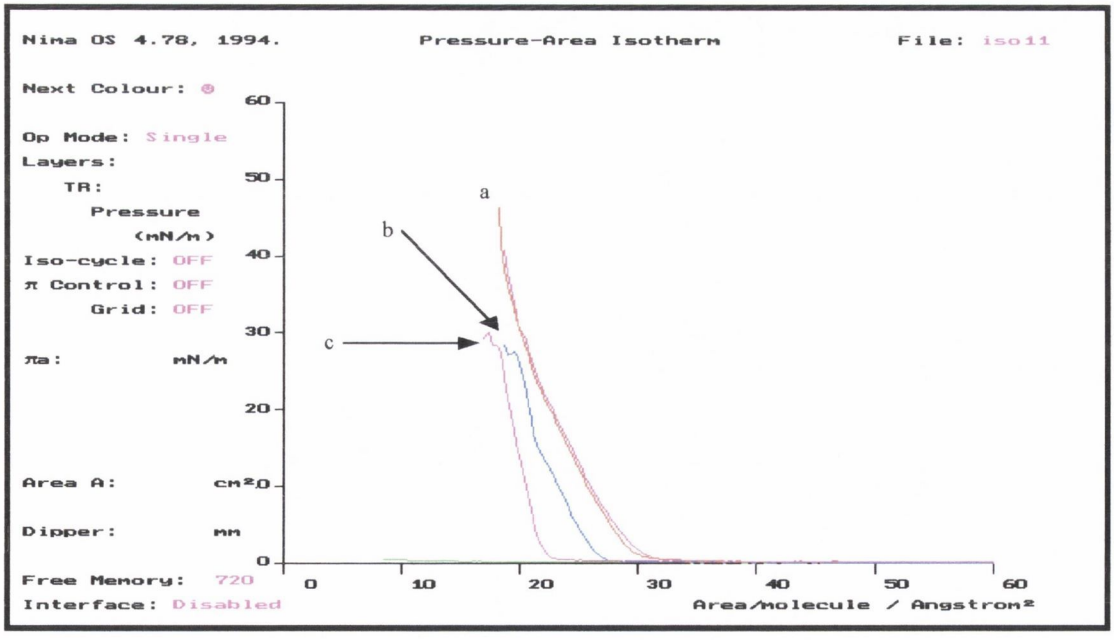

Figure 4.5: π-A isotherm for palmitic acid on pure water (a), $ZnSO_4$ 10^{-4} M (b) and $ZnSO_4$ 10^{-3}M (c)

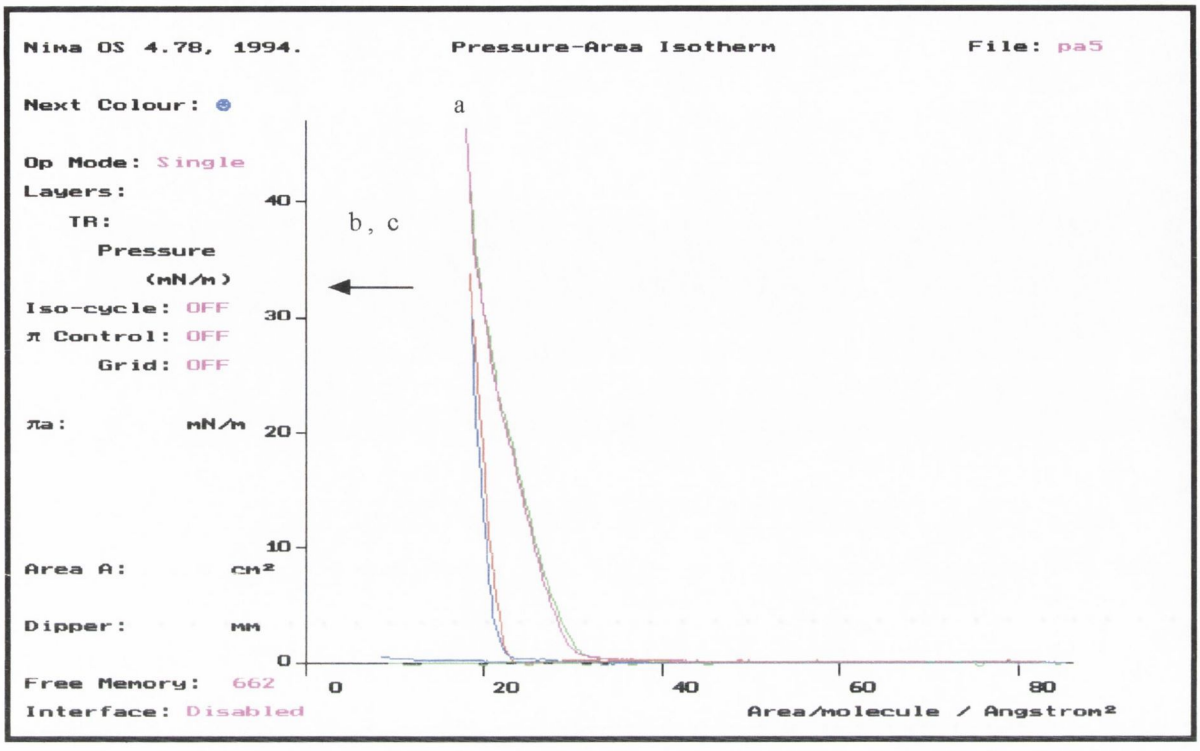

Figure 4.6: π-A isotherm for palmitic acid on pure water after 2 compressions (a), $CdCl_2$ 10^{-4} M (b) and $CdCl_2$ 10^{-3}M (c).

A maximum collapse pressure of 30 mN/m was recorded for palmitic acid formed on a 10^{-3}-10^{-4} mol dm^{-3} $ZnSO_4$ and $CdCl_2$ subphase. The molecular area for palmitic acid is initially 25 $Å^2$ and changes to a final area of 21 $Å^2$ for a palmitic acid monolayer formed on a 10^{-3} mol dm^{-3} $CdCl_2$ and $ZnSO_4$ subphase. Results are summarised in Table 4.1.

The incorporation of Cd^{2+} and Zn^{2+} metal ions under a monolayer of oleic acid was also investigated. Oleic acid as already described, forms an expanded (gas like) monolayer throughout compression. The surface pressure-area isotherm of oleic acid was examined on pure water and on similar concentrations of $ZnSO_4$ and $CdCl_2$ to those used previously. Figures 4.7 and 4.8 illustrate the effect on the oleic acid monolayer of introducing different concentrations of metal ions into the subphase.

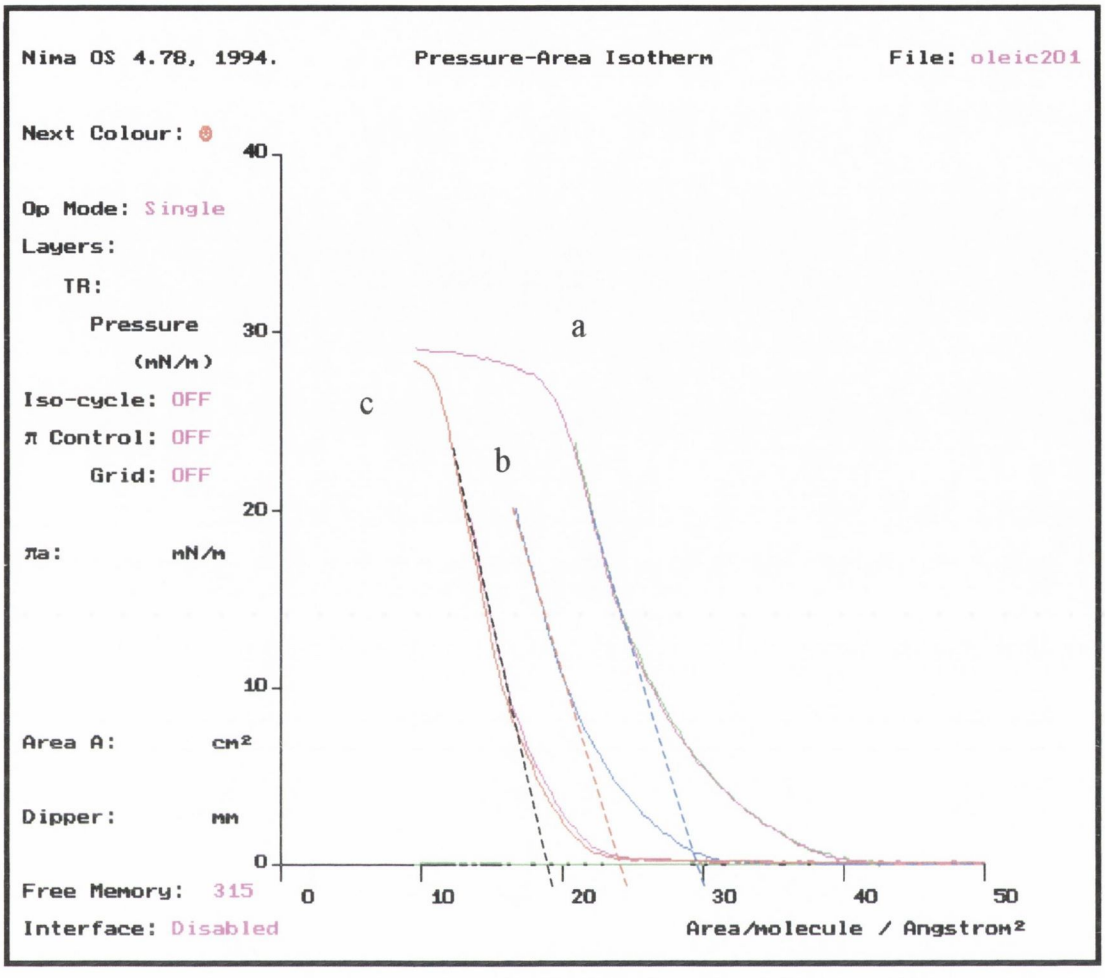

Figure 4.7: π-A isotherms for oleic acid on pure water (a), on $CdCl_2$ 10^{-5} M (b) and $CdCl_2$ 10^{-4} M (c).

A large decrease in molecular area was observed for a monolayer of oleic acid compressed on a subphase containing either 10^{-5} or 10^{-4} mol dm^{-3} $CdCl_2$. The oleic acid monolayer shows a decrease in molecular area from an initial value of 30 $Å^2$/molecule on pure water to 25±1 $Å^2$/molecule and 19±1 $Å^2$/molecule on $CdCl_2$ 10^{-5} and 10^{-4} mol dm^{-3} respectively. The slope of each isotherm shown in figure 4.7 extrapolated from π = 20 mN/m remains relatively constant. This would suggest that the presence of Cd^{2+} metal ions at different concentrations have no condensing characteristic towards oleic acid monolayer films. Figure 4.8 shows the effect of an increase in Zn^{2+} concentration from 10^{-5} mol dm^{-3} to 10^{-4} mol dm^{-3} on a monolayer of oleic acid.

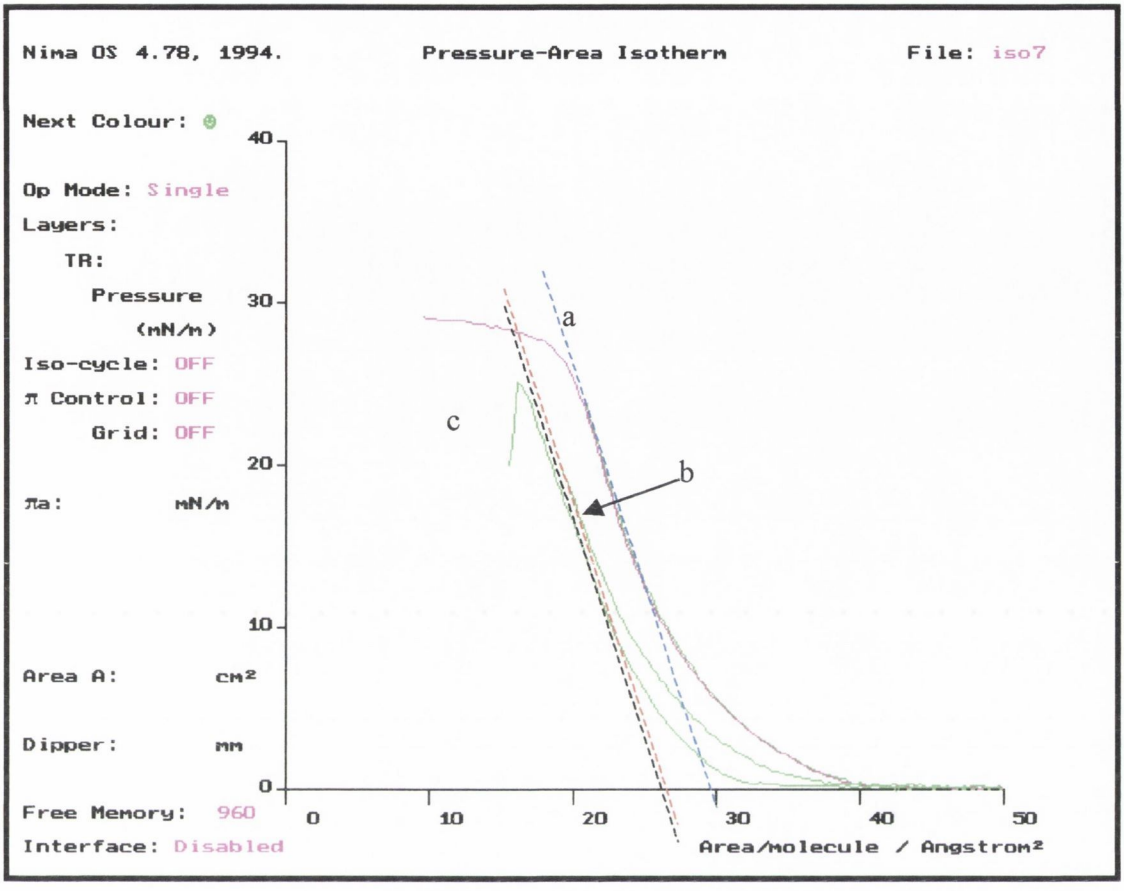

Figure 4.8: π-A isotherms for oleic acid on pure water (a), on $ZnSO_4$ 10^{-5} M (b), on $ZnSO_4$ 10^{-4} M (c).

A decrease in oleic acid molecular area was found to occur with increasing $ZnSO_4$ concentration from an initial value of 30 ±1 $Å^2$/molecule for pure water to 27 ±1 $Å^2$/molecule and 26 ±1 $Å^2$/molecule for an oleic acid monolayer on 10^{-5} and 10^{-4} $ZnSO_4$ subphase respectively. Once more, there was no observed change in isotherm slope for an increase in $ZnSO_4$ concentration. Again this highlights the inability of Zn^{2+} ions for condensing oleic acid monolayers.

Monolayer	[Metal ion] (mol dm^{-3})	Collapse pressure (mN/m)	Molecular area ($Å^2$)
Stearic acid	water	55	25
	$CdCl_2$ 10^{-3}	34	21
	$CdCl_2$ 10^{-4}	38	22
	$CdCl_2$ 10^{-5}	40	24
	$ZnSO_4$ 10^{-3}	32	22
	$ZnSO_4$ 10^{-5}	38	23
Palmitic acid	water	50	26
	$CdCl_2$ 10^{-3}	34	21
	$CdCl_2$ 10^{-4}	34	21
	$ZnSO_4$ 10^{-3}	28	21
	$ZnSO_4$ 10^{-4}	28	24
Oleic acid	water	28	30
	$CdCl_2$ 10^{-4}	28	19
	$CdCl_2$ 10^{-5}	28	25
	$ZnSO_4$ 10^{-5}	25	26
	$ZnSO_4$ 10^{-4}	25	25

Table 4.1: Conditioning of carboxylic acid monolayers on aqueous metal ion subphases.

4.1.3 Influence of trivalent cation concentration on LB phase behaviour.

In this study, the isotherm behaviour of both stearic and oleic acid is reported using trivalent Ti^{3+} metal ions in the aqueous subphase of the LB trough. Monolayers of these molecules were formed using Ti^{3+} ions in the concentration range 10^{-6}-10^{-3} mol dm^{-3}. Figure 4.9 shows the corresponding isotherms for a stearic acid monolayer at different $TiCl_3$ concentrations. These isotherms show a reduction in the liquid expanded region and thus resemble those formed on similar concentrated subphases of $CdCl_2$ and $ZnSO_4$.

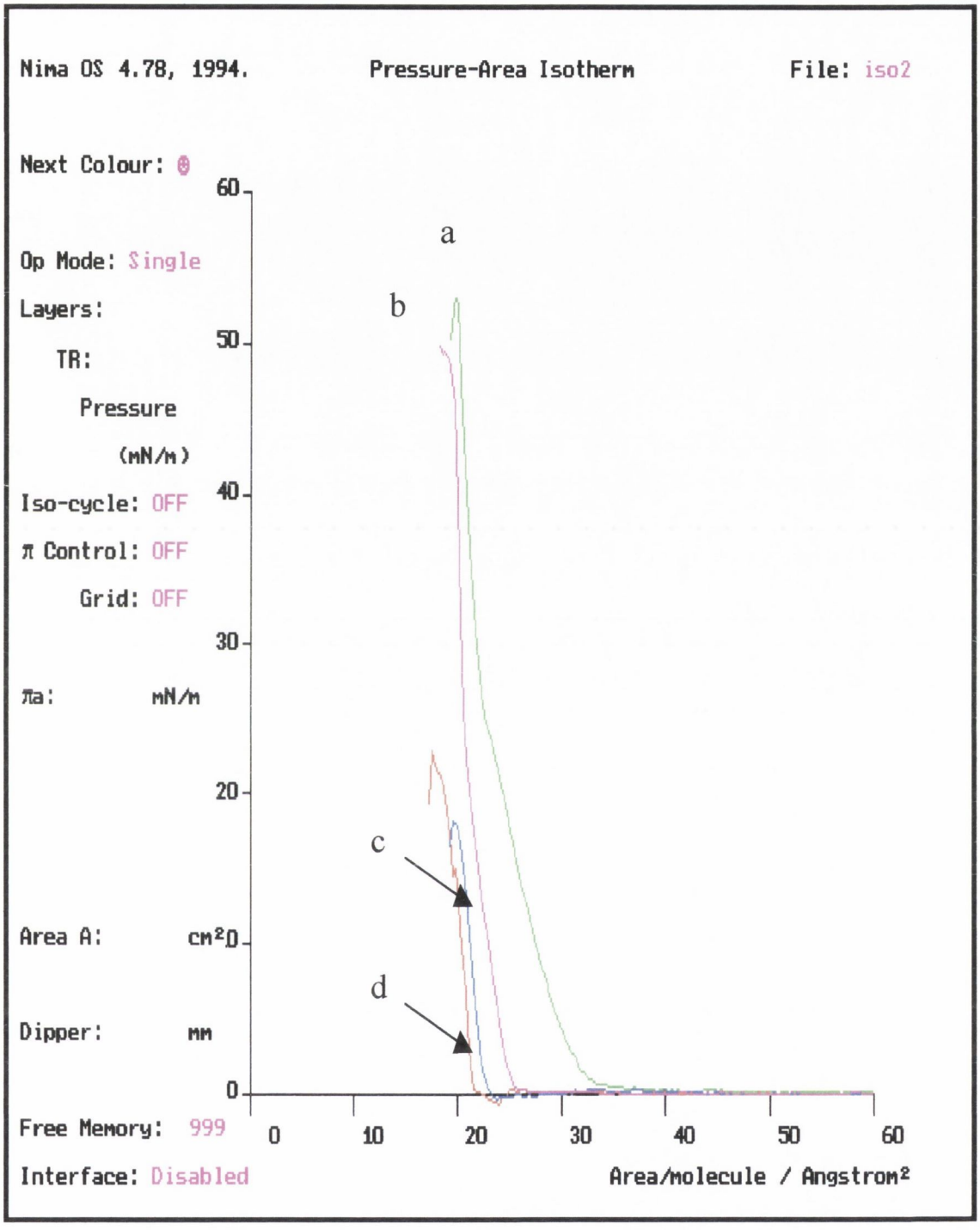

Figure 4.9: π-A isotherms for stearic acid on pure water (a) and on subphase solutions of $TiCl_3$ 10^{-5} M (b), $TiCl_3$ 10^{-4} M (c) and $TiCl_3$ 10^{-3}M (d).

The area extrapolated to $\pi=0$ is 22 $Å^2$/molecule for stearic acid on $TiCl_3$ 10^{-5} mol dm^{-3} compared to 24 $Å^2$ per molecule for the same monolayer spread on 10^{-5}M $CdCl_2$.

When the subphase concentration of Ti^{3+} ions is increased above 10^{-5} mol dm^{-3} the resulting isotherms are unstable (shown by a low collapse pressure of 20 mN/m) at the air water interface and appear to buckle and collapse in the subphase at the liquid condensed phase. Thus it appears that $TiCl_3$ at a subphase concentration of 10^{-5} mol dm^{-3} is sufficient for producing stable monolayer films showing collapse pressures of 50 mN/m and extended liquid-condensed and solid phases which are a fundamental requirement for successful monolayer deposition.

Similar studies were also performed using oleic acid monolayers spread on different subphase concentration of $TiCl_3$. Figure 4.10 shows the isotherms for oleic acid on different subphase concentrations of Ti^{3+} metal ions.

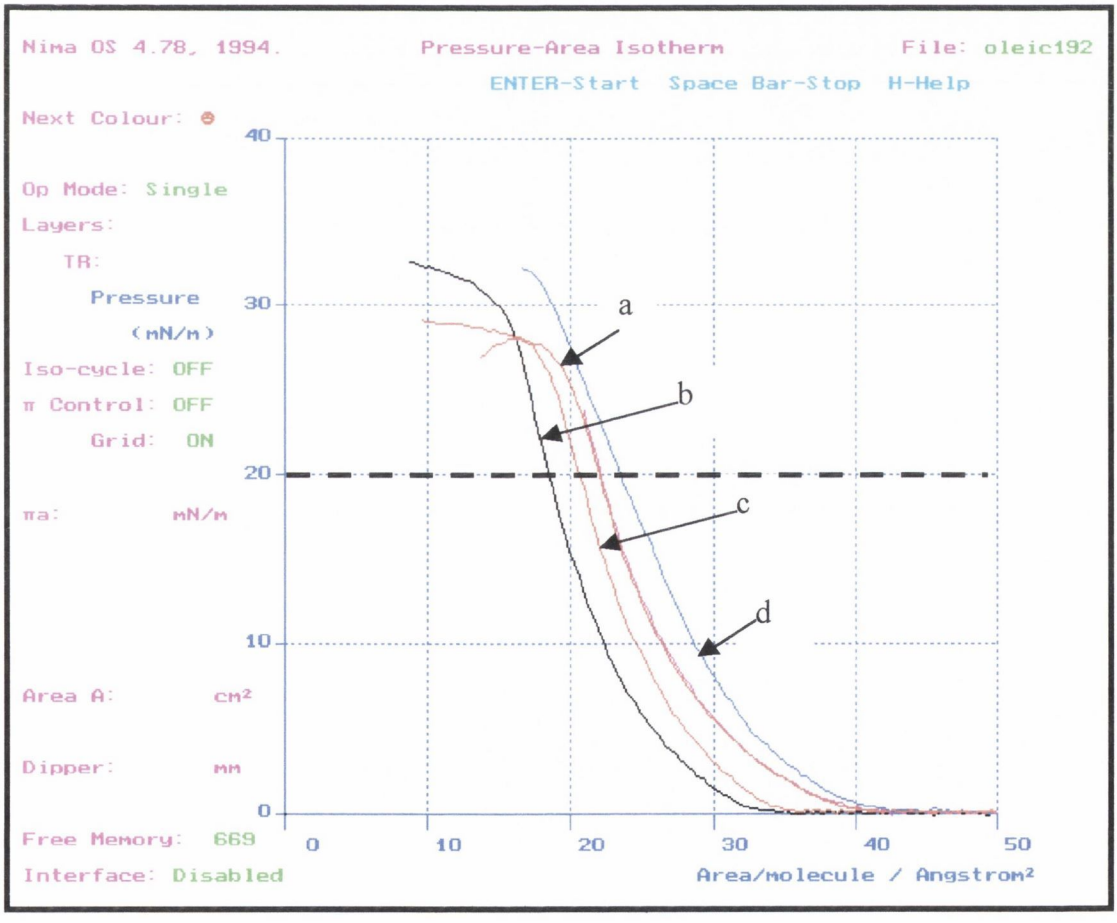

Figure 4.10: π-A isotherms for oleic acid on pure water (a), on $TiCl_3$ 10^{-6} M (b), $TiCl_3$ 10^{-5} M (c) and $TiCl_3$ 10^{-4}M (d).

An increase of oleic acid molecular area was observed on increasing the Ti^{3+} ion concentration from 10^{-6} mol dm^{-3} to 10^{-4} mol dm^{-3}. At a subphase pH of 4 ($TiCl_3$ 10^{-4} mol dm^{-3}) the mean molecular area where the initial rise in surface pressure occurs is 41Å^2. Increasing the pH (decreasing the $TiCl_3$ concentration) the molecular area where the initial rise in surface pressure occurs is continuously suppressed, having values of 35± 1Å^2 and 33± 1Å^2 for a 10^{-5} and 10^{-6} and $TiCl_3$ subphase (pH 5 and 6 respectively).

4.1.4 Cadmium stearate LB film transfer.

LB films of cadmium stearate (Cd-St) were deposited on glass and quartz slides using a 10^{-5}M $CdCl_2$ aqueous subphase as previously described (section 3.1.2). The decrease in area of the water surface occupied by the monolayer divided by that of the substrate covered with the monolayer for each stroke is called the transfer ratio. This serves as an indicator of whether the deposition is proceeding normally. Examining the transfer ratio bar chart for this material, compares the deposition of a multilayer Cd-stearate film. Figure 4.11 shows the transfer ratio bar chart for the deposition of 25 layers of Cd-stearate at 10 mN/m. The deposition ratios for the raising and lowering of the substrate should be 100% respectively. However rearrangements of the molecules, monolayer dissolution or incomplete transfer may occur during transfer giving rise to higher or lower ratios. Figure 4.12 shows the pressure-area vs. time axis for 25 layers of Cd-St transferred on glass treated with ferric stearate (Fe-St) at a monolayer surface pressure of 10 mN/m. At a constant surface pressure of 10 mN/m, the transfer ratio is $\cong$ 1.0 for the first five layers, indicating successful deposition. However the ratio begins to decrease rapidly on the up stroke, this is illustrated in figure 4.11 up to the first 25 layers of Cd-St.

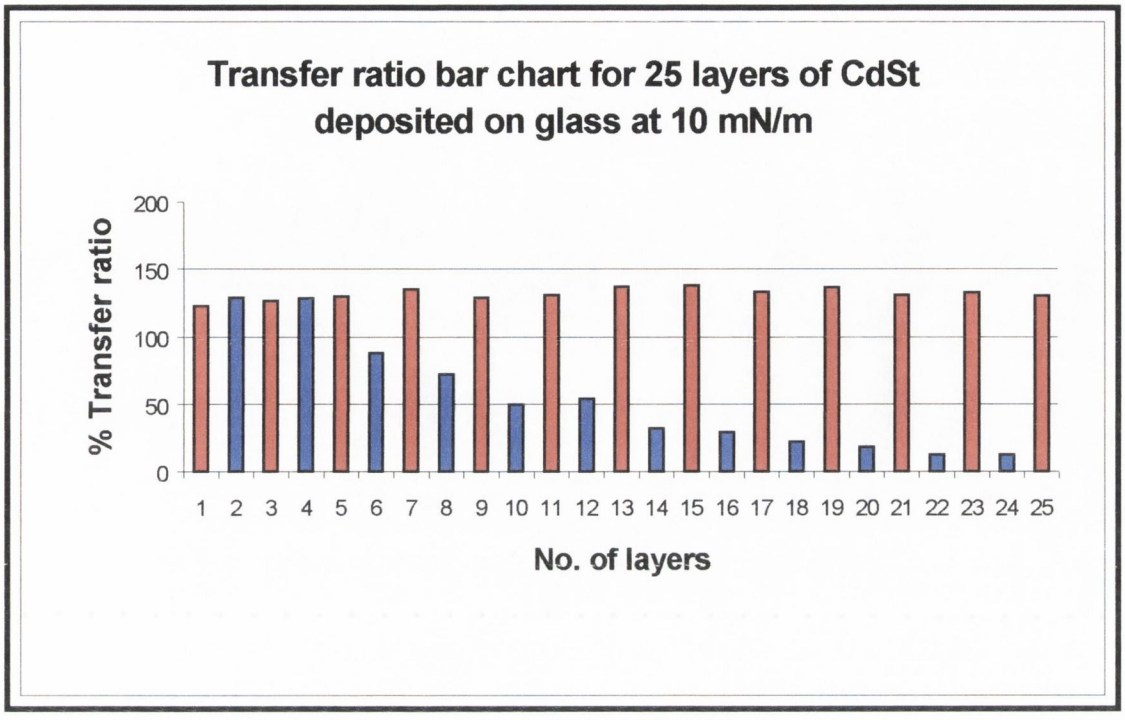

Figure 4.11: Transfer ratio bar chart showing deposition of Cd-St at a surface pressure at 10 mN/m (red = downstroke, blue = upstroke).

Above a surface pressure of 10 mN/m the liquid condensed phase is reached and monolayer transfer is more uniform up to a maximum of 25 mN/m with higher transfer ratios reached for both dipping directions. Figures 4.13-4.15 confirm these higher transfer ratios, while Table 4.2 shows the mean transfer ratios for the deposition of up to 25 layers of Cd-St at surface pressures of 15, 20 and 25 mN/m respectively.

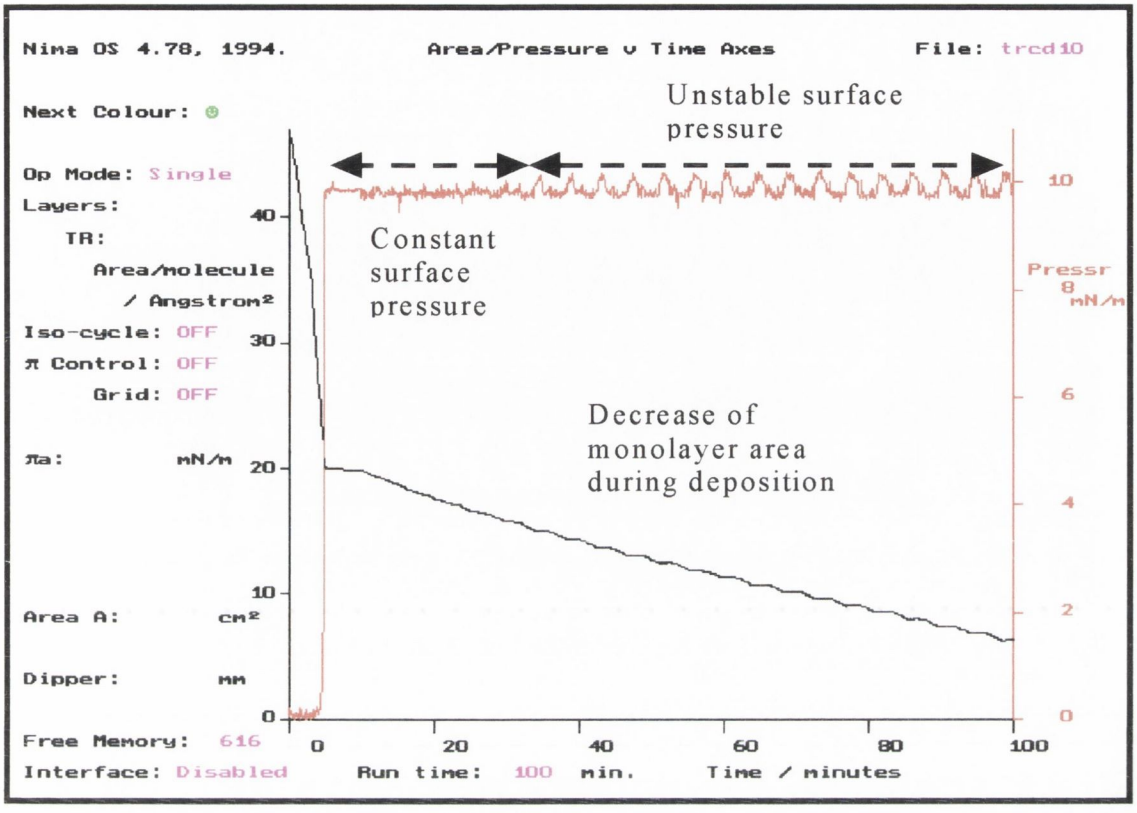

Figure 4.12: Area-Pressure vs time axis for the deposition of Cd-St at a surface pressure of 10mN/m.

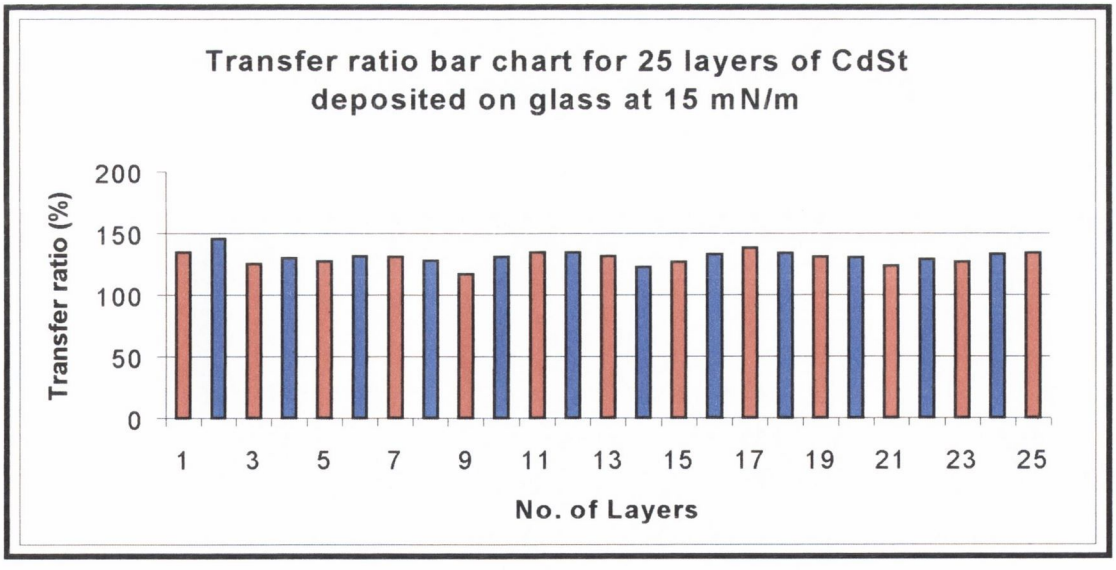

Figure 4.13: Transfer ratio bar chart showing transfer of Cd-St monolayers at a surface pressure of 15mN/m.

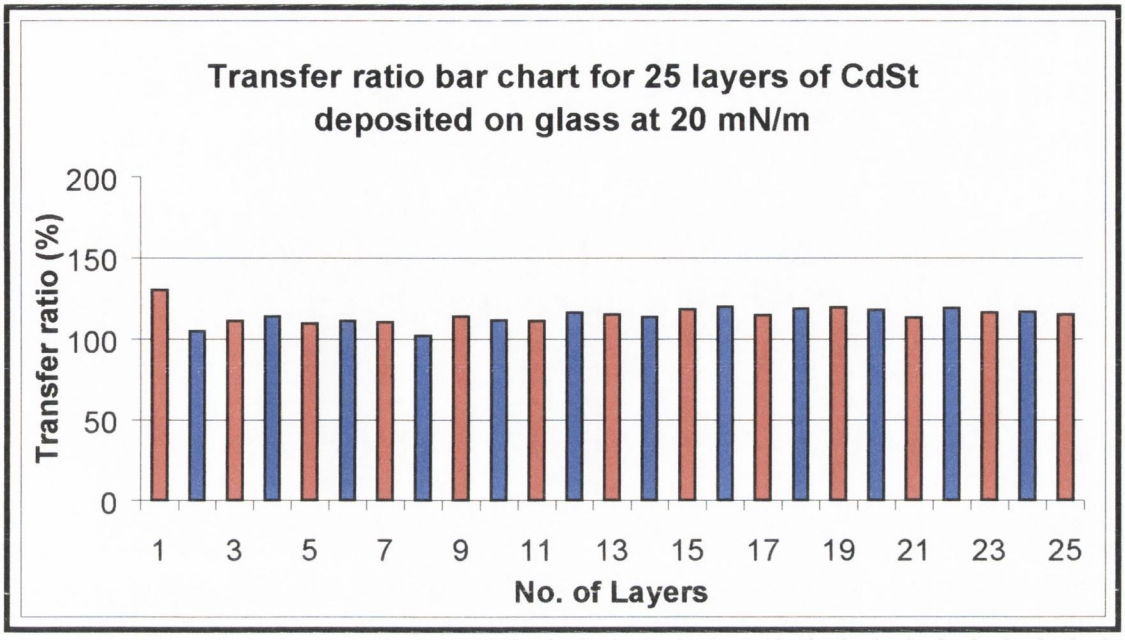

Figure 4.14: Transfer ratio bar chart showing transfer of Cd-stearate monolayers at a surface pressure of 20 mN/m.

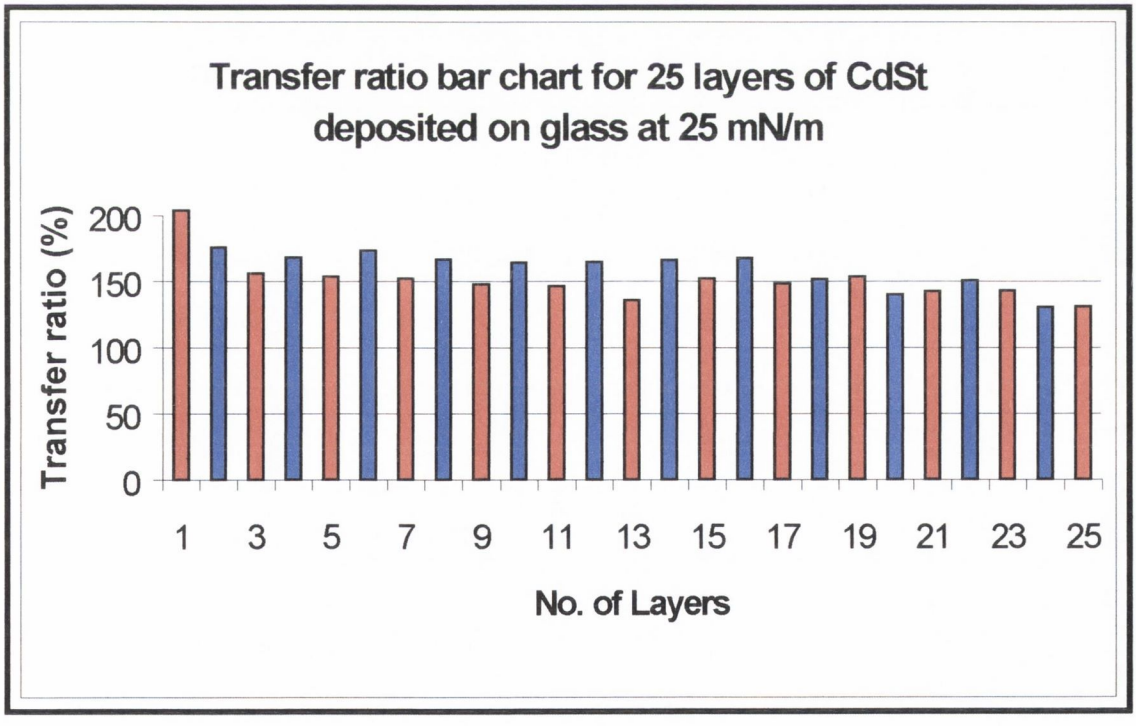

Figure 4.15: Transfer ratio bar chart showing transfer of Cd-St at a surface pressure of 25mN/m

Surface pressure (mN/m)	Avg. transfer ratio (% T.R. D_d/D_u)
10	0.2
15	1.0
20	1.0
25	1.0

Table 4.2 Average transfer ratio for the deposition of 25 layers of Cd-St at different surface pressures (D_d and D_u – dipper down-stroke and dipper upstroke respectively).

4.1.5 Titanium stearate LB film transfer.

Similar investigations relating transfer ratio to surface pressure were recorded during multilayer deposition of titanium stearate (Ti-St). Deposition of Ti-St multilayer films was achieved using a stearic acid monolayer film spread on a 10^{-5} mol dm^{-3} $TiCl_3$ subphase. Three different target pressures: 10, 12.5 and 15 mN/m were employed for multilayer deposition. Experiments were carried out to deposit Ti-St films at target pressures above 20 mN/m, however poor monolayer deposition was achieved because the films became too rigid and peeled off the substrate.

Figures 4.16-4.18 illustrate the transfer ratios for 25 layers of titanium stearate deposited at 10, 12.5 and 15mN/m. Table 4.3 shows the corresponding average transfer ratios at these surface pressures. A higher transfer ratio was achieved at lower target pressure (10 mN/m) using trivalent ions, contrasting with a low transfer ratio at a similar pressure with a divalent ion in the subphase. The higher transfer ratio demonstrates the increased capability of Ti^{3+} ions to organise monolayer films, even at low target pressures, so that effective monolayer deposition can occur.

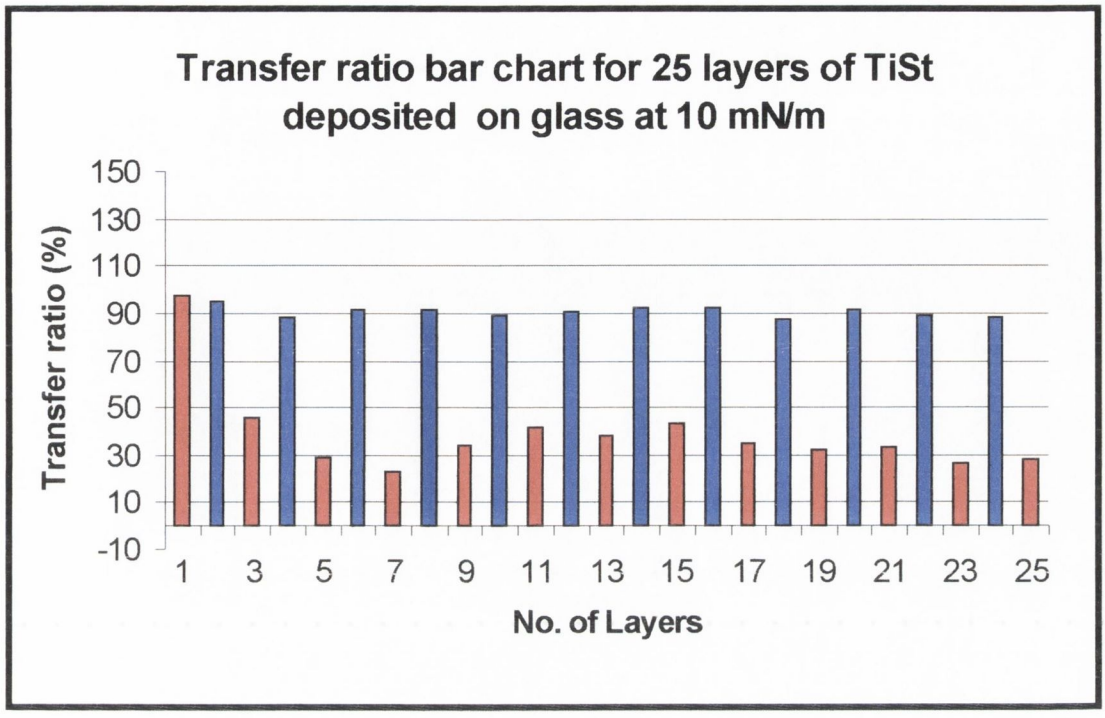

Figure 4.16: Transfer ratio bar chart showing transfer of Ti-St monolayers at a surface pressure of 10mN/m.

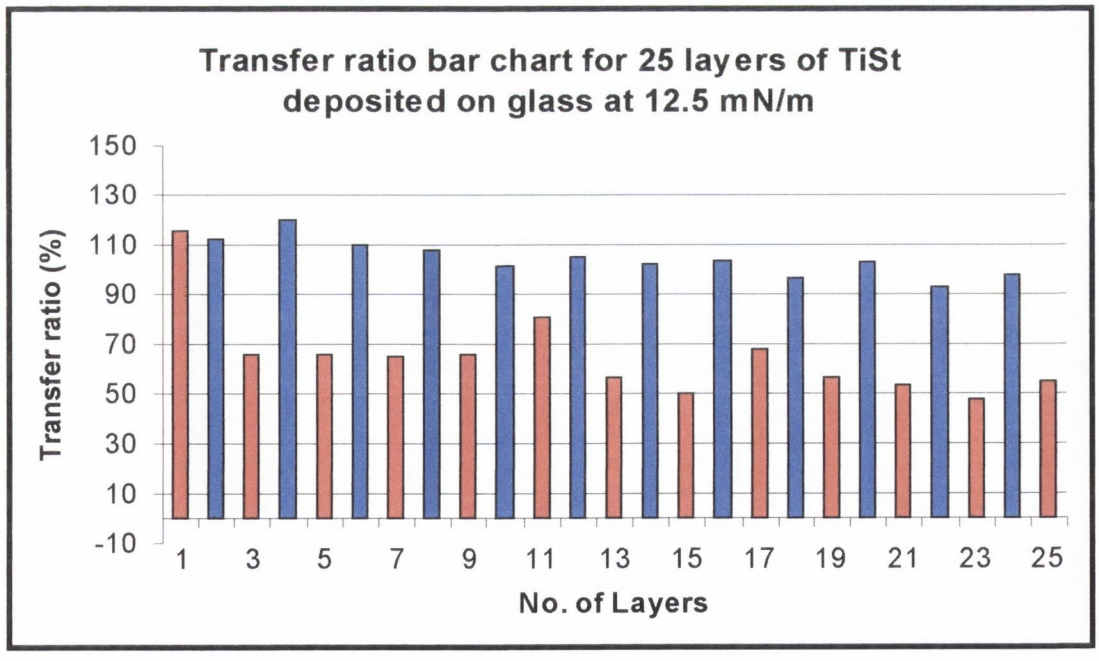

Figure 4.17: Transfer ratio bar chart showing transfer for Ti-St monolayers at 12.5mN/m.

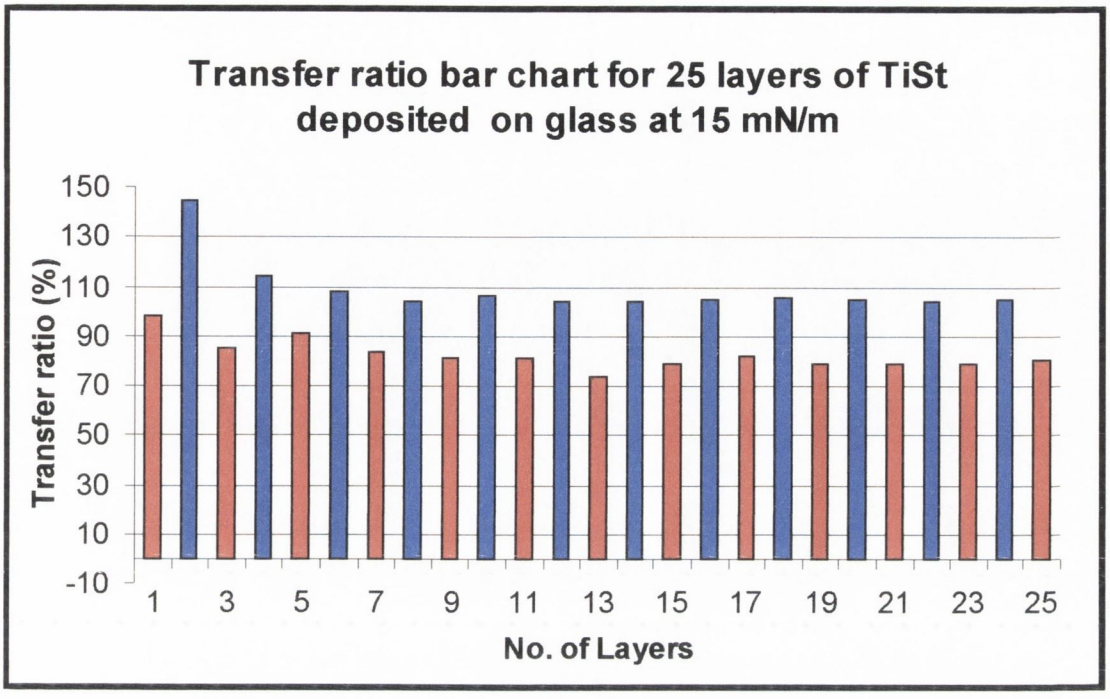

Figure 4.18: Transfer ratio bar chart showing transfer for Ti-St monolayers at a surface pressure of 15 mN/m.

Target Pressure (mN/m)	Avg. transfer Ratio (%T.R. D_d/D_u)
10	0.6
12.5	0.6
15	0.8
20	film peels off

Table 4.3: Average transfer ratio for the deposition of 25 layers of Ti-St at different surface pressures (D_d and D_u – dipper down-stroke and dipper upstroke respectively).

4.1.6 A model system for building LB films

This study has so far focused on investigating and optimising the conditions necessary for a suitable model system, which is capable of producing LB films containing divalent and trivalent metal ions. Table 4.4 below summarises the different conditions such as metal ion concentration, pH, temperature and nature of substrate used to

construct such films. LB films of Cd-St and Ti-St having different thickness were deposited using the conditions outlined above.

Type of metal ion	[metal ion] in subphase (mol dm^{-3})	Surface pressure during film transfer (mN/m)	pH of subphase	Temp. (K)	substrate
Ti (III)	1×10^{-5}	15	3.2	293	Quartz/glass coated with ferric stearate
Cd (II)	1×10^{-5}	15-20	5.0	293	Quartz/glass coated with ferric stearate.

Table 4.4: Optimum conditions for the formation of high quality Ti-St and Cd-St films.

4.1.7 TiO_2 LB films.

After depositing LB films of Ti-St it was possible to form TiO_2 by firing the LB films for 2hr at 450°C. This ensures complete decomposition of the stearate matrix and oxidation of Ti^{3+} to TiO_2. The amount of TiO_2 formed after firing the LB film was calculated as shown in table 4.5, assuming that each Ti^{3+} co-ordinates with 3 carboxylic acid molecules and 100% transfer ratio occurred. For 98 layers (Y-type) of titanium stearate a sample calculation is included below.

Substrate area covered by the titanium stearate film = 25 mm x 30 mm $\equiv 7.5 \times 10^{16}$ $Å^2$. The area occupied by a single molecule in the solid phase (π=0) = 22 $Å^2$/ molecule. A single layer of the carboxylic acid will contain: 3.4×10^{15} molecules
Since the ratio of carboxylic acid: $Ti^{3+} \equiv 3:1$.

$\Rightarrow$ No. of Ti^{3+} ions present = $3.4 \times 10^{15}/3$

$= 1.13 \times 10^{15}$ ions $\equiv 1.87 \times 10^{-9}$ moles $\equiv 1.5 \times 10^{-4}$ mg TiO_2 (mw 79.9 g/mol).

Film no.	**Film type**	**No. of layers**	**Method of forming TiO_2**	**Amount of TiO_2 present in the film (mg)**
1	Titanium stearate	250	Film heated for 3hr.at 50°C in oxygen	3.8×10^{-2}
2	Titanium stearate	30	Film fired at 450°C for 2hr.	4.5×10^{-3}
3	Titanium stearate	98	Film fired at 450°C for 2hr.	1.5×10^{-2}
4	Cadmium stearate	130		2.8×10^{-2} (Cd^{2+} ions)

Table 4.5: Methods of forming Ti-St, Cd-St and TiO_2 thin films.

4.1.8 Surfactant stabilised TiO_2

The second approach investigated for the formation of stable TiO_2 particles involved the use of colloidal dispersions of TiO_2. The TiO_2 sols were prepared in a chloroform-propanol mixture by the arrested hydrolysis of titanium tetraisopropoxide (TTIP) as outlined previously (3.1.4).

The use of either cetyltrimethyl ammonium bromide (CTAB) or dioctadecyldimethyl ammonium bromide (DODAB) as stabilisers provides significant hydrophobicity to the TiO_2 particles, ensuring that the particles remain at the air-water interface of the LB trough. Figures 4.19 and 4.20 show the structures for both surfactant molecules.

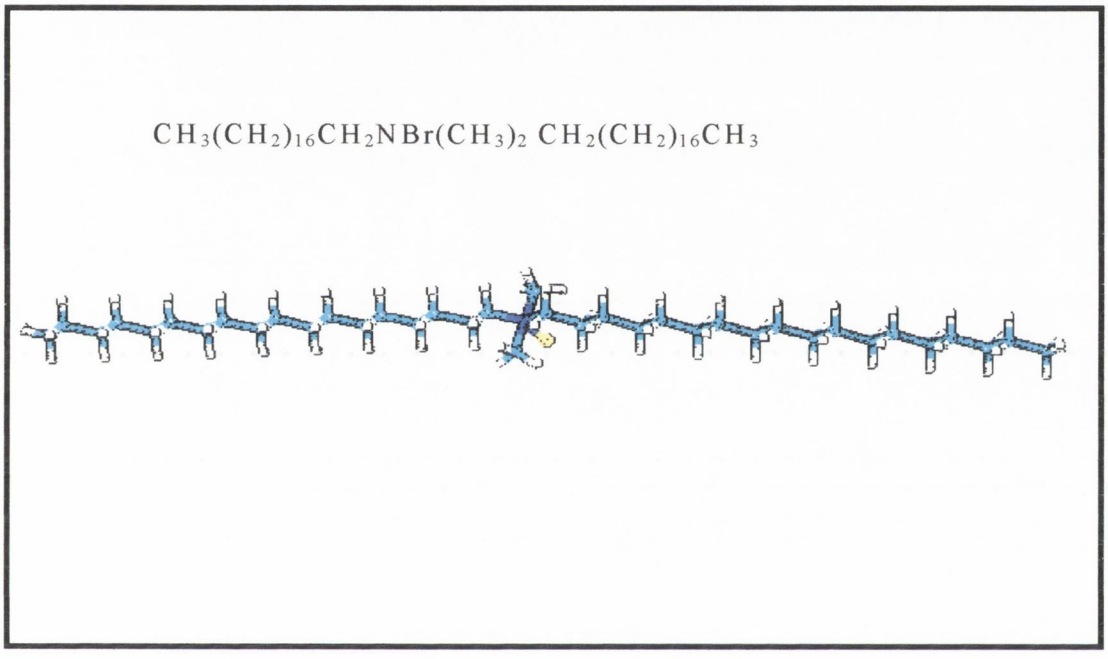

Figure 4.19: Structure and formula for cetyltrimethyl ammonium bromide (CTAB)

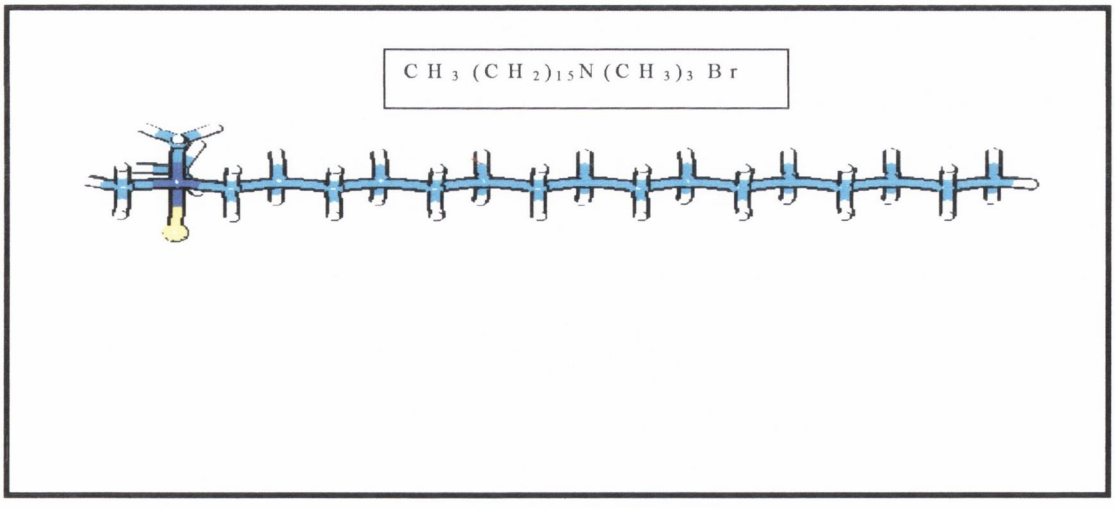

Figure 4.20: Structure and formula of dioctadecyldimethylammonium bromide (DODAB)

The concentration of TiO_2 nano-particles in the spreading solutions of both CTAB and DODAB were calculated on the basis of assumptions, as outlined by Fendler[2]:

I. Complete hydrolysis of titanium tetraisopropoxide (TTIP) to TiO_2 occurs.

II. The density of TiO_2 (anatase, formed at temperatures < 800°C) formed by hydrolysis is presumed similar to the bulk value of $3.8g/cm^3$.

III. TiO_2 particles are spherical in nature and thus have a volume of $4/3\pi r^3$.

The diameter of the TiO_2 nanoparticles within the sols were evaluated from the measured uv-vis absorption thresholds A_p by the semi-empirical relationship proposed by Fendler[2].

$$A_p = A_b + C_1/R^2 + C_2/R \qquad [4.1.1]$$

Where A_p is the measured absorption threshold (wavelength of maximum absorption), A_b is the absorption threshold of the bulk TiO_2 semiconductor and C_1 and C_2 are constants, determined as 82.8 $Å^2$ eV and 2.58 Å eV from data derived from high-resolution TEM images of TiO_2 particles and their corresponding threshold values[2].

4.1.9 Phase behaviour of surfactant LB films.

The surface-pressure vs area isotherms measured during conditioning (compression and subsequent relaxation) of a monolayer of CTAB stabilised TiO_2 sol is shown in figure 4.21. The surface pressure-area isotherms were obtained 45 mins after the introduction of the TiO_2 sol onto the water surface. This time limit allows for complete evaporation of the chloroform-hexane spreading solvent before compression. The isotherm represents initial compression of a CTAB stabilised TiO_2 monolayer to 5 mN/m with subsequent expansion and compression of the monolayer to higher π values. After each compression, the expansion isotherm rapidly collapsed

[2] K.C. Yi, J.H. Fendler, Synthetic Metals 1995, 71, 2109-2110.

to π=0 mN/m indicating the irreversible nature of the film. Subsequent compression of the monolayer to higher π values occurs at lower molecular areas. The surface-pressure vs area isotherm for CTAB stabilised TiO_2 was found to be both irreversible and unstable with respect to conditioning at the air-water interface. This result is illustrated in figure 4.21, where the highest surface pressure reached was only 25mN/m.

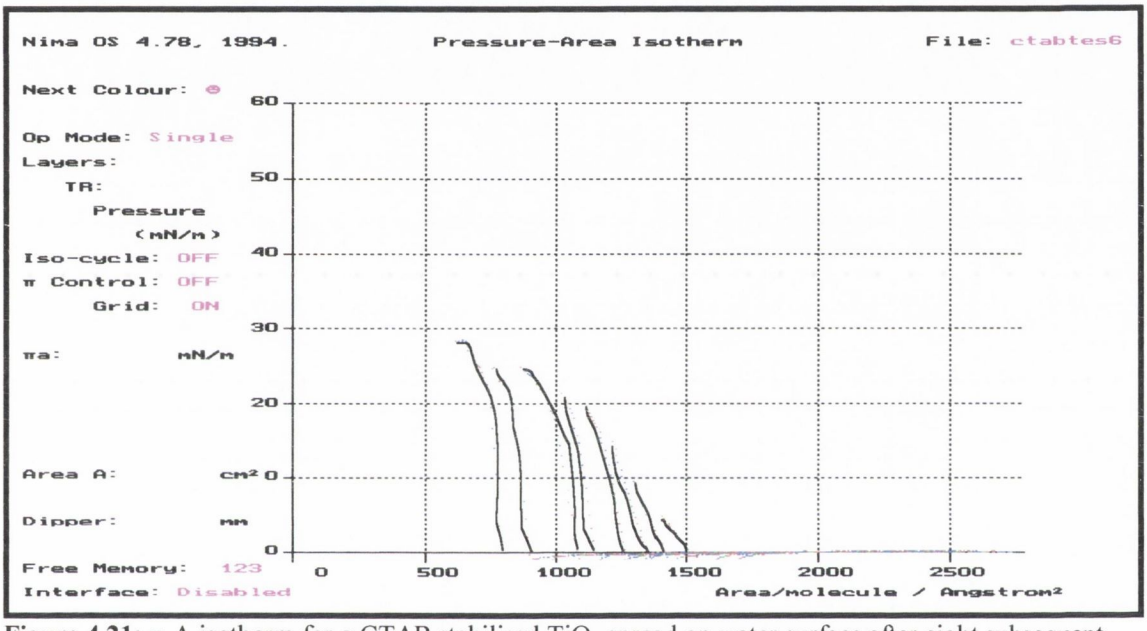

Figure 4.21: π-A isotherm for a CTAB stabilised TiO_2 spread on water surface after eight subsequent compression-expansion cycles to higher π values.

Similar investigations involving DODAB stabilised TiO_2 were carried out with the prospect of forming more stable monolayers at the air-water interface. Preliminary LB studies involving DODAB surfactant spread at the air-water interface were made in order to investigate the stability of the monolayer and determine its corresponding molecular area in the solid phase. Figure 4.22 shows a typical π-A isotherm for DODAB at the air-water interface after 3 successive compression-expansion cycles to π=20, 40 and 45mN/m. The isotherm shows minimal or no decrease in molecular area and is stable, showing an increase in surface pressure up to 45 mN/m. By extrapolation of the isotherm at π = 40 mN/m to π = 0 a molecular cross sectional area for a single DODAB molecule was estimated to be ca. 78± 2Å^2/molecule.

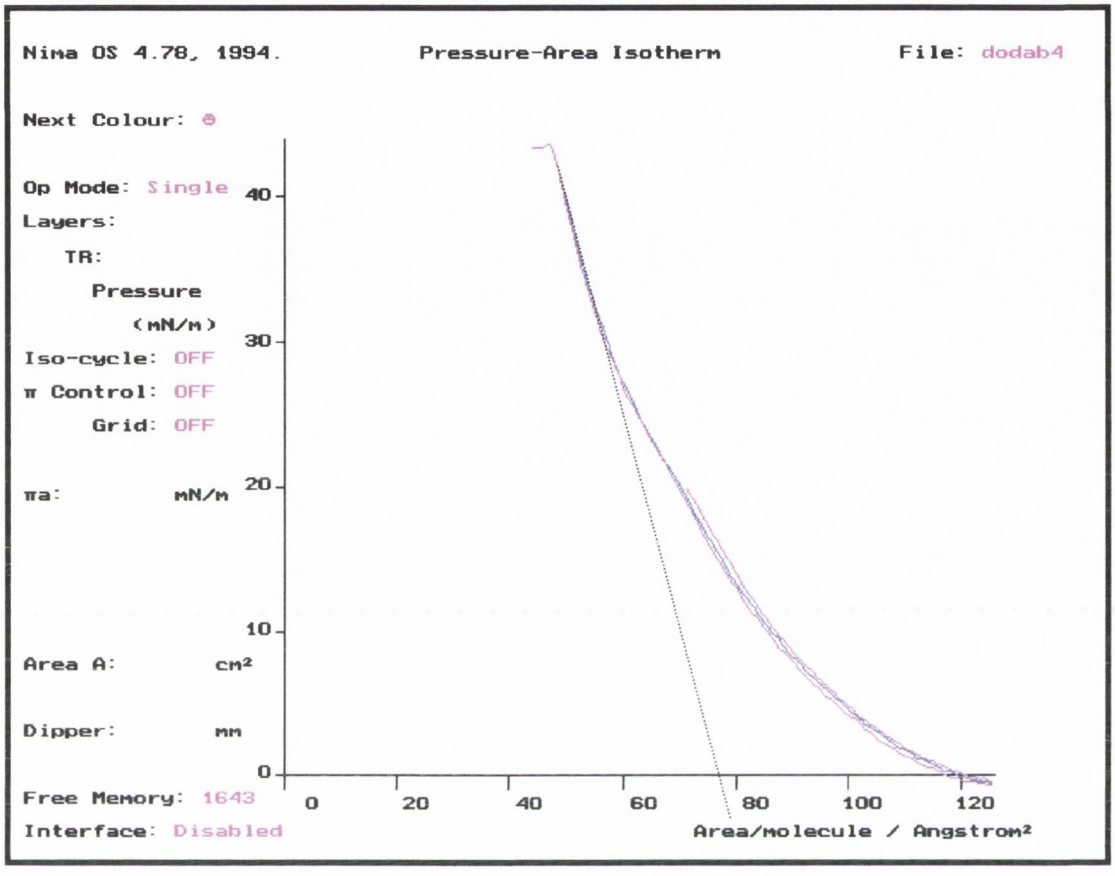

Figure 4.22: π-A isotherm for a DODAB monolayer on a pure water surface.

Similar investigations involving DODAB spread on a $(NaPO_3)_6$ aqueous subphase reveals a different shape isotherm, with a different molecular area compared to a DODAB monolayer spread on a water subphase. Figure 4.23 shows the pressure-area isotherm for DODAB spread on a $(NaPO_3)_6$ subphase (2×10^{-4}M). The monolayer was initially compressed to 30 mN/m and after expansion was further compressed to 55 mN/m at which point the collapse pressure of the molecule was reached. The DODAB monolayer exhibits a plateau in its isotherm between 15 and 20 mN/m. Finally a solid phase is observed at 18mN/m which extends right up to the collapse pressure for the monolayer at 50mN/m. A decrease in molecular area was also observed on compressing the monolayer, initially to 30 mN/m (68 $Å^2$/molecule) and then to 55mN/m (64 $Å^2$/molecule) (figure 4.23).

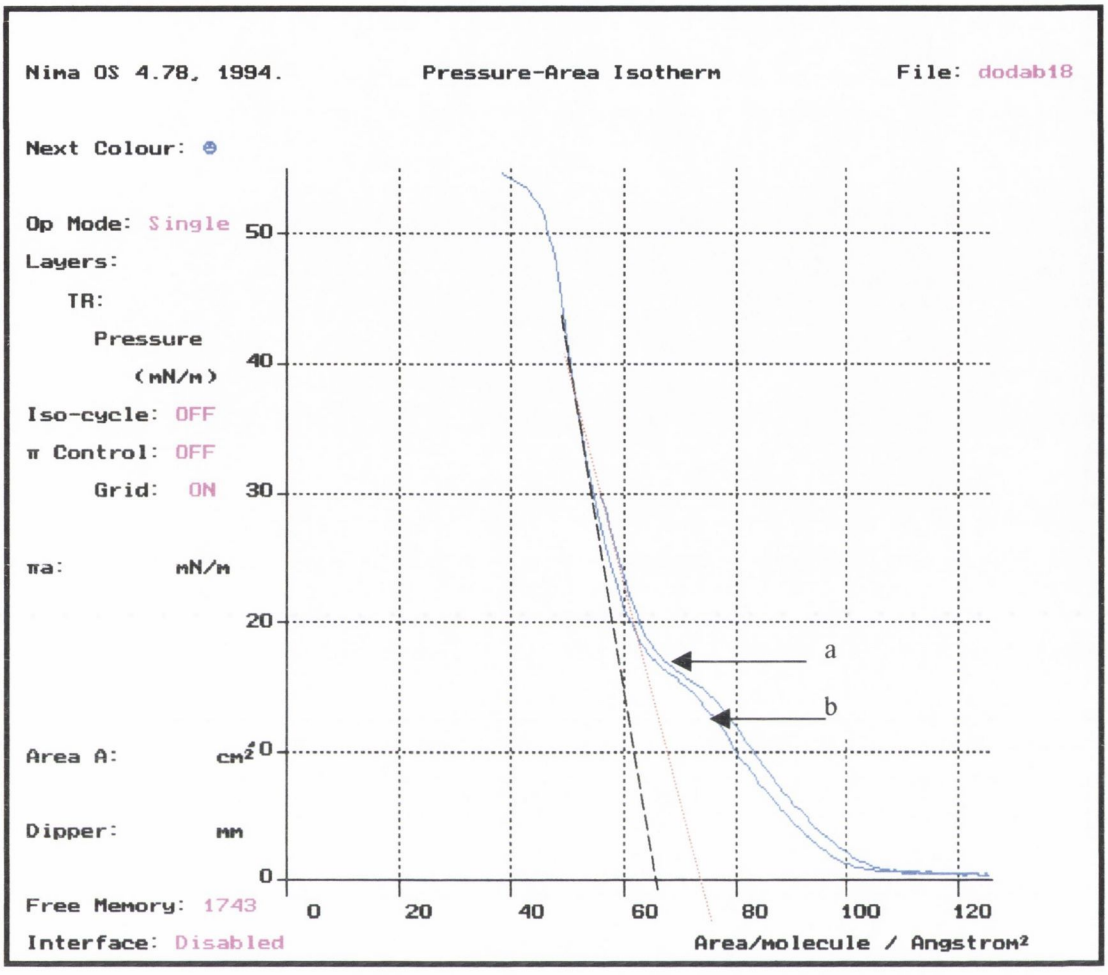

Figure 4.23: π-A isotherm for a DODAB monolayer spread on 2×10^{-4}M $(NaPO_3)_6$ surface (a) 1 compression-expansion cycle and (b) 2 compression-expansion cycles.

The extent of DODAB dissolution was also examined by initially compressing the monolayer to a surface pressure of 5mN/m, followed by subsequent expansion - compression cycles to higher π values (10, 15, 20, 25, 30, and 35mN/m). Figure 4.24 shows a total of eight compression-expansion cycles.

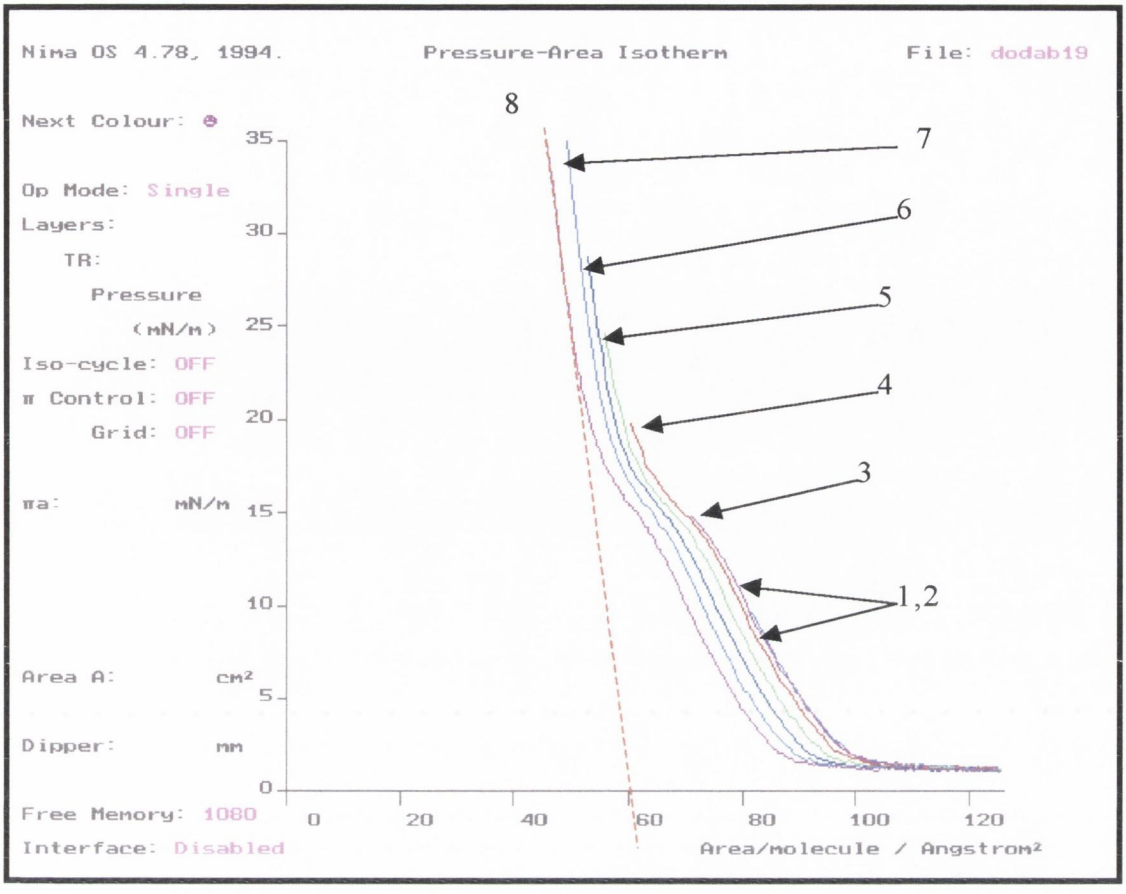

Figure 4.24: π-A isotherm for a DODAB monolayer spread on 2×10^{-4}M $(NaPO_3)_6$ subphase, showing compression and subsequent expansion cycles (1-8) to higher π values.

For monolayer compression up to 20 mN/m there is little or no decrease in DODAB molecular area. Above 20 mN/m DODAB dissolution occurs. Each compression-expansion cycle was found to be reversible contrary to that found with CTAB. The molecular area of the DODAB at 35mN/m was determined to be 61 $Å^2$/molecule as shown in figure 4.24.

The formation of DODAB stabilised TiO_2 monolayers at the air-water interface were investigated. 20 μL of DODAB stabilised TiO_2 (0.362 mg/ml) was applied to a water surface contained in an LB trough. After 45 mins solvent evaporation, the monolayer was compressed as shown in figure 4.25, initially to a surface pressure 5mN/m, followed by repeated expansion and subsequent compression of the monolayer to increasing surface pressures. Maximum surface pressures of 20 mN/m were recorded

and the corresponding pressure-area vs time axis, figure 4.26 shows a steady decrease of molecular area with an increase of surface pressure, indicating the formation of a stable DODAB monolayer. The cross sectional area of the DODAB stabilised TiO_2 was estimated to be 12,690 $Å^2$ by extrapolating the surface pressure at π = 20 mN/m to π = 0 mN/m.

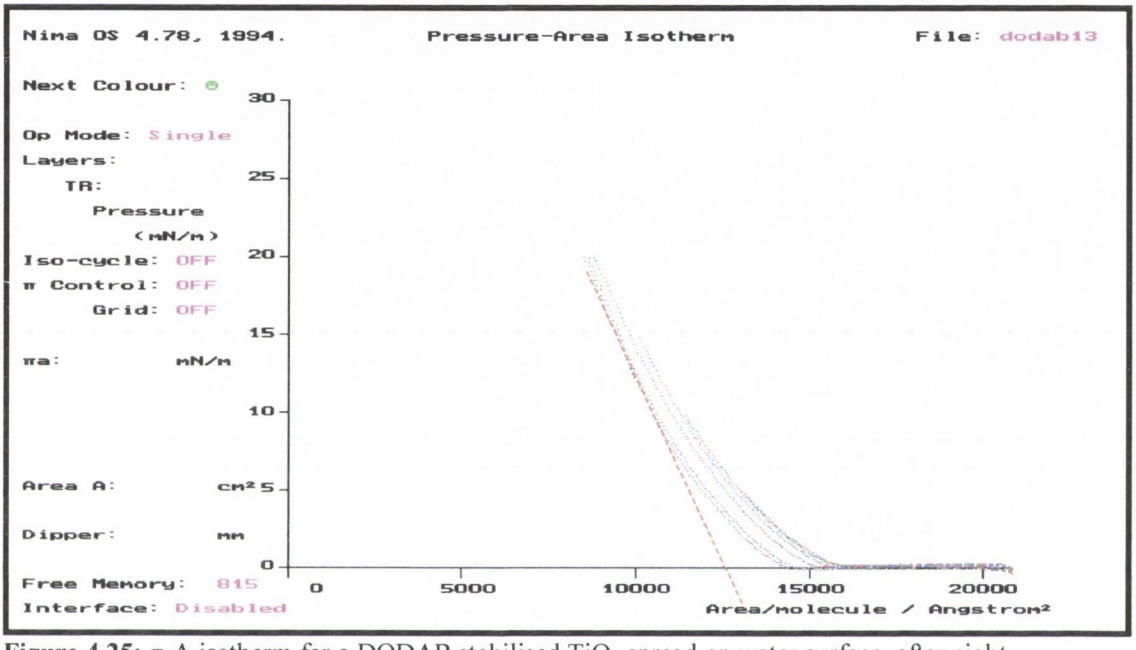

Figure 4.25: π-A isotherm for a DODAB stabilised TiO_2 spread on water surface, after eight compression-expansion cycles to higher π values.

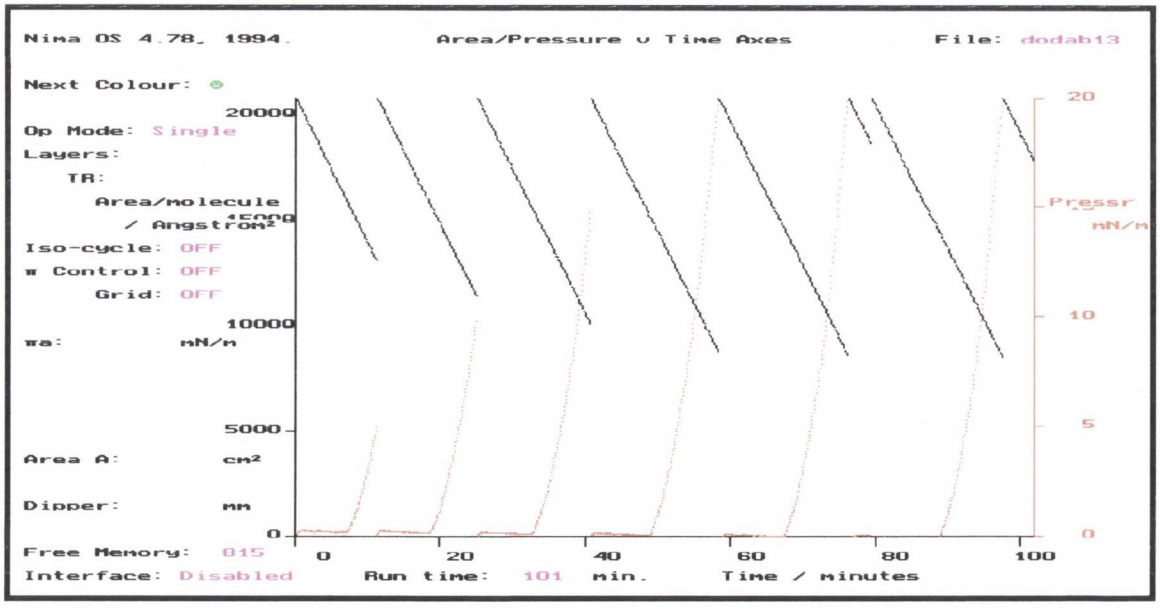

Figure 4.26: Pressure-area vs time axis for the compression and subsequent expansion of DODAB to higher π values.

4.2.1 Introduction

Absorption spectroscopy proved to be a very important technique during this work. It allowed examination of the stability of TiO_2 particles in Nafion, LB films and surfactant stabilised sols. This technique also provided information regarding the band gap and hence indirectly the particle size of the TiO_2.

4.2.2 Nafion bound TiO_2

The incorporation of Ti^{3+} metal cations in Nafion, from either $TiCl_3$ aqueous (route 1) or $TiCl_3$/MeOH (route 2) solutions was initially studied. The chemical behaviour of the Ti^{3+} cations at different KOH concentrations was monitored, and the formation of the corresponding metal oxide was examined using uv-vis spectroscopy.

By stirring a clean Nafion membrane in an aqueous solution of excess (0.1 mol dm^{-3}) $TiCl_3$ under N_2 conditions, incorporation of Ti^{3+} into the membrane was achieved after 3hrs. Immersing a membrane in acidic solution (pH <1) containing excess hydrogen peroxide yielded the orange peroxo $Ti^{(IV)}$ complex $[Ti(O_2)OH]^+$ (λ_{max} = 405 nm) [3] confirming the successful exchange of Ti^{3+} ions.

Exposure of a Ti^{3+}-Nafion exchanged membranes to 0.01M KOH under N_2 conditions results in the formation of the metal oxide as shown in figure 4.27. Time–dependent changes in the position of the absorption spectra for TiO_2 confined within each Nafion membrane was also observed. Complete oxidation of Ti^{3+} to TiO_2 occurs after a period of 60 mins. A pronounced increase of optical absorption occurs and is measured at 320 nm from an initial value of 0.38 after the first 5 min to a final value of 1.5 after 60 mins. This is evident from figure 4.27.

[3] R. Cotton, P. Premovic, L. Stavdal, P. West, Chem Comm. 1980, 863.

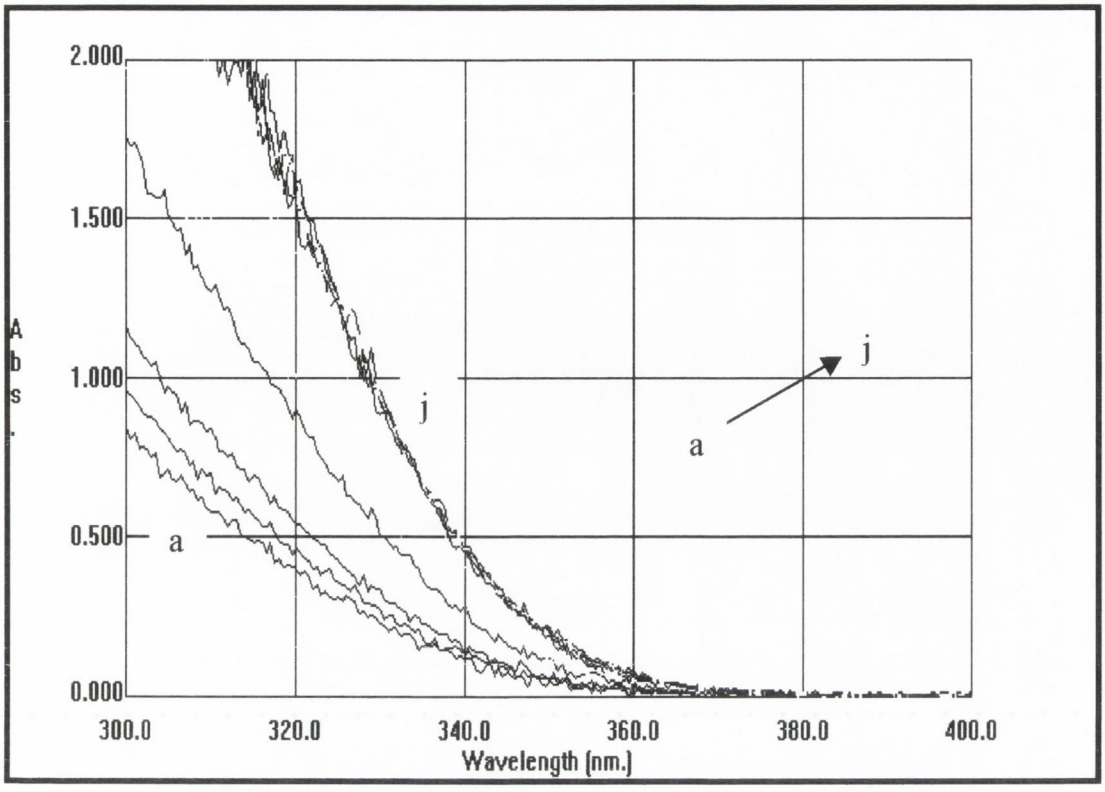

Figure 4.27: Absorbance spectra for TiO_2 precipitated in Nafion using 0.01 mol dm^{-3} KOH, over a time period of 1.5 hr (a) after 5 min, (b) 10 min (c) 15 min (d) 30 mins. (e-j) additional 10 min intervals (route 1).

Using the relationship[4]:

$$E_g = 1240/\lambda \qquad [4.2.1]$$

$$\Rightarrow \quad E_g = 1240/A_p$$

$$= \quad E_g\,(eV)$$

It is possible to estimate the band edge absorbance associated with TiO_2 particles by substituting the wavelength of maximum absorbance in eq. [4.2.1]. The onset of absorbance for each time period was calculated by drawing a tangent to the curve initially after 5 mins followed by tangents of similar slopes to subsequent curves throughout 1.5hrs. The initial and final onsets of absorption were estimated to be 327 nm and 355 nm, corresponding to band gap absorptions of 3.79 and 3.49 eV respectively.

[4] M. Gratzel. 'Heterogeneous photochemical electron transfer', 1989, CRC Press, Inc. New York.

Table 4.6 shows the wavelength of absorption A_p (nm.) and corresponding band gap energy B_g (eV) for TiO_2 precipitated in Nafion over a period of 1.5 hr using KOH 0.01 mol dm^{-3}.

Exposure to 0.01mol dm^{-3} KOH (mins)	**Abs. Onset (A_p) (nm ±1)**	**Band Gap (B_g) (eV± 0.02)**
5	327	3.79
10	330	3.75
15	336	3.69
30	345	3.60
40	347	3.57
50	352	3.52
60	355	3.49
70	355	3.49
80	355	3.49
90	355	3.49
Overnight	355	3.49

Table 4.6: Onset of UV-absorbance and corresponding band gap energy for TiO_2 particles incorporated in Nafion using KOH 0.01 mol dm^{-3}.

The effect of an increase in KOH concentration on the absorption onset of precipitated TiO_2 particles was also investigated. This particular study was carried out using Nafion membranes containing Ti^{3+} ions, which were previously incorporated into the membranes using either aqueous (route 1) or MeOH (route 2) solutions containing 0.1 mol dm^{-3} $TiCl_3$. Ti^{3+} containing membranes were subsequently exposed to KOH for a period of 24 hrs; these experimental conditions ensure complete hydrolysis of Ti^{3+} and the maximum amount of TiO_2 precipitation. Figure 4.28 shows the absorbance spectra at different KOH concentrations, corresponding to the formation of TiO_2.

particles in Nafion (route 1). Table 4.7 shows the wavelength of absorption and corresponding band gap energies for TiO_2 particles precipitated using between 0.01-5 mol dm^{-3} KOH.

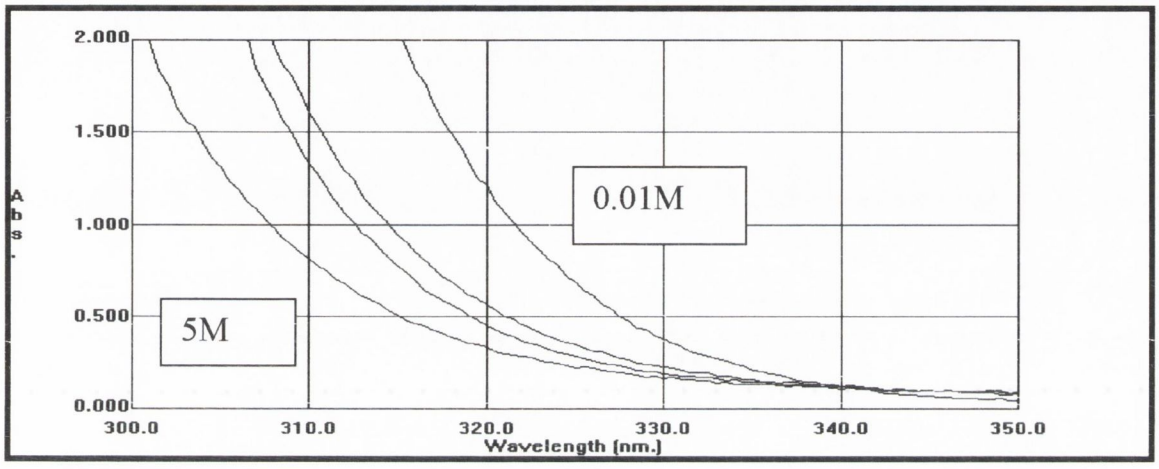

Figure 4.28: Absorbance spectra at different KOH concentrations, for the formation of TiO_2 particles in Nafion (route 1-aqueous).

[KOH] mol dm^{-3}	Abs. Onset (A_p) (nm ± 1)	Band gap (B_g) (eV ± 0.02)
0.01	331	3.75
0.1	329	3.77
0.25	322	3.85
0.5	320	3.88
5	314	3.95

Table 4.7: Absorption thresholds and corresponding band gap energies for TiO_2 particles precipitated in Nafion using between 0.01-5M KOH (route 1-aqueous).

Figure 4.29 shows the absorbance spectra at different KOH concentrations, corresponding to the formation of TiO_2 particles in Nafion (route 2- MeOH). Table 4.8 shows the corresponding increase in band gap absorption for TiO_2 particles precipitated using this technique.

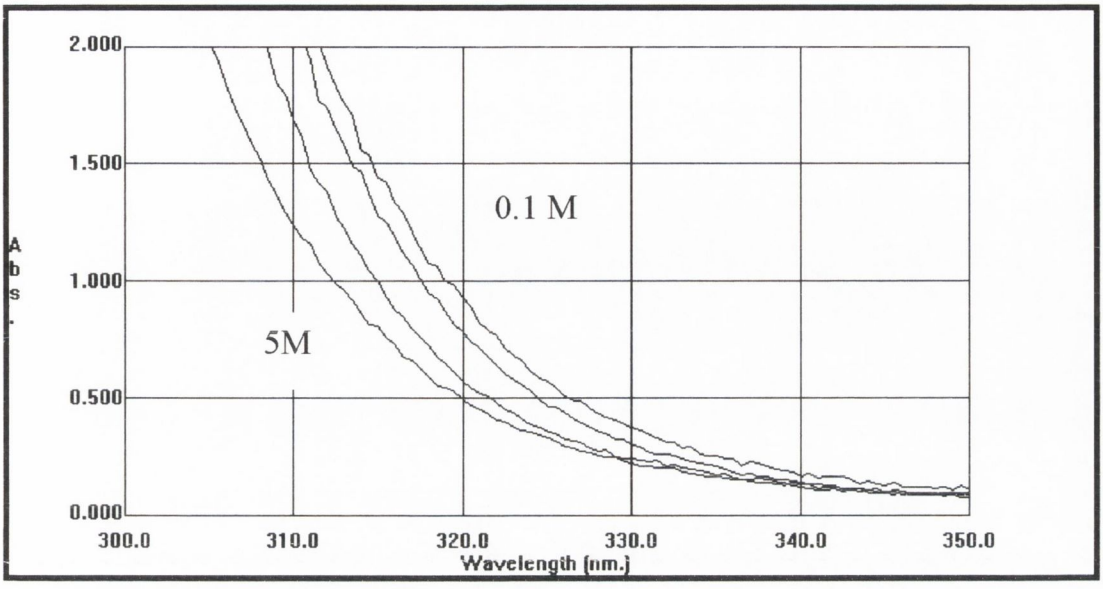

Figure 4.29: Absorbance spectra at different KOH concentrations, for the formation of TiO_2 particles in Nafion (route 2- MeOH).

[KOH] mol dm^{-3}	Abs. Onset (A_p) (nm ± 1)	Band gap (B_g) (eV ± 0.02)
0.1	329	3.77
0.25	326	3.80
0.5	325	3.82
5	320	3.88

Table 4.8: Absorption thresholds and corresponding band gap energies for TiO_2 particles precipitated in Nafion using between 0.1-5M KOH (route 2 MeOH).

Figures 4.28 and 4.29 illustrate that size quantisation of TiO_2 occurs irrespective of the particular solvent used during Ti^{3+} exchange. Both uv-vis spectra show an increase of wavelength associated with TiO_2 band edge absorption, for a corresponding decrease in KOH concentration from 5 mol dm^{-3} to 0.1 mol dm^{-3}. Tables 4.7 and 4.8 show the corresponding increase in band gap absorption for TiO_2 particles. The amount by which the band edge is blue shifted is significantly different for the two solvent systems. Using route 1, the overall increase in wavelength associated with TiO_2 particle absorption is 15 nm from an initial value of 314 nm using 5 mol dm^{-3} KOH to a final value of 329 nm, using 0.1 mol dm^{-3} KOH.

Using route 2 ($MeOH/Ti^{3+}$) the band edge absorption is increased to an initial value of 320 nm for TiO_2 precipitated using 5 mol dm^{-3} KOH to 329 nm for TiO_2 particle absorption after precipitation using KOH 0.1 mol dm^{-3}, a difference of only 9nm. In both cases, the largest decrease in wavelength associated with TiO_2 particle absorption is observed after TiO_2 precipitation using 5 mol dm^{-3} KOH.

4.2.3 TiO_2 LB films

The incorporation of TiO_2 particles between the head-groups of stearic acid and from fired LB film precursors of similar material was examined. The size dependent properties of TiO_2 within the above matrices are discussed in terms of the intensity and position of the corresponding uv-vis absorption spectra, in a similar manner to that previously described for Nafion incorporated TiO_2.

The transfer properties associated with titanium stearate LB films were first investigated up to a maximum transfer of 20 layers. Figure 4.30 represents the absorbance of 10, 14, 16 and 20 layers of Ti-St after subsequent firing of each film.

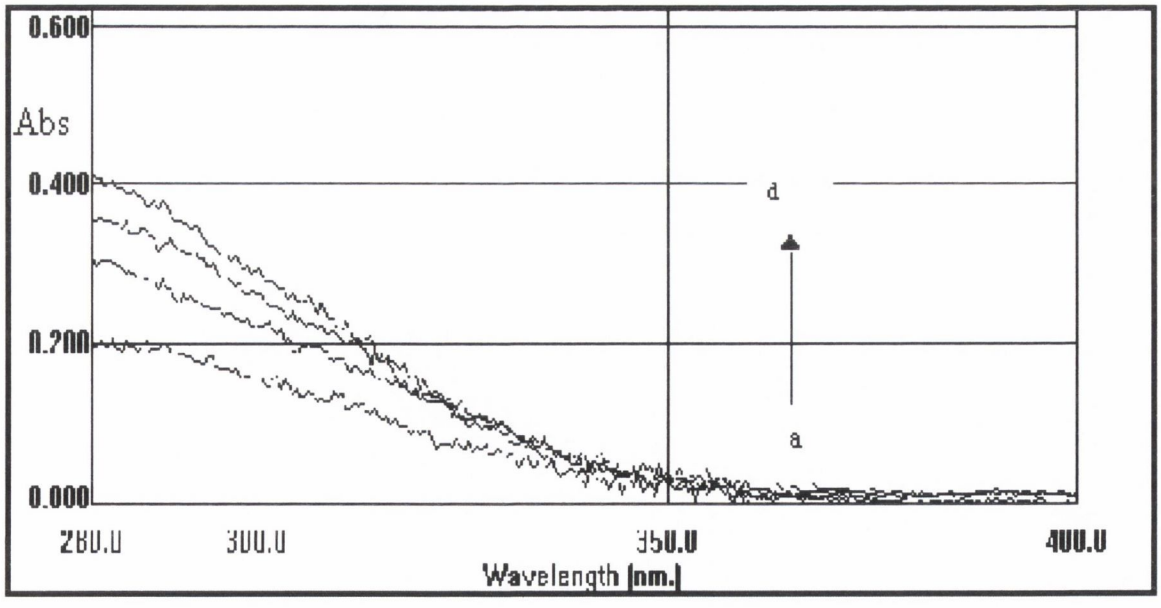

Figure 4.30: Absorbance spectra for different amounts of fired Ti-St monolayers (a) 10 layers (b) 14, (c) 16 and (d) 20.

The absorbance increases and is dependent on the number of layers of Ti-stearate originally deposited. Figure 4.31 shows an almost linear plot of film absorption versus number of fired Ti-St layers, suggesting uniform titanium stearate film transfer with minimum effects associated with interdigitation. There is very little change in the absorption onset with increase in the number of Ti-stearate layers; thus the particle size is independent of the number of layers up to 20 layers of Ti-stearate. One might have expected a red shift in the absorption edge with larger particles being formed due to particle aggregation during firing of the Ti-stearate film, however this is clearly not observed.

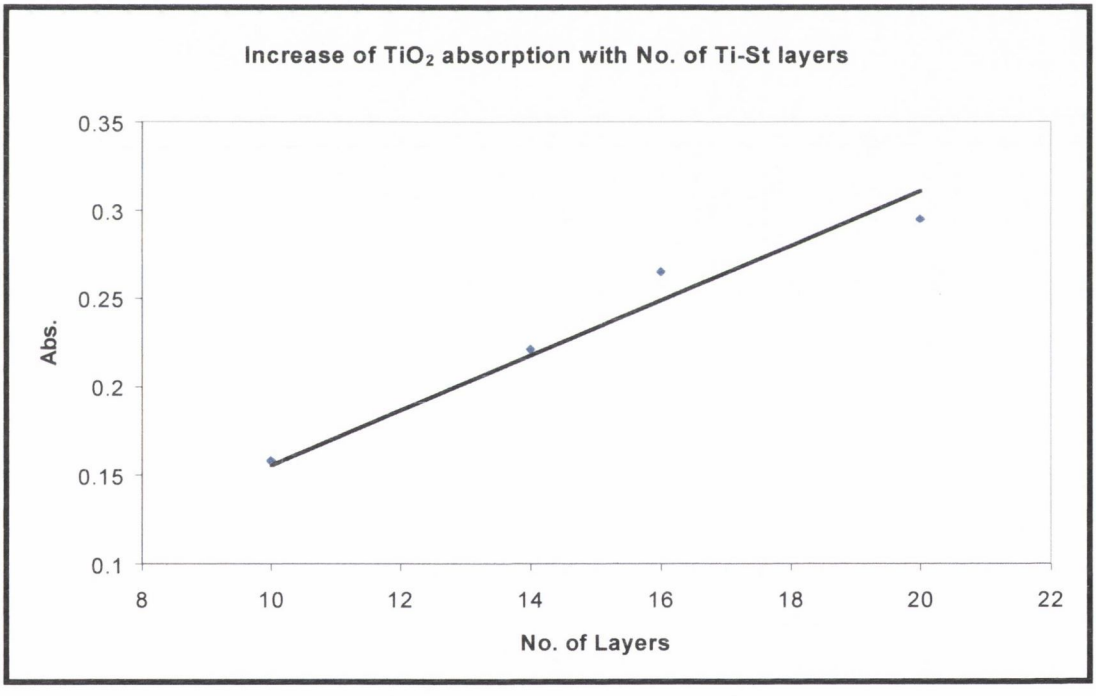

Figure 4.31: Absorbance of TiO_2 film at 300 nm vs No. of Ti-St layers

Increasing the number of Ti-St layers causes a corresponding increase in absorption. Figure 4.32 shows the uv-vis absorbance spectra for TiO_2 incorporated in 250 layers of stearic acid.

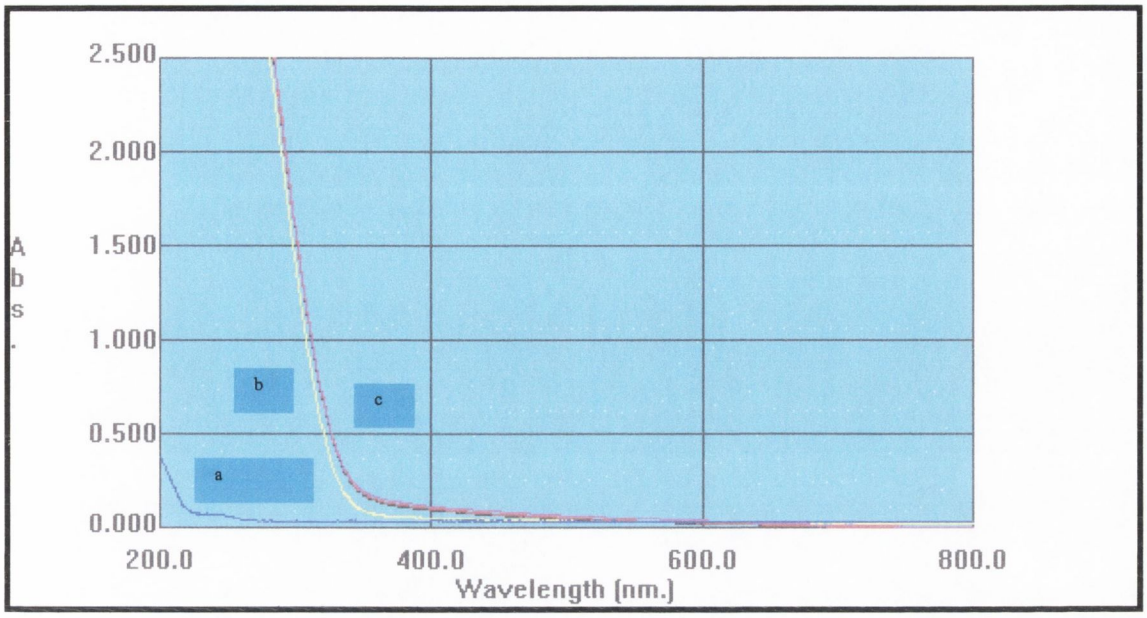

Figure 4.32: UV-Vis absorbance spectra for 250 layers of TiO_2 formed using the LB technique. (a) blank quartz slide, (b) after initial deposition and (c) after 4 days.

The onset of absorption occurs at 337 nm, indicating that size quantisation of TiO_2 particles in LB films has occurred. For bulk TiO_2 the onset should occur at 387 nm, corresponding to a band gap energy of 3.2 eV. Here the band gap is blue shifted to 3.68 eV, corresponding to a change in band gap energy of 0.48 eV using equation 4.2.1. It is also evident from the same spectra that at least medium term stability has been achieved with minimum change of film absorption after a time period of 4 days. However this film was unstable to a change in pH and readily dissolved after immersion in buffer pH 10.

The stability of TiO_2 films, formed by firing LB films of titanium stearate was thus investigated. Figure 4.33 shows the absorption spectra for TiO_2 after immersion in buffer pH 7. TiO_2 was previously formed by firing an LB film of 98 layers of titanium stearate at 450°C. The spectra obtained shows an onset of absorption at 337 nm and the film remains intact indicating that firing the sample helps to immobilise the TiO_2 on the substrate and renders the TiO_2 stable to pH change.

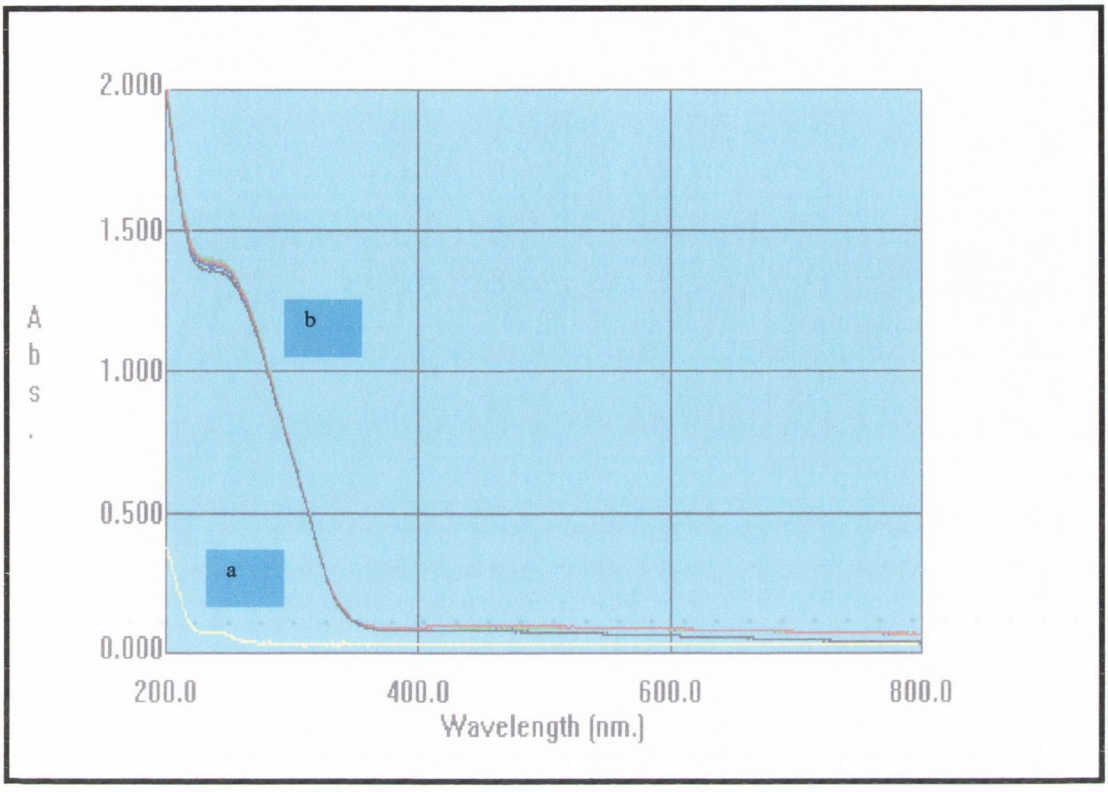

Figure 4.33: UV-Vis absorbance spectra (a) Blank quartz and (b) for TiO_2 on quartz after immersion in buffer pH 7 for 1 hr.

4.2.4 Surfactant stabilised TiO_2 sols.

The stability of the nanoparticle TiO_2 sols was investigated by absorption spectroscopy as shown by figure 4.34. The band edge absorption of the surfactant stabilised TiO_2 particles was measured and related to the particle size as previously described for TiO_2 LB films. Both CTAB and DODAB sols were stable for at least one month, after which the TiO_2 precipitates out of the sol. Figure 4.35 shows absorption spectra for CTAB stabilised TiO_2 using different amounts of CTAB (0.153 g / 4.4×10^{-4} mol dm^{-3} and 0.612 g / 1.8×10^{-3} mol dm^{-3} respectively). This spectrum indicates that increasing the amount of CTAB or DODAB surfactant has no effect on the particle size and consequently the band gap absorption of the material.

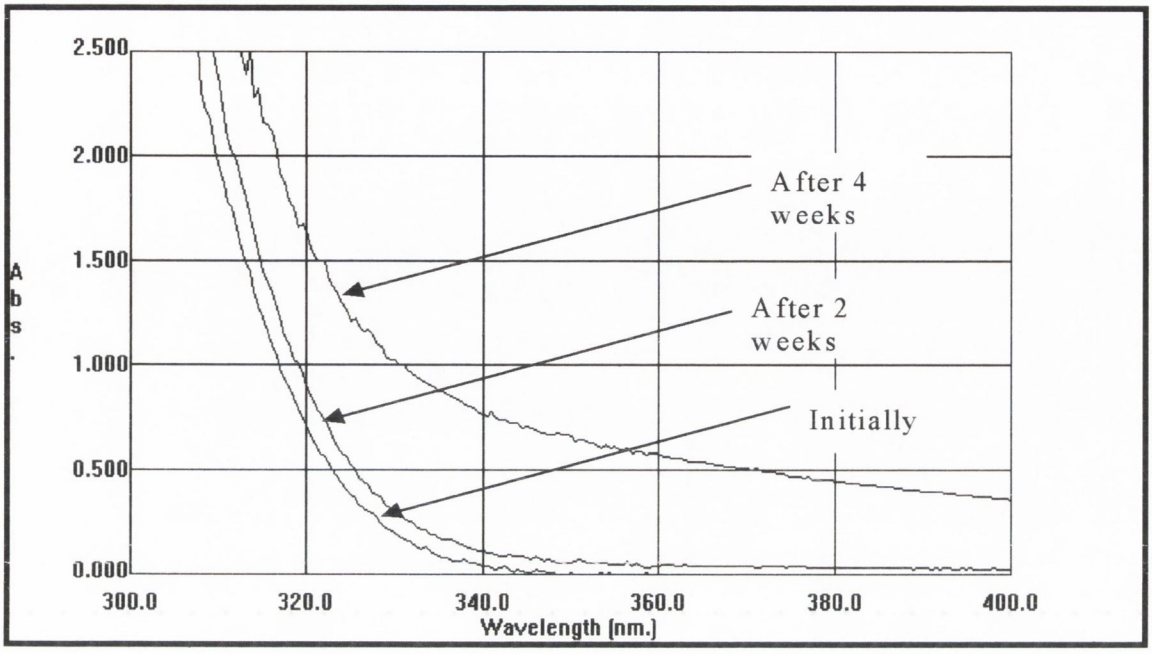

Figure 4.34: UV-Vis showing the stability of CTAB initially and after 1 month.

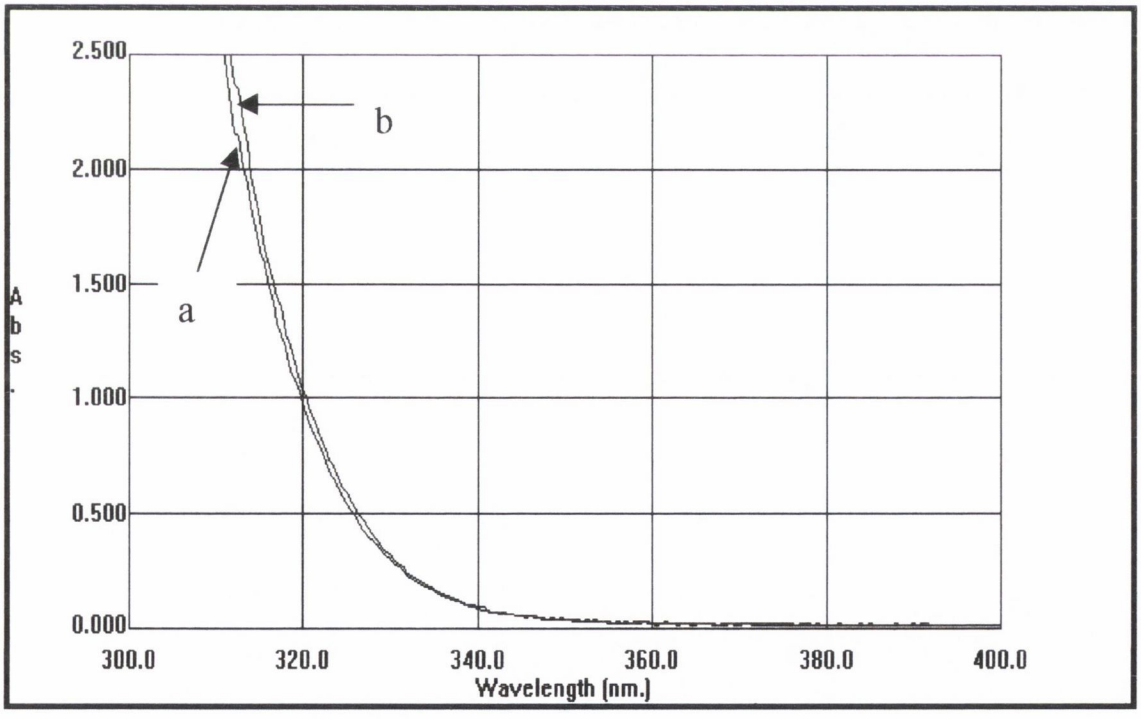

Figure 4.35: Formation of CTAB stabilised TiO_2 particles using 2 different concentrations of CTAB: (a) 4.4×10^{-4} mol dm^{-3} and (b) 1.8×10^{-3} mol dm^{-3}.

The arrested hydrolysis of TTIP with water using two different concentrations of DODAB showed no change in onset of absorption for each DODAB concentration (as previously shown for CTAB figure 4.35). Figure 4.36 shows the absorption spectrum for DODAB ($4.5x10^{-4}$ moles) stabilised TiO_2.

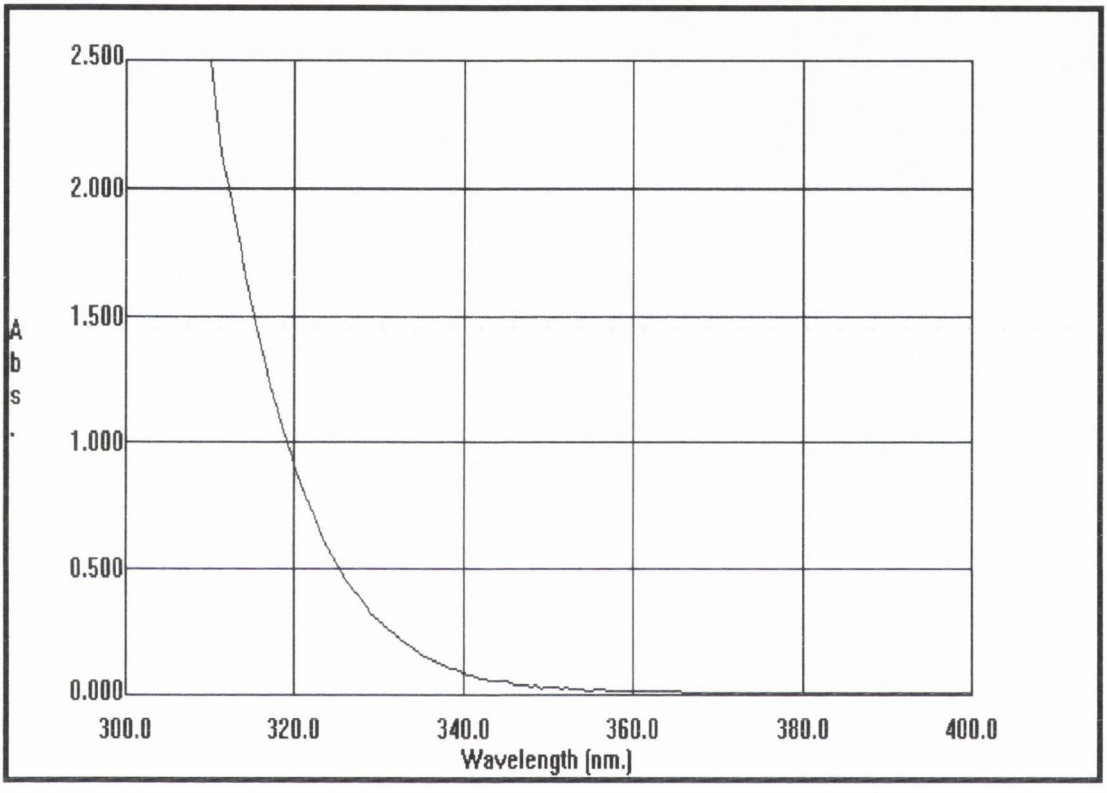

Figure 4.36: UV-Vis spectrum for DODAB stabilised TiO_2.

The diameters of the TiO_2 particles in all three media, namely: LB films, Nafion and surfactant stabilised sols were evaluated from the measured absorption band edges, A_p, using the semiempirical relationship [4.1.1] as outlined on page 98. Equation [4.1.1] is a generalised form of the theoretical relationship proposed by Brus[5]

$$E_x = E_g + h^2\pi^2(1/m_e + 1/m_h)/2R^2 + 1.786e^2/\varepsilon \qquad [4.2.2].$$

where E_x corresponds to the absorption threshold, E_g = band gap of the bulk semiconductor, the second term : $h^2\pi^2(1/m_e + 1/m_h)/2R^2$ is equal to the sum of the

[5] R. Rossetti, S. Nakahara, L.E. Brus. J. Chem. Phys. 1983, 79, 1086.

confinment energies for the electron and hole and the last term: $1.786e^2/\varepsilon$ is the coulombic interaction energy. Accordingly, substitution of 337, 314-320, 329 and 336 nm in eq. [4.1.1], yields 21.5, 17.9-18.7, 20.0 and 21.2Å for the mean diameters of TiO_2 particles incorporated in LB films, Nafion, CTAB sol and DODAB sol respectively.

The incorporation of TiO_2 nanoparticles has been achieved in LB films, Nafion and two surfactant sols. Table 4.9 summarises the corresponding onset absorptions and band gap energies for TiO_2 particles in each material.

Material	**TiO_2 abs. (A_p) (nm ±1)**	**Band gap (B_g) (eV± 0.02)**
LB film	337	3.68
Nafion	314-320	3.88-3.95
CTAB sol	329	3.77
DODAB sol	336	3.69

Table 4.9: Absorption onset and band gap energies for TiO_2 formed in: (a) 60 layer fired LB film, (b) Nafion (5 mol dm^{-3} KOH), (c) CTAB sol and (d) DODAB sol.

4.3.1 Introduction

It has been reported previously that the photocatalytic activity of TiO_2 particles is influenced by the crystal structure, surface area, size distribution, porosity and surface hydroxyl group density[6]. These parameters have an effect on the production of electron hole pairs, the surface adsorption/desorption process, and the redox process during photolysis.

In an effort to improve the photocatalytic efficiency of these processes, a number of catalytic properties such as: the chemical nature of dispersed TiO_2, its particle size and catalytic environment have been investigated during the photo-oxidation of cyanide. In addition, the reaction conditions such as pH and amount of catalyst material have been varied.

4.3.2 Cyanide photo-oxidation using TiO_2

The rate of cyanide photo-oxidation was investigated using both unsupported micron sized or supported nano-sized TiO_2 particles. For micro particulate studies, two commercially different micron sized titanium oxides were investigated: Degussa P25 and Kronos APF. Degussa P25 is mainly anatase in nature although some rutile TiO_2 (ca. 75% anatase, 25% rutile) is evident from the XRD, figure 4.51 section 4.4.2. Degussa P-25 is used regularly in photocatalytic studies because of its high photo-activity, low cost and ease of formation. This semiconductor modification is formed by the hydrolysis of $TiCl_4$ in a hot flame which produces TiO_2 with a high surface area ~50 m^2/g, an average particle diameter of 0.030 μm and a particle size distribution of 0.015-0.040 μm[7] as shown in figure 4.37.

Kronos APF, was the second commercial source of TiO_2 used in this study and can be formed using a technique similar to that used during Degussa P-25 formation, except at a lower annealing temperature. Kronos APF appears to be 100% anatase from XRD studies (figure 4.52, 4.4.2) and consists of individual spherical particles of average diameter in the size range 0.075-0.2 μm as shown in figure 4.38.

---

[6] A. Wold, Chem. Mater, 1993, 5, 280-283.
[7] S.T. Martin, D.W. Bahnemann, W. Choi, D.W. Hoffmann, Chem. Rev. 1995, 95, 69-97.

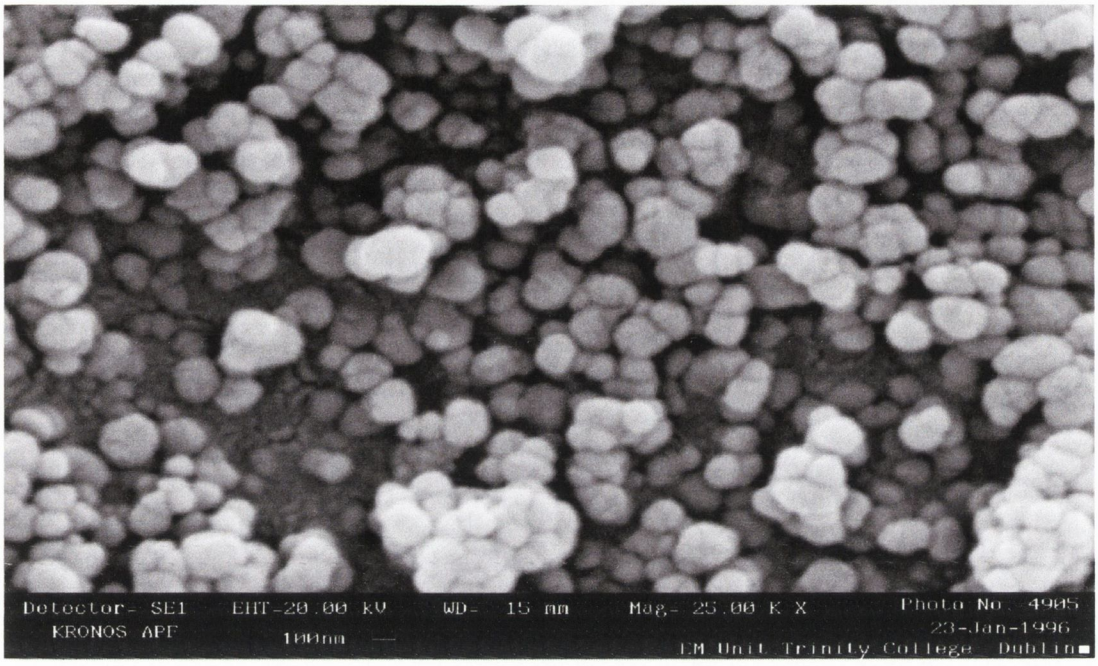

Figure 4.37: Scanning electron micrograph for Degussa P-25 TiO_2

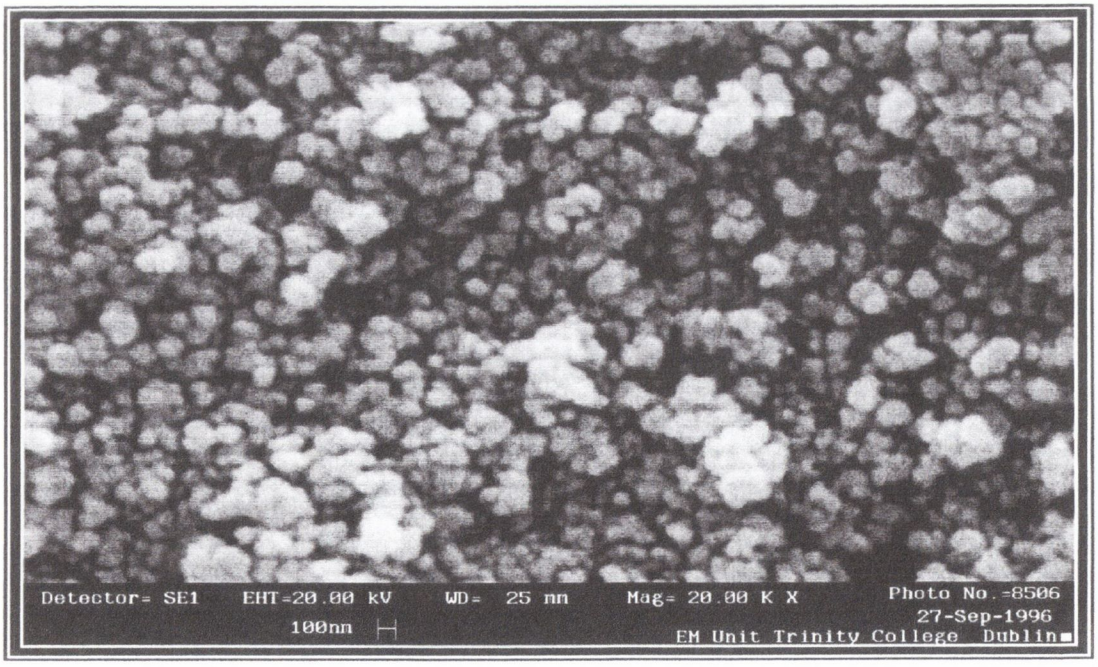

Figure 4.38: Scanning electron micrograph for Kronos APF TiO_2.

Two independent methods of cyanide analysis were used to detect the amount of cyanide remaining in solution following cyanide photo-oxidation with unsupported micron sized particles. These were a colorimetric and potentiometric method, (sections 3.3.2 and 3.3.4 respectively). Control experiments run in the absence of light and the absence of TiO_2 showed no decrease in cyanide concentration over a period of 1 hr using both methods. Experiments were performed in the absence of O_2 and showed less than 5% decrease in cyanide concentration over a period of 2 hours. Control experiments with irradiated cyanide solutions, in the absence of TiO_2, or TiO_2 containing solutions in the absence of irradiation showed that little or no oxidation of cyanide occurred under these conditions. When nitrogen was bubbled through the solution during irradiation, the rate of CN^- oxidations decreased to less than 10% of the value found with oxygen bubbling for each pH value. This indicates the necessity of O_2 and its influence on enhancing reaction rate. Frank and Bard have reported similar results[8].

4.3.3 Colorimetric method

The colorimetric method for cyanide analysis involves determination of the concentration of cyanide remaining in solution by relating this concentration to a corresponding visible absorbance maximum at 582 nm. This particular wavelength is characteristic of a charge transfer complex[9] formed during cyanide complexation with pyridine barbituric acid. Increasing the cyanide concentration results in a corresponding increase in absorbance at 582nm as shown in figure 4.39. This method of cyanide detection has been described previously in section 3.3.2). A calibration curve (Figure 4.40) was constructed by plotting the absorbance values from figure 4.39 against the corresponding cyanide concentration (0.1-1ppm). Using this calibration curve, cyanide concentrations were calculated at various time intervals during irradiation of a 20 ppm cyanide solution containing either Degussa P-25 or Kronos APF.

[8] S.N. Frank, A.J. Bard, J. Phys. Chem. 1977, 81, 1484.
[9] R. Clark, 'Comprehensive Inorganic Chemistry', 1st Ed. 1973, p 402.

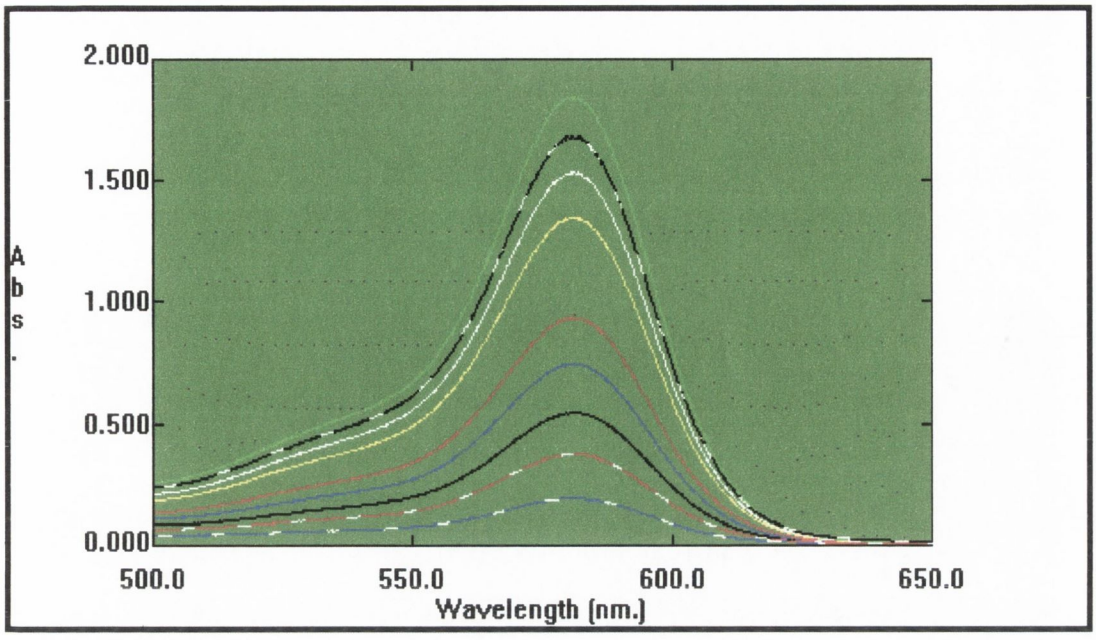

Figure 4.39: Absorbance vs concentration for the complexation of cyanide (0.1-1.0 ppm) with pyridine barbituric acid.

The calibration curve is linear in the concentration range 0.1 ppm. to 1 ppm. At lower cyanide concentrations < 0.1 ppm, the corresponding absorbance is small and insignificant, also for cyanide concentrations > 1 ppm, the observed absorbance value at 582 nm is large and outside the limits of the spectrophotometer. The calibration plot obeys the Beer-Lambert law:

$$A = \varepsilon c l \qquad [4.3.1]$$

Where:A= absorbance, ε = molar extinction coefficient ($mol.^{-1}dm^3cm^{-1}$), l = path length of the solution (1cm).

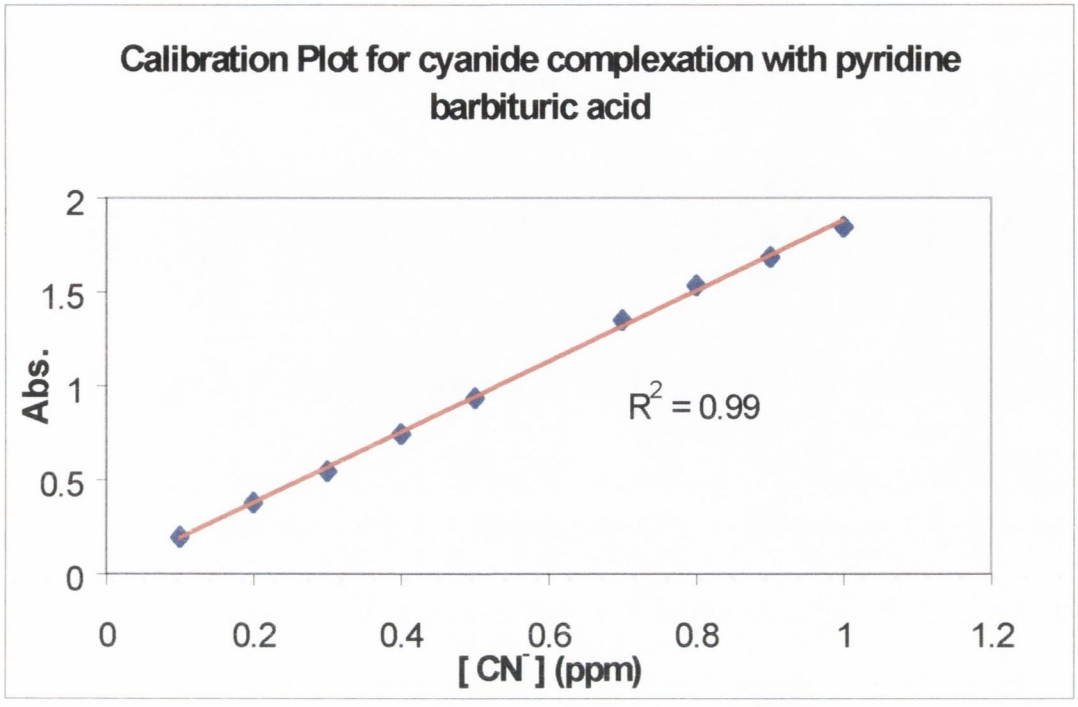

Figure 4.40: Calibration curve for the detection of cyanide using the colorimetric method.

The slope of the calibration curve (ε) is 48,700 mol.$^{-1}$dm^{3}cm^{-1}, such a high extinction coefficient would suggest that charge transfer occurs within the complex. Figure 4.41 shows a proposed mechanism[10] for the reaction of pyridine-barbituric acid with cyanide at 582nm. The reaction of pyridine with barbituric acid is pH dependent and involves formation of the pyridinium chloride complex with keto-enol tautomerisation of barbituric acid followed by an SN_2 addition of cyanide to yield a highly conjugated molecule and the elimination of OH^-. Finally the pyridinium chloride complex reacts with the available hydroxide to regenerate pyridine.

[10] Private commun. N. Hanly, University of Limerick 1996.

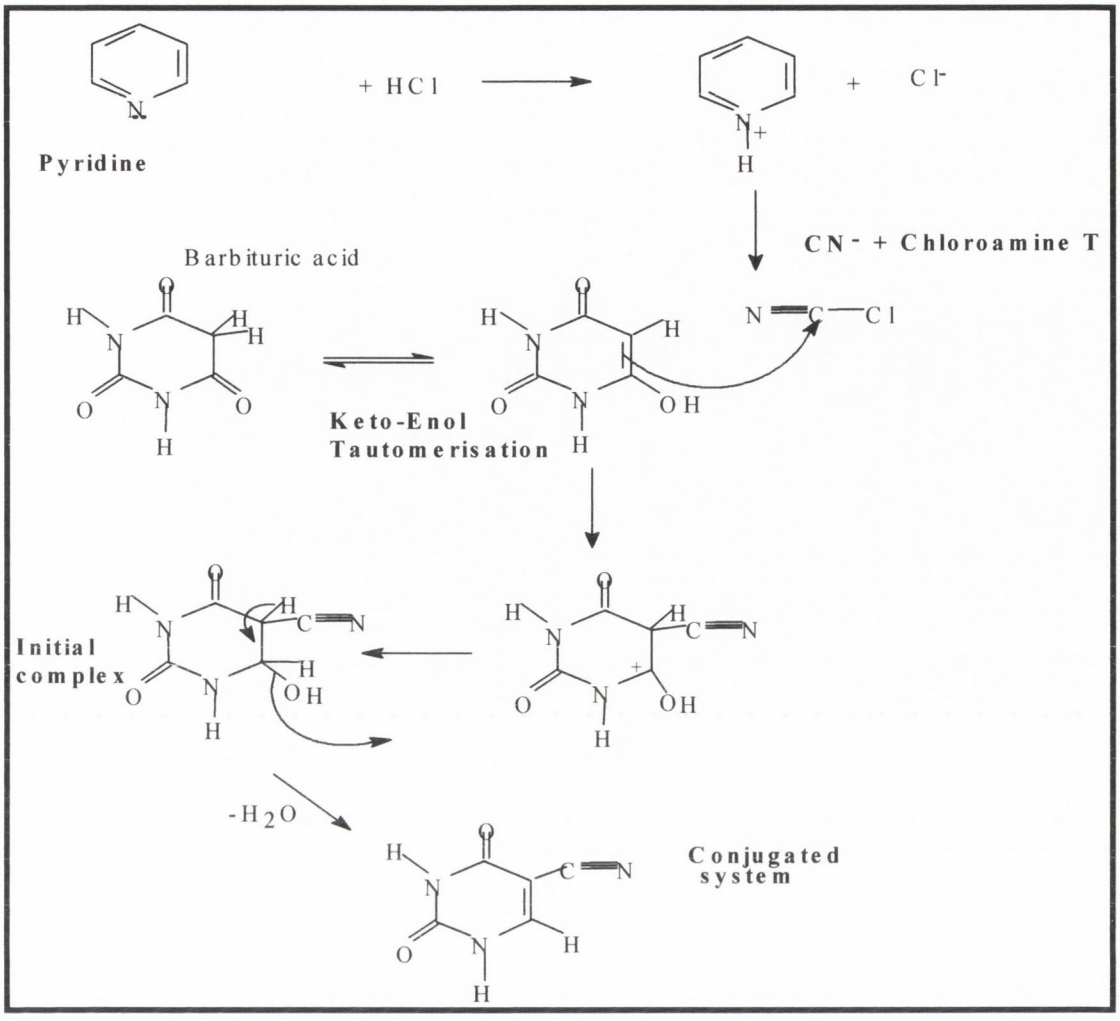

Figure 4.41: Proposed reaction mechanism for the reaction of pyridine barbituric acid with cyanide

Knowing the molar extinction coefficient for the absorption of pyridine-barbituric acid complexed with cyanide, it is possible to determine the exact concentration of cyanide present in the solution at any given time during photolysis, using the Beer Lambert Law [4.3.1]. The concentration of cyanide remaining in solution after cyanide photo-oxidation for 25 min was detected by substituting the measured absorbance for the reaction of cyanide with pyridine-barbituric at this time interval in the Beer Lambert Law:

Example

$$1.16 = 48{,}736\ [CN^-]\ X\ (1)$$

$$[CN^-] = (1.16)/(48736)$$

$$= 2.3 \times 10^{-5}\ \text{mol dm}^{-3}$$

Since each sample was diluted 1 in 20 ml. and converting from moles to ppm:

$\Rightarrow$ $[CN^-] = (2.3 \times 10^{-5} \text{ mol dm}^{-3}) \times (26000 \text{ mgmol}^{-1}) \times (20)$

$= 12.37$ ppm

However there are a number of disadvantages associated with this technique, they include:

I. The TiO_2 sample must be removed from the cyanide suspension after photolysis, so that the cyanide remaining in solution can be determined accurately. Otherwise large amounts of scatter and incorrect absorption results arising from TiO_2 absorption will occur.

II. The complexation of cyanide with pyridine barbituric acid is photo unstable and uv-vis measurements must be recorded almost immediately after complexation.

III. Both pyridine and barbituric acid are toxic substances and need to used in the fumehood and disposed of separately.

4.3.4 Potentiometric method

Therefore the I.S.E. method was adopted for further investigations into the rate of cyanide photo-oxidation using supported and unsupported TiO_2. The choice of this method over the colorimetric method is simply attributed to ease of working conditions. The potentiometric method for cyanide detection showed better first order kinetic plots compared to the colorimetric method and also allowed for the in-situ continual monitoring of the reaction with no need for sample removal, TiO_2 filtration, or time loss, important when examining the kinetics associated with the reaction. This technique measures the amount of cyanide remaining in solution and relates this cyanide concentration to a potential (mV) using an ion selective electrode. The electrode response follows a Nernst relationship and its slope is calculated from a plot of the measured electrode potential vs log $[CN^-]$ as shown in figure 4.42.

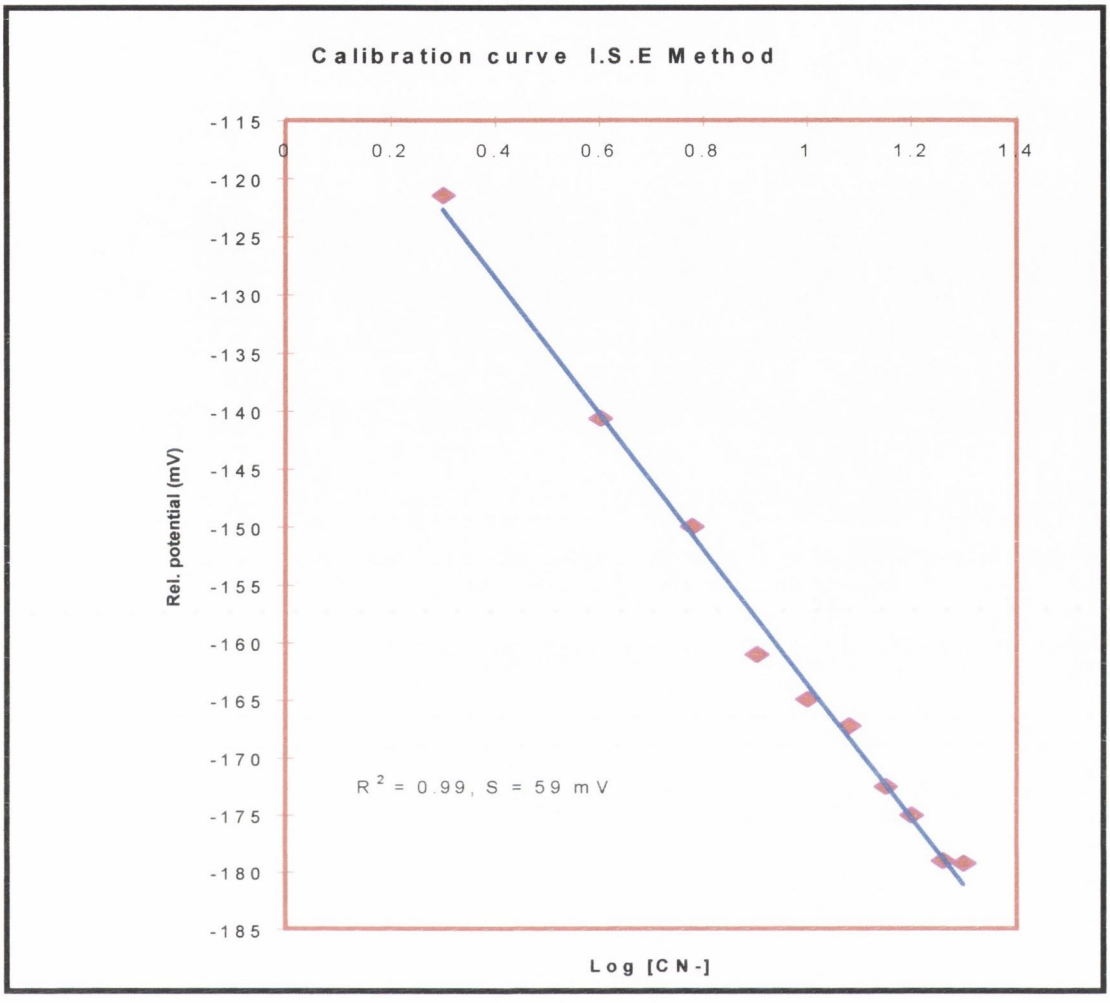

Figure 4.42: Calibration curve for cyanide detection using the potentiometric method

4.3.5 Reaction kinetics

If the rate-determining step for the loss of cyanide is first order in cyanide concentration, the rate expression can be expressed as follows:

$$\frac{-d[CN^-]}{dt} = k_{obsd}\,[CN^-] \qquad [4.3.2]$$

Integrating the above equation between the limits 0 and t gives the following:

$$\ln\left(\frac{[CN^-]_t}{[CN^-]_0}\right) = -k_{obsd}\,t \qquad [4.3.3]$$

A linear plot of ln $[CN^-]_t/[CN^-]_0$ vs time (t) was observed for cyanide photo-oxidation using both unsupported micron and supported nano-sized TiO_2 particles. The observed rate constants were determined from the linear sections of the plots up to 60% conversion of cyanide. Figure 4.43 shows two first order plots for cyanide photo-oxidation over two different commercially available TiO_2 semiconductors at pH 10 in the presence of O_2, in which the cyanide remaining in solution was detected using the colorimetric method.

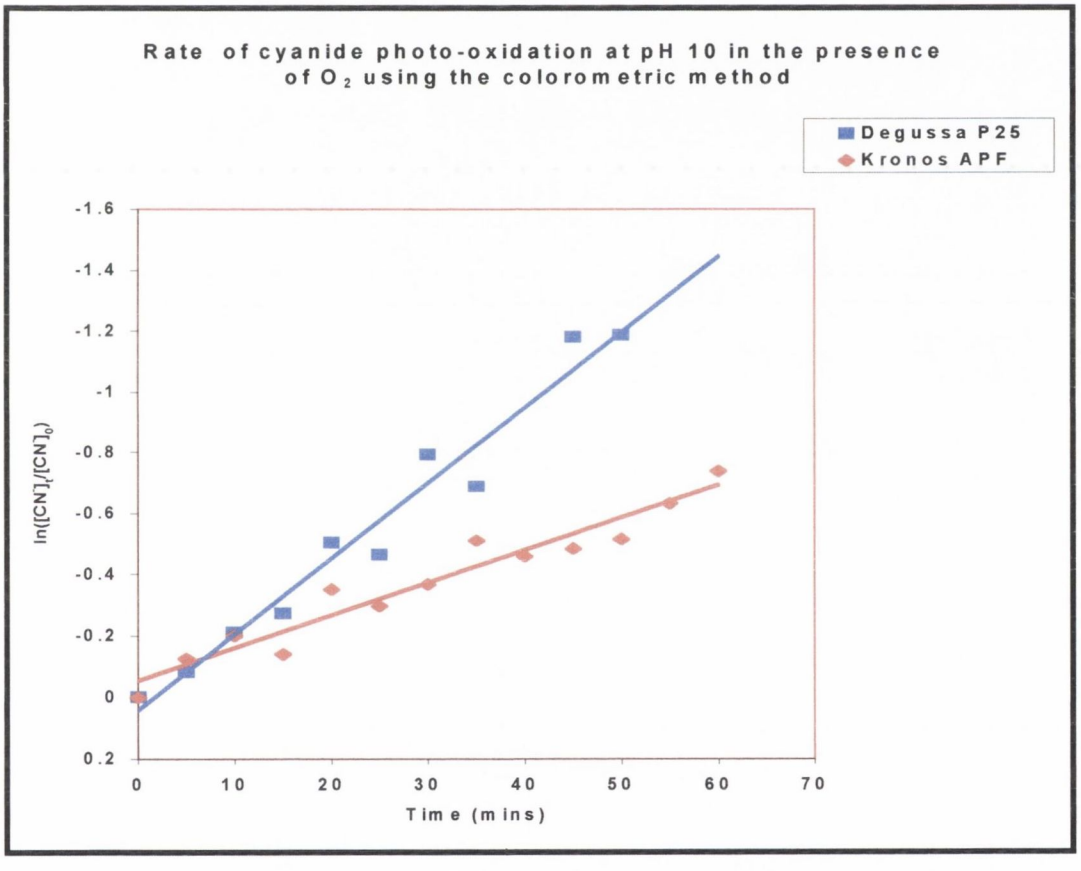

Figure 4.43: Cyanide photo-oxidation using two commercially available semiconductors.

Both plots (figure 4.43) show a decrease in cyanide concentration, with Degussa P-25 exhibiting the higher rate constant. A summary of reaction rate constants is shown in table 4.11(a). The relatively high reaction rate constant associated with Degussa P-25 compared to Kronos APF has encouraged further use of this material for the photo-oxidation of cyanide at different pH values.

A decrease in cyanide concentration as a function of pH was measured for a 20 ppm cyanide solution containing 0.1g TiO_2/100 cm^3 cyanide. Figure 4.44-4.46 each show two similar plots of ln ($[CN]_t/[CN^-]_0$) against time for the same reaction of cyanide photo-oxidation at pH 9, 10 and 14 in the presence of O_2 using the potentiometric method for cyanide analysis. The plots show an upper and lower rate constant limit at each pH in between which a number of rate constants have been recorded, so that these results are simply representative examples taken from a number of experiments. The plots of ln ($[CN]_t/[CN^-]_0$) against time at each pH show a first order decrease in cyanide concentration over a period of at least 60 mins. The observed rate constants associated with these photochemical experiments are summarised in table 4.11. The average rate constant for cyanide photo- oxidation was estimated from each plot at the different pH values. Figure 4.47 shows the average decrease in cyanide concentration for pH 9, 10 and 14.

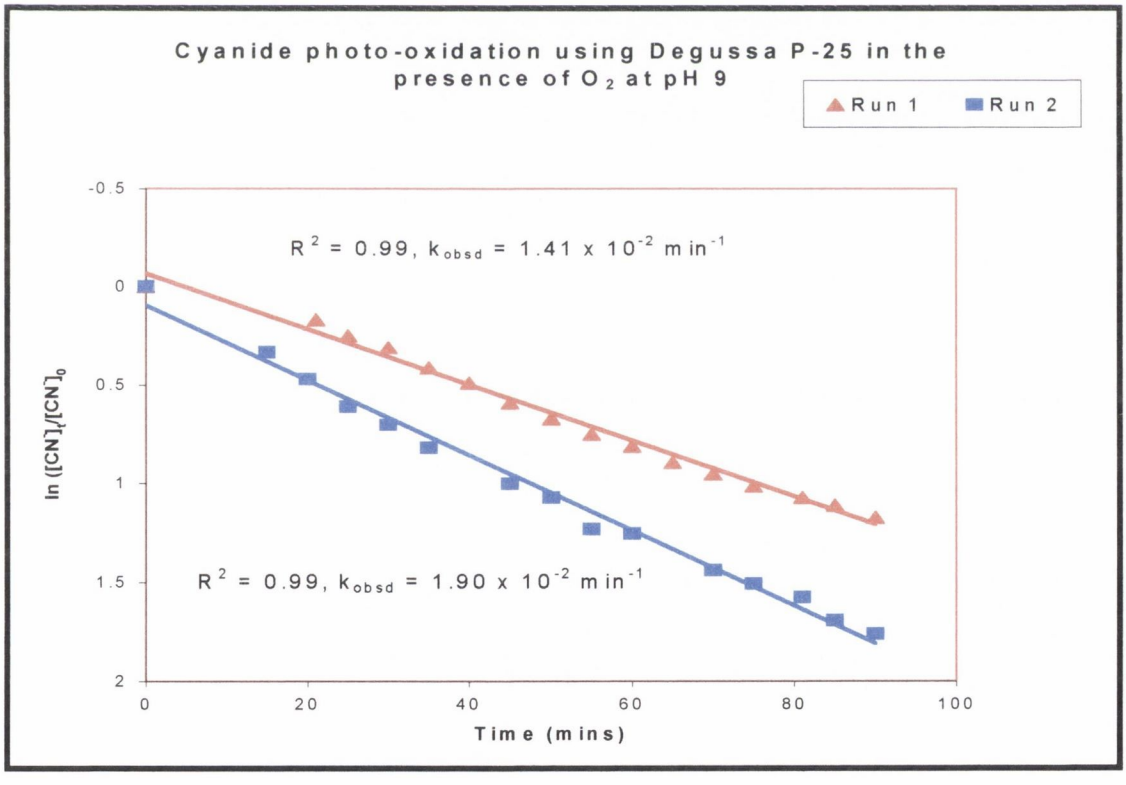

Figure 4.44: Cyanide photo-oxidation at pH 9

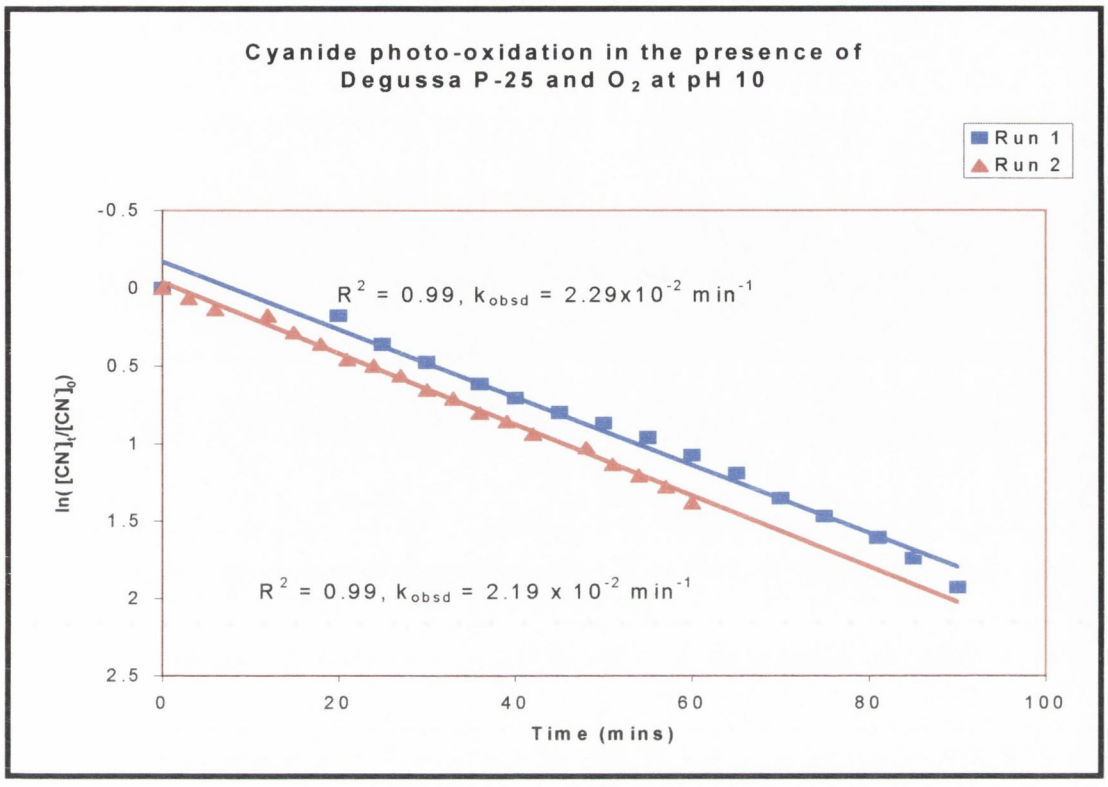

Figure 4.45: Cyanide Photo-oxidation at pH 10

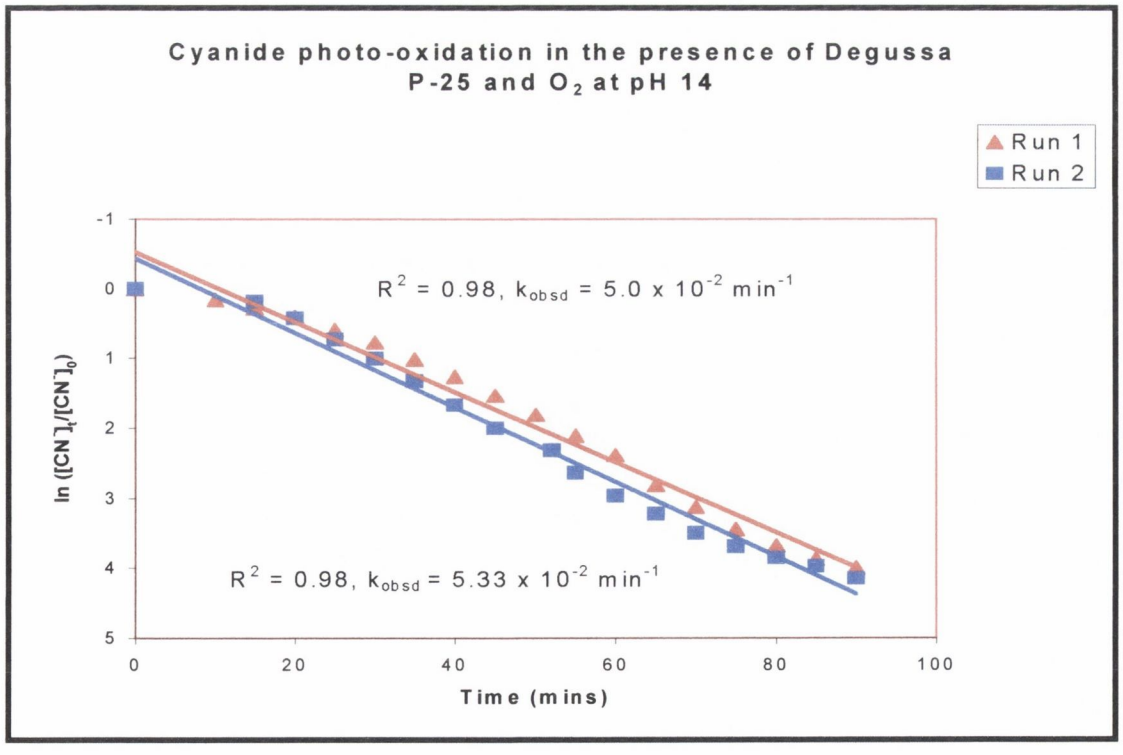

Figure 4.46: Cyanide photo-oxidation at pH 14.

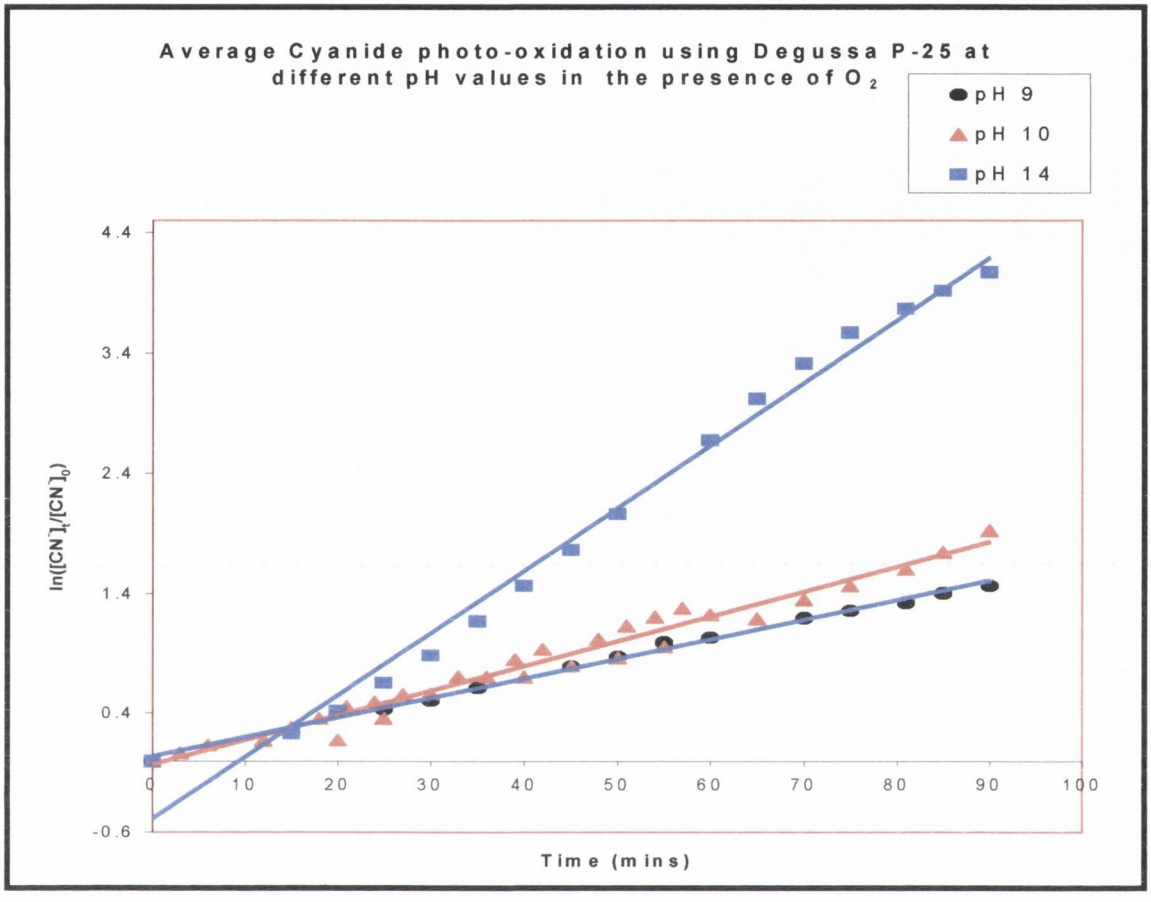

Figure 4.47: Cyanide photo-oxidation.

4.3.6 Cyanide photo-oxidation using Nafion immobilised TiO_2

Similar photochemical experiments on cyanide photo-oxidation were investigated using TiO_2 nanoparticles formed in a Nafion ion exchange. The immobilisation of TiO_2 nanoparticles in either Nafion or LB films were investigated with the view of:

I. Enhancing the behaviour of TiO_2 particles towards cyanide photo-oxidation.

II. Reducing the need of TiO_2 separation after photo-oxidation.

With both of these objectives in mind, a number of experiments have been carried out in order to investigate the efficiency of host TiO_2 particles towards cyanide decomposition. Photocatalytic oxidation of cyanide using TiO_2 incorporated Nafion was first investigated, and involved the precipitation of TiO_2 in Nafion from aqueous

solutions of $TiCl_3$, with subsequent Ti^{3+} base hydrolysis using 0.5M and 5M KOH as described previously (Section 3.2.2)

Each Nafion membrane was estimated to contain ca. 17 mg of TiO_2 as shown in table 4.10. This calculation was made, assuming that 100 % incorporation of Ti^{3+} in the membrane had occurred and that each Ti^{3+} cation is co-ordinated with 3 SO_3^- anions. Knowing the initial weight of a dry Nafion membrane and assuming a Nafion equivalent weight of 1200g/mol, it is possible to estimate the amount of TiO_2 incorporated in Nafion.

Membrane	Mass of membrane (g)	No. of SO_3^- ions (mol.)	No. of Ti^{3+} ions (mol.)	Amount of TiO_2 in membrane (g)
1	0.7596	6.33×10^{-4}	2.11×10^{-4}	1.69×10^{-2}
2	0.7650	6.38×10^{-4}	2.13×10^{-4}	1.70×10^{-2}

Table 4.10: Amount of TiO_2 incorporated in 2 different Nafion membranes after hydrolysis with 0.5M (1) and 5M (2) KOH respectively.

The decrease in cyanide concentration was measured for a 20-ppm cyanide solution as before, using the above TiO_2 incorporated Nafion membranes, at a pH of 10 in the presence of O_2. Figure 4.48 shows a first order kinetic plot of cyanide photo-oxidation with time. This result is a representative example from a number of repeated reproducible results. First order kinetic plots are linear and show a considerable decrease in cyanide concentration from an initial concentration of 20 ppm to a final concentration of 8.8 and 6.3 ppm after 60 mins. Subsequently, higher photocatalytic efficiency was achieved with membrane 2 for cyanide photo-oxidation compared to membrane 1.

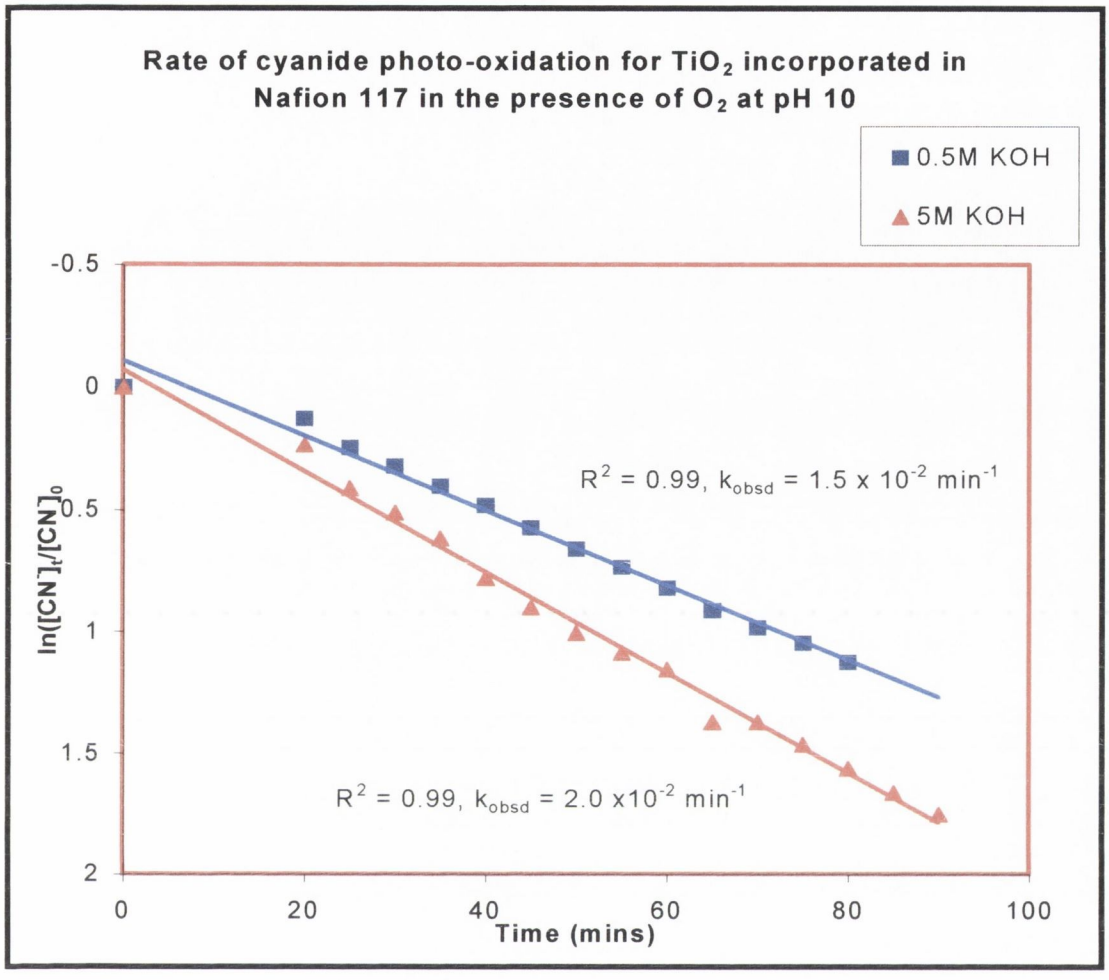

Figure 4.48: Cyanide photo-oxidation using Nafion incorporated TiO_2.

4.3.7 Cyanide photo-oxidation using LB immobilised TiO_2

Similar investigations were carried out using fired LB films of Ti-St, which results in the formation of TiO_2 after a period of 2hrs. The preparation of these films was previously described in section 3.1.2. Two different samples of fired titanium stearate were used for photo-oxidation of cyanide in order to examine whether or not different amounts of TiO_2 could influence the efficiency of cyanide oxidation.

The amount of TiO_2 formed from 10 and 42 layers of titanium stearate was estimated (section 4.1.7) to be 1.5μg and 6.3 μg respectively. Figure 4.49 shows a linear decrease of cyanide concentration observed for both TiO_2 film samples over a period

of 90 mins. The higher rate constant was achieved for cyanide photo-oxidation using 42 layers of fired titanium stearate (3.91×10^{-3} min^{-1}), in which the initial cyanide concentration decreased from 20 ppm to 13.2 ppm. A lower rate constant of 2.27×10^{-3} min^{-1} was estimated for 10 layers of fired Ti-St, with a corresponding decrease in cyanide concentration from 20 ppm to 17.7 ppm.

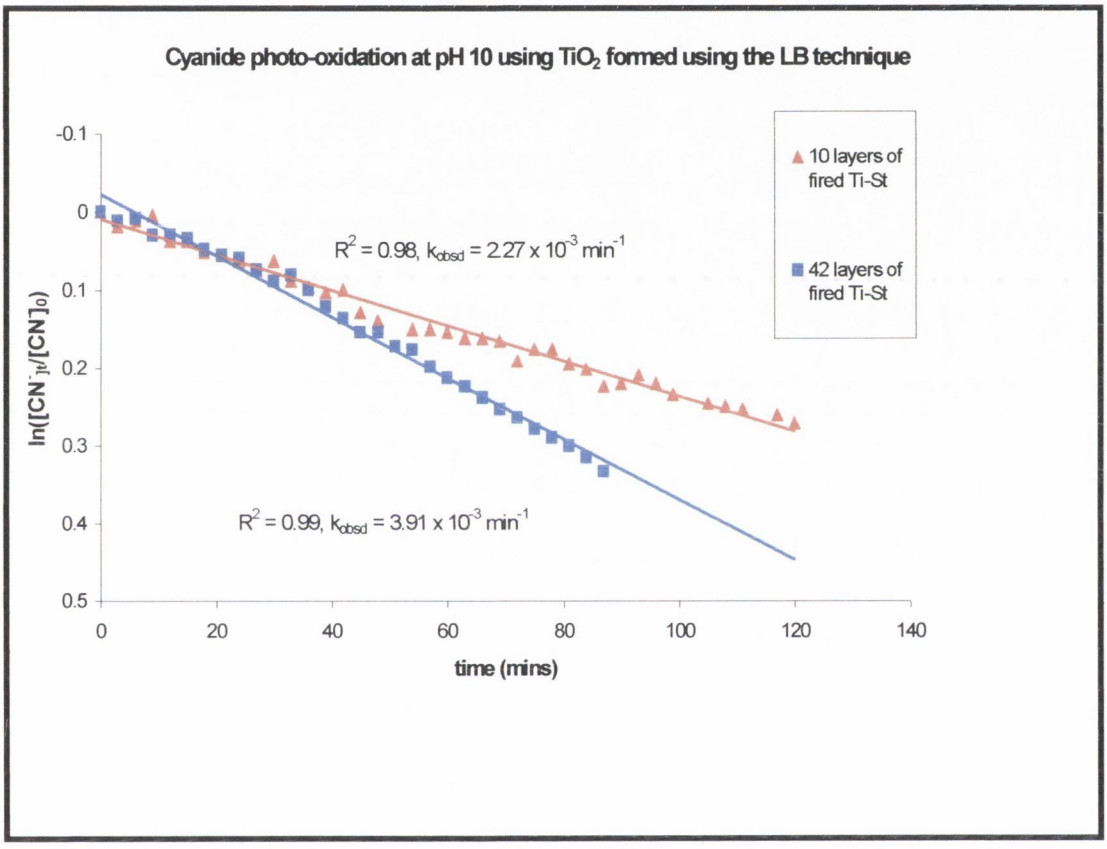

Figure 4.49: Cyanide photo-oxidation using two different TiO_2 films.

4.3.8 Sample calculation Surface area / g of TiO_2

Nafion average particle diameter: = 18.7Å

Volume of TiO_2/ particle ($4/3\pi r^3$) = 3.42×10^{-21} cm^3

Mass of each TiO_2 particle (Density x Volume) = (3.42×10^{-21} cm^3) x (3.9 g/cm^3)

= 1.33×10^{-20} g

Surface area of particle ($4\pi r^2$) $= 1.098 \times 10^{-17}$ m^2/particle.

Calculated mass of TiO_2 = 17 mg

No. of TiO_2 particles $= 17 \times 10^{-3}$ g/1.33×10^{-20}g

$= 1.275 \times 10^{18}$ particles.

Surface area of TiO_2 (17mg) $= 1.098 \times 10^{-17}$ m^2/particle x 1.275×10^{18} particles

$= 14 m^2$/ 17mg $\equiv$ 824 m^2/g TiO_2

Table 4.11 summaries the average particle diameters (measured from uv-vis studies) and surface areas for different TiO_2 particles used in this study.

TiO_2	Average particle diameter Å	Surface area (m^2/g)
Kronos APF	2000	7.7
Degussa P25	300	25.6
Nafion	17.918.7	824-854
LB films	21.5	716

Table 4.11 Shows the average particle diameter and calculated surface areas for immobilised and unsupported TiO_2 particles.

TiO_2	TiO_2 / 100 cm^{-3} CN^-	Solution pH	Residual [CN^-] (ppm) after 1hr.	k_{obsd} min^{-1}	k^1_{obsd} min^{-1}
Degussa P25	0.1g	9	7.1	$1.66x10^{-2}$	$1.65x10^{-2}$
		10	6.8	$2.24x10^{-2}$	$2.35x10^{-2}$
		14	4.1	$5.17x10^{-2}$	$5.43x10^{-2}$
Kronos APF	0.1g	10	10.2	$1.06x10^{-2}$	$1.02x10^{-2}$
1 Nafion	16.9 mg	10	8.8	$1.53x10^{-2}$	$1.53x10^{-2}$
2	17.0 mg	10	6.3	$2.06x10^{-2}$	$2.06x10^{-2}$
10 layers LB films	1.5μg	10	17.7	$2.27x10^{-3}$	$2.25x10^{-3}$
42 layers	6.3μg	10	13.2	$3.91x10^{-3}$	$3.97x10^{-3}$

Table 4.11(a): Summary of kinetic data obtained for 20 ppm cyanide photo-oxidation using unsupported and immobilised TiO_2.

Table 4.11(a) summaries the kinetic data obtained for the photo-oxidation of cyanide using unsupported micron size and immobilise nano size TiO_2 particles. k^1 represents the recalculated k values for cyanide photo-oxidation. k^1 allows for a variable induction period in which cyanide photo-oxiadtion is slow to react at high cyanide concentrations and then becomes first order with respect to cyanide. Figure 4.50 shows a graphical representation, summarising the kinetic data obtained using different TiO_2 Particles for cyanide photo-oxidation.

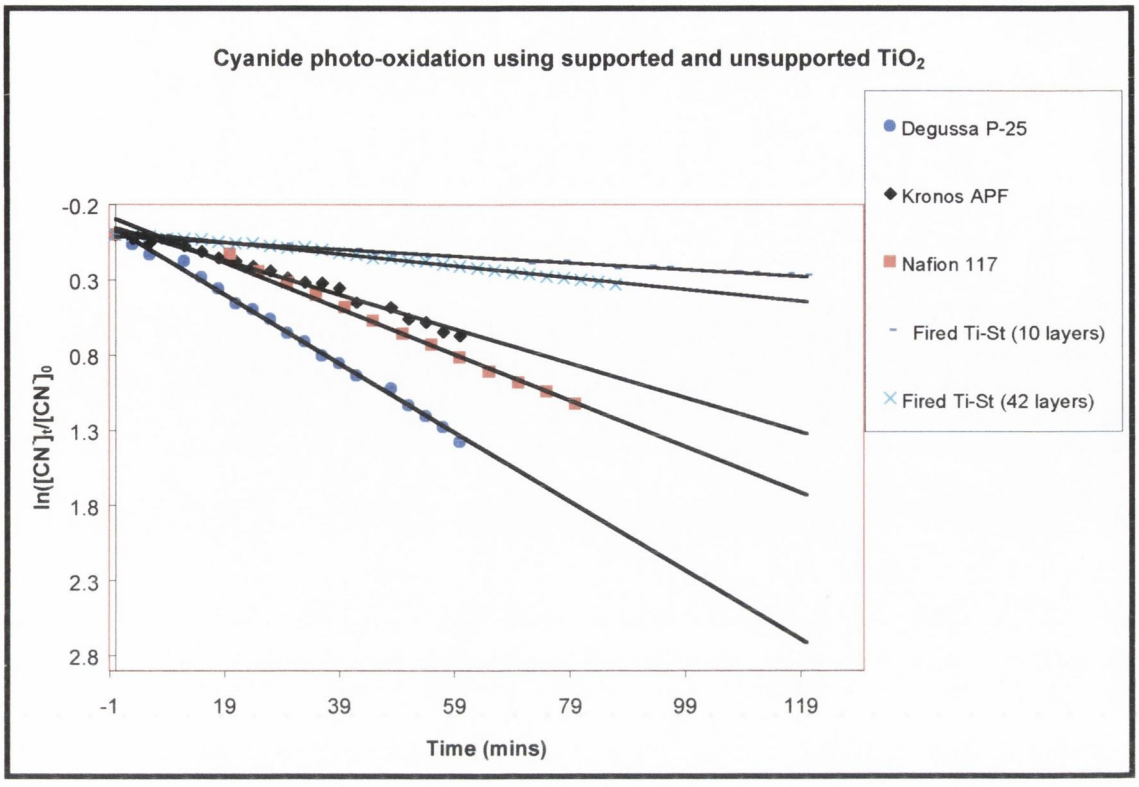

Figure 4.50: Cyanide photo-oxidation using supported and unsupported TiO_2

Chapter 4: Section IV: X-Ray Diffraction Measurements

4.4.1 Introduction

Powder X-Ray diffraction was used in order to classify the nature of the oxide material, which was formed in Nafion membranes, from LB film precursors or obtained commercially. The X-Ray beam is scattered at various Bragg angles, corresponding to the inter-planar spacing (d) for the particular oxide(s) present.

The Bragg equation is adequate for predicting the position of diffraction maxima

$$n\lambda=2d \sin \theta \qquad [4.4.1]$$

Here *d* is the inter-planar spacing, *n* is an integer and is dependant on the diffraction order, λ is the wavelength and θ is the angle between the direction of the incident beam and the lattice plane under consideration and the angle between the direction of the diffracted beam and this plane.

4.4.2 Diffraction studies on micron size TiO_2

X-Ray diffraction studies were carried out using commercially available samples of TiO_2, in order to confirm the chemical nature of the oxide(s) present. Figure 4.51 shows the corresponding wide angle X-Ray scattering (WAXS) pattern for commercially available micron sized Degussa P25 compared with both the anatase and rutile forms of TiO_2 (JCPDS 21-1272 and 21-1276). A distinct and well-resolved WAXS pattern between $2\theta = 10°$ and 90° was recorded for the Degussa sample. This sample appears to be mainly anatase in nature, however there is some evidence for the presence of rutile TiO_2. This is confirmed from the XRD pattern which shows a distinct peak at $2\theta = 27.4°$ corresponding to rutile TiO_2 ($2\theta = 27.4 °\equiv$ 100, $39.2°\equiv$ 27, $36.1°\equiv$ 15). A WAXS pattern was also obtained for the second commercially available TiO_2 sample (Kronos APF). Figure 4.52 shows this well resolved pattern compared to Degussa P25. It appears that Kronos APF is totally anatase in nature ($2\theta = 25.3 \equiv 100$, $48.1 \equiv 35$ and $37.8 \equiv 20$) when compared with Degussa P25. Evidence for this is shown in figure 4.52 by the absence of a diffraction peak at $2\theta = 27.4°$ corresponding to the most intense peak of rutile TiO_2.

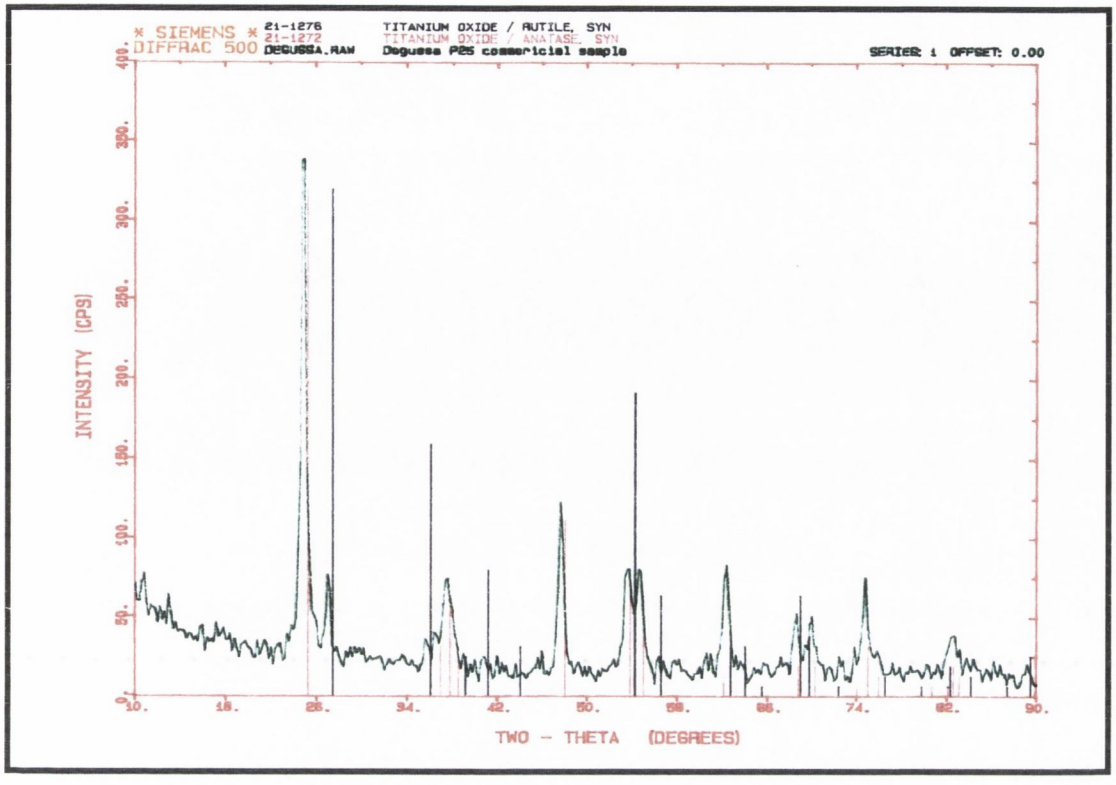

Figure 4.51: Wide angle X-Ray Diffraction Pattern recorded for TiO_2 (Degussa P-25).

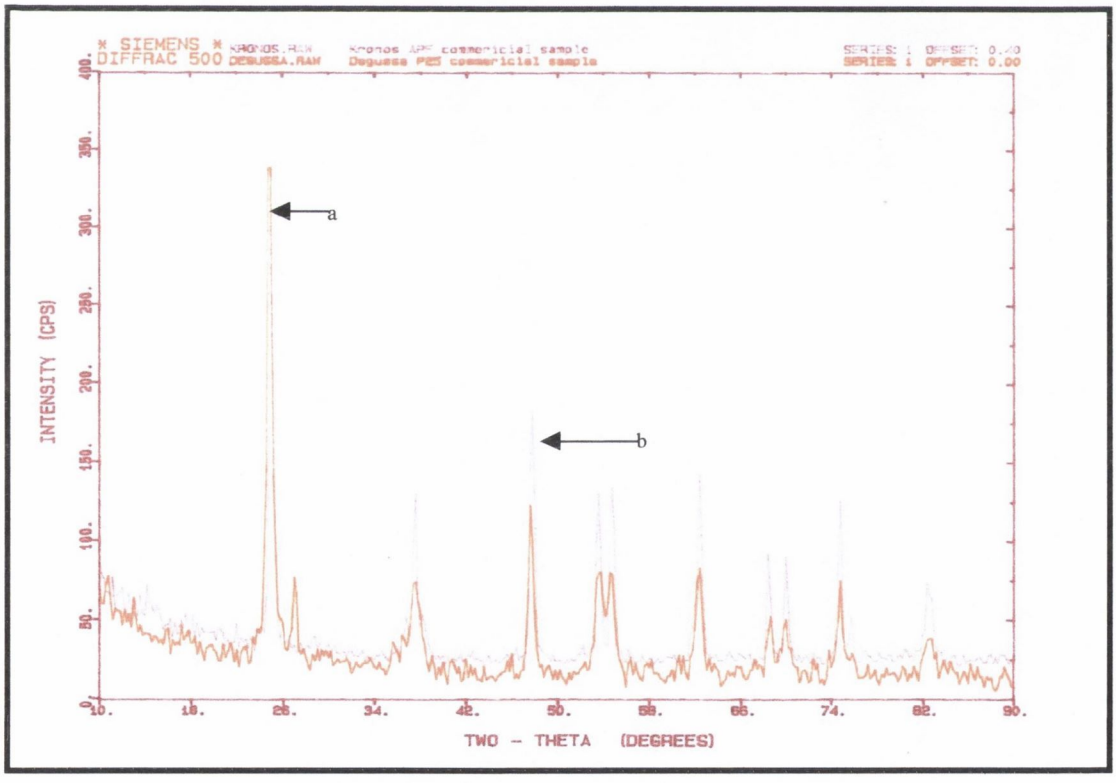

Figure 4.52: Wide angle X-Ray Diffraction Pattern recorded for TiO_2 (a) Degussa P-25.and (b) Kronos APF.

4.4.3 Diffraction studies on LB films

The XRD of cadmium stearate (130 layers) was obtained in order to examine and compare this spectrum with a WAXS pattern obtained for Ti-St. It has been previously reported[11] that cadmium stearate LB films provide a WAXS patterns with quite distinct intensity maxima. Figure 4.53 shows this distinct and well-resolved WAXS pattern initially between 2θ = 5 and 55° for 130 layers of cadmium stearate deposited on quartz at 20 mN/m.

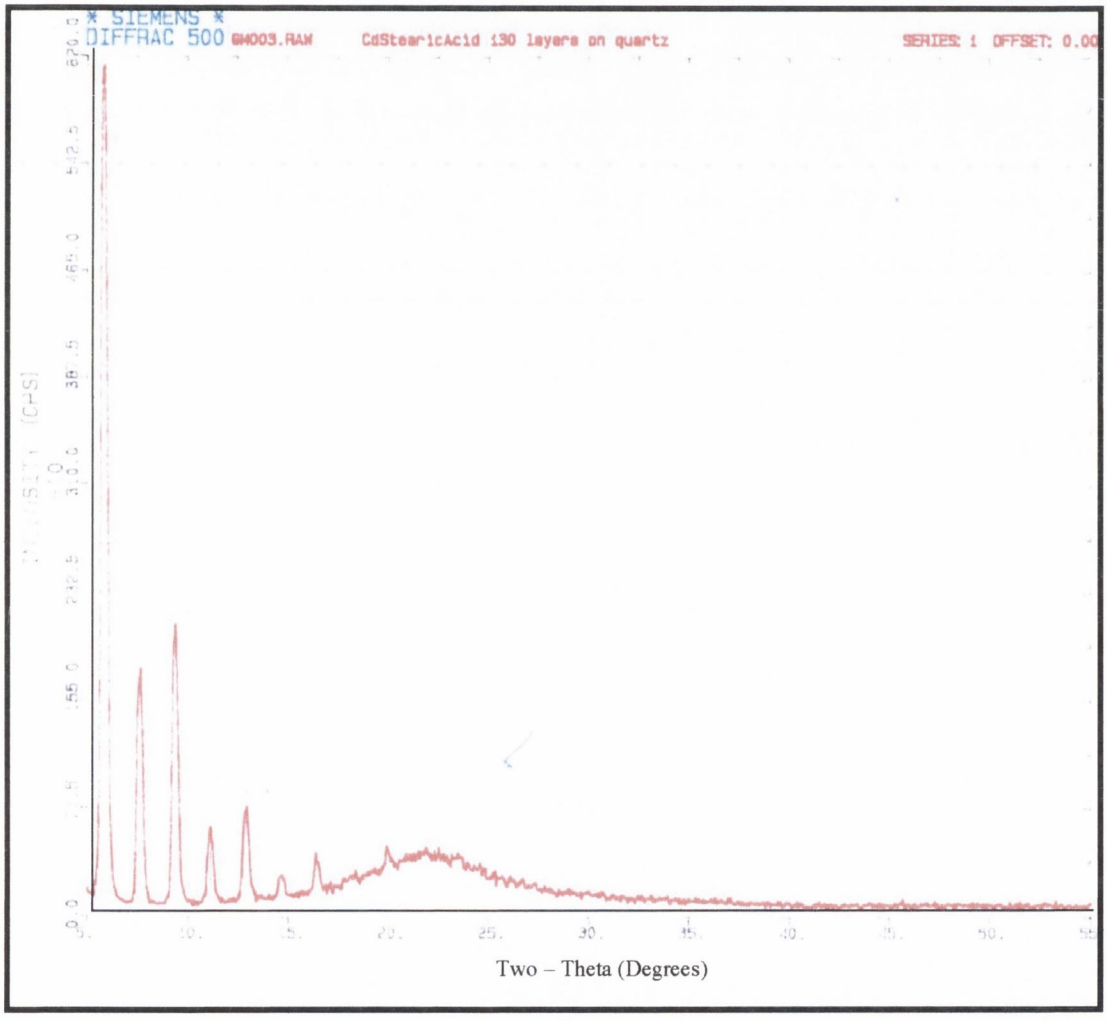

Figure 4.53: Wide angle X-Ray Diffraction Pattern recorded for a cadmium stearate (Cd-St) multilayer films (130 layer).

[11] V. Erokhin, L. Feigin, G. Ivakin, V. Klechkovskaya, Y. Lvov, N. Stiopina, Makromol. Chem., Macromol.. Symp. 1991, 46, 359-363.

Knowing the angle of diffraction θ from the WAXS pattern (figure 4.53) the values (table 4.12) between the second and fifth orders of X-Ray diffraction were estimated using the Bragg equation:

n	2θ	θ	Sinθ	2d (nm.)	d (nm.)	d (Å)
1	1.965	0.982	0.0171	9.01	4.51	45.1
2	3.669	1.385	0.0320	9.63	4.82	48.2
3	5.439	2.719	0.0471	9.84	4.92	49.2
4	7.271	3.637	0.0634	9.72	4.86	48.6
5	8.912	4.450	0.0777	9.92	4.96	49.6

Table 4.12: Apparent d values for 5 orders of X-Ray diffraction on 130 layers of cadmium stearate deposited on quartz at 20 mN/m.

Preliminary structural investigations on LB films of stearic acid containing titanium stearate and TiO_2 were conducted using wide angle X-Ray scattering (WAXS). The patterns recorded for LB films containing TiO_2 show a broad diffraction pattern with a maximum intensity at $2\theta = 22°$, even at low scan rates ($0.05° \text{ sec}^{-1}$), indicating a lack of crystallinity for the material present. Figure 4.54 shows the WAXS pattern recorded for TiO_2 in 250 layers of stearic acid previously deposited on a quartz slide.

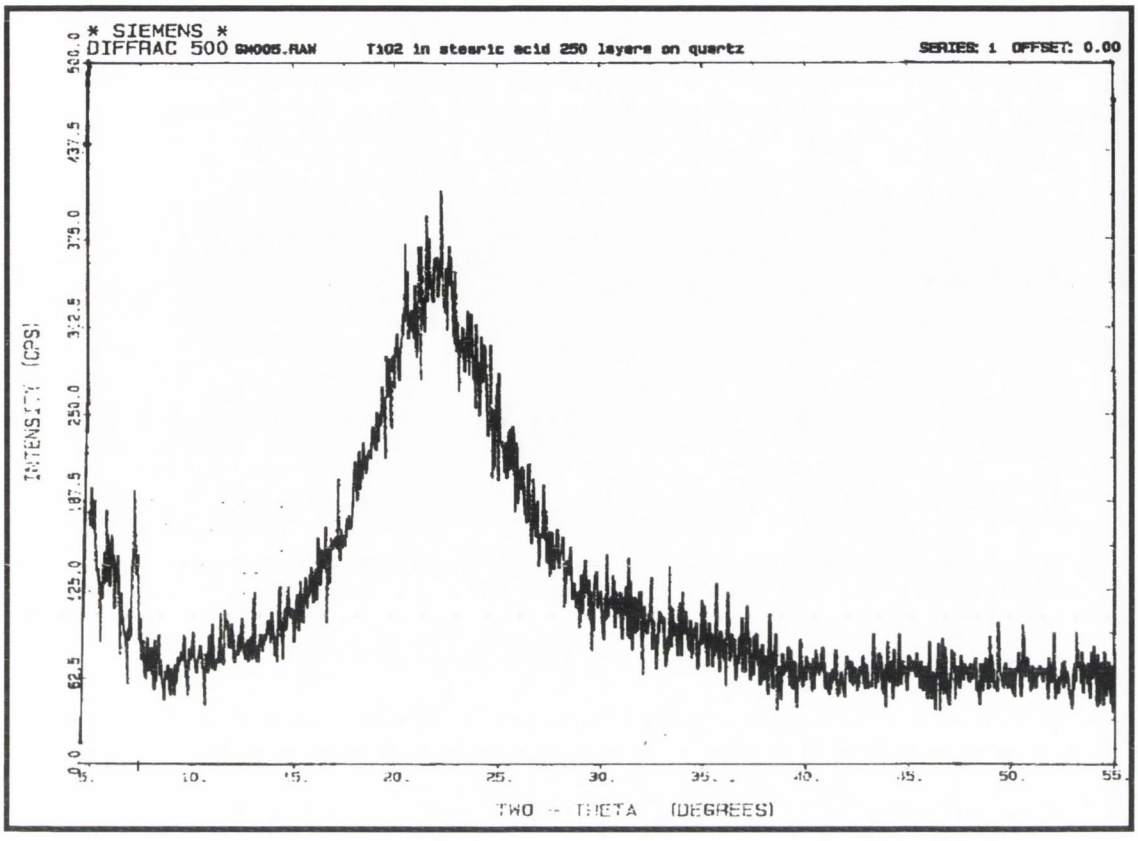

Figure 4.54: Wide angle X-Ray Diffraction Pattern recorded for a titanium stearate (Ti-St) multilayer film (250 layers).

In an effort to encourage crystallinity, LB films containing titanium stearate were deposited under an N_2 atmosphere and were immediately fired at 450°C for 30 min as previously outlined in section 3.1.2.

4.4.4 Diffraction studies on Nafion bound TiO_2

Similar structural investigations for TiO_2 precipitated within a Nafion membrane were performed again using powder X-Ray diffraction techniques. As described previously, this technique showed a marked absence of TiO_2 diffraction related to any crystalline TiO_x within the membrane. Figure 4.55 shows the WAXS pattern for recorded for a Nafion membrane containing TiO_2 at the surface. The two broad bands are due to Nafion[12].

[12] D.J. Vaughan, Dupont Innovation, 1973, 4, 10.

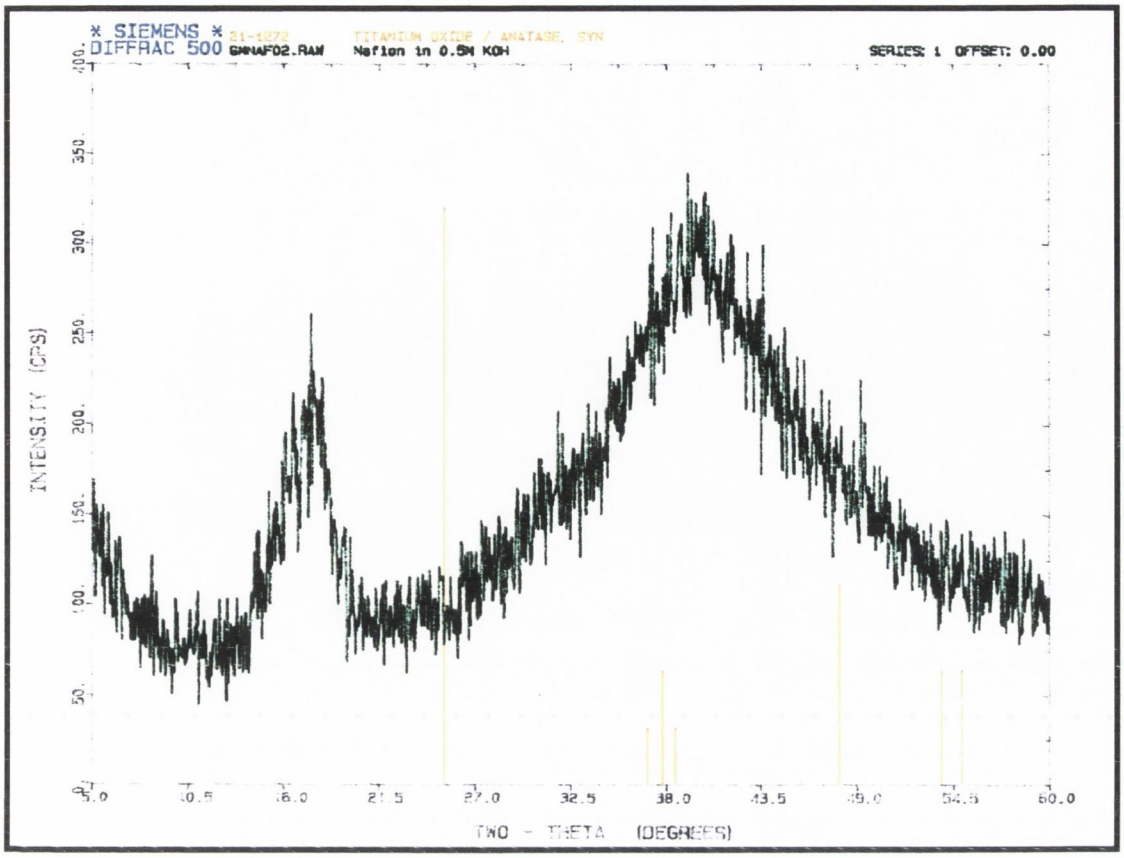

Figure 4.55: Wide angle X-Ray Diffraction Pattern recorded for TiO_2 precipitated in Nafion by forced hydrolysis using KOH.

Chapter 4: Section V: Scanning Electron Microscopy

4.5.1 Introduction

The incorporation of TiO_2 between the head groups of stearic acid LB films was examined using scanning electron microscopy (SEM) in conjunction with energy dispersive x-ray analysis (EDAX). Both techniques proved highly useful for investigating the morphology and presence of elemental deposits at the LB and Nafion surface.

4.5.2 LB films

I. Analysis of non-heat treated Ti-St films by SEM indicates that such films are thermodynamically unstable under high vaccumn. Figure 4.56 shows a typical SEM for 250 layers of titanium stearate formed at 15 mN/m using the LB technique (section 3.1.2). The surface of the film appears to have cracked through its length, when compared to the blank slide (L.H.S.), however this cracking was anticipated when one considers that the film is exposed to such a high vacuum of 10^{-7} torr.

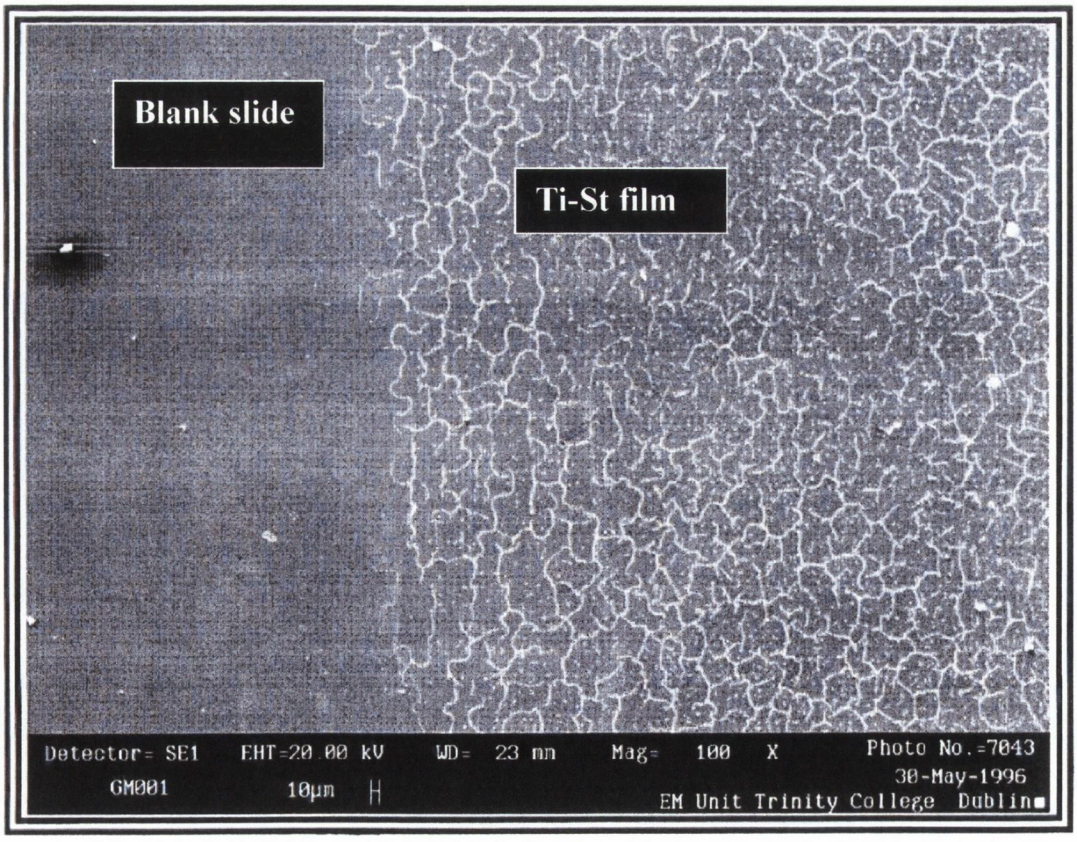

Figure 4.56: Scanning Electron Micrograph for 250 layers of Ti-St formed using the LB technique.

In an effort to increase TiO_2 stability as a durable photocatalyst the film was fired at 450°C for 2hrs. Figure 4.57 shows the corresponding EDAX for the same 250 layer LB film surface after subsequent firing of the film. The EDAX spectrum does indicate the presence of titanium, which is presumably present as TiO_2. Spot analysis of the same sample showed no change of intensity maxima indicating the same amount of TiO_2 formed throughout the fired film.

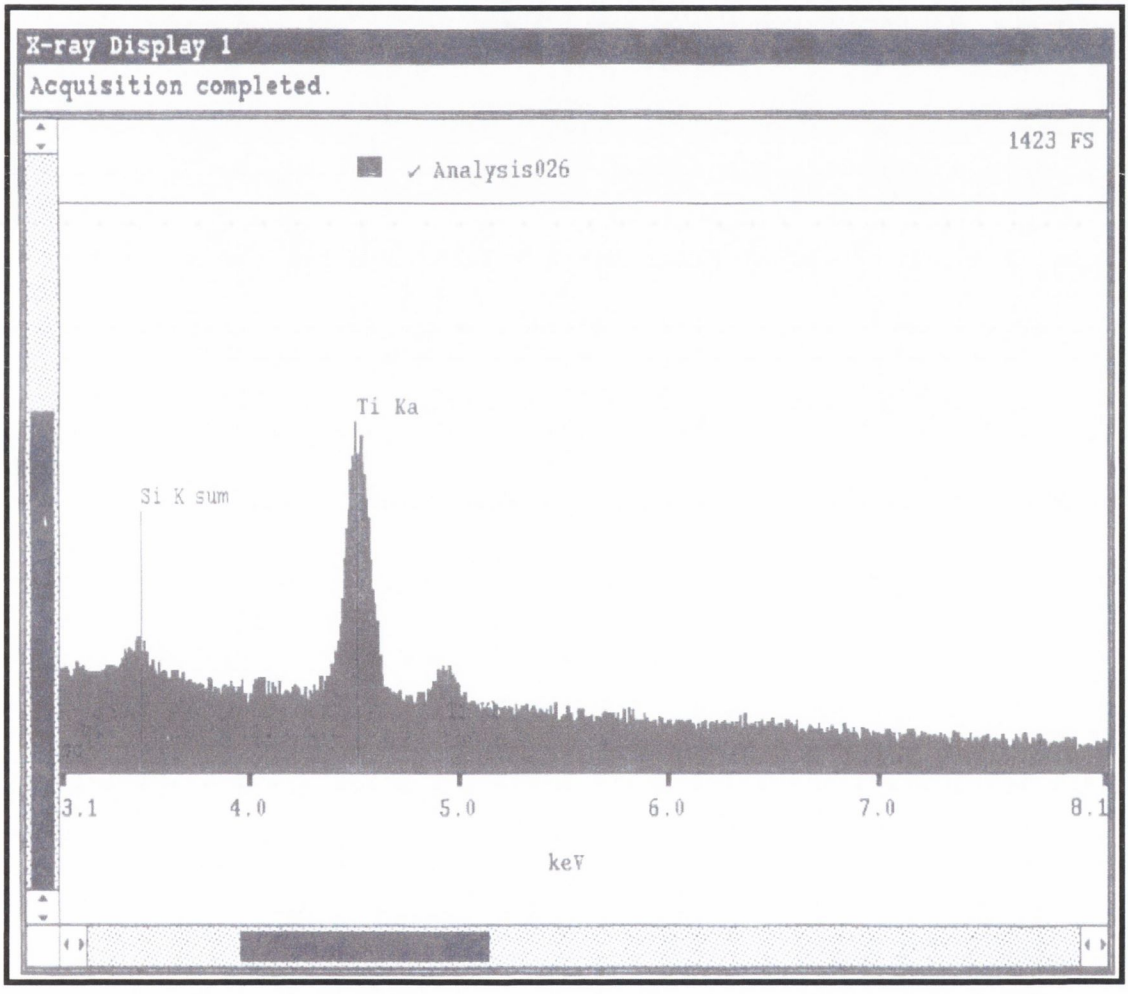

Figure 4.57: EDAX Spectrum for TiO_2 after firing a 250 layer Ti-St LB film on quartz for 2hrs.

4.5.3 TiO_2 incorporated in Nafion

Similar surface structural analysis using SEM and EDAX were carried out for Nafion samples containing TiO_2. Examination of a Nafion surface using SEM reveals a 'grain like' morphology as shown in figure 4.58. TiO_2 was previously precipitated in

Nafion using KOH in the concentration range 0.01-5 mol dm^{-3}. There is evidence for the presence of TiO_2 particles at the membrane surfaces, especially after Ti^{3+} base hydrolysis with 5 mol dm^{-3} KOH. However it was difficult to obtain a particle size for TiO_2 based on the fact that all SEM analysis was performed at low magnification to prevent decomposition of the sample. However TEM analysis from a section of the same film shows the presence of TiO_2 particles having a maximum diameter of 10 nm as shown in figure 4.69. Figure 4.59 shows the EDAX spectrum for the spot analysis of a Nafion membrane in which TiO_2 was previously precipitated using 0.5 mol dm^{-3} KOH.

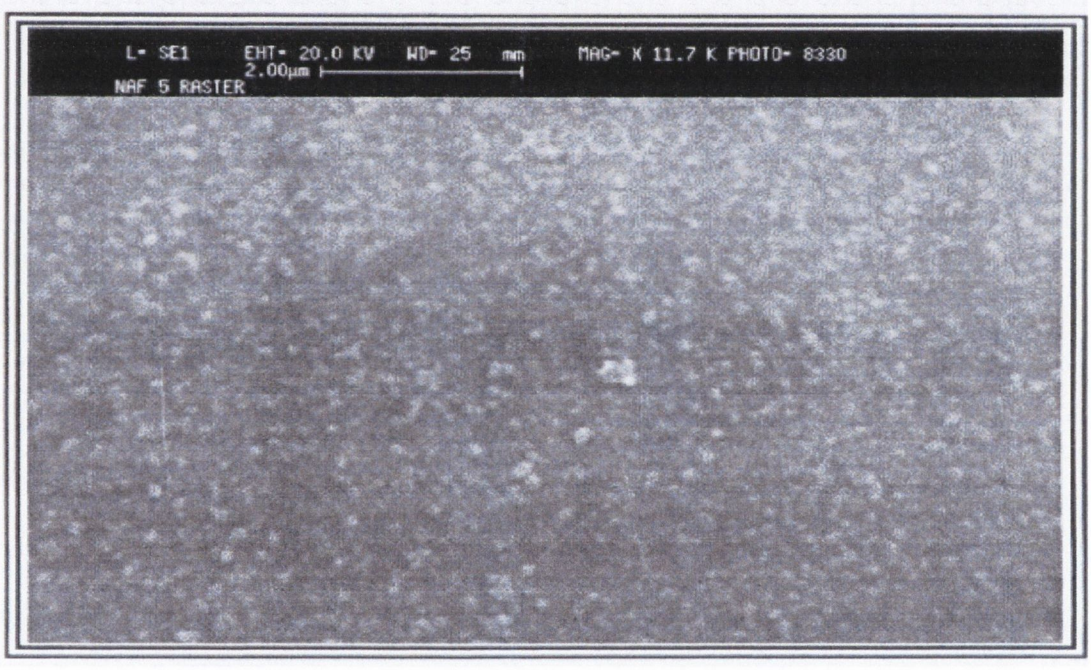

Figure 4.58: SEM for TiO_2 precipitated in Nafion using 5 mol dm^{-3} KOH.

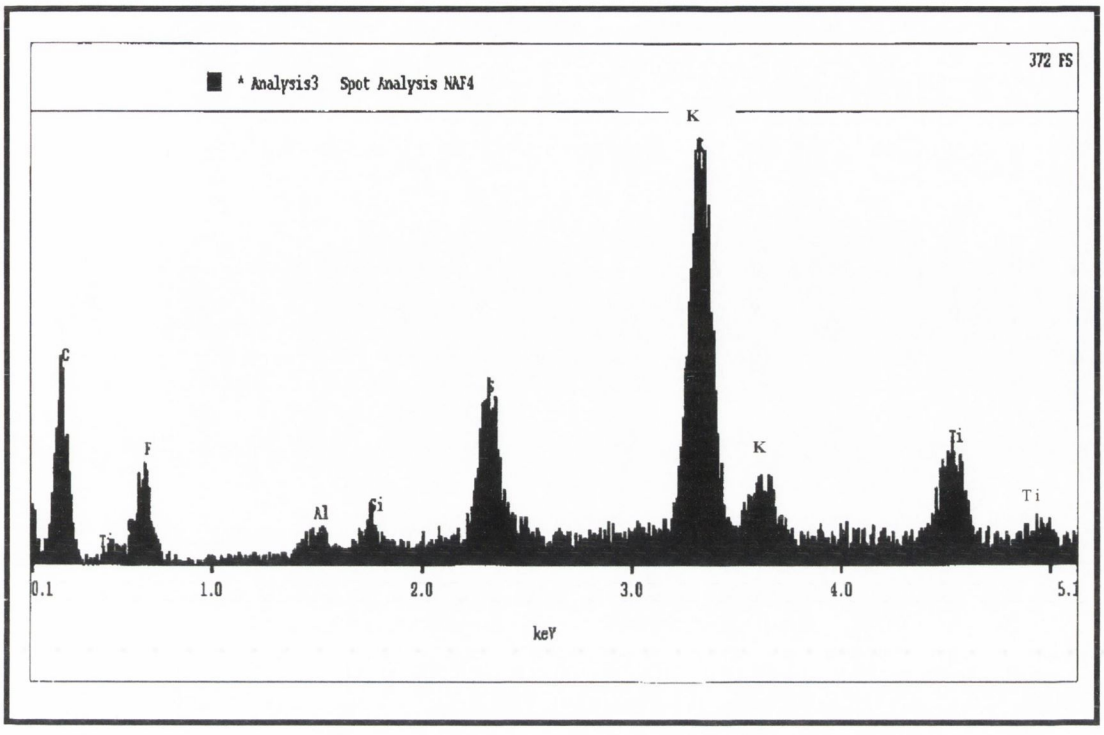

Figure 4.59: EDAX for TiO_2 incorporated in Nafion using 0.5 mol dm^{-3} KOH

Following spot analysis of the membrane there appeared to be no change of peak intensity at 4.5 keV for Ti, which may be attributed to the fact that the amount of TiO_2 at the surface of this particular membrane is constant over the entire membrane. The low count rate of 372 FS again signifies that there is very little TiO_2 present at the surface.

EDAX measurements were also obtained after exposing a Nafion membrane containing Ti^{3+} ions to 5 mol dm^{-3} KOH. This EDAX spectrum (figure 4.60) shows a considerable peak intensity associated with Ti at 4.5 keV (1009). There is a large difference in peak intensity associated with Ti, which is precipitated using two different OH^- concentrations, 0.5 and 5 mol dm^{-3} respectively.

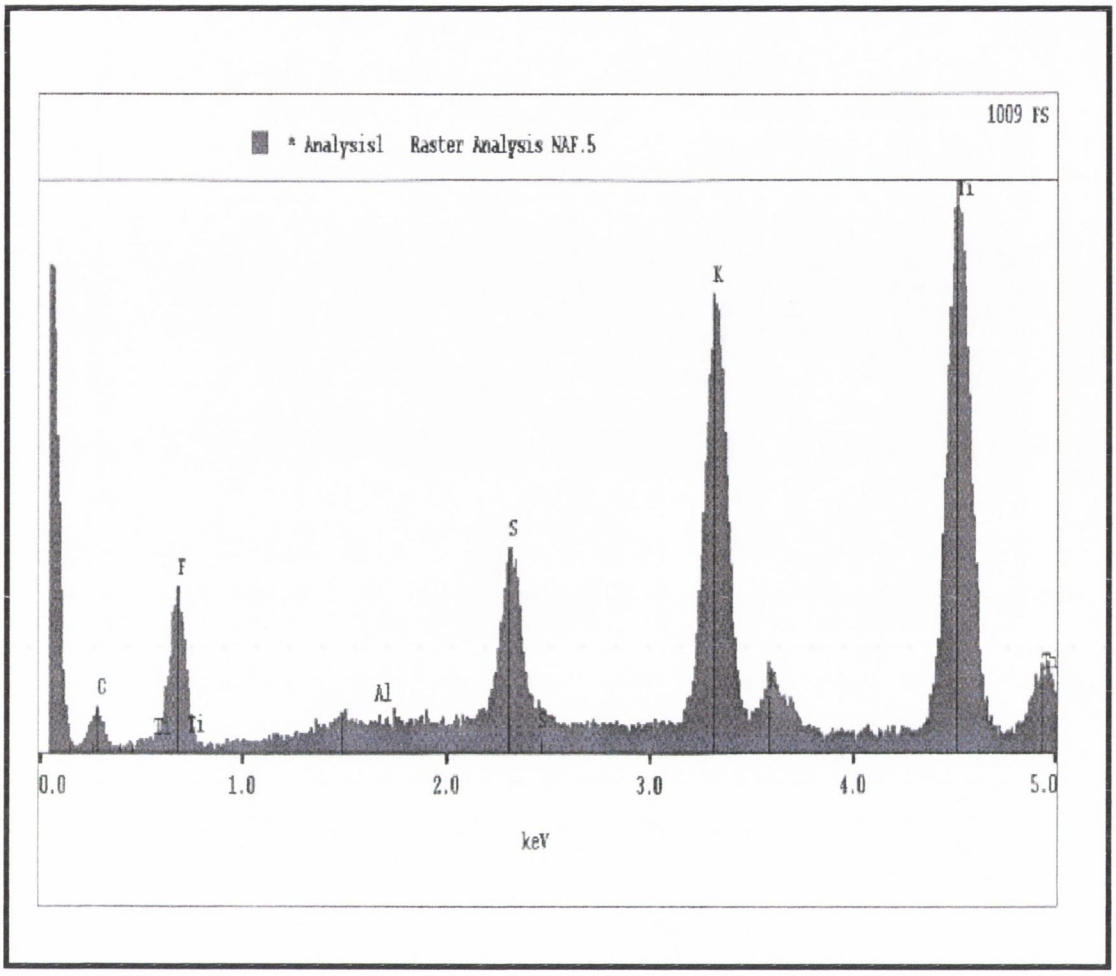

Figure 4.60: EDAX for TiO_2 incorporated in Nafion using 5 mol dm^{-3} KOH.

This apparent increase in intensity illustrates the effect of high KOH concentrations and its influence towards forming greater amounts of TiO_2 at the membrane surface.

Chapter 4: Section VI: Transmission Electron Microscopy

4.6.1 Introduction

The formation of TiO_2 particles within a Nafion matrix or by the LB film technique has been investigated using transmission electron microscopy. In conjunction with TEM studies, high-energy (100kV) electron diffraction was also performed over different sections of each material. TEM and ED results are also reported for Cd-stearate LB films.

4.6.2 LB films.

A Transmission Electron Micrograph for a fired LB film containing TiO_2 is shown in figure 4.61. A uniform distribution of dense TiO_2 (black particles) is observed throughout the entire length of the membrane. It is possible to estimate the maximum diameter of these particles [scale: 1mm =7.15nm]. TiO_2 particles were estimated to have a maximum diameter of ca. 7nm = 70 Å for a 98 layer titanium stearate fired film.

In conjunction with TEM studies, ED studies of fired LB films containing titanium stearate were carried out in order to examine the degree of particle crystallinity in the sample. If the samples under consideration are crystalline, electron diffraction will produce a series of rings. By estimation of the radius R of the rings, it is possible to deduce the lattice spacings d for the sample concerned knowing the camera length L and using the following relationship:

$$R\,d = \lambda L \qquad [4.6.1]$$

Table 4.13 shows the electron diffraction data for a fired sample of titanium stearate (98 layers) formed at 15 mN/m using the LB technique. The data set was estimated using the above equation and determining the radius of the diffraction rings from the electron diffraction patterns shown in figure 4.62.

2R	R	d^A	d^1	d^2	d^3
34.0	17.0	0.348	0.351	0.351	0.324
-	-	-	-	0.290	-
51.0	25.5	0.232	0.238	-	0.249
64.5	32.3	0.184	0.189	-	
72.5	36.3	0.163	0.166	-	0.169
82.5	41.3	0.142	0.148	-	-
		Absent		0.347	

Table 4.13: Electron diffraction data for a fired LB film of titanium stearate (98 layers) with some possible crystalline fits d^1, d^2 and d^3

*Joint Committee of Powder X-Ray Scattering (JCPDS)

d^1- TiO_2 (Anatase) JCPDS 21-1272

d^2- TiO_2 (Brookite) JCPDS 29-1360

d^3- TiO_2 (Rutile) JCPDS 21-1276

d^A- Pattern recorded for a fired LB film of titanium stearate

It appears that d^1, the data set for TiO_2 Anatase; JCPDS 21-1272 best fits the experimental data d^A. Therefore it is possible to assign a crystal structure of anatase to TiO_2 formed by firing LB films containing titanium stearate.

As stated previously, TEM and ED studies were performed on LB samples of cadmium stearate. Figure 4.63 shows the corresponding TEM for 130 layers of Cd-Stearate formed on quartz at a surface pressure of 20 mN/m. This micrograph was included to illustrate the stability of Cd-stearate LB films with respect to oxidation. The corresponding electron diffraction pattern for this sample is shown in figure 4.64. The clear diffraction pattern consisting of a number of distinct spots is direct evidence that crystalline material does exist. Measuring the radius (mm) of each spot from the centre of the diffraction pattern allows for the calculation of d-spacings as outlined previously. Table 4.14 shows this data set for the diffraction pattern shown in figure 4.64.

2R	R	d	2θ	d^1	d^2
14	7	0.422	21.03	21.60	21.55
24	12	0.246	36.49	36.28	36.24
32	16	0.185	49.20	47.00	-
42	21	0.140	66.76	-	-

Table 4.14: Electron diffraction data and corresponding 2θ values for cadmium stearate (130 layers).
d^1 Stearic acid, JCPDS 9-618.
d^2 Stearic acid, JCPDS 9-622.

4.6.3 TiO_2 incorporated in Nafion

For TEM analysis, Nafion samples containing TiO_2 as previously described in section 3.2.2) were encapsulated in a supporting resin, sectioned (microtomed) and analysed. Figures 4.65-4.69 show the corresponding TEMs for TiO_2 incorporated into five different Nafion strips following base hydrolysis with KOH 0.01, 0.1, 0.25, 0.5 and 5 mol dm^{-3} respectively. Micrographs 4.67-4.69 show the effectiveness of this particular technique in producing a dense distribution of well-defined nanoparticles through each membrane material. From each scale (1mm = 5 nm.) it is possible to estimate a maximum particle diameter for TiO_2 within each membrane. Larger TiO_2 nanoparticles were precipitated using higher concentrations of KOH. From TEM analysis it is estimated that TiO_2 particles of 10 nm average diameter were precipitated in Nafion using 5 mol dm^{-3} KOH figure 4.69. Reducing the KOH concentration results in a decrease in particle size, membranes containing particles having diameters below 10 nm are observed.

In conjunction with TEM studies, high-energy (100 kV) electron diffraction was also performed over a section of a Nafion sample. Unfortunately these results proved less fruitful in that the diffracted intensity was too broad to be measured accurately indicating a lack of TiO_2 crystallinity within the membrane. It is also possible that perhaps there was no constructive diffraction at all in that the material precipitated is amorphous.

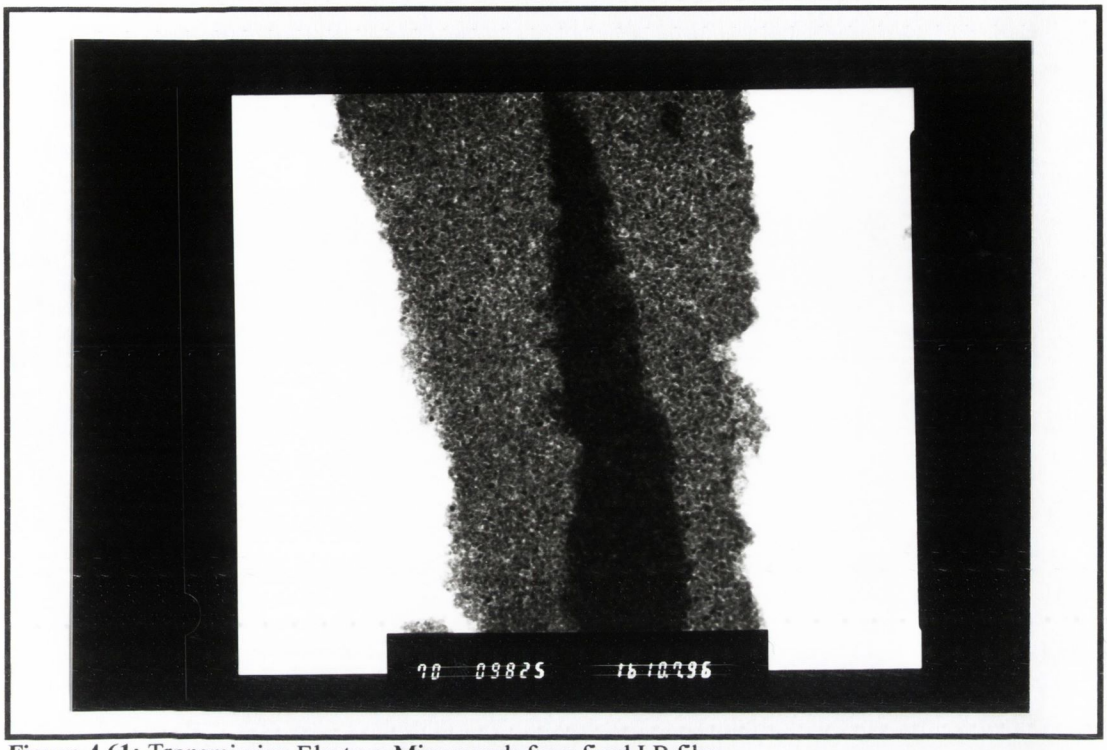

Figure 4.61: Transmission Electron Micrograph for a fired LB film (98 layers) of Ti-St deposited on quartz.

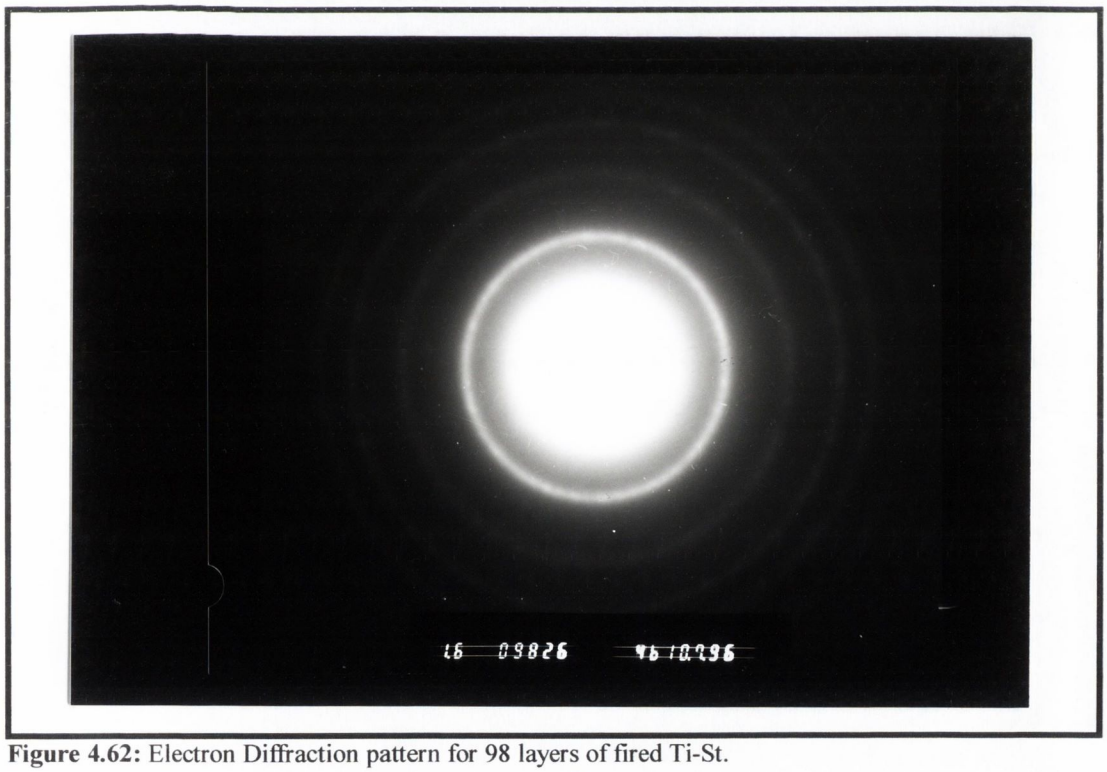

Figure 4.62: Electron Diffraction pattern for 98 layers of fired Ti-St. Camera length = 1.6 m $\lambda_{el.}$ = 0.0037 nm.

Figure 4.63: Transmission Electron Micrograph for Cd-St (130 layers) deposited on quartz.

Figure 4.64: Electron diffraction pattern for Cd-St (130 layers) deposited on Quartz.
Camera length = 0.8 m $\lambda_{el.}$ = 0.0037 nm

Figure 4.65: Transmission Electron Micrograph for TiO_2 precipitated in Nafion using 0.01 mol dm^{-3} KOH.Magnification = 100,000; Scale 1mm ≡ 5nm.

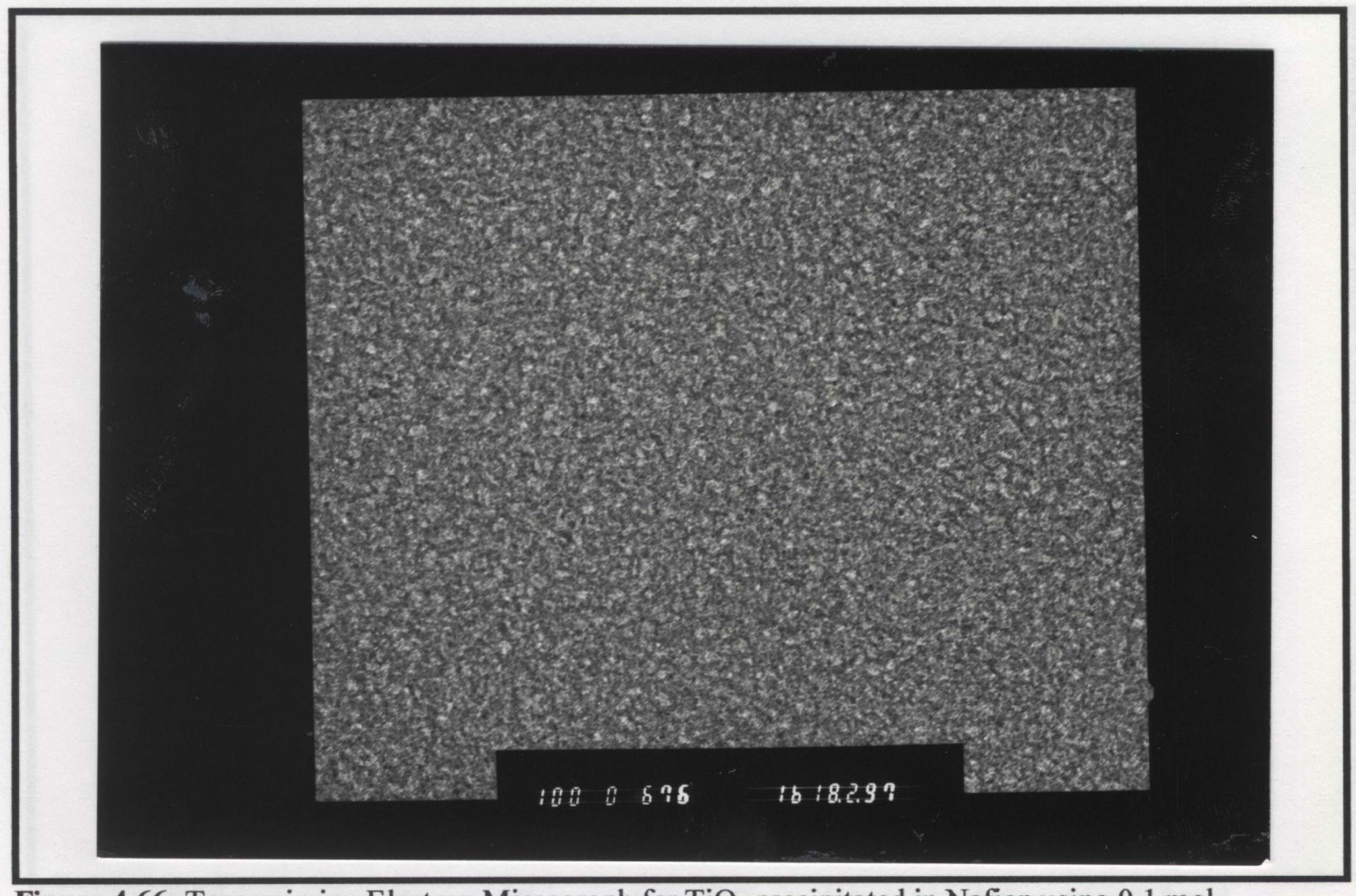

Figure 4.66: Transmission Electron Micrograph for TiO_2 precipitated in Nafion using 0.1 mol dm^{-3} KOH. Magnification = 100,000; Scale 1mm ≡ 5nm.

Figure 4.67: Transmission Electron Micrograph for TiO_2 precipitated in Nafion using 0.25 mol dm^{-3} KOH.Magnification = 100,000; Scale 1mm ≡ 5nm.

Figure 4.68: Transmission Electron Micrograph for TiO_2 precipitated in Nafion using 0.5 mol dm^{-3} KOH. Magnification = 100,000; Scale 1mm ≡ 5nm.

Figure 4.69: Transmission Electron Micrograph for TiO_2 precipitated in Nafion using 5 mol dm^{-3} KOH.Magnification = 100,000; Scale 1mm ≡ 5nm.

Chapter 4: Section VII: Atomic Force Microscopy

4.7.1 Introduction

AFM images were obtained for LB films of titanium stearate and fired titanium stearate. All LB film-AFM images were recorded for films deposited on either quartz or glass slides, previously coated with ferric stearate, and images were obtained for LB films of titanium stearate up to a maximum of 20 layers. Different scan areas were used for probing each sample from a minimum scan area of 7×7 μm up to a maximum scan area of 70×70 μm.

4.7.2 AFM imaging of glass substrate

AFM imaging was carried out at room temperature under normal atmospheric conditions. Figure 4.70 shows the AFM profile images for ferric stearate deposited on a glass slide over a scan area of 70x70 μm. This scan shows a uniform surface prior to LB deposition. It is almost impossible to fully prevent contamination of the sample during measurement. Sample contamination is shown in the cross section profile (figure 4.71) where dust particles cause cantilever z-deflection of approximately 17 nm. Nevertheless, the corresponding topographic cross section (70x70 μm) profile, figure 4.71 shows that the substrates are fairly even, having a z-height difference of about 4 nm.

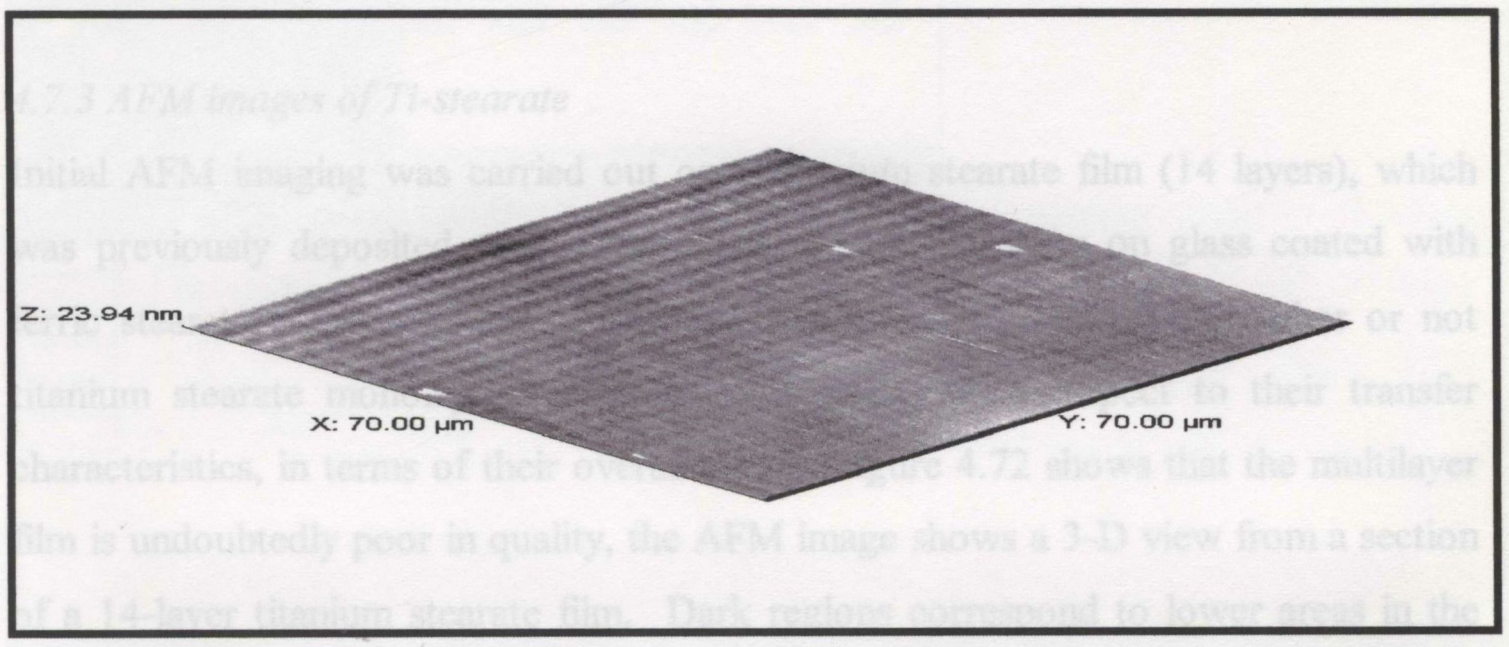

Figure 4.70: Low-resolution AFM image of the ferric stearate coated glass substrates 70 x 70 μm^2

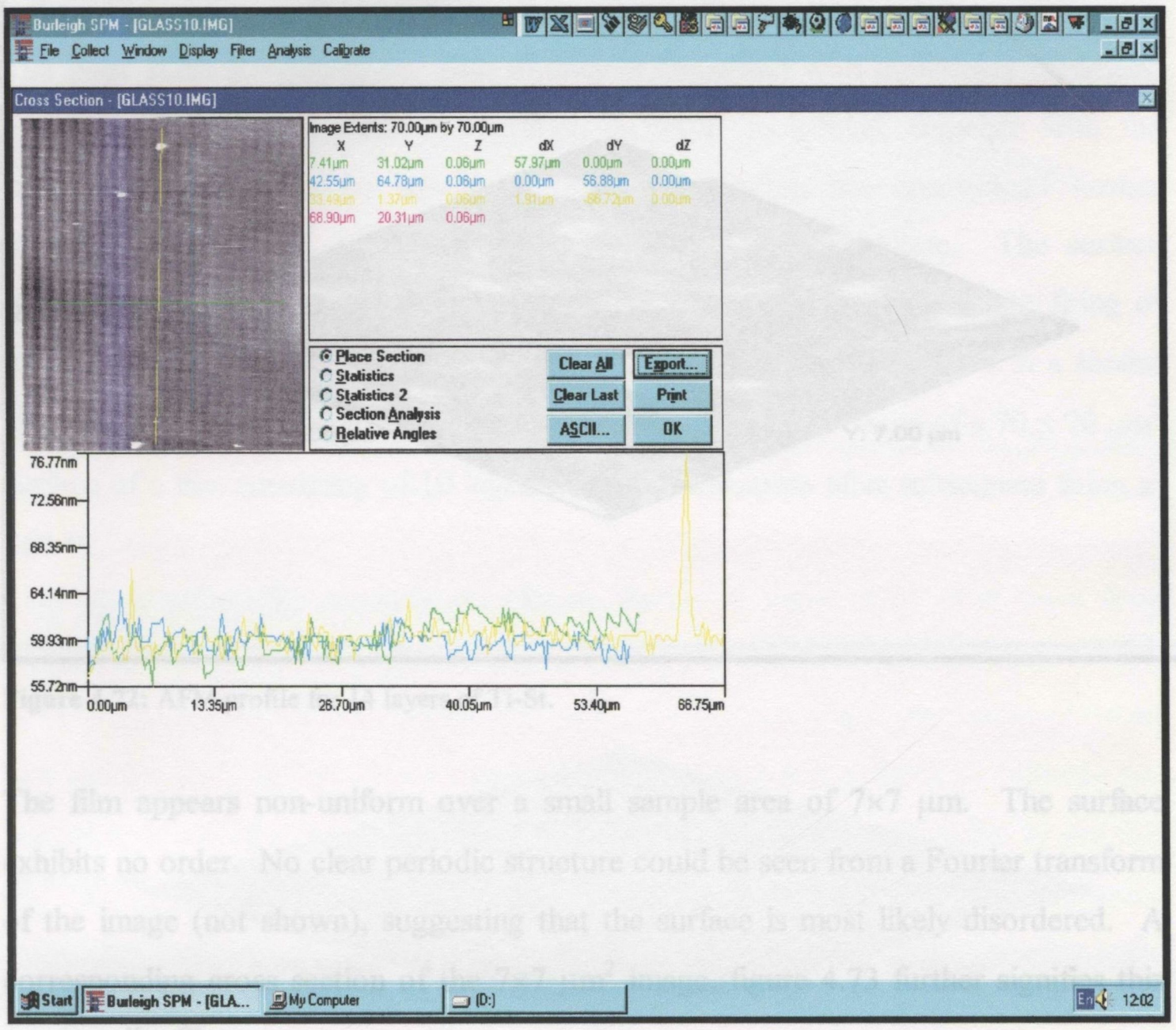

Figure 4.71: Vertical height distance profile (cross section) for a low resolution AFM image of glass coated with ferric stearate.

4.7.3 AFM images of Ti-stearate

Initial AFM imaging was carried out on a titanium stearate film (14 layers), which was previously deposited at a surface pressure of 15 mN/m on glass coated with ferric stearate. The purpose of this experiment was to determine whether or not titanium stearate monolayers were of good quality with respect to their transfer characteristics, in terms of their overall order. Figure 4.72 shows that the multilayer film is undoubtedly poor in quality, the AFM image shows a 3-D view from a section of a 14-layer titanium stearate film. Dark regions correspond to lower areas in the image.

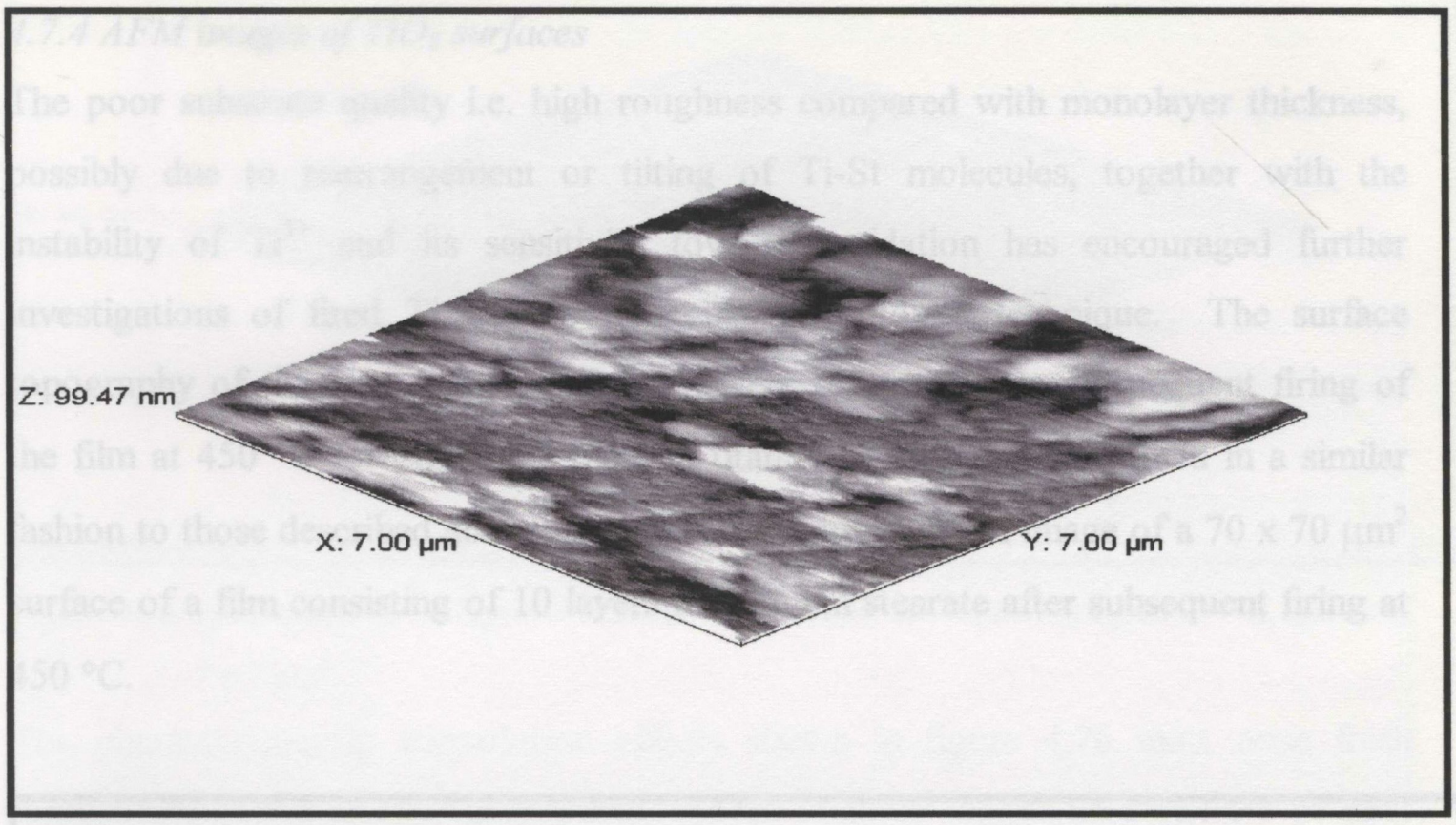

Figure 4.72: AFM profile for 14 layers of Ti-St.

The film appears non-uniform over a small sample area of 7×7 µm. The surface exhibits no order. No clear periodic structure could be seen from a Fourier transform of the image (not shown), suggesting that the surface is most likely disordered. A corresponding cross section of the 7×7 μm^2 image, figure 4.73 further signifies this poor quality film.

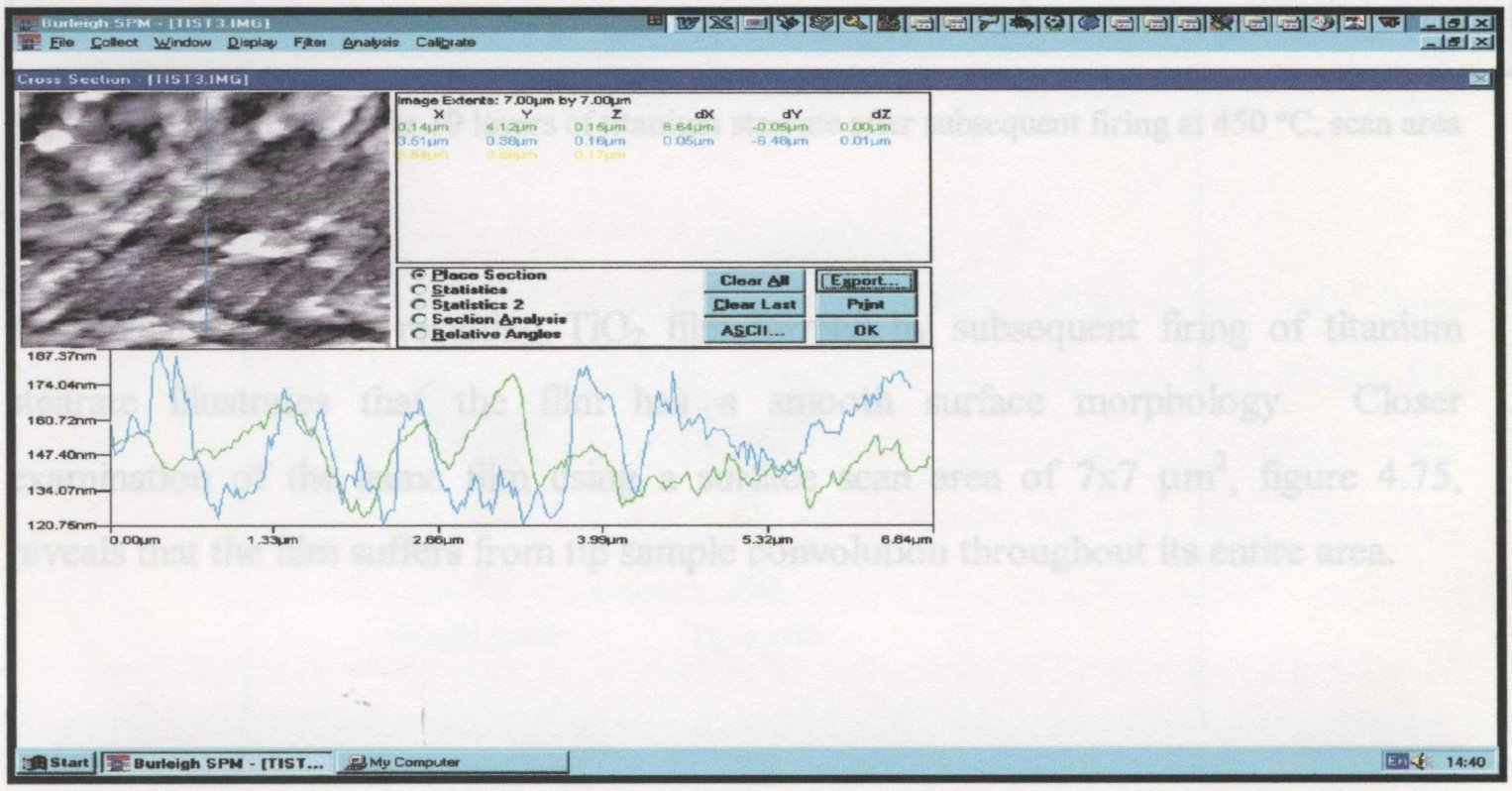

Figure 4.73: Vertical height distance profile (cross section) for a low resolution AFM image of Ti-St (14 layers).

4.7.4 AFM images of TiO_2 surfaces

The poor substrate quality i.e. high roughness compared with monolayer thickness, possibly due to rearrangement or tilting of Ti-St molecules, together with the instability of Ti^{3+} and its sensitivity towards oxidation has encouraged further investigations of fired Ti-stearate films using the AFM technique. The surface topography of titanium stearate LB films were examined after subsequent firing of the film at 450 °C for 2hrs. LB films of titanium stearate were formed in a similar fashion to those described above. Figure 4.74 shows an AFM image of a 70 x 70 μm^2 surface of a film consisting of 10 layers of titanium stearate after subsequent firing at 450 °C.

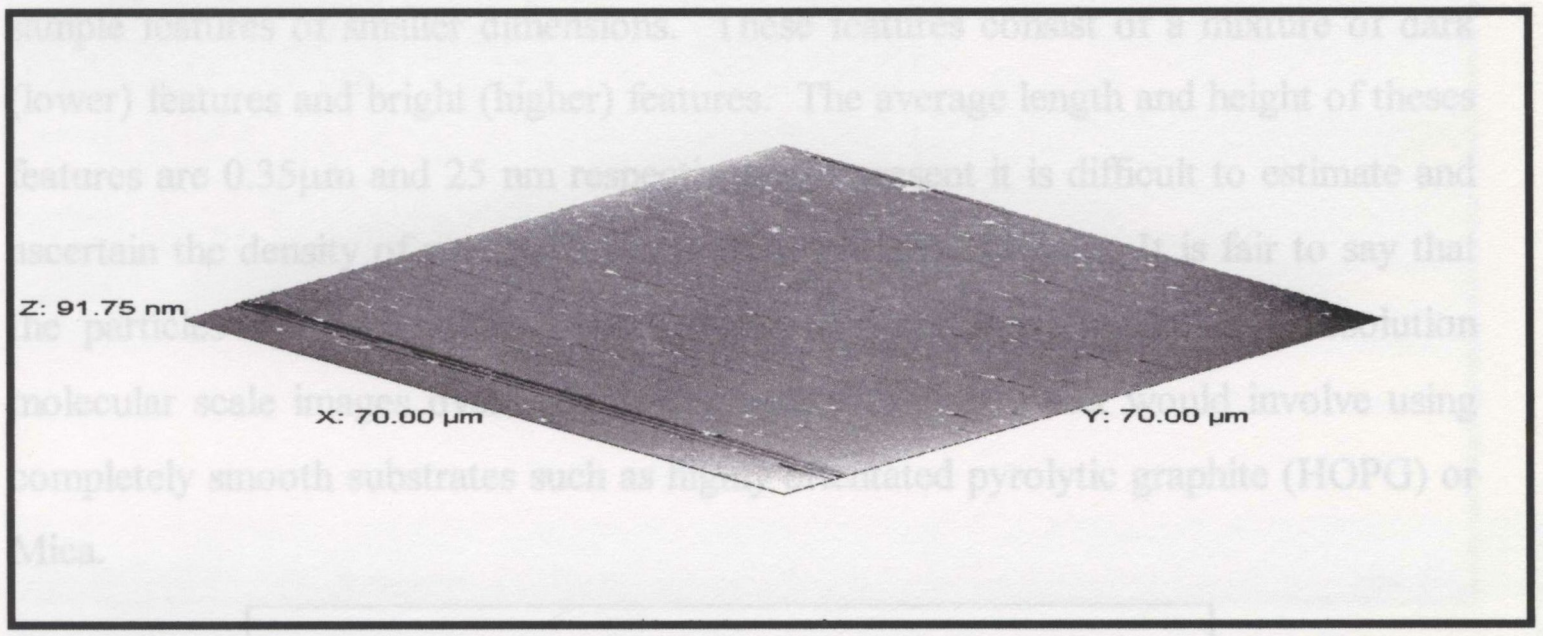

Figure 4.74: AFM image for 10 layers of titanium stearate after subsequent firing at 450 °C, scan area 70 x 70 μm^2.

AFM analysis of the resulting TiO_2 film formed by subsequent firing of titanium stearate illustrates that the film has a smooth surface morphology. Closer examination of the same film using a surface scan area of 7x7 μm^2, figure 4.75, reveals that the film suffers from tip sample convolution throughout its entire area.

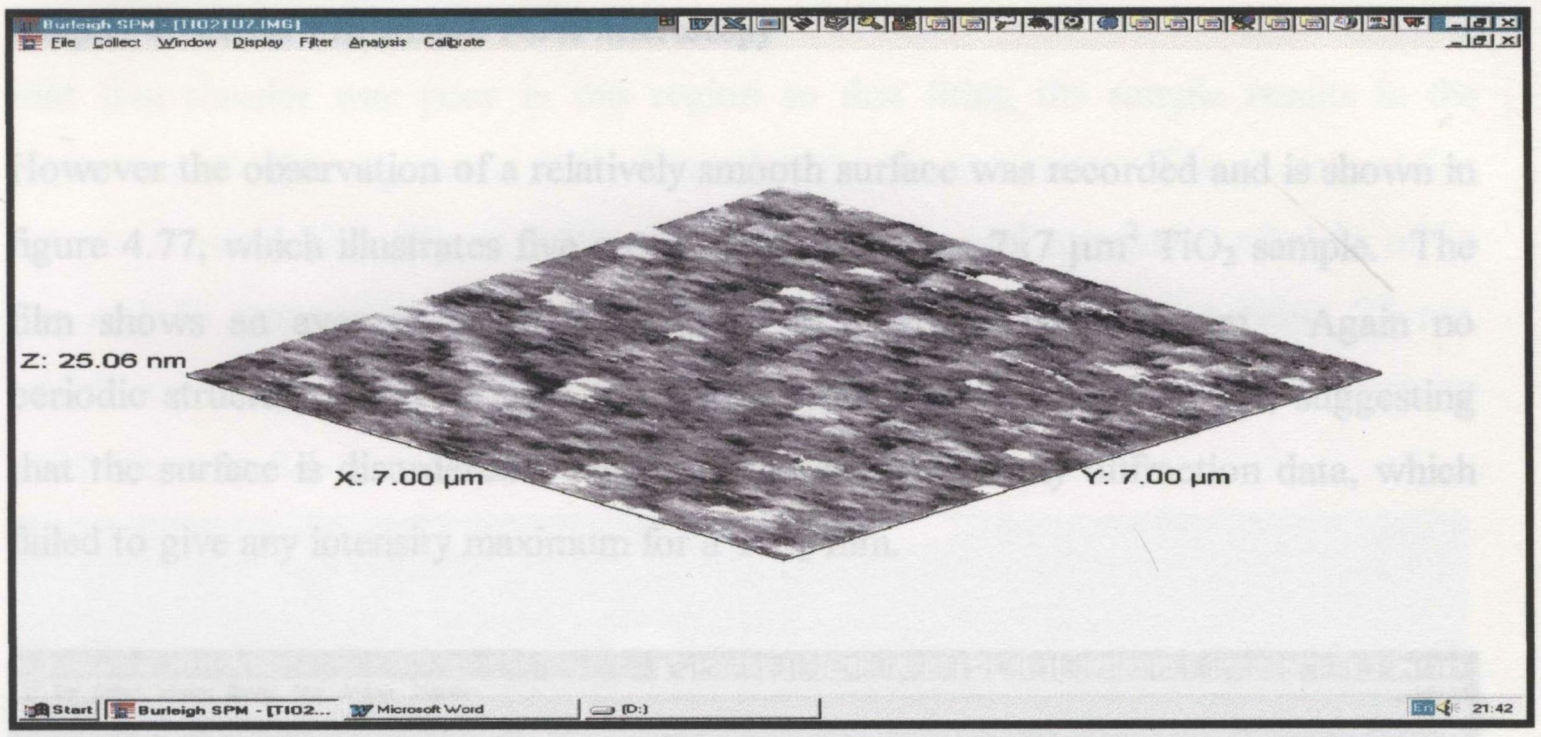

Figure 4.75: AFM image for 10 layers of titanium stearate after subsequent firing at 450 °C, scan area $7 \times 7\ \mu m^2$

The characteristic tip convolution effects shown in figure 4.76 must arise from sample features of smaller dimensions. These features consist of a mixture of dark (lower) features and bright (higher) features. The average length and height of theses features are 0.35µm and 25 nm respectively. At present it is difficult to estimate and ascertain the density of particles or defects in the TiO_2 surface. It is fair to say that the particles are below 0.35 µm, clearly one would need to get high resolution molecular scale images over larger scan areas. This in effect would involve using completely smooth substrates such as highly orientated pyrolytic graphite (HOPG) or Mica.

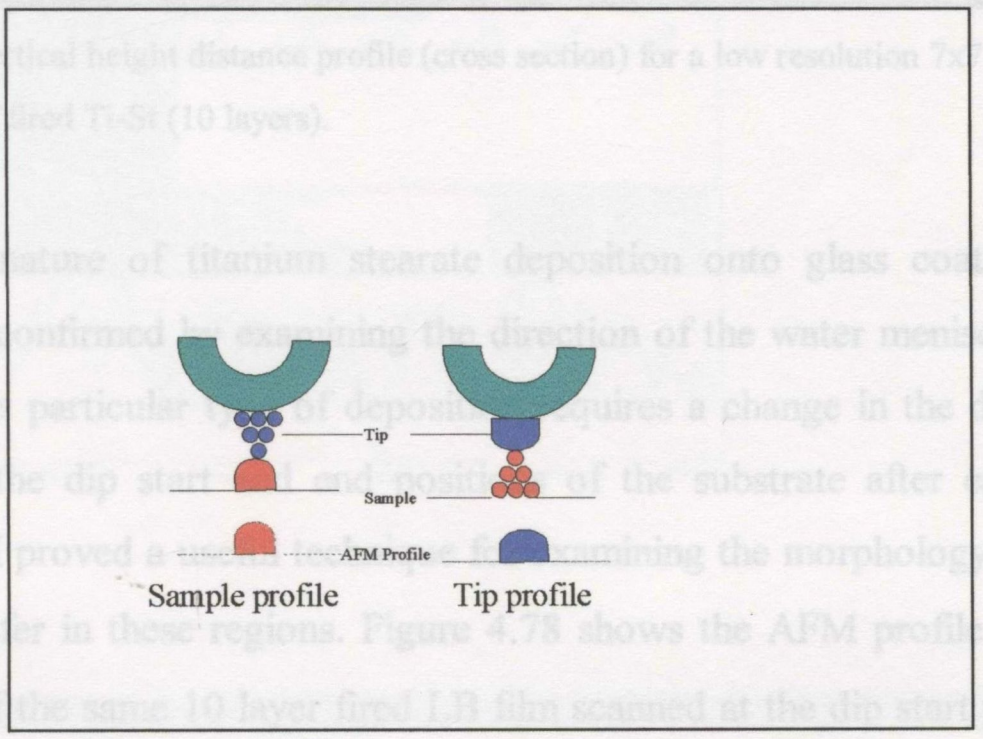

Figure 4.76: Tip sample convolution.

However the observation of a relatively smooth surface was recorded and is shown in figure 4.77, which illustrates five cross sections along a 7×7 μm^2 TiO_2 sample. The film shows an average surface roughness of approximately 5.5 nm. Again no periodic structure could be seen from a Fourier transform of the image, suggesting that the surface is disordered. This is consistent with X-ray diffraction data, which failed to give any intensity maximum for a TiO_2 film.

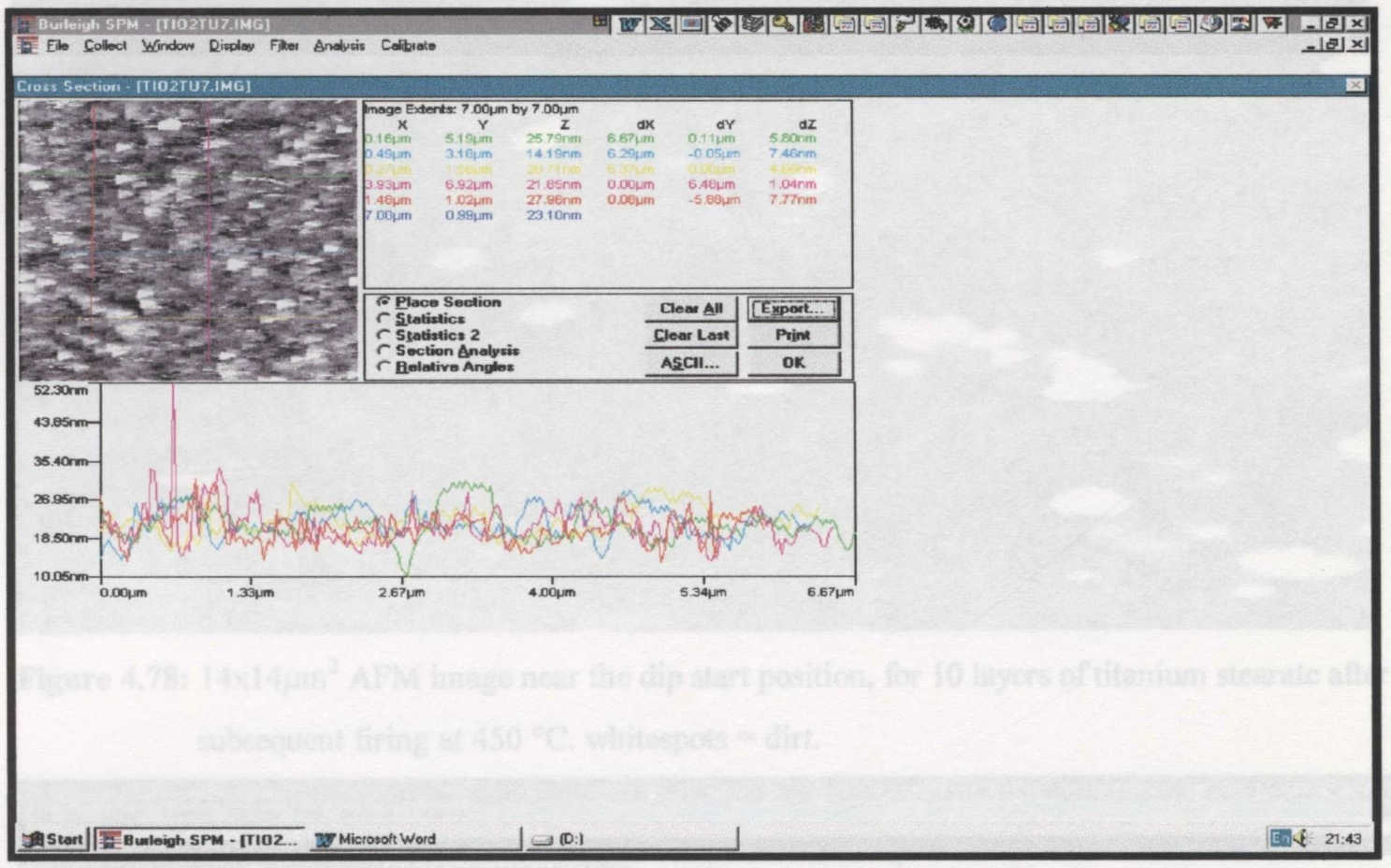

Figure 4.77: Vertical height distance profile (cross section) for a low resolution 7x7 µm AFM image of fired Ti-St (10 layers).

The Y-type nature of titanium stearate deposition onto glass coated with ferric stearate was confirmed by examining the direction of the water meniscus during film transfer. This particular type of deposition requires a change in the direction of the meniscus at the dip start and end positions of the substrate after each deposition stroke. AFM proved a useful technique for examining the morphology and quality of the film transfer in these regions. Figure 4.78 shows the AFM profile for a 14 × 14 μm^2 image of the same 10 layer fired LB film scanned at the dip start position. 'The web-like' nature of this film might suggest

that film transfer was poor in this region so that firing the sample results in the formation of inhomogeneous TiO_2 formation on the substrate. The corresponding sample cross section (figure 4.79) shows a minimum and maximum z-height of 36 nm and 63 nm respectively. The maximum difference in z-height being 27 nm, which correlates with a thickness of 10 layers of titanium stearate. The film contains voids between 0.5-1μm in diameter.

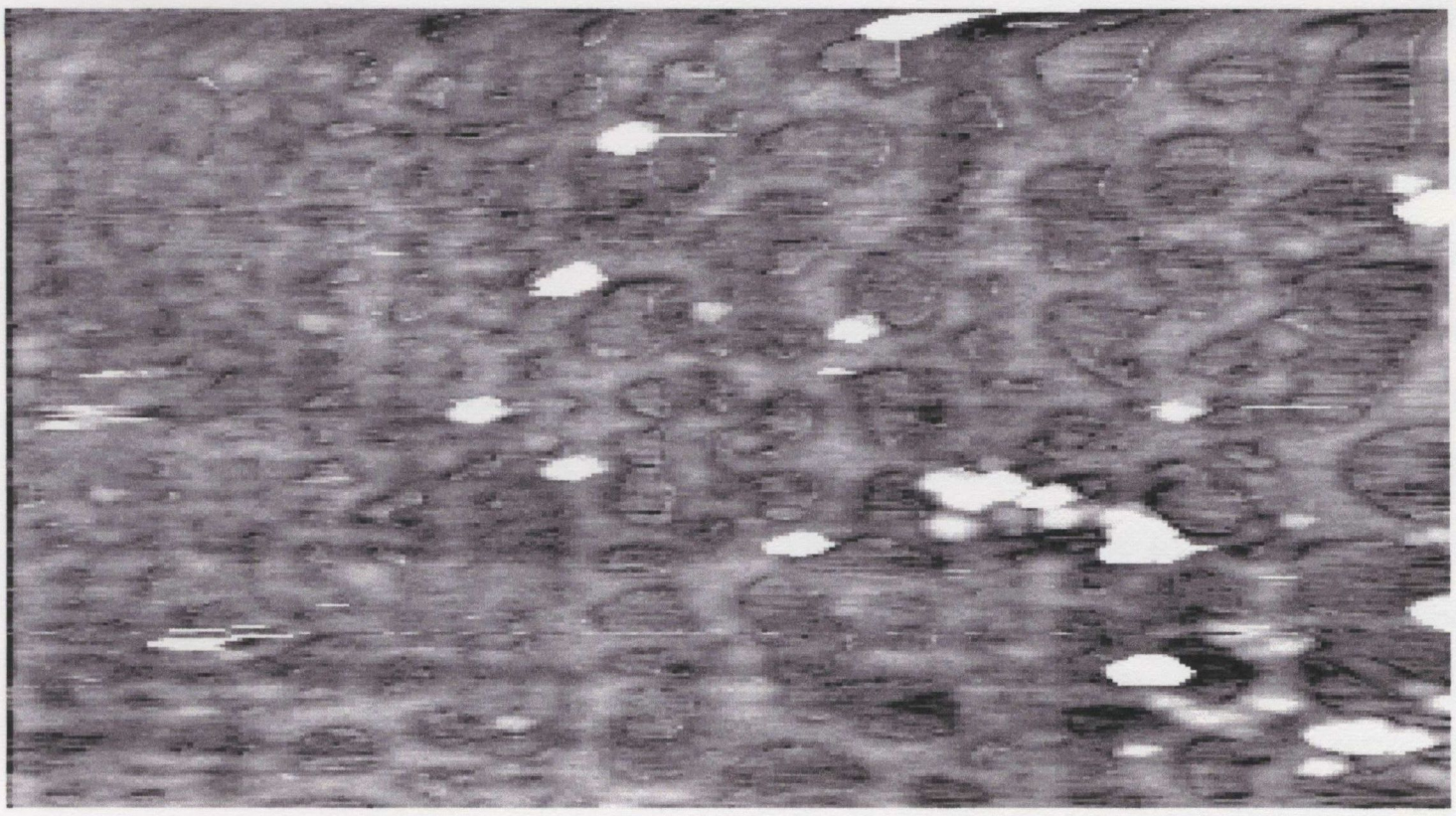

Figure 4.78: 14x14μm^2 AFM image near the dip start position, for 10 layers of titanium stearate after subsequent firing at 450 °C. whitespots = dirt.

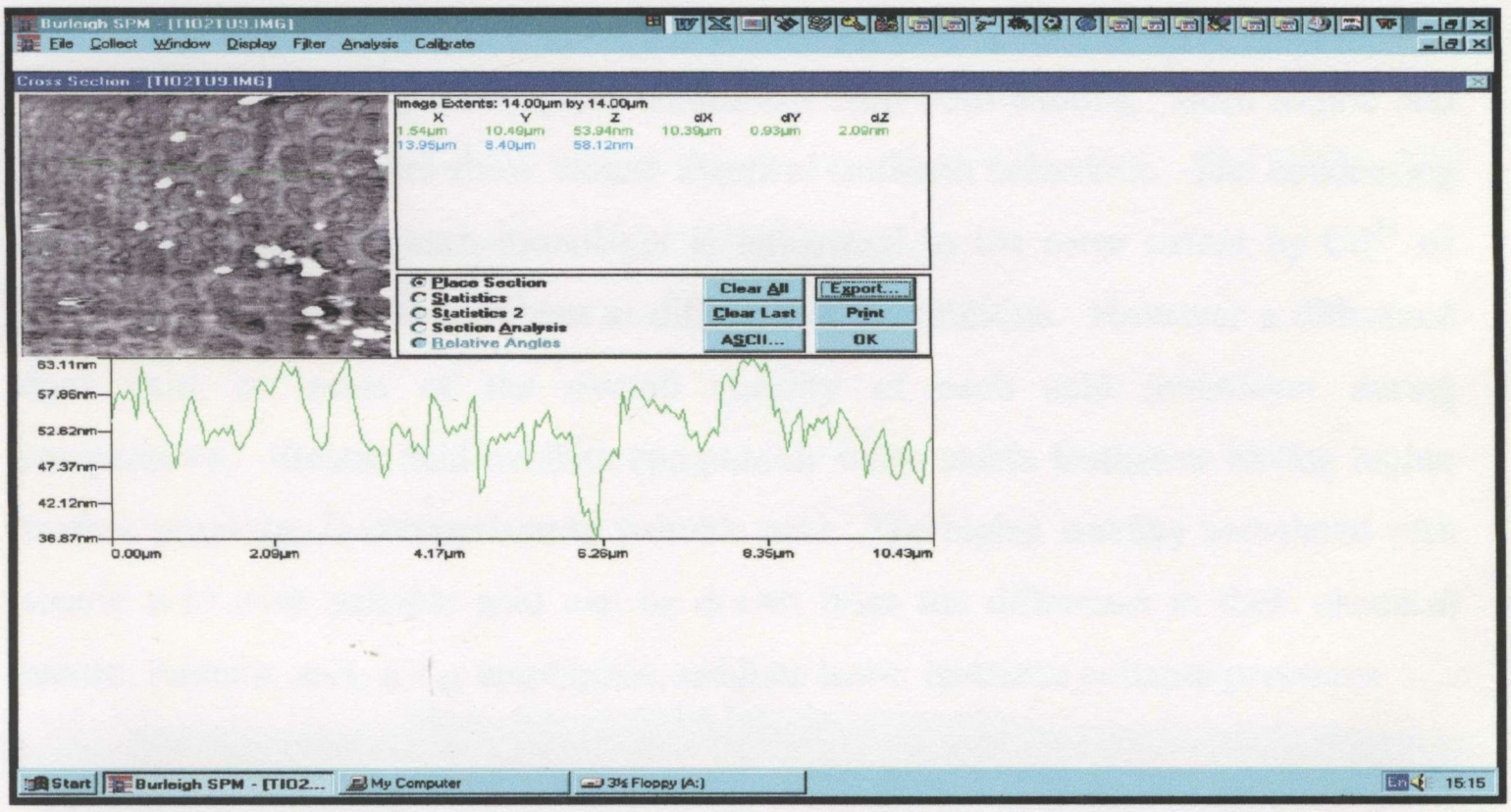

Figure 4.79: Vertical height distance profile (cross section) for a low resolution 7x7 μm AFM image of fired Ti-St (10 layers).

Chapter 5

Discussion

Chapter 5, Section I: Langmuir-Blodgett films

5.1.1 LB studies.

As has been previously reported, (section 2.3.6) both nano-sized CdS and TiO_2 particles can be precipitated within LB films of amphiphilic material. This has been made possible using essentially three different colloid chemical approaches as outlined in section 2.3.6. The incorporation of semiconductor nanoparticles within an LB matrix requires prior investigation of LB monolayer film behaviour as a prerequisite to monolayer deposition.

Pressure area isotherms were recorded for stearic, palmitic and oleic acid on a pure water subphase as outlined previously. The reported transitions together with the extrapolated areas per molecule for a fully compressed monolayer 22-25$Å^2$ are in good agreement with those values reported previously[1,2]. Stearic and palmitic acid exhibit a pressure-area isotherm representative of a condensed film, while oleic acid displays a much more expanded isotherm. The smooth increase of surface pressure with decreasing area is attributed to the steric hindrance associated with successive oleic hydrocarbon molecules during compression, arising from double bond character and angle of orientation of the monolayer to the subphase.

5.1.2 Influence of divalent cations

Stearic and palmitic acid monolayers at pH 5.5 and temperature 293K in the presence of Cd^{2+} and Zn^{2+} form carboxylate complexes with both cations. Both stearic and palmitic acid monolayers show almost identical isotherm behaviour. The condensing effect experienced by each monolayer is influenced to the same extent by Cd^{2+} or Zn^{2+} ions present in the subphase at different concentrations. However a difference does exist in terms of the overall stability of each acid monolayer during compression. Stearic acid exhibits comparably more stable isotherms having higher surface pressures in comparison to palmitic acid. The higher stability associated with stearic acid over palmitic acid can be drawn from the difference in their chemical nature. Palmitic acid, a C_{16} amphiphile, exhibits lower isotherm collapse pressures

[1] D.J.M. Lindén, J.P.K. Peltonen, J.B. Rosenholm, Langmuir 1994, 10, 1592-1595.

Compared to stearic acid C_{18} resulting from its lower hydrophobicity and ability to dissolve in the subphase.

The increase of divalent ion concentration results in a decrease in apparent monolayer molecular area. Stearic and palmitic acid both show a reduction in the number of isotherm transitional phases during compression with a highly condensed solid type isotherm predominating at high divalent ion concentrations. The condensing effect for a particular concentration of each divalent cation towards both stearic and palmitic acid monolayers is noticeably different. It appears that Cd^{2+} ions at all concentrations promote to a larger extent the liquid condensed-solid (LC-S) regions of the isotherm for both acids compared to a similar system containing Zn^{2+} ions. As already outlined the chemistries of Cd^{2+} and Zn^{2+} are very similar, however the hydroxide $Cd(OH)_2$ is more basic than $Zn(OH)_2$ and this gives $Cd(OH)_2$ greater electropositive character for interaction with carboxylic head groups. It has been previously reported[14] that successive addition of small amounts of HCl into a subphase of $1x10^{-3}$ mol dm^3 Zn^{2+} supporting a stearate monolayer causes transformation of the alkanoate/Zn^{2+} complex from the bidentate chelating structure to the free acid complex. This will result in increased head-group repulsion with high surface pressures at high molecular areas. Therefore it is possible that at a pH of 5.5 that the monolayer of zinc stearate co-exists as the bidentate chelated structure (figure 5.1) in which bonding occurs by covalent binding to the Zn^{2+} and the free acid structure in which bonding occurs by a non specific ionic interaction with hydrogen.

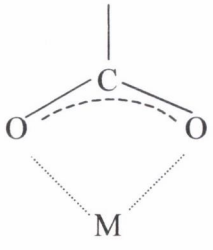

Figure 5.1: Chelating bidentate interaction

[2] P. Martin, M. Szablewski, 'Tensiometers & Langmuir-Blodgett Troughs', Operating Manual 4th Ed. F. Grunfeld, Nima Technology Ltd. (1995).

Moreover, the pK_a value (pH of a half-ionised monolayer) for a stearic acid monolayer on a 10^{-4} mol dm^{-3} Cd^{2+} subphase is reported to be 5.6 with complete ionisation occurring at 6.4[3]. Even at half ionisation, close to the pK_a value it is reported by Yazdanian et al.[14] that a specific type of interaction occurs between the Cd^{2+} and alkanoic headgroups, namely specific covalent binding through a chelating bidentate complex. The higher amount of acid dissociation on a Cd^{2+} subphase in contrast to a Zn^{2+} subphase would explain the increased condensing effect of Cd^{2+} on both stearic acid and palmitic acid monolayers

The sensitivity of oleic acid monolayers to $CdCl_2$ and $ZnSO_4$ introduced into the subphase was investigated in this study as a function of subphase concentration. A decrease in oleic acid molecular area occurs for a corresponding increase in metal ion concentration. This decrease is larger for Cd^{2+} compared with Zn^{2+} for each specific concentration similar to that found with stearic and palmitic acid. Initially, this change in molecular area was assigned to the condensing effect of the metal ions towards the oleic acid monolayer, arising out of a more ordered monolayer film with better packing capability. For this to occur there would certainly be a definite change in isotherm slope as the monolayer becomes more ordered during compression with a significant reduction of the liquid expanded phase and extension of the liquid condened phase. Clearly there is little evidence for a change in phase behaviour and the decrease in oleic acid molecular area can only be attributed to dissolution. The low collapse pressure of oleic acid at each metal ion concentration supports this belief. Thus the decrease in molecular area with increasing Cd^{2+} concentration can only be attributed to oleic acid dissolution into the subphase. There are three possible modes by which Cd^{2+} ions may attract oleic acid monolayers into the subphase:

(i) Cd^{2+} ions may interact with successive carboxylic groups through electrostatic attraction, although if this particular type of interaction was to predominate, it would add considerable order to the monolayer film.

(ii) Specific covalent binding[14] between Cd^{2+} ions and successive oleic acid double bonds close to the air-water interface.

(iii) Specific covalent binding between Cd^{2+} ions and successive undissociated oleic acid molecules.

However there is a significant difference between figures 4.7 and 4.8 in terms of the isotherm positions for a given concentration. Cd^{2+} ions present in the subphase at all concentrations appear to have a greater influence towards reducing the molecular area of oleic acid through dissolution compared to Zn^{2+} ions. This may be attributed to the fact that Zn^{2+} ions are less stable than Cd^{2+} ions in aqueous solution, resulting in the formation of $Zn(OH)_2$ with considerably less attraction towards the monolayer and decreased dissolution as outlined above.

5.1.3 Influence of trivalent cations

The effect of Ti^{3+} ions in the aqueous subphase beneath either stearic or oleic acid monolayers is also reported. Increasing the concentration of Ti^{3+} ions under stearic or oleic acid appears to affect each monolayer differently. Initially it appears that Ti^{3+} ions under stearic acid monolayers cause an increasing reduction in the liquid expanded and gas phase, as the concentration is increased (figure 4.9). It is suggested that the hydrocarbon chains may be tightly packed prior to compression forming a rigid monolayer on the trivalent aqueous subphase. This assumption is supported by the fact that the gas and liquid expanded phase transitions are absent with considerable extension of the liquid expanded and solid regions of the isotherm. However, close examination of the isotherms illustrates that this reduction is largely due to the stearic acid dissolution and complete monolayer instability above 10^{-4} mol dm^{-3} Ti^{3+}. Along with this, the pH of the solution at or above this particular Ti^{3+} concentration is ≤ 4, so that there is very little carboxylic acid dissociation occurring, resulting in very low electrostatic interaction between Ti^{3+} and COOH groups. This view is further supported by the low collapse pressure of 15-20 mN/m observed above10^{-4} mol dm^{-3} Ti^{3+} owing to considerable monolayer instability. The opposite

[3] J. Peltonen, D. Lindén, H. Fagerholm, E. Györvary, F. Eriksson, Thin Solid Films. 1994, 242, 88-91.

effect is observed with oleic acid monolayers in that the isotherms become more expanded on increasing the Ti^{3+} concentration (reducing the pH, figure 4.10). One possible explanation for this dissimilarity in isotherm behaviour may be attributed to the fact that increasing the Ti^{3+} concentration results in a corresponding decrease of subphase pH, since the original stock $TiCl_3$ solution contains 10% by wt. HCl. Increasing the pH of the subphase increases the amount of oleic acid dissociation and may promote improved monolayer packing. This is achieved by the fact that there is reduced hydrogen bonding present, a reduction of the 2-D vacum with a tendency of the film to condense at high molecular areas. The lower molecular area of stearic acid associated with subphases containing trivalent ions is presumably attributed to both the increased Ti^{3+}-stearate interaction and reduced ionic radius of Ti^{3+} (Zn^{2+} - 0.69Å, Cd^{2+} - 0.92Å and Ti^{3+} - 0.62Å) and also increased dissolution.

5.1.4 LB deposition of Cd-St and Ti-St multilayers.

The deposition of both cadmium and titanium stearate onto coated ferric stearate substrates was carried out from aqueous subphases of either 10^{-5} mol dm^{-3} $CdCl_2$ or $TiCl_3$. During LB deposition it is important to maintain the surface pressure within the monolayer at a constant value, so that the density of the molecules is constant and a stable uniform LB layer is formed. It has been reported[4] that monolayer deposition is poor at target pressures below ca. 15 mN/m, when the film exists in its liquid expanded phase. Insufficient monolayer packing leads to poor film transfer.

Successful deposition of Cd-St multilayer films was possible up to target pressures of 25 mN/m compared to 20 mN/m for Ti-St LB films. The presence of trivalent cations in the aqueous subphase facilitated the deposition of stearate films at lower target pressures. In the case of Cd-St, evidence for Y-type deposition is shown by a well resolved XRD figure 4.53.

[4] T. Richardson. Chemistry in Britain 1989, 12, 1218.

5.1.5 Pressure-area isotherms of TiO_2 stabilised sols.

The preparation and π-A characteristics of TiO_2 nano-particle sols have been a subject of this present research. The behaviour of colloidal nanoparticle TiO_2 monolayers was investigated by examining their isotherm behaviour at the air-water interface. Important information regarding monolayer stability orientation and size was recorded by investigating the collapse pressure, shape and molecular area of the monolayer formed. The relative hydrophobicity of TiO_2 nanoparticle sols was established for two cationic surfactants, CTAB and DODAB. DODAB stabilised TiO_2 particles proved to be considerably more stable at the air-water interface which implying that these sols are more hydrophobic than CTAB sols, and they may have potential as transfer material for forming LB films. The increased hydrocarbon content for DODAB (figure 4.20), adds greater hydrophobicity compared to CTAB (figure 4.19). This hydrophobicity was confirmed in this study to add to the overall stability of TiO_2 particles at the air-water interface. The stability of DODAB stabilised TiO_2 particles is reflected in the relatively high target pressure (35 mN/m) reached compared to CTAB (25 mN/m) stabilised TiO_2.

Similar studies were performed using DODAB monolayers spread on a subphase containing $2x10^{-4}$ mol. dm^{-3} sodium polyphosphate ($(NaPO_3)_6$). Sodium polyphosphate is capable of altering the shape of the isotherm. The positively charged DODAB head groups electrostatically attract the negatively charged polyphosphate ions.

There is evidence of phase transitional behaviour associated with DODAB particularly when spread on a aqueous subphase containing polyphosphate ions. Phosphate ions under the DODAB monolayers assist in the packing and organisation of the monolayer at the air-water interface similar to Cd^{2+}, Zn^{2+} and Ti^{3+} ions using carboxylic acids. Further evidence for this is supported by the large decrease in molecular area from 78±2Å^2/molecule for DODAB on pure water to 64± 2Å^2/molecule for DODAB on $(NaPO_3)_6$. In the absence of $(NaPO_3)_6$ there is no evidence for phase transitional behaviour associated with DODAB. Electrostatic

repulsion between adjacent DODAB headgroups is strong and monolayer compression produces an expanded isotherm showing high surface pressures at high molecular areas. The expanded (gas-type) film is evident up to a surface pressure of 45mN/m (figure 4.22). Adding $(NaPO_3)_6$ to the subphase beneath the DODAB monolayer surface has a condensing effect on the DODAB monolayer. Figure 4.23 shows a considerable reduction of the gas phase up to 15mN/m where a change in phase occurs. The plateau observed between 15 and 20 mN/m may be attributed to the co-existence of two phases (liquid expanded and solid phase) arising out of an equilibrium state, set-up by the addition of $(NaPO_3)_6$. There are two contributing factors, which may give rise to the co-existence of two phases they are monolayer condensed (PO_3^- interaction) regions and expanded regions (absence of PO_3^- interaction) at the air-water interface. The decrease in DODAB molecular area on the second compression cycle may be attributed to DODAB dissolution or monolayer condensation. However, since there is no change in isotherm slope this would suggest that the decrease is most likely attributed to surfactant dissolution.

The degree of hydrophobicity associated with DODAB molecules contributes to the increased stability of the molecules at the air-water interface compared to a similar system containing CTAB. A more stable isotherm was recorded for DODAB stabilised TiO_2 compared to CTAB stabilised TiO_2. This is evident from the surface pressure-area curve, figure 4.25, which shows reproducible surface pressure-area isotherms up to 20mN/m. This extremely high area of DODAB stabilised TiO_2 is attributed to the packing arrangement of the cation surfactant around the negatively charged TiO_2. A single DODAB molecule consists of two equivalent octadecyl aliphatic chains, with the hydrophilic head group at the centre as shown in figure 4.20, thus attraction of DODAB molecules towards negatively charged TiO_2 particles will increase the diameter of the sol with the TiO_2 particle at the centre. The formation of TiO_2 particles using DODAB requires many DODAB molecules for complete stabilisation, thus increasing the hydrophobicity and cross sectional area of the sol.

5.2.1 Discussion

The incorporation of dispersed semiconductor particles within polymer, LB membranes and surfactant stabilised sols forming integrated chemical systems possessing new and interesting photophysical and photocatalytic properties have been extensively studied and reported previously with particular emphasis towards CdS. However little attempt has been made so far to prepare TiO_2 particles in polymer films of Nafion, in LB films and surfactant stabilised sols.

With reference to TiO_2 bound Nafion membranes, variations in experimental conditions have been included in this study, such as the time necessary for membrane exposure to Ti^{3+} cations, the concentration of KOH used during forced hydrolysis of Ti^{3+}, the solvent used and the degree of membrane dehydration.

In this particular study, the application chosen for these TiO_2 incorporated films is with a view towards the photocatalytic oxidation of cyanide. Therefore it was desirable to precipitate the maximum amount of TiO_2 both within and at the membrane surface. At the same time it was desirable to control the size of the precipitated particles. These considerations play an important role in enhancing the photocatalytic behaviour of TiO_2 towards contaminants in aqueous solution, as already outlined in section 2.1.3. The time necessary for complete precipitation of TiO_2 particles was investigated. It is clear from these results that TiO_2 particles are precipitated fully after a period of 1.5 hrs, and display blue shifts in the absorption spectra from the bulk band gap energy of 3.2 eV. (387 nm) to a band gap energy of 3.49 eV. No further change in the shape of the onset for optical absorption is observed and there is no evidence of excitonic absorption. It is evident from figure 4.28 that absorption of TiO_2 particles at each time interval is occurring over a wide range of wavelengths, this would indicate a large particle size distribution of TiO_2 within the Nafion membrane, this distribution remains relatively unchanged throughout hydrolysis. One possible explanation for this result is related to the preparation conditions during controlled hydrolysis. If one considers that the

membrane is repeatedly exposed to atmospheric conditions at each time interval during uv-vis measurement and the membrane is also fully hydrated, there is a strong that different polymorphs TiO_2 will form, thus increasing the probability of forming TiO_2 of different particle sizes. However, even after exposing the same Nafion membrane to 0.01 mol dm^{-3} KOH overnight, we still achieve size quantisation with no evidence for bulk TiO_2 formation. This may be attributed to the fact that very little TiO_2 is precipitated using such a low KOH concentration, so that aggregation of TiO_2 particles is not a problem.

5.2.2 Effect of KOH concentration on TiO_2 particle size.

Consequently, TiO_2 particles were precipitated using higher KOH concentrations up to 5 mol dm^{-3}, in order to determine any correlation between KOH concentration and particle size. Prolonged exposure of Nafion membranes containing Ti^{3+} to KOH of different concentrations over a period of 24hrs ensured complete and maximum precipitation of TiO_2 within each membrane. The longer time period associated with TiO_2 precipitation was necessary at high KOH concentrations, because the diffusion capability of Ti^{3+} ions to the membrane surface becomes increasingly more difficult through precipitation. Nevertheless, exposure of each Nafion membrane to KOH over this time period appears to form TiO_2 particles with very little difference in size with respect to their band gap energies. A small increase of band gap energy occurs for particles precipitated using higher KOH concentrations. One possible explanation for this may be as a result of Ostwald ripening, where small TiO_2 particles dissolve and reprecipitate out on larger ones, however there is minimal evidence for this statement.

Furthermore, it would appear that Ti^{3+} exchanged Nafion membranes from aqueous $TiCl_3$ solutions are more suitable TiO_2 precursors forming in some cases smaller TiO_2 particles after hydrolysis with KOH.

5.2.3 Optical properties of TiO_2 incorporated into LB films.

With reference to TiO_2 LB film preparation this technique has not yet become fully exploited owing to the reactive nature of the Ti^{3+} cations to oxidation. Secondly although LB film forming materials of stearic acid are somewhat stable in ambient air conditions, from a practical viewpoint they are unsuitable as hosts for TiO_2 nanoparticles at different solution pH values. It was therefore necessary to fire these films in O_2 after which the resultant TiO_2 showed good stability in aqueous solution at high pH values. The fact that there is no change in the absorption onset after firing the film would suggest that all the Ti^{3+} ions have previously been oxidised to TiO_2. However the stearic acid matrix is successfully decomposed and the film appears to adhere more strongly on the quartz substrate. The absorption of the TiO_2 film extends over a broad range of wavelengths again suggesting a large particle size distribution within the film.

5.2.4 Optical properties of TiO_2 stabilised sols.

This study has been focussed on controlling TiO_2 particle size with the aid of two different surfactant stabilisers, CTAB and DODAB. Briefly, this technique involves the formation of surfactant stabilised TiO_2 sols which are capable of been spread at the air-water interface.

CTAB and DODAB sols showed pronounced capability for restricting particle size distribution, however CTAB shows complete instability compared to DODAB, which shows pronounced stability and significant LB film characteristics. Stabilised TiO_2 films may have potential applications in photocatalysis and solar energy conversion, thus stability of the films is a major requirement and must be investigated.

5.3.1 Discussion

Metal oxides and chalcogenides semiconductor particles suspended in aqueous solutions have been previously reported to show a weak dependence of reaction rate with solution pH[5] [6, 7]. This is somewhat surprising, considering that particle size, particle charge and positions of valence and conduction bands are strongly influenced by pH[8]. Typical reaction rates have been reported to vary by less than one order of magnitude from pH 2 to pH 12. The isoelectric point for TiO_2 in water is about pH 6 with particles exhibiting positive surface charges at lower pH values due to protonation, and negative surface charges at higher pH values corresponding to hydroxylation.

In all of these investigations, hydroxyl and other oxygen containing radicals are known to be necessary to the photocatalytic process[8]. It is proposed that the $OH^{\bullet}$ radical[43] is the primary oxidant predominating in this process. Cyanide photo-oxidation has been investigated in the presence of TiO_2 and O_2 at different pH values ≥ 9 using UV light from a 400W medium pressure mercury lamp. This ensures a high level of OH^- or H_2O groups at the catalyst surface during irradiation. During photolysis, oxidation of OH^- or H_2O to $OH^{\bullet}$ will only occur if the oxidation potentials of these adsorbed electron donors lie above (more negative) the energy of the semiconductor valence band so that the following reactions can occur:

$$Ti^{IV}\text{-}OH^- + h^+ \rightarrow Ti^{IV}\text{-----}OH^{\bullet} \qquad [5.3.1]$$

$$Ti^{IV}\text{-}H_2O + h^+ \rightarrow Ti^{IV}\text{-----}OH^{\bullet} + H^+ \qquad [5.3.2]$$

These processes are measured by the redox potentials, which are a measure of the adsorbents electron affinity with respect to a particular electrolyte. The valence band of anatase and rutile TiO_2 lies approximately at 2.6 V vs NHE at neutral pH and

---

[5] F. Sabin, T. Türk, A. Vogler, J. Photochem. Photobiol. A: Chem. 1992, 63, 99.
[6] H. Harada, T. Ueda, T. Sakata, J. Phys. Chem. 1989, 93, 1542.
[7] J. Sabate, M.A. Anderson, M.A. Aguado, J. Guminez, S. Cerveramarch, C.G. Hill, J. Mol. Catal. 1992, 71, 57.

varies as –0.059 V / pH unit increase. Thus valence band holes are more positive at lower pH values. However under both acidic and basic conditions the oxidation of surface bound OH^- or H_2O by valance band holes is expected to occur within the entire pH range. Similarly the redox potential of the photogenerated conduction band electrons must be sufficiently negative to be able to reduce adsorbed oxygen to the superoxide radical anion $O_2^{-\bullet}$. The position of the conduction band also varies as -0.059 V/pH unit increase. Thus electrons are more readily available at a higher pH values. Adsorbed O_2 is capable of trapping photo induced e^- charge carriers at the semiconductor surface and preventing electron-hole recombination. As a consequence the super oxide radical anion $O_2^{\bullet-}$ is produced and can be further reduced to the peroxide di-anion O_2^{2-} or, alternatively form surface hydroxide species by oxidation of H_2O_2[9] .

In this work TiO_2 was observed to provide an active photocatalyst over long irradiation times using either nano size immobilised or micron size unsupported TiO_2 particles. Previous studies have provided a detailed understanding of the mechanism and surface properties operating in the TiO_2 mediated photocatalytic process[9, 10].

Earlier investigations involving the photo-oxidation of cyanide have shown an independence of reaction rate on cyanide concentration in the range 20 – 2500 ppm ≡ 1-100 mM CN^- at light intensities from a 2.5 kW Hg-Xe lamp[11]. Other investigations have shown a first order dependence of reaction rate on the initial cyanide concentration, however at low light intensities from a 150 W Xe lamp[12]. Rose and Nanjundiah[12] have investigated the decrease of cyanide concentration as a function of pH. Reaction rates were enhanced by using small (0.015-250 μm) platinised TiO_2 (anatase) particles and by decreasing the pH from 11 to 9.

---

[8] A.Mills, R.H. Davies, D. Worsley, Chem. Soc. Rev. 1993.
[9] C.S. Turchi, D.F. Ollis, J. Catalysis. 1990, 122, 178-192.
[10] E. Pelizzetti, C. Minero, Electrochimica Acta, 1993, 38, 47-55.
[11] S.N Frank, A.J. Bard, J. Am. Chem. Soc. 1977, 99, 303.
[12] T.L. Rose, C. Nanjundiah, J. Phys. Chem. 1985, 89, 3766.

In our studies we have observed similar first order dependence on [CN^-] at 20 ppm ≡ 0.7 mM CN^- using irradiation from a 400 W Hg lamp. These results would suggest that the rate of reaction is dependent on the initial cyanide concentration.

5.3.2 Cyanide photo-oxidation at different pH values

In this particular study the rate of photocatalytic oxidation of cyanide was not found to be strongly dependent on pH, showing a increase of reaction rate of less than one order of magnitude between pH 9 and 14. This would suggest that the redox potential of the CN^-/CNO^- couple is largely independent of pH. The effects of pH on the rate constant for photo-oxidation of cyanide using micron sized TiO_2 particles is given in table 4.11(a).

The rate of cyanide photo-oxidation was measured over the pH range 9-14 using 0.1g Degussa P-25 in 100 ml. of a 20 ppm cyanide solution. TiO_2 catalyst is reported to exhibit higher photo-oxidation activity in acidic media [13]. The CN^- is removed as HCN gas and therefore the kinetics associated with CN^- oxidation can only be fully optimised under alkaline conditions. The reaction rate constants obtained in this study appear to increase with increasing pH, however with less than one order of magnitude. From table 4.11(a) it is evident that the change in the reaction rate constant is not directly proportional to the ratio of OH^- and CN^- ions. Previous investigations have reported a zero order dependence on OH^- concentration of the rate of cyanide photo-oxidation. However in this study at pH values below 11 the ratio of OH^- : CN^- is less than 1. It is suggested that both OH^- and CN^- exist at the semiconductor surface at a pH below 11 and at a cyanide concentration of 20 ppm. According to Frank and Bard[14] the following process occurs for oxidation of CN^- on TiO_2 semiconductor particles:

$$TiO_2 + 2h\nu \rightarrow TiO_2^*(2e^- + 2h^+) \qquad [5.3.3]$$

$$CN^- + 2OH^- + 2h^+ \rightarrow CNO^- + H_2O \qquad [5.3.4]$$

$$O_2 + 2e^- + 2H_2O \rightarrow H_2O_2 + 2OH^- \qquad [5.3.5]$$

---

[13] K. Kogo, H. Yoneyama, H. Tamura, J. Phys. Chem. 1980, 84, 1705.
[14] S.N. Frank, A.J. Bard. J. Phys. Chem. 1977, 81, 1484.

The conduction band electrons reduce oxygen, while the valance band holes cause the oxidation of cyanide. At low pH conditions, it is suggested that direct hole scavenging by CN^- may occur at the semiconductor surface to produce $CN^\bullet$ radicals

$$CN^- + h^+ \rightarrow CN^\bullet \qquad [5.3.6]$$

These radicals prevent hole trapping by surface OH^- groups and reduce the number of $OH^\bullet$ radicals formed:

$$2OH^- + 2h^+ \rightarrow 2OH^\bullet \qquad [5.3.7]$$

If as expected, OH^- ions are the limiting reagent the above reaction will occur to a lesser extent. In effect this causes a reduction in both cyanate (CNO^-) formation and thus the decomposition of cyanide is reduced at low pH. The presence of reaction intermediates and end products during cyanide photocatalysis have been previously reported. The OCN^- intermediate is subsequently oxidised to CO_3^{2-} and N_2 at pH 12 according to the following reaction:

$$OCN^- + 2H_2O + 3h^+ \rightarrow CO_3^{2-} + \tfrac{1}{2}N_2 + 4H^+ \qquad [5.3.8]$$

However Pollema and Peral performed similar experiments below pH 10 and observed partial hydrolysis of CNO^- solutions to ammonium as follows:

$$OCN^- + 2H_2O \rightarrow CO_3^{2-} + NH_4^+ \qquad [5.3.9]$$

Similar studies carried out by Rose and Nanjundiah[12] showed an increase in cyanide photo-oxidation with decreasing pH with no direct change in the rate constant with a change in the of OH^-: CN^- ratio. In fact this is not the expected behaviour from a thermodynamic point of view because both the band gap potential of TiO_2 and the redox potential of the CN^-/OCN^- couple show the same pH dependence towards

anodic potentials[15]. This would suggest that CN^- is more easily oxidised at higher pH values. However in the studies carried out by Rose and Nanjundiah the ratio of OH^-: CN^- was always ≥ 1 so that there was always a number of OH^- ions at the semiconductor surface, thus making the approach of CN^- ions to the surface more difficult to achieve at high pH values.

It has been observed from electrochemical studies[16] that the potential of CN^- oxidation is independent of changes in pH. As the pH is reduced, therefore, the increased efficiency of CN^- oxidation reported by Rose and Nanjundiah can be explained by the cathodic shift in the potential of the photogenerated holes towards $OH^\bullet$ formation, with no change in the oxidation potential of the CN^-. This yields a higher rate of cyanide oxidation as pH decreases.

For application as photocatalysts TiO_2 particles must be capable of producing electron-hole pairs which are stable, have low recombination lifetimes and are effective in transferring these charge carriers from the particle surface to the adsorbed species or contaminant[17]. Both anatase and rutile TiO_2 possess these characteristic catalytic properties. Nevertheless large differences do exist between each phase with respect to their over photocatalytic capabilities.

5.3.3 Cyanide photocatalysis using unsupported micron sized TiO_2

In this study the highest observed rate constants were achieved for cyanide photo-oxidation using commercially available micron sized Degussa P-25 samples. As already outlined this particular commercial semiconductor has reasonably well defined nature of 75:25 anatase:rutile mixture, a BET surface area of 55 ± 15 m^2/g, average particle size 30 nm. The valance band positions of both rutile and anatase are comparable, in that they each have similar oxidising capabilities. However large differences in valance band oxidising power do exist and are related to the different charge transfer capabilities of each lattice for the transportation of photo-induced

[15] J.S. Curran, J. Domènech, N Jaffrezic-Renault, R. Philippe, J. Phys. Chem., 1985, 89, 957.
[16] T. Arikado, C. Iwakura, H. Yoneyama, H. Tamura, Electrochim. Acta, 1976, 21, 1021.

holes to the particle surface as outlined by Kunst et al.[18]. With respect to photocatalytic efficiency, the difference between the two modifications usually is explained by the fact that the conduction band of anatase is about 0.3 eV more positive than that of rutile. Consequently, excess electrons in the conduction band of anatase possess higher driving forces towards reduction of adsorbed species or contaminants at the particle surface. Degussa P-25 TiO_2 obtains its characteristic photocatalytic activity from its band structure. Electrons created in the conduction band of the anatase powder may be transferred to the rutile powder, since the conduction band of rutile is lower in energy than the anatase. The fact that the samples are n-doped means there will be more electrons present in the conduction band for transfer to the rutile phase. Furthermore since hole mobility is much lower than electron mobility[18] holes in the valance band of anatase will become deep trapped and this would prevent transfer of holes to the rutile part of the powder thus, preventing recombination and increasing charge carrier lifetimes. Kronos APF which is 100% anatase is less effective than Degussa P-25, 75% anatase, with respect to cyanide photo-oxidation. Other factors affecting rates of cyanide photo-oxidation include the degree of particle protonation, hydroxlation or adsorption of contaminants. In turn these factors depend on the availability of oxygen vacancies at the particle surface. It is well established that Ti^{3+} defect sites can be created on a TiO_2 surface by particle annealing at high temperatures. Increasing the temperature causes an increase in the number of defect sites. On a fully oxidised TiO_2 surface, all the surface Ti cations are in the +IV oxidation state. Increasing the temperature causes desorption of oxygen forming oxygen vacancies.

5.3.4 Immobilised TiO_2 particles and films

Most photocatalyst studies involving cyanide photo-oxidation to date have examined ca. 0.1% w/w suspensions of TiO_2 particles within the size range 0.1-30 μm

[17] A. Wold, Chem. Mater, 1993, 5, 280-283.

depending on the source[19]. Recovery of micron sized and particularly nano-sized semiconductor particles from a treated liquid can be difficult, time consuming and expensive. In order to limit these problems, a number of alternative approaches have been attempted to attach the photocatalyst by means of immobilisation on beads[20], on the inside of tubes of glass[19], teflon[21], fibre glass[22] and woven mesh[23]. The catalytic potential of TiO_2 as evidenced by Ollis et al. have proved that trichlorethane (TCE) and chloroform can be photo-oxidised using a recirculating TiO_2 reactor[24]. Matthews et al. have studied the solar decomposition of a variety of contaminants including phenol and salicylic acid using TiO_2 particles immobilised on a glass mesh, sand or with a glass coil. However, the convenience of catalyst immobilisation as outlined above, is bought at an expense, the major disadvantage being that there is a considerable reduction in reaction rate arising out of decreased photon efficiency. For instance Matthews et al. reports the degradation of phenol at an initial concentration of 100 μM in a free TiO_2 suspension to be 3 times more efficient than that with the photocatalyst immobilised on sand[25].

This decrease of photo-efficiency is associated with the immobilisation of relatively small particles on progressively larger supports and is related to a phenomenon known as 'mass transfer limitation'[26]. Essentially the diffusion distance of solute molecules to the immobilised semiconductor surface is large compared to a fine particle suspension were the distance is relatively small. In the latter case the solute molecules are capable of accepting or donating electron hole pairs to or from the

---

[18] K.M. Schindler, M. Kunst, J. Phys. Chem. 1990, 94, 8222-8226.
[19] R.W. Matthews Australian patent appl.:Canberra, Australia, 7/22/86.
[20] N. Serpone, Solar Energy 1986, 14, 121.
[21] R.W. Matthews, M. Abdullah, G. Low, Anal. Chim. Acta. 1990, 233, 171.
[22] R.W. Matthews, Solar Energy 1982, 38, 405.
[23] M. Robertson, R.B. Henderson. U.S. patent 4,892,712: Washington, DC, Jan. 9, 1989.
[24] S. Ahmed, D.F. Ollis, Solar Energy, 1984, 32, 597.
[25] R.W. Matthews, S.R. McEvoy, Solar Energy, 1993, 49, 507.
[26] R. Venkatadri, R.W. Peters, Hazardous Waste & Hazardous Materials. 1993, 10, 107.

valance and conduction band. Moreover, for a given particle size, the surface to volume ratio of suspended catalytic particles in the bulk solution will always be greater than similar immobilised particles. Consequently there will be greater numbers of photo-active sites available for adsorption of electron donors or acceptors.

These limitations are more pronounced for immobilised photocatalysts and appear to discourage catalyst immobilisation as an efficient technique for effective photocatalyst. Nevertheless, with careful manipulation of particle size it has been observed in this research that photocatalytic activity can be enhanced to a degree where there is very little difference between rate constants for cyanide photo-oxidation using TiO_2 dispersed and immobilised. Maximising both catalyst and photon efficiency is one of the subjects in this present work. Investigations were carried out to immobilise TiO_2 particles of different diameters in both an ion exchange Nafion membrane and as a thin ceramic film using the LB technique. Earlier photocatalytic studies involving first order cyanide photo- oxidation using Degussa P-25 are reported in terms of apparent rate constants and a comparison is made between freely suspended and immobilised TiO_2 in terms catalyst amount and size.

Photocatalytic oxidation of cyanide in the presence TiO_2 is reported in terms of the overall observed rate constant. Each first order rate constant was calculated correspondingly from the slope of a linear plot of ln $([CN^-]_t/[CN^-]_o)$ vs time. For each experiment, data was recorded for the decrease in cyanide concentration over time. This data was analysed using zero and second order rate equations, however the data showed a best fit to first order kinetics. The removal of cyanide from aqueous solutions appears to follow first order kinetics, independently of whether or not the sample is immobilised. This is evident from figure 4.50, which summarises the behaviour of both supported and unsupported TiO_2 towards cyanide during photo-oxidation. A variable induction period is apparent from the kinetic

plots of Ln $[CN^-]_t$/ Ln $[CN^-]_0$ vs time, particularly at high OH^- concentrations as shown in figure 4.47. It appears that below a time period of 20 mins, the level of cyanide in solution remains relatively constant, after which time, the reaction proceeds and a linear decrease in cyanide concentration occurs. To account for this variable induction period, the calculated rate constants were also estimated by neglecting data points at times < 20 minutes.

5.3.5 Cyanide photocatysis using Nafion supported TiO_2

A significant amount of cyanide photo-oxidation occurs for TiO_2 incorporated in Nafion. The destruction of cyanide using Nafion incorporated TiO_2 membranes shows a first order dependence on initial cyanide concentration with a 69% and 56% removal of cyanide over a period 60 mins using Nafion membranes 1 and 2 respectively. These results are reported for TiO_2 incorporated in 2 different Nafion membranes after base hydrolysis with 0.5 and 5 mol dm^{-3} KOH respectively. The absorption thresholds and corresponding band gap energies associated with these TiO_2 particles were given in table 4.7. Increased photo-efficiency was observed for TiO_2 particles precipitated using 5 mol dm^{-3} KOH compared to TiO_2 particles precipitated using 0.5 mol dm^{-3} KOH.

There are a number of possible reasons for this result:

I. The larger band gap TiO_2 (3.9 eV) compared to the bulk material (3.2 eV), precipitated using 5 mol dm^{-3} KOH, provides a larger thermodynamic driving force towards the formation of charge carriers at the semiconductor surface. Subsequently these higher energy charge carriers will have a greater influence for the formation of $OH^{\bullet}$ and $O_2^{-\bullet}$ radicals at the particle surface (as outlined by the reaction mechanism).by hole and electron trapping respectively.

II. The smaller particle size of TiO_2 formed using 5 mol dm^{-3} KOH will in effect reduce the mass transfer limitation and increase photo efficiency.

III. There are a higher ratio of Ti^{IV} sites and shallow energy traps (Ti^{IV}-O^{2-}- Ti^{IV}) available as the particle size is decreased (as shown schematically in figure 2.6 p 25).

IV. The greater photocatalytic efficiency may be attributed to the fact that there is more TiO_2 precipitated at the surface of the membrane using 5 mol dm^{-3} KOH (membrane 2). This assumption is supported by later EDAX analysis (figure 4.60).

A significant amount of TiO_2 is present at the Nafion membrane surface after precipitation using high KOH concentrations. TiO_2 is predominantly precipitated at the Nafion surface as a result of the Donnan effect. A Donnan potential is caused by a build up of negative charge at the membrane surface as the hydroxide ions try topenetrate the surface. In doing so there is an attraction between the anions at membrane surface which draws cations from the membrane interior towards the surface, so that photocatalysis of cyanide occurs predominately at the surface of the Nafion membranes. The apparent first order decrease in cyanide concentration using two Nafion membranes, 1 and 2, (Table 4.10) each containing ca. 1.70×10^{-2} g of TiO_2 was 2.0×10^{-2} min^{-1} and 1.5×10^{-2} min^{-1} respectively. These rate constants compare well to those obtained using freely suspended Degussa P-25 (2.1×10^{-2} min^{-1}) for the same initial cyanide concentration (20 ppm). TiO_2 particles incorporated in Nafion membranes show comparable rate constants using much less catalyst material (16.9mg) as opposed to 0.1g using Degussa P-25. Thus the reduction in catalyst amount and size, highlights the effectiveness of smaller particles, with high surface areas (Table 4.11(a)) towards increased photo-efficiencies. Comapring the Nafion results with those reported by Rose[12] for cyanide photo-oxidation at similar pH values it appears that comparable reaction rates are possible (2×10^{-2} min^{-1}) using 16.9 mg of TiO_2 in Nafion, compared to 1g of unsupported TiO_2 i.e. using 6 times less photocatalyst.

5.3.6 Cyanide photocatysis using LB supported TiO_2

Similar first order kinetics was observed for TiO_2 films towards cyanide photo-oxidation as shown in figure 4.49. TiO_2 membranes formed from LB film precursors, show promising photocatalytic activities for the removal of cyanide from

aqueous solutions. Photocatalytic activity was observed to increase as the amount of TiO_2 increased. Rate constants of $2.27x10^{-3}$ min^{-1} and $3.91x10^{-3}$ were estimated for cyanide photo-oxidation over a period of 1hr using 1.5 μg and 6.3 μg of immobilised TiO_2 respectively. The initial concentration of cyanide was again 20 ppm similar to previous experiments. Again, these rate constants are compared to those of Rose[12] it is plausible to say that TiO_2 formed using LB films shows considerable photo activity using 1.5×10^4 and 6.5×10^5 less photocatalyst. From transmission electron microscopy studies, these ceramic TiO_2 LB films were found to consist of spherical particles with a maximum diameter of 7 nm. However the average particle diameter was estimated by uv-vis measurements to be ca. 2.2 nm.

These results clearly illustrate particle size quantisation effects within TiO_2 LB films. As previously demonstrated for TiO_2 Nafion membranes these films show increased photo-efficiencies compared to Degussa P-25. Although these particles have a large particle size distribution between 2-7 nm, they are still relatively small. This study confirms the potential of Nafion and LB immobilised TiO_2 to be efficient photocatalytic systems. On the basis of catalytic efficiency it is estimated that comparable photo-efficiencies to those of 0.1g Degussa P-25 may be achieved using 61μg of TiO_2 which is equivalent to firing 400 layers of Ti-St. Table 4.11(a) summarises the photocatalytic activity of unsupported and immobilised TiO_2 towards cyanide photo-oxidation.

5.3.7 Langmuir-Hinselwood Kinetics

The importance of substrate pre-adsorption on a given photocatalyst can be probed by the use of Langmuir-Hinselwood kinetics[27,28]. The model has a number of assumptions associated:

I. At equilibrium the number of surface adsorption sites is fixed.

II. Only one substrate may bind at each surface site.

III. Heat of adsorption by the substrate is identical for each site and is independent of surface coverage.

---

[27] B. Jenny, P. Pichat, Langmuir 1991, 7, 947.
[28] R.W. Matthews J. Chem. Soc. Faraday Trans. 1989, 85, 1291.

IV. No interaction between adjacent adsorbed molecules occurs.

V. Rate of surface adsorption is greater than the rate of any subsequent chemical reaction. In the Langmuir-Hinselwood treatment of heterogeneous surface reaction, the rate of photochemical degradation is expressed for the photo-oxidation of cyanide in general terms as follows:

$$-d[CN^-]/dt = k\theta CN^- \qquad [5.3.10]$$

k is the photo oxidation rate constant, θCN^- represents the fraction of adsorbed cyanide to the photocatalyst surface. The equilibrium constant for adsorption of $CN^=$ is assumed to be readily determined from the classical Langmuir adsorption isotherm. In this case, the surface concentration of cyanide is related to the corresponding concentration in the bulk aqueous phase as follows:

$$\theta CN^- = K_{ads}\,[CN^=]/1 + K_{ads}\,[CN^-] \qquad [5.3.11]$$

The rate of cyanide decomposition can be written as a single component L-H rate expression as follows:

$$-d[CN^-]/dt = kK_{ads}\,[CN^=]/1 + K_{ads}\,[CN^-] \qquad [5.3.12]$$

When the concentration of cyanide adsorbed at the semiconductor surface is high, i.e. when $K_{ads}[CN^-] >> 1$:

$$-d[CN^-]/dt = k \qquad [5.3.13]$$

and the reaction is zero order with respect to cyanide oxidation.

During cyanide photo-oxidation, as the reaction proceeds the concentration of cyanide adsorbed at the photocatalyst surface decreases, so that $K_{ads}\,[CN^-] << 1$ so that equation [5.3.10] becomes:

$$-d[CN^-]/dt = kK_{ads}\,[CN^=] \qquad [5.3.14]$$

and the decomposition is first order.

The kinetic data presented in this thesis for the photo-oxidation of cyanide, appears to show Langmuir-Hinselwood behaviour. This is apparent from figures 4.44-4.46 for cyanide photo-oxidation at pH 9, 10, 14. Similar Langmuir-Hinselwood behaviour is exhibited for cyanide photo-oxidation, using TiO_2 incorporated Nafion membranes. This behaviour is evident in all cases and is shown by the initial slow decrease in cyanide concentration, which changes to first order behaviour after an induction period of ca. 20 mins.

5.4.1 Discussion

Powder X-ray diffraction proved to be a particularly useful technique for examining the structure of unsupported micron sized TiO_2. However initial structural investigations involving supported TiO_2 nanoparticles in both LB films and Nafion showed a marked absence of intensity maxima related to any crystalline material present. We have observed well-defined XRD intensity maxima associated with anatase and rutile TiO_2 polymorphs, which were present as a mixture in commercially available Degussa P-25, and as pure anatase in Kronos APF.

5.4.2 X-Ray Diffraction of LB films

Given that LB film transfer was Y-type (determined by examining the direction of the meniscus during deposition) one would expect the thickness of one repeat unit of LB forming material would be twice the length of the amphiphilic molecule placed end to end (length of stearic acid molecule $\cong$ 25 Å)[29] thus the repeat distance of a cadmium stearate bilayer film is ca. 50 Å. The average value obtained in this work was 49 $Å^2$, which is within experimental error and provides evidence that the film is well ordered. A number of factors can however influence this result. When examining the carboxylic acid films formed from a subphase containing multivalent cations, it is necessary to allow for the space occupied by the cations between alternative bilayers. For many LB film materials, stable multilayers are formed in which the hydrocarbon chains are tilted at an angle (often > 30°) from the normal to the surface plane, thus reducing the repeated long spacing associated with the stearate film. There is also the possibility of interdigitation to some degree. This has the effect of reducing the repeat distance and lowering the intensity maxima. The incorporation of Cd^{2+} ions between the headgroups of stearate multilayer films, results in films having long range order in a direction normal to the plane. Cadmium has a high electron density and is therefore useful for obtaining strong diffraction peaks. In no case did we observe crystallinity of TiO_2 particles. There is no evidence for the formation of either anatase or rutile TiO_2, in LB films or Nafion using this technique. With reference to titanium stearate

LB films the XRD figure 4.54 would suggest that there is no evidence for any TiO_2 or Ti-St structure, thus producing a broad diffraction pattern. This broad diffraction pattern between $2\theta = 15°$ and 30° may suggest that the LB technique can induce the formation of amorphous TiO_2. Alternatively, it may also suggest that the stearic acid matrix is out of phase or not sufficiently ordered after TiO_2 precipitation so to give distinct intensity maxima. There is also the possibility that there is an apparent lack of crystallinity due to the fact that the particles are too small and as a consequence diffraction peak broadening[30] becomes important.

In this instance a diffraction pattern was not obtained which may be attributed to the fact that there is only a small amount of TiO_2 present (98 LB layers of Titanium stearate $\equiv 1.5 \times 10^{-2}$ mg of TiO_2 at 100 % deposition of titanium stearate compared to powder samples 2-3 mg).
The lack of diffraction intensity associated with Ti-St or TiO_2 films may be attributed to the following:

I. Titanium stearate is unstable and the Ti^{3+} species is readily oxidised to TiO_2 reducing the order of the film as shown by the corresponding XRD figure 4.54.

II. It is possible that the packing of titanium stearate during film transfer is not as well defined as cadmium stearate because of the trivalent nature of this ion and subsequent attraction of three carboxylate groups as opposed to two using Cd ions.

III. For a LB film containing 98 layers of titanium stearate the maximum amount of TiO_2 formed even after firing of the film is merely 1.5×10^{-2} mg, so that there is insufficient material present for any significant diffraction to occur. It might be argued that the amount of material present is not that much different to that used for cadmium stearate films. However Cd-St LB films showed

[29] R.H. Tredgold. 'Order in thin organic films'. Cambridge University Press. 1994

diffraction, possibility due to the high electron density of cadmium which is helpful in obtaining relatively strong diffraction peaks compared to Ti-St with titanium having a lower electron density.

Finally, the decomposition product of these fired LB films showed no XRD activity owing to the insignificant amount of TiO_2 present (3.8×10^{-2} mg, film 1, table 4.5, p96). Other factors affecting the XRD intensity may include: the low electron density of Ti and the fact that with such thin films a beam of X-rays normal to the film intercepts too thin a layer of material to give an easily detected diffracted beam. With such films it is necessary to focus the beam a few degrees from the tangent to the film using low angle X-ray diffraction[29].

5.4.3 X-Ray Diffraction of TiO_2incorporated Nafion membranes

For TiO_2 incorporated in Nafion membranes, the membrane itself is simply too amorphous to distinguish any crystalline material when measuring diffraction from such small amounts of material. The scarcity of crystallinity associated with TiO_2 exchanged Nafion may be attributed to the following:

I. X-Ray diffraction associated with TiO_2 particles must be sufficient to overcome the background signal associated with the amorphous Nafion membrane.

II. The apparent lack of crystallinity may be due to the fact that the particles precipitated at the membrane surface are presumably too small making it almost impossible to obtain a consistent intense scattered signal.

The resolution of X-Ray diffraction maxima will decrease with decreasing crystallite size and increasing disorder within the crystal. In fact for crystallite sizes < 500 Å[58] diffraction peak broadening becomes significant and will result in a broad amorphous type pattern.

---

[30] B. Wunderlich, 'Macromolecular Physics' Academic Press, 1973.

5.5.1 Discussion.

Scanning electron microscopy was to some extent useful in this study for examining the morphological nature of Ti-St LB films and Nafion containing TiO_2. Ti-St LB films examined by SEM showed a cracked surface and film delamination. For Nafion bound TiO_2, this technique was particularly poor for measuring particle size at Nafion surface. A low SEM magnification was used to prevent sample decomposition, however at the expense of low particle size resolution.

5.5.2 EDAX analysis of LB films and Nafion membranes containing TiO_2

EDAX was used in conjunction with SEM analysis and this technique proved particularly more fruitful. EDAX patterns were obtained for fired LB films of Ti-St, figure 4.57 and Nafion membranes containing TiO_2, previously precipitated using different concentrations of KOH, figures 4.59 and 4.60.

EDAX analysis of fired Ti-St films (TiO_2) showed no difference of intensity maxima at 4.5 eV for Ti throughout the entire film, this would indicate an homogeneous film throughout. The same technique showed a marked difference of intensity with respect to Ti at 4.5 eV for TiO_2 incorporated in Nafion. The intensity was greater (1009 FS) for TiO_2 precipitated in Nafion using 5 mol dm^{-3} KOH compared to a lower intensity (372 FS) for TiO_2 precipitated in Nafion using 0.5 mol dm^{-3} KOH. These results would suggest that there is a greater amount of TiO_2 at Nafion surfaces after precipitation with KOH 5 mol dm^{-3}

There are a number of additional factors affecting film stability:

I. Evaporation of trace amounts of sorbed water from the stearate matrix during analysis may cause film shrinkage and cracking.

II. In addition to water loss there is also a probability that TiO_2 precipitation within the matrix causes disorder and strain between successive stearate headgroups. This assumption is supported by the fact that TiO_2 particles

contain negative surface charges, consequently they may repel adjacent carboxylic head groups this reduces film order.

From LB studies a single stearate molecule over a Ti^{3+} ion subphase is estimated to have a cross sectional area of ca. 21-22$Å^2$ per molecule. This low molecular area of the stearate is associated with ionic attraction of Ti^{3+} ions towards the carboxylic head groups. After precipitation this ionic attraction will be reduced and the polar carboxylic head groups may repel each other, causing film disorder.

5.6.1 Discussion.

Transmission electron microscopy (TEM) together with electron diffraction (ED) were both particularly useful techniques for examining the particle size and crystallinity of TiO_2 which was previously precipitated in Nafion membranes and from LB films. ED studies also provided evidence for CdSt LB film formation.

Figure 4.61 shows the corresponding TEM after firing an LB film (98 layers) of Ti-St at 450° for 2hr. This micrograph shows particles with a maximum diameter of 70Å. ED analysis of the same sample figure 4.62, shows gives lattice spacings (table 4.13) which compare well to those for anatase TiO_2. TEM and ED data was also recorded for 130 layers of Cd-St, figure 4.63 and 4.64 shows the corresponding TEM, and ED pattern recorded for this sample. The TEM is clear and the presence of CdO is absent, the electron diffraction pattern exhibits crystallinity. Table 4.14 shows the corresponding d-spacings. These results compare well with those reported for stearic acid (JCPDS 9-618). Figure 4.64 shows an intense diffraction pattern with a radius of 7 mm corresponding to a d value of 0.422 nm. Using the Bragg equation [4.4.1] it is possible to calculate the appropriate diffraction angle (2θ), this was estimated to be 21.03° and corresponds to the most intense diffraction maximum when compared to stearic acid (JCPDS 9-618 and 9-612) as shown in table 4.14. Lower angles of diffraction associated with cadmium stearate are known to exist and were recorded as shown in the corresponding XRD, figure 4.53. Electron diffraction shows a marked absence of diffraction spots for angles below 20°.

With reference to TiO_2 incorporated Nafion membranes there is evidence for TiO_2 precipitation at different KOH concentrations for all membranes as shown by TEMs figures 4.65-4.69. Moreover it appears that TiO_2 particles having larger diameters (10 nm) are precipitated using higher concentrations of KOH (5 mol dm^{-3}) and vice versa. However, the average particle diameter was estimated to be 21.5Å by relating the particle absorption threshold (337 nm, 3.68 eV) for this film to the particle diameter

as previously described by Fendler[31]. The average particle diameter of 21.5Å, together with a maximum particle diameter of 70Å would suggest that there is indeed, a large particle size distribution throughout the sample or that the TEM illustrates particle aggregates of size 70Å made up of individual particles of 21.5 Å. This particle size distribution is observed in figure 4.32, by absorption over a wide range of wavelengths.

[31] Y. Tian, C.Wu, J.H. Fendler, J. Phys. Chem. 1994, 98, 4913-4918.

5.7.1 Discussion of AFM results

We have demonstrated the ability of the AFM to non-destructively determine the quality of LB films of fired titanium stearate. The AFM was incapable of resolving individual molecules of titanium stearate or TiO_2. The lack of molecular resolution may be attributed to the particular AFM mode used during this investigation, with the non-contact mode the image is relatively poor because the image data is a convolution of the macroscopic shape of the tip. This mode is ineffective for molecular resolution as outlined in section 3.4.3, p65. Molecular resolution also requires completely smooth and highly orientated surfaces such as HOPG or mica. We have not attempted to examine the samples using the contact mode, because of the possibility of tip damage during measurement, clearly more work is required in order to determine its feasibility.

Nevertheless the non-destructive nature of the AFM technique, particularly for examining TiO_2 catalyst films, makes this technique particularly useful in this study. Surface uniformity of fired titanium stearate LB films has been confirmed using this technique. Ti-St samples show a lack of order, there is a definite change in surface roughness after deposition of 14 layers of titanium stearate as shown in figure 4.73. Examination of the z-height profile in both the x and y direction shows a difference in z-height of 50 nm and 67 nm receptively attributed to the increase in surface roughness. Assuming a chain length of 2.5 nm for stearic acid, one would expect a z-height difference of 35 nm + 0.86 nm, allowing for Ti^{3+} ions between alternative stearate head groups. Clearly this is not the case, the lack of film order and significantly high z-height difference may be attributed to the following:

I. It is possible that interdigitation is occurring between successive titanium stearate monolayers thus, resulting in non-uniform transfer of titanium stearate. The increase in z-height from the expected value may be attributed to the presence of non-uniform ferric stearate on the glass slide.

II. It is also possible that titanium stearate is unstable and the Ti^{3+} species is readily oxidised to TiO_2, reducing the order of the film.

Chapter 5: Section VII: Atomic Force Microscopy.

The formation of TiO_2 LB films from Ti-St precursor shows a significant difference in surface roughness. After firing the film at 450°C for 2 hrs, the film appears more uniform. However this film suffers from tip sample convolution, which is a characteristic (figure 4.75) of blunt tips. The tip image is superimposed on the sample surface. Tip sample convolution can arise out of blunt tips, which attempt to image surface features smaller in dimensions than the tip apex, in such a case the sample feature actually images the tip. Figure 4.77 illustrates this phenomenon.
Areas of poor LB film deposition are also identified (figure 4.78) at the dip start and end positions during film transfer.

Chapter 6

General conclusions and future work.

Chapter 6: General Conclusion and Future work.

From the results reported in this thesis, it would appear that there are useful applications associated with LB films, Nafion ionomer membranes and surfactant stabilised sols, each containing TiO_2 particles. The incorporation of TiO_2 particles was carried out within each of the above mentioned heterogeneous hosts. The photophysical and photochemical properties of TiO_2 were examined as a function of decreasing its particle size. Initial investigations were devoted to the chemical precipitation of TiO_2 nanoparticles within each host material.

Nafion

In the case of Nafion bound TiO_2 membranes, it was found that by variation of the reaction conditions, mainly changing the KOH concentration during hydrolysis, it was possible to precipitate TiO_2 particles preferentially at the membrane surface or evenly throughout the membrane. Controlled base hydrolysis of Ti^{3+} exchanged Nafion membranes, monitored using uv-vis spectroscopy, yields extremely small particles of size 17.9-18.7Å forming particle aggregates of 100Å with very little difference in terms of their respective absorption maxima, irrespective of the particular solvent used. Wavelengths between 314-320 nm, associated with TiO_2 band gap absorption were recorded for particles precipitated using KOH in the concentration range 0.01-5 mol dm^{-3}. The corresponding band gap energies and average diameters of these particles are in the range 3.88-3.95 eV and 17.9-18.3Å respectively. It should be noted that such particles are above the threshold at which size quantisation effects are evident for TiO_2.

EDAX studies indicate that TiO_2 was most abundant at Nafion membrane surfaces using higher concentrations of KOH, typically 5 mol dm^{-3} during hydrolysis of Ti^{3+} to TiO_2. TEM data indicates that the particles, which were formed, exist as clusters with diameters of up to 150 Å and the particle size decreased with decreasing KOH concentration. Such a high cluster diameter clearly indicates that particle aggregation occurs within these membranes.

Evidence for the crystallinity of such particles is altogether absent from electron diffraction studies, which shows, after many attempts, an amorphous ring structure. It should also be noted that wide angle X-ray diffraction was not productive in assigning a particular phase to TiO_2 particles, since diffraction peak broadening becomes significant for crystalline particles less than 50 nm. There is also the problem of the amorphous background diffraction pattern associated with Nafion membranes, which may superimpose any diffraction maxima associated with TiO_2.

Initial photochemical studies focussed on examining the photocatalytic behaviour of micro-sized unsupported TiO_2 particles, namely Kronos APF and Degussa P-25, from two different commercially sources. These studies were undertaken in order to determine the rate constants associated with cyanide photo-oxidation. The I.S.E. method was the principal method adopted for measuring the decrease of cyanide concentration over time. Cyanide photo-oxidation was examined at different pH values, and the rate was not found to be strongly dependent on pH. Conditions for cyanide photo oxidation were optimised and the photocatalytic efficiency of unsupported micron-sized and supported nano-sized particles, in terms of the overall rate constants for cyanide photo-oxidation, were compared.

The photocatalytic behaviour of TiO_2 incorporated in Nafion has been investigated. Results recorded would suggest that: photocatalytic oxidation of aqueous cyanide solutions using Nafion bound TiO_2 membranes is quite possible. The most efficient TiO_2 Nafion membrane used for the photo-oxidation of cyanide was that prepared by forced hydrolysis using 5 mol dm^{-3} KOH. The TiO_2 particles precipitated in these membranes are efficient in the reduction of oxygen, a fundamental requirement for trapping conduction band electrons and promoting hydroxyl radical formation through valance hole trapping. Charge transfer from the semiconductor surface to adsorbed electron donors or acceptors occurs mostly at the Nafion surface. Evidence for this is based on the fact that TiO_2 particles are mainly precipitated at the surface using 5 mol dm^{-3} KOH, and a membrane so treated shows greater photocatalytic activity than a similar membrane containing less TiO_2 at the surface.

The first order rate constants recorded for the decrease in cyanide concentration, using Nafion membranes containing TiO_2, (precipitated using KOH 5 mol dm^{-3}) appear similar (2.1×10^{-2} mol^{-1} min^{-1}) to those reported for micron sized Degussa P-25 (2.1×10^{-2} mol^{-1} min^{-1}) TiO_2. However these rate constants were recorded using considerably less photocatalyst (17μg for Nafion and 0.1g Degussa P-25). The photo-oxidation of cyanide using TiO_2 incorporated Nafion membranes also shows very little interference due to mass transfer effects.

In general it can be said that TiO_2 bound Nafion membranes show different photophysical and consequently photochemical effects compared to the free bulk oxide material. This is most likely the result of changes in band gap energies associated with decreasing particle size, with a corresponding blue shifts of the absorption spectra. The decrease of particle size results from the restricted membrane area during precipitation.

It was thought initially that the increase in photocatalytic activity was primarily attributed to the larger band gaps associated with these particles, however uv-vis studies indicate an absorption over a wide wavelength range corresponding to a large particle size distribution and decreased quantum efficiency. Enhanced rates of photocatalytic activity at present may be attributed to increased cyanide adsorption on TiO_2 particles with high surface areas, since the surface to volume ratios of these particles are large.

LB studies

The second heterogeneous host investigated for the incorporation of TiO_2 particles involved the use of a multilayer mono-molecular LB film matrix. The isotherm behaviour of stearic and oleic monolayers over subphase solutions of divalent ions such as Cd^{2+} and Zn^{2+} was first investigated. Phase behaviour for these materials is reported in terms of the overall stability, shape and position of each isotherm.

The results indicate that it is possible to form stable monolayer films of Cd-stearate and Cd-oleate or Zn-stearate and Zn-oleate using between 10^{-3} and 10^{-5} mol dm^{-3} $CdCl_2$ and $ZnCl_2$ solutions. These isotherms show high collapse pressures up to 40 mN/m for Cd

$ZnCl_2$ solutions. These isotherms show high collapse pressures up to 40 mN/m for Cd or Zn stearate and 28 mN/m in the case of Cd or Zn oleate with reduced molecular areas of 21-25Å^2 and 25-30 Å^2 respectively.

The study was extended to trivalent ion subphases such as Ti^{3+} ions. Using Ti^{3+} ions instead of Cd^{2+} or Zn^{2+} there is a marked reduction in stearate film stability as the concentration of Ti^{3+} is increased. This reduction in film stability may be attributed to the increased charge and subsequent attraction of each Ti^{3+} towards multiple carboxylic head groups. This instability becomes significant and is apparent by collapse pressures as low as 20 mN/m at concentrations below 10^{-5} mol dm^{-3} $TiCl_3$. These isotherms also show fewer phase transitions as the area is reduced.

Highly oxidising Ti^{3+} ions have been incorporated into LB films of stearic acid, with the aim of forming mono-disperse, photochemically active TiO_2 particles possessing different photophysical properties compared to their bulk analogues. The process involved precipitation of TiO_2 between the head groups of stearic acid using forced hydrolysis with KOH as used with Nafion-TiO_2 membranes. However the films were unstable to a change in pH and readily dissolved on immersion in buffer pH 10.

TiO_2 ceramic films were formed by firing Ti^{3+}-stearate films at 450°C in air for 2hrs. Transmission electron microscopy indicates the particles formed to be less than 70 Å in diameter. Evidence for crystallinity of such particles can be found from electron diffraction data, which identifies TiO_2 in anatase form. Rutile TiO_2 is absent, this is not suprising if one considers that annealing temperatures of >800°C are necessary for its formation.

X-Ray studies proved ineffective for such TiO_2 films to clearly assign a crystalline form and diffraction peak broadening may be important at such low crystal dimensions. Using energy dispersive X-ray analysis (EDAX) it was found that a significant amount of Ti was present at the surface of the films, presumably as TiO_2. Spot analysis of the film after firing indicated no loss of Ti at different areas on the film surface.

Uv-vis spectroscopy results indicated the presence of extremely small particles of average diameters 21 Å exhibiting blue shifts in the absorption at 337 nm (3.68 eV) compared to 387 nm (3.2 eV) for bulk TiO_2. Again TiO_2 particle aggregation is apparent when comparing TEM and UV particle results as outlined in section 4.6.2.

AFM data was recorded for both non heat-treated and heat-treated samples of titanium stearate. Results indicate that Ti-St films are unstable after transfer. The films are particularly non-uniform at the dip start and dip end positions during transfer. The non-uniformity is shown by large pinholes present in the TiO_2 film after firing.

Similar photocatalytic experiments to those using Nafion membranes were performed with fired LB films (TiO_2) of Ti-St. The decrease in cyanide follows first order kinetics as before and the concentration of cyanide capable of being photo-oxidised appears to increase as the amount of TiO_2 present in the film increases. For a TiO_2 film fired from 10 layers of Ti-St (1.5μg TiO_2), the observed rate constant for cyanide photo-oxidation using this film was found to be 2.3×10^{-3} mol^{-1} min^{-1}. This rate constant increased to 3.9×10^{-3} mol^{-1} min^{-1} for a similar system containing 42 layers of fired Ti-St (6.3μg TiO_2).

Surfactant stabilised sols.

The third host material investigated for the precipitation of TiO_2 nanoparticles involved the use of surfactant stabilised sols. TiO_2 particles were precipitated within CTAB or DODAB surfactants by forced hydrolysis of TTIP. UV-vis results suggest that both CTAB and DODAB sols are capable of stabilising and preventing TiO_2 particle aggregation over a period of at least 1 month. The corresponding sols show blue shifts (compared to the bulk material 3.2 eV) in their absorption spectra with very little difference in their absorption onsets, 329 nm and 336 nm, corresponding to band gap energies of 3.77 eV and 3.69 eV respectively.

The isotherm behaviour associated with spreading each of these sols at the air water interface is reported. CTAB TiO_2 sols show poor stability even at low target pressures and subsequent dissolution into the subphase.

The isotherm behaviour associated with spreading each of these sols at the air water interface is reported. CTAB TiO_2 sols show poor stability even at low target pressures and subsequent dissolution into the subphase.

By comparison, DODAB sols show greater stability and more promising isotherms for effective film transfer. Both CTAB and DODAB monolayers are represented by a gas-type isotherm, which suggests that there are strong forces of repulsion between surfactant molecules during compression. In an effort to oppose this repulsion, further studies were undertaken involving DODAB TiO_2 sols spread on a subphase containing sodium polyphosphate. The introduction of polyphosphate ions into the subphase beneath a monolayer of DODAB TiO_2 sol appears to effect the position and shape of the isotherm. A change in monolayer phase occurs for the DODAB sol at 15mN/m corresponding to a molecular area of ca. 12,600 $Å^2$ / particle. This high molecular area associated with DODAB TiO_2 sols is attributed to the fact that DODAB molecules contain two large hydrocarbon groups. Transfer of the same sol material onto hydrophobic substrates is proposed in future work.

Future work

The pressure area isotherm behaviour associated with a number of 'conventional' LB film forming materials was reported in section 4.1 of this thesis. Such monolayer materials are useful for examining the fundamental characteristics such as monolayer stability, collapse pressure and molecular area on different multivalent metal ion subphase solutions. However their mechanical, thermal and chemical properties are occasionally not as robust as desired, particularly for applications as photocatalysts.

A study is proposed for using alternative monolayer films such as high molecular weight polymers, which can be polymerised either before or after deposition. Molecules containing the diacetylene group, acrylic and diene derivatives may have interesting π-A characteristics when compressed and transferred from Cd^{2+}, Zn^{2+} and Ti^{3+} subphase solutions. Moreover, when these molecules are exposed to high-energy UV radiation,

they may polymerise and offer greater film stability by preventing TiO_2 particle dissolution.

The precipitation of less TiO_2 particles in Nafion using the ion dilution technique is also proposed, firstly by exchanging Ti^{3+} and Ca^{2+} ions within the membrane with subsequent exposure of each membrane to KOH. This may have the effect of increasing contaminant adsorption, increasing charge carrier separation with an overall increase in photocatalytic efficiency.

There already exist, a large number of reports outlining pollution degradation and subsequent mineralistion of many contaminants, including cyanide, to less harmful inorganic products. The kinetics and mechanisms associated with the photo degradation of these contaminants using micron size TiO_2 is already well established. With this wealth of information, there exists the possibility for examining and comparing the photocatalytic degradation of alternative model contaminants using TiO_2 LB films as described previously in section 3.3 c).

Degussa P-25, which consists of 75% anatase, 25 % rutile, exhibits the highest photocatalytic activity, which may be attributed to electron flow from anatase to rutile TiO_2. On the basis of this phenomenon, it is proposed that a number of TiO_2 samples be produced as before, however containing a composite mixture of anatase and rutile TiO_2.

Finally, we might also suggest extending the formation of surfactant stabilised TiO_2 sols capable of being transferred onto suitable substrates and expand these studies to ZnO, CdS and ZnS sols. We might also examine the possibility of electron transfer from the semiconductor particle surface across the surfactant material and investigate the photocatalytic activity of the unsupported and immobilised sols towards cyanide degradation.